

ABSTRACT

HARIBAL, VASUDEV PRALHAD. Light Alkane Valorization using a Redox Approach.
(Under the direction of Dr. Fanxing Li).

Availability of shale gas, coupled with an increasing demand for chemicals due to growing population, has shifted the focus towards fuel-to-chemical conversion, with methane and ethane being the primary feedstocks. Chemical Looping processes offer efficient, cost-effective and environmentally friendly options for these fuel-valorization routes. This is achieved through a cyclic redox scheme where the gaseous oxidants are replaced by the oxygen from the lattice of an oxygen carrier, also called a redox catalyst. Production of syngas and olefins like ethylene, which constitute a crucial block of the petrochemical industry, can be intensified *via* chemical looping. They also have the ability to valorize CO₂ and water into carbon monoxide and hydrogen respectively. The redox properties of the oxygen carrier, which are crucial for this process, can be tuned by changing the intrinsic redox properties or modifying the catalytic surface. Process simulation and analyses serve as guidelines for further development and also provide a broader perspective. With the aim to push the conversion of lower-chain alkanes to chemicals using redox approaches, this study focuses on *i*) the development of an active and low-cost material for methane-to-syngas and steam-to-hydrogen conversion; *ii*) low temperature CO₂-to-CO conversion with the ability to utilize the industrial waste heat; *iii*) an energy and exergy analysis for intensification of ethylene production using ethane and naphtha and *iv*) the development of an efficient modular scheme to obtain liquid fuels from ethane.

Firstly, a rationalized strategy to optimize transition-metal-oxide-based redox catalysts for hydrogen production from steam and syngas generation from methane, in a hybrid solar-redox scheme is proposed and validated. Experimental studies on BaMn_{0.5}Fe_{0.5}O_{3-δ} confirm the Density

Functional Theory (DFT) predictions, demonstrating 90% steam conversion and over 90% syngas yield under repeated redox cycles. Compared to the state-of-the-art processes, it can provide a 10-fold increase in splitting steam into hydrogen at a significantly lower temperature.

Later, to tackle the global CO₂ emissions, a Hybrid Redox Process (HRP) is presented, where lanthanum-modified ceria, promoted by rhodium, is shown to convert CO₂ to CO and methane to syngas for low temperature (<700 °C) operations. Near-complete CO₂ conversion with a syngas yield of up to 83% are achieved. Along with low-temperature CO₂ utilization, this scheme provides an attractive route for chemical production from CO₂ and methane, with the integration of industrial waste heat leading to appreciably lowered overall CO₂ emissions.

In the following section, the Chemical Looping-Oxidative Dehydrogenation (CL-ODH) process to produce ethylene from ethane, is simulated with AspenPlus® using experimental data on a Mn-based redox catalyst and compared with steam cracking. Results indicate that the CL-ODH process, with 85% single-pass ethane conversion, provides 82% reduction in overall energy demand and CO₂ emissions. With the help of exergy analysis, this study demonstrates the potential of CL-ODH to transform ethylene production.

Further, to better utilize the low-value ethane at isolated sites, a Modular Ethane-To-Liquids (M-ETL) system is reported, which can efficiently convert ethane and natural gas liquids to gasoline using chemical looping strategies. Process analysis of this simplified scheme showing a reduced energy demand, along with an experimental proof-of-concept on M-ETL CL-ODH, is carried out. It is demonstrated that a simple, single-pass configuration can be economically viable at geographically isolated gas processing facilities.

To expand the scope of CL-ODH, the Redox Oxy Cracking (ROC) process is introduced, which can intensify conversion of naphtha to ethylene and propylene. The ROC process is modeled with AspenPlus® based on experimental data from recently developed redox catalysts. Compared to traditional naphtha cracking, the ROC process can provide up to 52% energy and CO₂ savings. Moreover, it produces 28% more ethylene and propylene per unit mass of naphtha feedstock.

© Copyright 2019 by Vasudev Pralhad Haribal

All Rights Reserved

Light Alkane Valorization using a Redox Approach

by
Vasudev Pralhad Haribal

A dissertation submitted to the Graduate Faculty of
North Carolina State University
in partial fulfillment of the
requirements for the degree of
Doctor of Philosophy

Chemical Engineering

Raleigh, North Carolina
2019

APPROVED BY:

Dr. Fanxing Li
Committee Chair

Dr. Phillip R. Westmoreland

Dr. Gregory Parsons

Dr. Joseph DeCarolis

DEDICATION

To *Amma, Appa and Vaju Anna* who are the pillars of my life

This is in loving memory of my dear *Annajja*, Dr. Govardhan M. Katti, who will always be an archetype of grit, hard work, finesse and love; and my dear *Tai Ajji*, Shobha H. Haribal, whose wit and fortitude is awe-inspiring. This is for you. I wish you were here.

“There’s a pleasure in finding things out”

Richard P. Feynman

BIOGRAPHY

Vasudev Pralhad Haribal was born in Miraj, Maharashtra, India, a place known for its rich history and expertise in medical-care and design of musical instruments, to parents Pralhad and Nitya Haribal and as a younger brother to Vadiraj Haribal. In 1994, his family moved to Sohar, the ancient capital city of Oman, where he completed his elementary school. They moved back to Miraj in the 21st century, where he finished high school. Drawing inspiration from his father's process engineering experiences, in 2010, Vasudev joined the Department of Chemical Engineering at the Institute of Chemical Technology (ICT, formerly UDCT), in the most populous Indian city of Mumbai, for his baccalaureate studies. He was awarded the Summer Research Fellowship in 2012, by the Indian Academy of Sciences, to work with Prof. I. S. Shivakumara, at the Centre for Advanced Studies in Fluid Mechanics, Bengaluru, India, on applications of porous media flow. Upon graduating with a B. Chem. Engg. in 2014, he pursued graduate studies in chemical engineering at North Carolina State University, located in Raleigh, NC. Under the guidance of Prof. Fanxing Li, Vasudev worked on the development of chemical looping materials and processes for conversion of fossil fuels. In 2016, he received an M.S. in Chemical Engineering from NC State University. He also completed an internship, in 2018, with the Technology and Innovation team at SABIC, Mt. Vernon, IN, where he developed process models for different units in polycarbonate manufacture. During his time at NC State, Vasudev received recognition for his work at multiple conferences and symposiums. He is a passionate public speaker, a lifelong Toastmaster and a seeker.

ACKNOWLEDGEMENTS

“If I have seen further, it is by standing on the shoulders of Giants” – Sir Isaac Newton

There are many people in my life, from both personal and professional spheres, without whom I could not have walked this path and pursued this Ph.D. I cannot thank everyone who made this happen, but I would like to acknowledge several lives who have played a crucial role.

Appa and Amma: It all started with your teachings, guidance, direction and inspiration. Your constant support and encouragement is always empowering. All your sacrifices and hard work have brought me here. A mere ‘Thank you’ will never be enough. *Vadiraj:* I am walking the steps, which you have recently traversed. I have always learnt by mimicking you and you are the best person I have and will ever know. Your calmness, love and care is what has kept me on. I have always wanted to see you do the graduation walk and I know it will happen soon. *Vaju Anna,* I cannot imagine this without you. *Annajja and Ammamma:* You have always been my idol. It is your efforts that have laid the foundations for your grandchildren to learn and prosper. Always busy and always curious to learn new things. Hope I can be like you one day. Your unconditional and all-inclusive love for everyone are unparalleled. *Mama Ajja,* no one is fitter than you at 90! *Tai Ajji:* Your fighting spirit, even during the worst of hardships, has always been inspiring. I wish you were here.

Dr. Fanxing Li: I am privileged to be your student. Your passion and love for research is addictive and has motivated me in this journey. I am forever grateful for your support, encouragement, idea-stimulation and guidance. Thank you for your patience with me as I grew and learned to be a researcher. I hope I did not let you down. I am thankful to you for providing me with the opportunities both within and outside our lab. It has been a wonderful experience.

I would like to thank *Dr. Phillip Westmoreland, Dr. Gregory Parsons and Dr. Joseph DeCarolis* for serving on my dissertation committee. Thank you for your encouragement, helpful feedback, and guidance over the last 5 years.

Dr. Luke Neal: You were the go-to person for any question, clarification or query regarding any research hurdle; ranging from an equipment malfunction to checking simulation numbers to working principle of an instrument to technical writing. Thank you for teaching and mentoring me. Thank you for all your help and for those countless discussions and brainstorming sessions. I apologize for those delays in reaching the soft deadlines! *Dr. Junshe Zhang:* Your relentless application to work and accuracy was something I respect a lot. You taught me so many things, when I was new to the group. Working with you was enriching. I will never forget the teachings, both technical and philosophical, that I got from you. *Dr. Amit Mishra:* You were a great support and like an elder brother to me. I will miss all the great discussions about food (and research as well) and even our experiments (with food of course). I want to thank the entire *Li Research Group*, past and present, for their friendship, support and patience. I am grateful for the support and camaraderie provided by Seif Yusuf (you got the Ph.D. before me), Yunfei Gao and Ryan Dudek. Ryan, I wish you all the best! I want to specially thank Arya, Nathan and Feng, who welcomed me to the group in 2014 and helped me get started. I would have loved to work more with Emily Krzystowczyk and Daniel Jackson, but whatever I have got, I had a lot a fun. I hope Coach Emily will eventually be less intimidated by me (she has CLAS though). I also want to thank the other members of the group: Yuan Tian, Dr. Jian Dou, Dr. Xijun Wang, Junchen Liu, Toluwalashe Omotunde, Leo Brody, Qiongqiong Jiang, Dr. Xing Zhu, Dr. Fang Hao and Dr. Yun Chen. Thanks to the undergraduate students who worked with me in the lab: Dylan Jackson, Pedro Ramos and especially Courtney Paulus.

There is no celebration or joy of success without family. All the members of my family have a major role to play in my achievements. Thank you for your love and support: Raju Mama (Sameer Katti, the handsome trend-setter) and Sukanya Mami, Jaggu Mama (Jagadish Katti, the bold and caring, I miss you!) and Shobha Mami, Pammu Mama (Dr. Pramod Katti, the one who I resemble the most) and Suma Mami. I want to thank all my ever-energetic cousins, the Katti Gen-Z, for their encouragement and love: (eldest to youngest) Vasudha, Nidhi, Sharadhi, Madhwesh and Bhargavi. Satya Maushi, Santosh Uncle, Medha Maushi and Srinivas Uncle have given me a home, away from home and I am very grateful for all the love.

Diidaa: How can I forget my dear, stylish and suave Dii: Rinita Banerjee! She has been my strong support system in Raleigh. Thank you for all those endless discussions about Bollywood songs, binge-watching Criminal Minds, Law and Order: SVU, Person of Interest and for the countless number of times you made the vintage Aaloo Capsicum (potato and green pepper curry) for me! That would just light up my day after a bad outing in the office. Thank you, Dii! I really wish you were here for this!

Sudarshan: My buddy, Sudarshan, has been my best friend and my confidant, since 2010. He constantly inspires me to be better and always has something new to teach in every encounter of ours. We have been in this chemical engineering journey of 9 years together: competing, discussing, learning and growing and I wish it continues. Thank you for being Sudarshan Ganesh, my funny, honest, smart, straightforward and bold friend!

ICT faculty and friends: I owe a lot to my alma mater, the prestigious *Institute of Chemical Technology, Mumbai*. This is where I learnt all the chemical engineering. Right from the inspirational speech by Dr. Vilas Gaikar (VGG) on Day 1 (26th July 2010) to the ultra-engaging

lectures of Mass Balance and Transport Phenomena by Dr. Ashwin Patwardhan (AWP): this is what inspired me to continue my journey with chemical engineering. I want to thank Dr. Yatin Gokarn (my senior design advisor), Dr. Mohan Narayan and Dr. S. Kasturirangan (for those captivating statistical mechanics classes), Dr. Sharad Sontakke and Dr. Anand V. Patwardhan (AVP) (for his enthusiasm and passion for the field). Special mention to all my friends from the 2014 batch of ICT (formerly UDCT): Abhilasha (and her cool quantum dots), Bhagyasha, Rutvik Marathe (thank you for being there), Deeksha Jain, Aakash Kategeri, Jignesh Vanjaria and Manjiri Moharir.

SABIC Team: I would like to thank the Technology and Innovation team at SABIC, Mt. Vernon, IN: Dr. Prashant Kumar for being a friend and mentor (and for those cricket discussions), Dr William Hollar (my role-model in process development industries), Dr. Joe Anderson, Dr. Jim Schobbo and Dr. Rahul Patil. I would also want to thank Sid Panditrao and Sripradha Suresh for being such great company in the summer of 2018.

Campus Toastmasters: Thank you for being a supportive and enthusiastic group. I got so much to learn from you guys: Julie Long (your bird speech was my first impression of Campus TM), Elizabeth de Jongh/da Bombo (or Jane Goodall, angry young girl: have fun in NZ), Thomas Long (when are you going to Oxford?), Angkana Bode (ever-enthusiatic and smiling), Linda Schumacher (witty statistics person), Nathalia Morales, Harish Rao Balaji (Table Topics champ), Rushikesh Ghatpande (bigger Table Topics champ), George Naderman (expert story-teller), Erwann Domalain (humorous guy), Theresa Piskáčková (soon to be a Weed Science Dr.) and all the other members! I am grateful to friends that made my time in Raleigh special, meaningful and provided support through difficult times: Dr. Dishit Parekh (you were of great help when I first

came to Raleigh), Dr. Anurodh Tripathi, Dr. Rohan Patil (fellow sci-fi enthusiast), STP Bharadwaja, Dr. Ishan Joshipura, Arnab Bose, Prachi Yadav, Amulya Pervaje and Han Jin.

Finally, I want to thank my teachers and friends from ‘back-home’ in Miraj and Sohar: Ravindra Shinde Sir (thanks for introducing the idea of chemical engineering to me), late Shrikant Abhyankar Sir (thank you for making Math so much fun), Mhaskar Sir (thank you teaching Physics the way you did), Ramachandran Sir (will never forget your Math and Science problems) and all my teachers who helped in laying the educational foundation and creating curiosity in me; (soon to be Dr.) Kulsum Syeda (my oldest friend), Anagha Balakrishnan (my lucky mascot), Dr. Neha Chadha (the great plastic surgeon), Dr. Dhruv Patil (the Doc), Remo Ingty (the cool guy from Buraimi) and Dr. Anish Isapure (the stylish orthopaedic surgeon). You all have had a great influence on me on a personal level. Thank you for that!

TABLE OF CONTENTS

LIST OF TABLES	xiii
LIST OF FIGURES	xv
CHAPTER 1 : INTRODUCTION.....	1
1.1 UTILIZATION OF FOSSIL FUEL RESERVES	1
1.2 GREENHOUSE GAS EMISSIONS	1
1.3 TOWARDS CHEMICAL PRODUCTION	3
1.3.1 <i>Chemicals from natural gas</i>	4
1.3.2 <i>From naphtha</i>	9
1.3.3 <i>From carbon dioxide</i>	10
1.4 TOWARDS SUSTAINABLE PROCESSES.....	11
1.4.1 <i>Chemical Looping</i>	11
1.5 SUMMARY	18
1.6 REFERENCES	21
CHAPTER 2 : IRON-DOPED BAMNO₃ FOR HYBRID WATER-SPLITTING AND SYNGAS GENERATION WITH EXCEPTIONAL CONVERSIONS.....	27
2.1 ABSTRACT	28
2.2 INTRODUCTION	28
2.3 RATIONAL STRATEGY FOR REDOX CATALYST OPTIMIZATION.....	32
2.4 EXPERIMENTAL VALIDATION OF THE REDOX CATALYST PERFORMANCE	37
2.5 CONCLUSIONS	40
2.6 EXPERIMENTAL SECTION	41
2.6.1 <i>Material synthesis</i>	41
2.6.2 <i>Characterizations</i>	42
2.6.3 <i>DFT Calculations</i>	42
2.6.4 <i>Fluidized bed experiments</i>	42
2.7 REFERENCES	44
CHAPTER 3 : MODIFIED CERIA FOR LOW-TEMPERATURE CO₂ UTILIZATION: A CHEMICAL LOOPING ROUTE TO EXPLOIT INDUSTRIAL WASTE HEAT.....	47

3.1	ABSTRACT	48
3.2	INTRODUCTION	48
3.3	RESULTS AND DISCUSSION.....	53
3.3.1	<i>HRP Redox Catalyst Design</i>	53
3.3.2	<i>Effect of La³⁺ substitution: DFT Calculation</i>	54
3.3.3	<i>Effect of Rh-promotion</i>	57
3.3.4	<i>Redox Catalyst Performance in HRP</i>	59
3.3.5	<i>Process Analysis</i>	61
3.3.6	<i>Potential Impacts</i>	63
3.4	CONCLUSION.....	64
3.5	EXPERIMENTAL PROCEDURES	65
3.5.1	<i>Material synthesis</i>	65
3.5.2	<i>Material characterization</i>	66
3.5.3	<i>Redox experiments</i>	67
3.5.4	<i>DFT Computation Methods</i>	67
3.5.5	<i>Process simulations</i>	69
3.6	ACKNOWLEDGEMENTS.....	70
3.7	REFERENCES	71

CHAPTER 4 : OXIDATIVE DEHYDROGENATION OF ETHANE UNDER A CYCLIC REDOX SCHEME – PROCESS SIMULATIONS AND ANALYSIS 74

4.1	ABSTRACT	75
4.2	INTRODUCTION	76
4.3	PROCESS DESCRIPTIONS	79
4.4	SIMULATION ASSUMPTIONS.....	85
4.5	PROCESS MODELING.....	87
4.6	RESULTS AND DISCUSSION	89
4.6.1	<i>Reactor product distributions</i>	89
4.6.2	<i>Energy distribution</i>	90
4.6.3	<i>Process comparisons</i>	91
4.6.4	<i>Emission comparisons</i>	98
4.7	SENSITIVITY ANALYSIS	100

4.7.1	<i>Ethylene yield</i>	100
4.7.2	<i>Effect of pressure drop</i>	105
4.7.3	<i>Regenerator air requirements</i>	106
4.8	FURTHER MODIFICATIONS IN ENERGY ANALYSES.....	107
4.9	SECOND LAW ANALYSIS.....	110
4.10	BROADER IMPACT.....	115
4.10.1	<i>CO₂ emission reduction</i>	115
4.10.2	<i>Transforming ethylene production</i>	117
4.11	CONCLUSION.....	119
4.12	ACKNOWLEDGEMENT.....	120
4.13	REFERENCES:.....	121
CHAPTER 5 : MODULAR SCALE ETHANE TO LIQUIDS VIA CHEMICAL LOOPING OXIDATIVE DEHYDROGENATION – REDOX CATALYST PERFORMANCE AND PROCESS ANALYSIS.....		124
5.1	ABSTRACT.....	125
5.2	INTRODUCTION.....	126
5.3	SUMMARY OF RESULTS.....	130
5.4	MATERIALS AND METHODS.....	131
5.4.1	<i>CL-ODH Catalyst Testing</i>	131
5.4.2	<i>Oligomerizer Product Distributions</i>	132
5.4.3	<i>Process simulation and Economic Analysis</i>	133
5.5	DISCUSSION.....	134
5.5.1	<i>Product distributions of CL-ODH and oligomerizer</i>	134
5.5.2	<i>Product Analysis and Process Configurations</i>	135
5.5.3	<i>Preliminary Techno-economic Analysis</i>	138
5.6	CONCLUSIONS.....	141
5.7	ACKNOWLEDGMENTS.....	141
5.8	REFERENCES.....	142

CHAPTER 6 : INTENSIFICATION OF ETHYLENE PRODUCTION FROM NAPHTHA VIA A REDOX OXY-CRACKING SCHEME – PROCESS SIMULATIONS AND ANALYSIS	144
6.1 ABSTRACT	145
6.2 INTRODUCTION	145
6.3 PROCESS DESCRIPTIONS	148
6.4 SIMULATION ASSUMPTIONS.....	152
6.5 RESULTS AND DISCUSSION	158
6.5.1 <i>Effect of feed compositions</i>	158
6.5.2 <i>Energy distributions in steam cracking</i>	160
6.5.3 <i>Process comparisons</i>	161
6.5.4 <i>Net demand and emission comparisons</i>	165
6.6 CONCLUSION.....	168
6.7 ACKNOWLEDGEMENT	169
6.8 REFERENCES	170
CHAPTER 7 : CONCLUSION AND FUTURE WORK	172
7.1 CONCLUSION.....	172
7.2 OUTLOOK.....	176
7.3 FUTURE WORK	176
7.3.1 <i>Towards low temperature methane partial oxidation and CO₂-utilization</i>	176
7.3.2 <i>Kinetics of ethane CL-ODH</i>	178
7.4 REFERENCES	191
APPENDICES	193
APPENDIX A: SUPPLEMENTARY INFORMATION FOR CHAPTER 2	194
APPENDIX B: SUPPLEMENTARY INFORMATION FOR CHAPTER 3.....	209
APPENDIX C: SUPPLEMENTARY INFORMATION FOR CHAPTER 4.....	230
APPENDIX D: SUPPLEMENTARY INFORMATION FOR CHAPTER 5	246
APPENDIX E: SUPPLEMENTARY INFORMATION FOR CHAPTER 6.....	253

LIST OF TABLES

Table 3.1: Near surface atomic compositions of the redox catalysts (oxygen free basis, numbers shown in parentheses correspond to expected compositions based on bulk stoichiometry)	56
Table 3.2: Exploitable High Temperature Waste Heat sources and CO ₂ -utilization capacity	64
Table 4.1: ASPEN Plus® modules, property methods and databanks	85
Table 4.2: Carbon yield for the two cases.....	86
Table 4.3: Simulation conditions and assumptions.....	89
Table 4.4: Column details	89
Table 4.5: Choice of refrigerant.....	91
Table 4.6: Exit gas and solid streams.....	93
Table 4.7: Comparison of the energy consumption	96
Table 4.8: $\Delta H_{\text{reaction}}$ and molar flow rate of the fuel	99
Table 4.9: Carbon yield for the different ethane ODH cases considered	101
Table 4.10: Exit gas composition of the ethane ODH cases.....	102
Table 4.11: Section wise Energy/Fuel Demand of Steam Cracking and ODH 85	110
Table 4.12: Section-Wise Exergy Loss Analysis.....	112
Table 4.13: CO ₂ production by source (tonne/tonne HVP)	115
Table 5.1: Required selling price of a barrel of liquid product at an initial capital cost of \$100,000/daily barrel capital cost and 25% gross margins	130
Table 5.2: Estimate of ethylene oligomerization product distributions from literature and Schulz-Flory distribution for C10+	132
Table 5.3: CL-ODH Product distributions (water free basis).....	135
Table 6.1: ASPEN Plus® modules, property methods and databanks	154
Table 6.2: Carbon yields for the cases investigated.....	155

Table 6.3: Simulation conditions and assumptions.....	157
Table 6.4: Details of the distillation columns	158
Table 6.5: Overall and unit-wise energy distribution for naphtha feed	159
Table 6.6: Comparison of the energy demands	163
Table 6.7: $\Delta H_{\text{reaction}}$ and molar flow rates of the byproduct (fuels)	166
Table 7.1: Models and the sources for kinetic modeling	182
Table 7.2: Product distribution for various models	183
Table 7.3: Comparing the output of SHC reaction addition with ethane cracking.....	190

LIST OF FIGURES

Figure 1.1: a) Past and predicted energy consumption in the U.S (source-wise) ^[1,3,4] ; b) Estimated U.S consumption in 2018 (end-use and source-wise) ^[5]	2
Figure 1.2: Past and predicted CO ₂ emissions in the U.S. (end-use and section-wise) ^[6,8]	3
Figure 1.3: Global population and percent contribution of the middle class ^[12,13]	4
Figure 1.4: U.S production of fossil-fuels ^[2] [1 BOE = 5.8 MMBtu]; b) Fossil-fuel feedstock values since 2001 ^[2] (average annual).	5
Figure 1.5: Chemical-production routes using syngas ^[17]	7
Figure 1.6: Chemicals produced from ethylene and propylene ^[17]	8
Figure 1.7: Conceptual illustration of the process for valorization of CO ₂ ^[11]	11
Figure 1.8: Schematic of chemical looping processes along with the diverse use of fuels, oxidants and products.	12
Figure 1.9: Schematic of chemical looping oxidative dehydrogenation (CL-ODH).....	15
Figure 2.1: (a) Ellingham diagram for the hybrid solar-redox reactions(the P _{O2} axis is at 950°C); (b) Equilibrium syngas yield (in methane PO _x) and steam conversion (in water-splitting) at different P _{O2} and temperatures (the boundaries of the shaded regions map the syngas yields at the specified temperatures; the corresponding colored dashed lines define the isothermal steam conversion lines).	33
Figure 2.2: DFT-calculated $\Delta E_{\text{vacancy}}$ for the materials and the corresponding equilibrium P _{O2} at 900°C. The grey dotted lines denote constant P _{O2} lines.....	36
Figure 2.3: (a) XRD patterns of as-prepared, reduced and oxidized BMFO; (b) in-situ XRD patterns under redox conditions; (c) Typical syngas yield profile during the methane PO _x step (H ₂ :CO = 2.1:1); (d) Instantaneous product distribution (N ₂ and H ₂ O-free basis) and steam conversion during the water splitting step as a function of time at 900 °C (cycle 15 data shown here); (e) Methane conversion, CO selectivity, steam conversion, and hydrogen purity (average value of the last five redox cycles with the error bars denoting 95% confidence interval); (f) Reported steam conversion and syngas yield	38
Figure 3.1: a) Schematic of HRP (considering acetic acid as the final product); b) Paths to synthesize chemicals from CO and syngas, obtained via HRP.	51

Figure 3.2: a) Computed energies of oxygen vacancy formation (ΔE_V); b) Energy barriers for oxygen vacancy migration for bulk and (111) surface of CeO_2 and $LaCeO_{3.5}$; c) Energy potential profile along the most favorable oxygen migration pathway on the (111) surfaces of CeO_2 and $LaCeO_{3.5}$; d) Electronic projected density of states (PDOS) of CeO_2 and $LaCeO_{3.5}$.	55
Figure 3.3: a) X-ray diffractogram for Rh-promoted ceria and LCO; b) CH_4 TPR + <i>in-situ</i> XRD on Rh/LCO; c) CH_4 TPR of Rh/LCO, LCO and ceria.	58
Figure 3.4: a) Performance comparison of Rh/LCO with Rh/Ceria for methane conversion; b) Representative product distribution for Rh/LCO under the HRP scheme at 650°C; c) Redox cycle results of Rh/LCO at 650°C: CH_4 and CO_2 conversion (X), CO selectivity (S) and Syngas yield; d) Phases of as-prepared and cycled Rh/LCO, showing stability over multiple redox cycles.	60
Figure 3.5: a) Schematic of HRP and CG (coal gasification), with similar downstream units [CG route requires H_2 and CO_2 removal to obtain syngas and pure CO]; b) Comparison of HRP with CG, using various parameters.	62
Figure 4.1: a) Simplified process flow diagram of ethane cracking process [DM: Demethanizer, DA: Deacetylenizer, DE: Deethanizer, DP: Depropanizer, DB: Debutanizer, C2 split: C2-splitter, C3 split: C3-splitter, PSA: Pressure Swing Adsorption] b) Simplified schematic of the cyclic redox ODH (CL-ODH) process (temperatures for key units and streams are listed for the reference case).	80
Figure 4.2: a) Section wise energy distribution and b) overall energy distribution for a steam cracking process.	95
Figure 4.3: Comparison of the energy distributions.	97
Figure 4.4: Relative energy demand (section wise and overall).	98
Figure 4.5: (Thermal) Energy surplus and emissions.	100
Figure 4.6: Thermal energy (MW_{th}) comparison for the ethane ODH cases.	103
Figure 4.7: % Reduction in the energy demand.	104
Figure 4.8: Thermal energy distribution comparison.	104
Figure 4.9: Thermal energy demand and emission comparison.	105
Figure 4.10: Effect of pressure drop.	106

Figure 4.11: Effect of excess air on the thermal energy demand (MW_{th}).	107
Figure 4.12: a) Modeling the ethane steam cracking furnace ^[32] ; b) AspenPlus® flowsheet for steam cracking with the furnace ^[6,32,33]	109
Figure 4.13: Idealized exergy conversion/loss for cracking and CL-ODH schemes at 850°C (GJ/tonne ethylene).	111
Figure 4.14: Process schematic and exergy/lost work (LW) schematic of a) Steam cracking of ethane and b) CL-ODH of Ethane [Results are in GJ/tonne of high value products (HVP)].	113
Figure 4.15: CO ₂ emissions of Steam Cracking and ODH processes under various assumptions:	117
Figure 4.16: Comparison of ethylene production techniques (Y is Yes and N is No).	118
Figure 4.17: Representative ethylene selectivity vs ethane conversion chart.	119
Figure 5.1: Simplified CL-ODH based M-ETL scheme	129
Figure 5.2: a) Product distributions in the single-pass case per 1 MJ of ethane feed for both the Base Conversion Case and High Conversion Case; b) Composition (carbon basis) of gaseous and liquid fractions from the post oligomerization flash.	136
Figure 5.3: Required selling price of liquids assuming \$24/MWh electricity cost, 10% ROI, and 25% gross margins a) vs. capital cost of the system at \$0.05/gal. ethane, and b) vs. the cost of ethane at a capital cost of \$75,000/daily barrel. “Base-Ideal Recycle” case assumes constant conversions a pass of the “vapor” through a second unit.	138
Figure 5.4: a) Value of products per bbl. liquids produced in the “Base” case vs price of electricity credit and liquid fuels price; b) Value of products per bbl. liquids produced vs. liquids vs. value of electricity when the electricity credit is capped at \$5.76/bbl.	140
Figure 6.1: a) Simplified process flow diagram of naphtha cracking process b) Simplified schematic of the ROC process.	150
Figure 6.2: Composition to represent complex naphtha, a) based on ^[2] and b) based on ^[22]	154
Figure 6.3: Section-wise energy distribution for naphtha cracking.	160
Figure 6.4: Section wise energy distribution for hexane cracking and ROC.	162

Figure 6.5: Comparison of the energy distributions in steam cracking and ROC processes.....	164
Figure 6.6: Normalized energy demand (section wise and overall) in steam cracking and ROC processes.	164
Figure 6.7: Schematic for net energy demand analysis.	166
Figure 6.8: Net (Thermal) Energy demand for ethylene production.	167
Figure 7.1: Concept of combining materials ^[7] : a) IC + EC; b) IC + MIEC; c) MIEC + MIEC [σ is the conductivity, ionic and electronic.	178
Figure 7.2: Ethane TPR results for mass 26 (ethylene), mass 18 (water) on Mn-Mg based CL-ODH redox catalysts ^[8]	179
Figure 7.3: Schematic for depicting the overall Cl-ODH reaction through kinetics.	180
Figure 7.4: Schematic for simulation of ethane cracking in a PFR using AspenPlus® and the corresponding ethane conversion (or ethylene yield, as only one reaction is considered).	181
Figure 7.5: Chemkin®PRO set-up.....	183
Figure 7.6: Product distribution of Model 4 ^[7] (isothermal) vs. reference literature values.....	184
Figure 7.7: Results from Model 4 ^[7] ; both isothermal and with a T-profile.....	185
Figure 7.8: Temperature profile in the cracking tube for different feeds [subset is the T-profile for ethane].	186
Figure 7.9: Compounds formed at different temperatures ^[7] as part of MWG reaction products (<i>highlighted ones are the important products in the CL-ODH study, based on experimental results shown in Chapter 4</i>).	187
Figure 7.10: Output results with and without the insertion of SHC reaction to Model 4.	188
Figure 7.11 Chemkin®PRO set-up for staged O ₂ injection to sliced PFR reactor scheme.	189
Figure 7.12: Rationale for integration of a UDF for capturing the CL-ODH kinetics.	190

CHAPTER 1: INTRODUCTION

1.1 Utilization of fossil fuel reserves

Fossil fuels, which include petroleum, coal and natural gas, are currently the world's primary energy source^[1-3]. Formed from organic material over the course of millions of years, fossil fuels have fueled the United States and global economic development, accounting for at least 80% of energy consumption in the U.S. for well over a century^[3]. In 2018, the overall energy consumption in the country reached 101 quadrillion British thermal units (Btu), of which >81 quadrillion Btu (or Quads) or 80% was from fossil fuels. The increase in fossil fuel consumption in 2018 was driven by increases in petroleum and natural gas consumption as shown in **Figure 1.1a**, with the dependence on coal falling to the lowest level since the 1970s^[1,3,4]. Four broad sectors utilize these fossil fuels, with specific distribution presented in **Figure 1.1b**, based on the survey of U.S. energy flow charts from Lawrence Livermore National Laboratory^[5].

1.2 Greenhouse Gas Emissions

The utilization of different fossil fuels leads to carbon emissions. The U.S. Energy Information Administration (EIA) predicts the overall energy-related CO₂ emissions to drop roughly by 4% by 2050 when compared to 2018^[6-9]. This is in line with the Paris Agreement, which aims to keep a global temperature rise this century well below 2°C above pre-industrial levels^[4,5,10]. Carbon dioxide (CO₂) intensity (emissions per energy unit) can vary greatly depending on the consumption of the mix of fuels in different end-use sectors. Historically, the transportation sector has had the highest CO₂ intensity, which continues in the projection because carbon-intensive petroleum remains the dominant fuel used in vehicles. Contributions from natural gas and renewables to the electric-power sector cause 25% decline in CO₂ emission from the mid-2000s to 2018 and this

trend would continue through 2050^[6,8]. As shown in **Figure 1.2**, the industrial sector is projected to increase its share by 13% and natural gas by 21%. Within the industrial sector, 78% is consumed in manufacturing activities, the contribution of which is projected to dominantly increase in 2050.

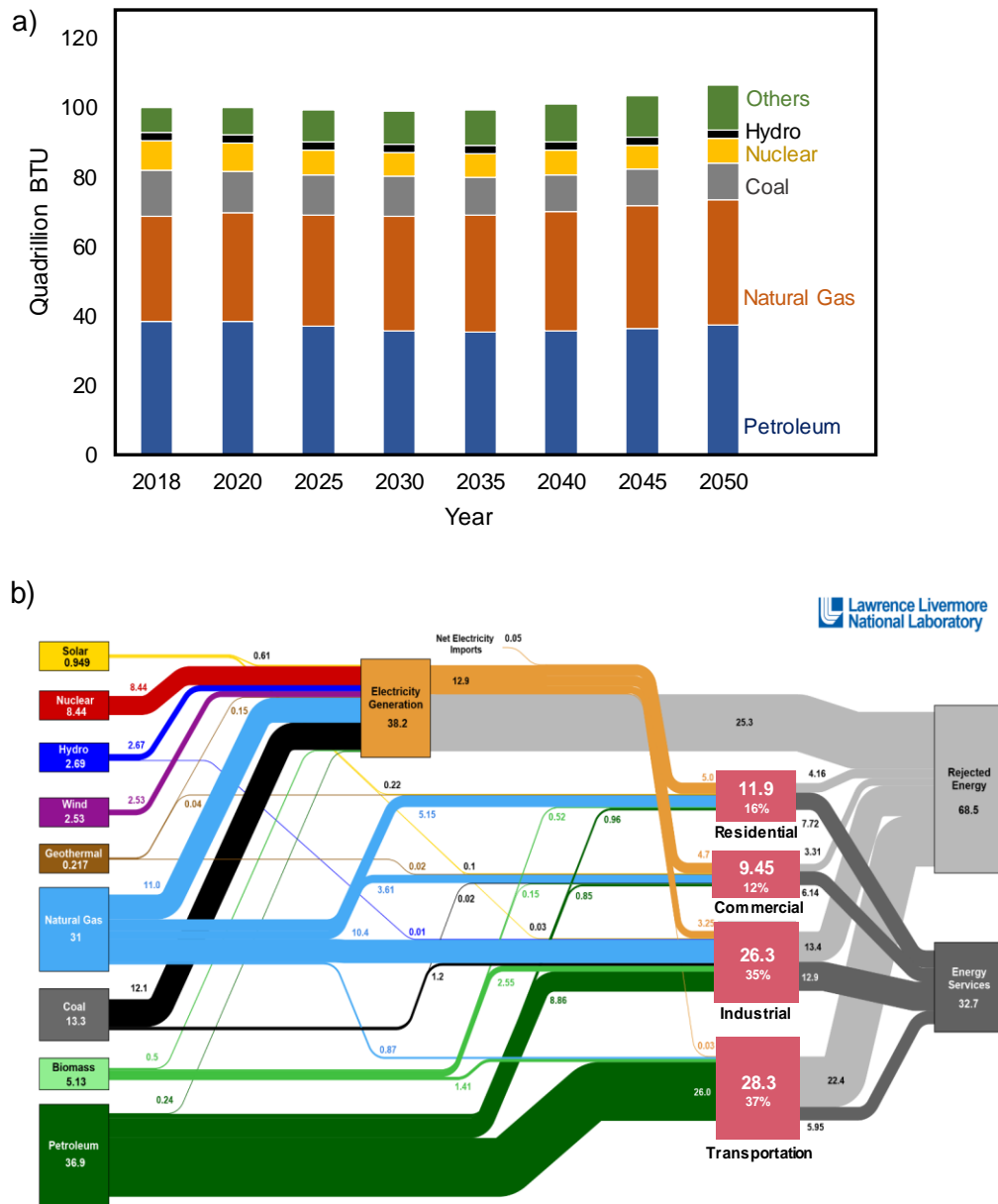


Figure 1.1: a) Past and predicted energy consumption in the U.S (source-wise)^[1,3,4]; b) Estimated U.S consumption in 2018 (end-use and source-wise)^[5].

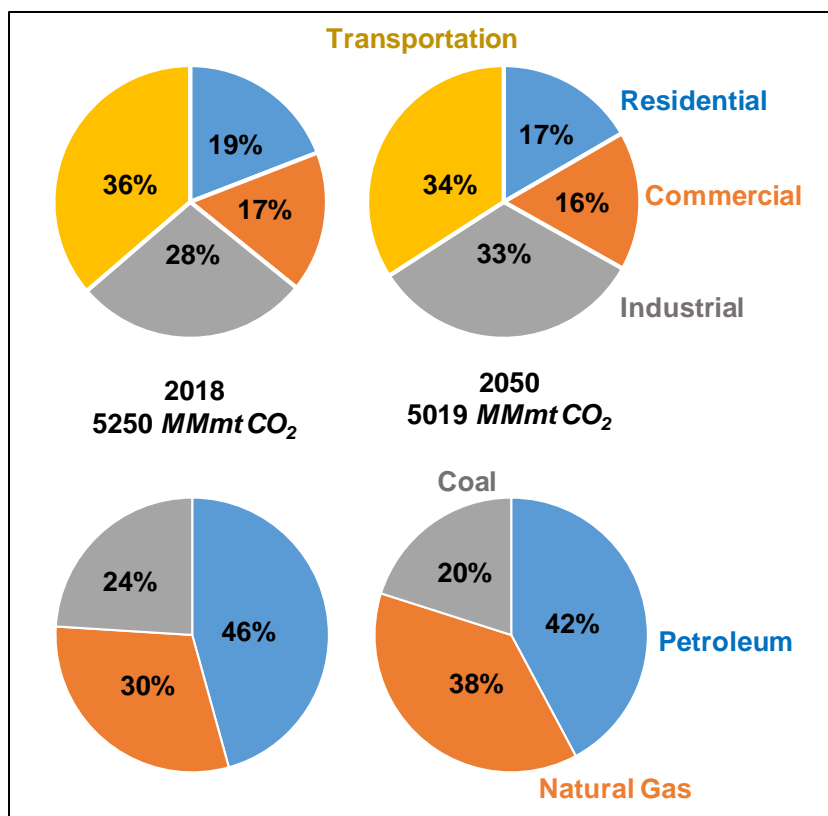


Figure 1.2: Past and predicted CO₂ emissions in the U.S. (end-use and section-wise)^[6,8].

1.3 Towards chemical production

An important utilization of the industrial fossil fuel-feed is the transformation to chemical products. The chemical industry comprises of companies converting raw materials into different products. It can be broadly classified into the following two categories^[10,11]:

- The *basic chemicals industry*, which manufactures polymers, bulk petrochemicals and intermediates, other derivatives and basic industrials, inorganic chemicals, and fertilizers.
- The *specialty chemicals* or *fine chemicals industry*, which produces electronic chemicals, industrial gases, adhesives and sealants as well as coatings, industrial and institutional cleaning chemicals, and catalysts.

Based on the LLNL surveys, roughly 50% of the industrially utilized resources from petroleum and natural gas are used for chemical production. From **Figure 1.1b**, 67.9 Quads come from these two main sources, out of which roughly 10 Quads are consumed for chemical production. Hence, in 2018, 15% of the utilized petroleum and natural gas ends up in chemicals. The United Nations projects the world population to hit 9.77 billion in 2050, with a major share being the global middle-class, as shown in **Figure 1.3**^[4,12,13]. The middle class comprises of those households with an annual income for a four-person middle-class household, of \$14,600 to \$146,000^[13]. This creates a need to boost the production of chemicals, which is crucial in serving the increasing population.

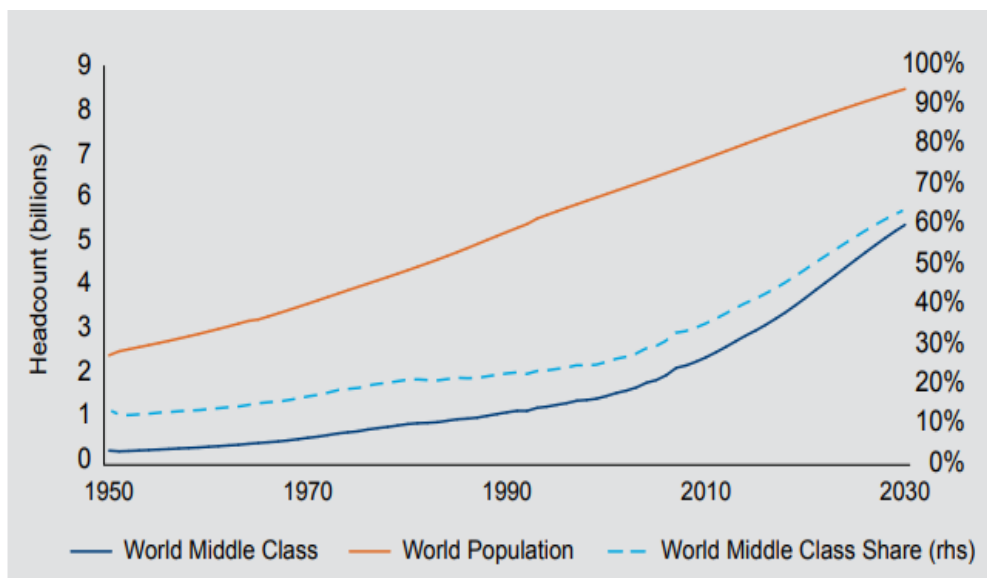


Figure 1.3: Global population and percent contribution of the middle class^[12,13].

1.3.1 Chemicals from natural gas

The shale gas revolution, which is now approximately 12 years old, has already had a profound impact on the U.S. energy and chemical production^[2,14]. Basically, shale gas is natural gas found in shale formations. It consists mostly of methane with varying amounts of heavier alkanes, carbon

dioxide, nitrogen, helium, hydrogen sulfide, and water. Shale gas with significant amounts of higher alkanes which can range from ethane up to pentane is considered ‘wet’. These shales were deposited as fine silt and clay particles at the bottom of relatively enclosed bodies of water. Some of the methane that formed from the organic matter buried with the sediments escaped into sandy rock layers adjacent to the shales, forming conventional accumulations of natural gas, which are relatively easy to extract, but some of it remained locked in the tight, low-permeability shale layers, becoming shale gas^[14–16]. The lower alkane components (methane, ethane, propane, etc.) are very useful as basic chemical feedstocks. With large natural gas reserves (**Figure 1.4a**), the nation has taken a global lead by engaging in a rapid expansion of the chemical industry. This expansion has caused a significant drop in cost of U.S. natural gas for consumers (**Figure 1.4b**), and has given the industry a cost advantage over global competitors. This has led to a growth of the domestic chemical industry and is expected to cut the country’s dependence on foreign oil^[2,15,17].

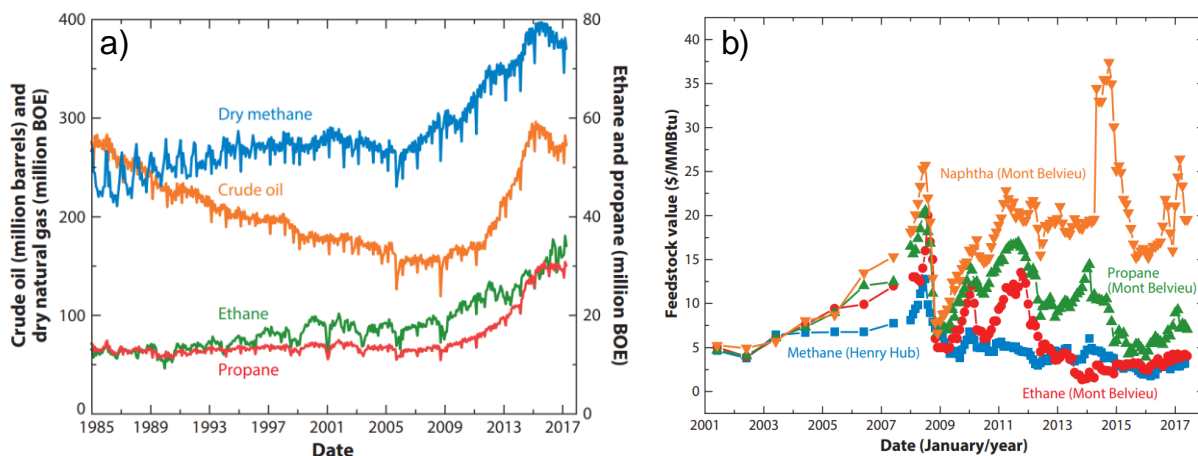


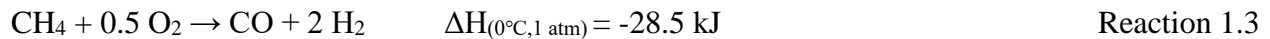
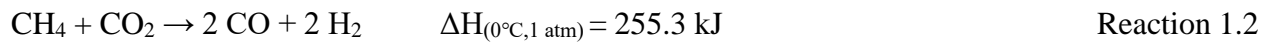
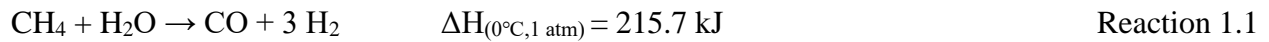
Figure 1.4: U.S production of fossil-fuels^[2] [1 BOE = 5.8 MMBtu]; b) Fossil-fuel feedstock values since 2001^[2] (average annual).

1.3.1.1 Methane-based chemical production

The principal component of natural gas is methane, which represents 70-90 % of natural gas^[15,17]. This makes methane an important feed-stock for the chemical industry. Reforming of methane to synthesis gas or syngas (CO + H₂) is a starting point for chemical production^[18,19], as highlighted in **Figure 1.5**^[17].

1.3.1.1.1 Methane reforming

Commonly investigated reforming methods to convert methane to syngas include: 1) steam reforming (Reaction 1.1) in the presence of steam, 2) dry reforming (Reaction 1.2) in the presence of CO₂, and 3) partial oxidation (Reaction 1.3) in the presence of gaseous oxygen^[20-25]. Unless carried out at ultra-high temperatures, the use of heterogeneous reforming catalyst is necessary, as methane is a highly stable molecule.



Steam reforming is a well-established commercial approach but it suffers from high operating costs due to the high endothermicity of the reactions^[20,21]. In addition, high steam-to-methane ratio is required in order to minimize coke formation. The use of large amount of steam causes additional energy penalty. Dry reforming suffers from catalyst deactivation caused by carbon formation from methane decomposition reaction^[25-27]. Partial oxidation, on the other hand, is an exothermic reaction. It is also the only method that produces syngas with proper hydrogen to carbon monoxide ratio for further processing in Fischer-Tropsch (F-T) synthesis which eliminates the need for hydrogen separation/addition^[19,20,28,29]. The F-T process involves a series of chemical

reactions that produce a variety of hydrocarbons, ideally having the formula $C_nH_{(2n+2)}$. The reaction can be represented by:



This makes partial oxidation a highly promising option. Within the last few decades, many catalysts such as transition metals and some noble metals were tested and proven active for partial oxidation of methane^[20,21,30,31]. However, these catalysts face challenges such as low selectivity, deactivation, and coke formation. Additionally, the needs for gaseous oxygen, which needs to be generated from an air separation unit (ASU), imposes significant capital and operating costs, making it less competitive from a process economic standpoint^[18,32].

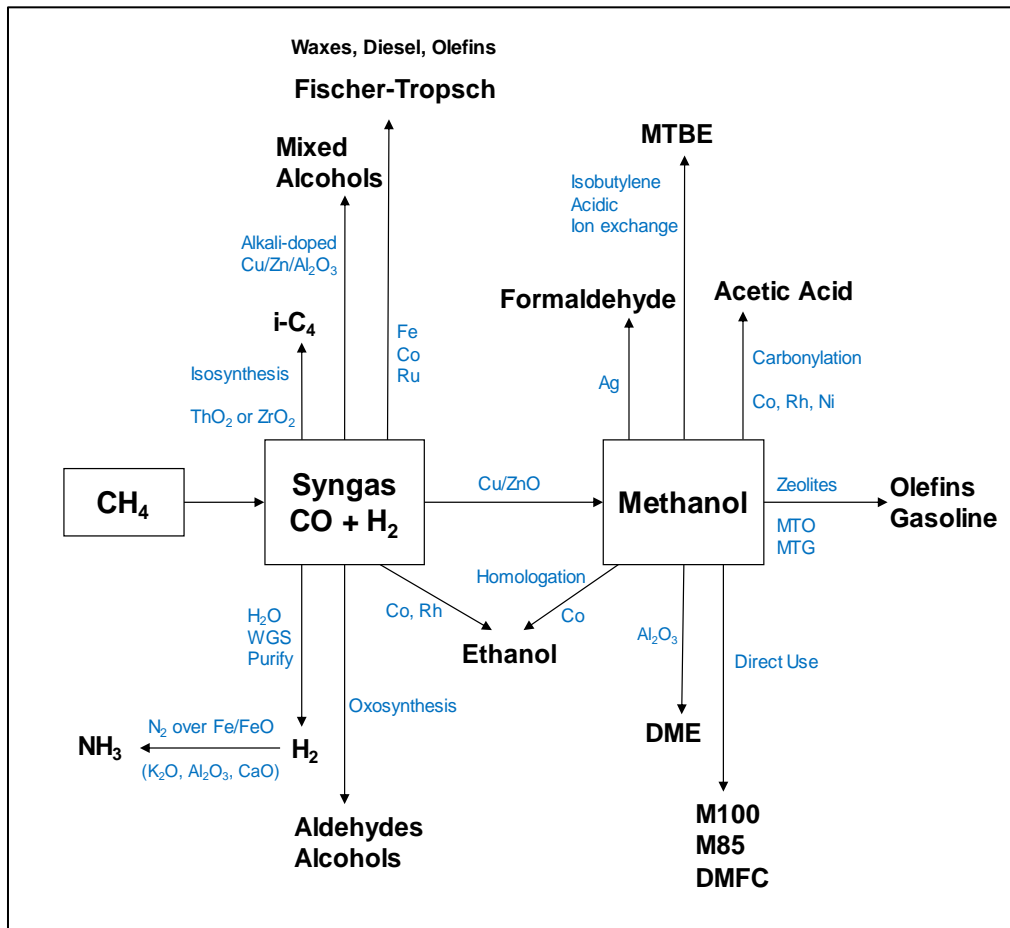


Figure 1.5: Chemical-production routes using syngas^[17].

1.3.1.2 From ethane

Ethane is primarily used in the industry to obtain ethylene *via* steam cracking^[33,34]. Ethylene is a key building block of the chemical industry. It is widely used in the production of various chemical intermediates including polyethylene, polyvinyl chloride, ethylene oxide and styrene. These polymers and intermediates contribute largely to the chemical industry and hold the key to the material-substitution era especially of polymers for natural fibers, metals, glass, wood, etc. The worldwide consumption for ethylene exceeded 150 million tons per year in 2017^[17,20,33,35]. Depending on the length of the carbon chain in the feedstock, different steam-cracking processes are utilized. In Western Europe and Japan, naphtha is the main feedstock for ethylene production due to its abundance. On the other hand, ethane as a feedstock for ethylene production is becoming mainstream in the U.S. due to the shale gas revolution^[2,33,34].

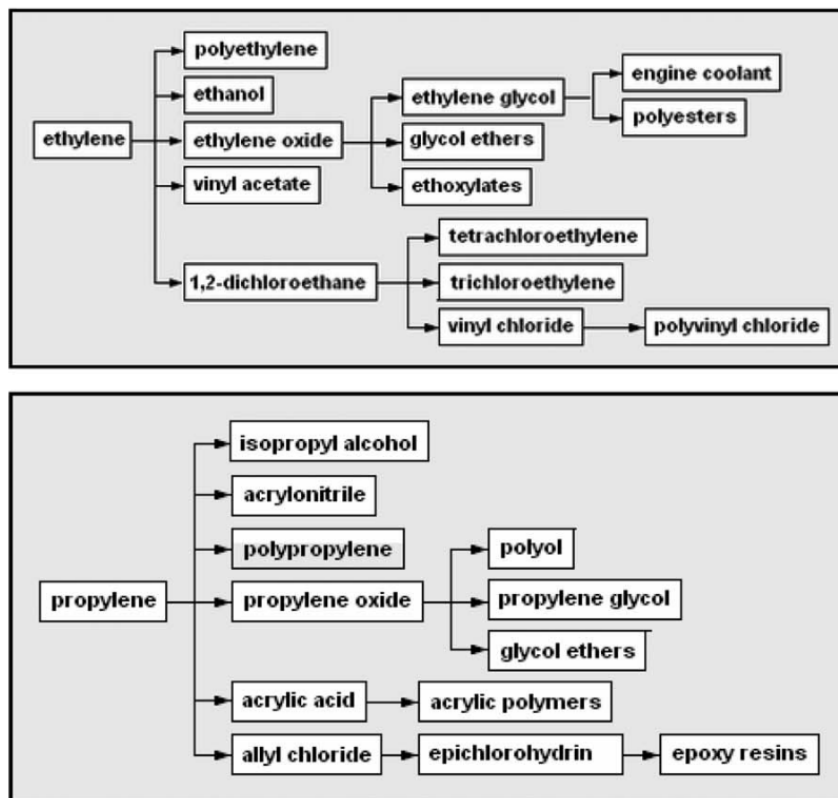


Figure 1.6: Chemicals produced from ethylene and propylene^[17].

1.3.1.2.1 Steam Cracking

Steam cracking involves the decomposition of ethane into ethylene and hydrogen, which is achieved through a complex network of gas phase radical reactions^[33,36].



1.5

It is limited to a practical single-pass ethane-conversion of 67-70% and an ethylene yield of around 55% due to equilibrium limitation and coke formation^[33, 34]. Although steam dilution reduces the rate of coke formation, steam cracking furnaces nevertheless need to be periodically shut down and regenerated with air to avoid coke build-up. The total energy demand of ethane cracking ranges between 15 and 25 GJ/tonne ethylene^[33, 34], which is satisfied by combustion of carbonaceous fuels such as methane. The high endothermicity of cracking reactions as well as the complex cryogenic separation schemes make these processes highly energy and carbon intensive, emitting 1 to 2 tons of CO₂ for each ton of ethylene produced depending upon the feedstock^[33,34]. Intensification of ethylene and propylene production along with the emission reduction would bolster the chemical industry. Therefore, new technologies that overcome these limitations are highly desirable. Similarly, propylene, which is a byproduct in ethane-to-ethylene conversion, can produce a slate of olefins^[17,33]. **Figure 1.6** further demonstrates the use of ethylene and propylene in the chemical industry, which in turn establishes the importance of ethane for chemical production.

1.3.2 From naphtha

Naphtha, which is a mid-range distillation cut of petroleum, is also one of the most abundant feedstocks for steam cracking, especially in Europe and the Asia-Pacific region. Steam cracking

of naphtha accounts for approximately 45% of the ethylene produced worldwide^[33,34,37,38]. As a highly endothermic thermal cracking process, conventional naphtha-based ethylene production is also subjected to intrinsic challenges such as equilibrium limitations, high energy intensity, significant CO₂ emissions, and tendency for coke formation. In fact, steam cracking of naphtha, which consumes up to 22 GJ of energy per ton of ethylene produced, is more energy-intensive than its ethane counterpart^[33,34]. Thus, it is desirable to seek naphtha conversion to ethylene using a more novel and economical approach.

1.3.3 From carbon dioxide

Carbon dioxide has been used for decades in enhanced oil recovery, as a refrigerant, as an extractive solvent, and as an additive in food and beverage products^[10,11,39]. Emerging CO₂-utilization schemes (**Figure 1.7**), including the mineral carbonation to produce construction materials, and the chemical or biological conversion of carbon dioxide to fuels and chemicals, could enable reduction in greenhouse gas emissions^[11]. Although chemical activity of CO₂ is low, CO₂ can be made active for chemical reactions with the presence of suitable catalysts and the appropriate operating conditions^[32,39-43]. Cost-effectiveness of industrial usage of CO₂ for chemicals depends on the energy demand. Reduction of the inherent energy requirement for the reaction through development of new catalysts, saving energy cost through strategic utilization of renewable energy sources, etc. will help in improving economics of reactions using CO₂^[10,11].

Transformation of the abundant waste CO₂ into valuable chemicals has the potential to operate with positive economic returns. A plethora of carbonyl compounds have carbon monoxide (CO) as the starting point, making it an indispensable carbonyl source for chemical production^[2,44]. CO₂-to-CO is a CO₂-utilization scheme which can help produce valuable chemicals efficiently.

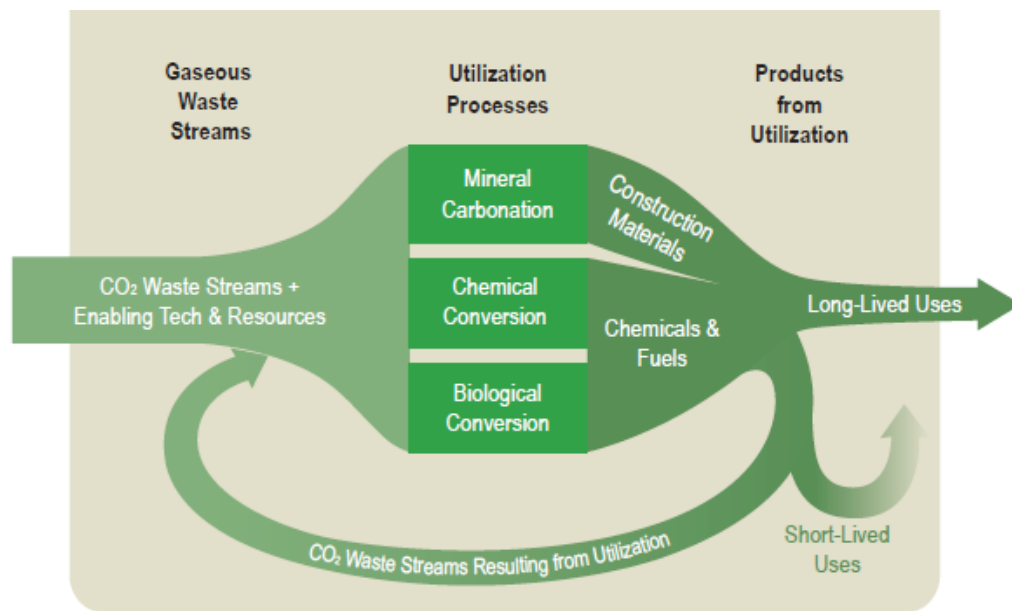


Figure 1.7: Conceptual illustration of the process for valorization of CO₂^[11].

1.4 Towards sustainable processes

In a 2006 report, the National Research Council defined a sustainable process as one that is economically competitive and does not cause harm to the environment and human health^[2]. For chemical production, a sustainable route would involve efficiently utilizing the abundant resources like methane, ethane (natural gas) and carbon dioxide as feed-stocks. This would allow for an economical operation considering the large availability and low price. Utilization of CO₂ towards chemical production is an effective way to fix CO₂ and heal the environment in an economical way. Efficient avenues of fuel-to-chemical and CO₂-to-chemical conversions are hence desirable.

1.4.1 Chemical Looping

Chemical looping offers a potentially efficient route to fossil fuel utilization and chemical production^[18,42,45–49]. In this process, a metal oxide undergoes a two-step redox process to provide pure oxygen for fossil fuel conversion. The first step of this redox process is oxidation of the fuel

through the lattice oxygen of a metal oxide in what is referred to as the reducer reactor. In the second step the metal oxide is oxidized back to its original state through a gaseous oxidant in what is referred to as the oxidizer reactor (regenerator). This redox scheme is versatile and can be used with different fuels like coal, natural gas or even biomass. As shown in **Figure 1.8**, different products can be obtained with different fuels, using the same approach. The key to the process is the metal oxide, which is typically referred to as an oxygen carrier (OC) or redox catalyst. The OC being oxidant-agnostic, different oxidants like air, H₂O (steam) or CO₂, can be utilized in the regenerator, depending on the chosen chemical looping process, OC and fuel. The reactors in this system are interconnected with the oxygen carrier circulating between the two beds. There are two main advantages to this process: i) if air is used, chemical looping can provide *in-situ* air separation and ii) if designed properly, chemical looping can provide efficient interaction between the OC and reactants. Chemical looping has most commonly been applied to carbonaceous fuel combustion using air as the oxidant. However, this can be extended to any process where oxidation of a fossil fuel is required.

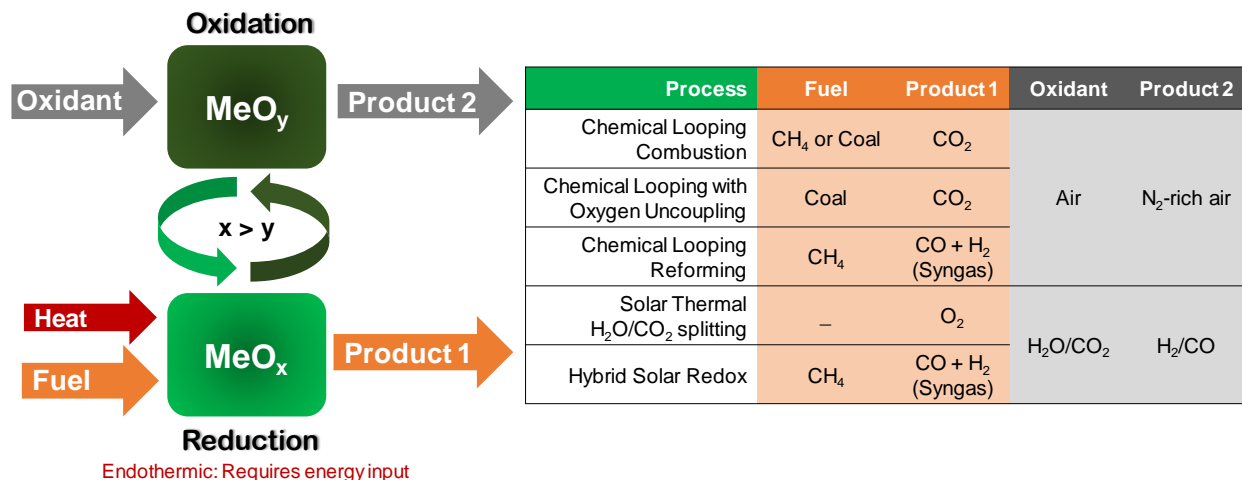
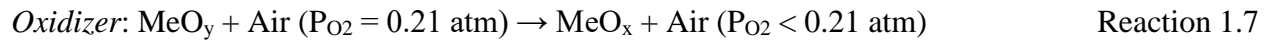


Figure 1.8: Schematic of chemical looping processes along with the diverse use of fuels, oxidants and products.

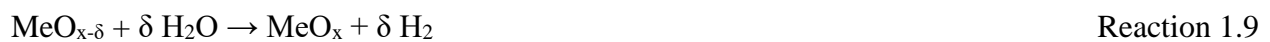
1.4.1.1 Chemical Looping Reforming (CLR)

Chemical looping reforming (CLR) is an important application of chemical looping, to reform methane to syngas and hence, initiate the chemical production schemes as shown in **Figure 1.5**. CLR requires an OC (or redox catalyst) capable of selectively oxidizing methane to hydrogen and carbon monoxide^[18,47,49–55]. In comparison to methane reforming techniques, chemical looping reforming accomplishes methane partial oxidation without an air separation unit. The ability of a redox catalyst to selectively oxidize a fuel is key to the success of chemical looping reforming. The reactions occurring in the reducer reactor and the oxidizer reactor are shown below (Reaction 1.6 and 1.7).



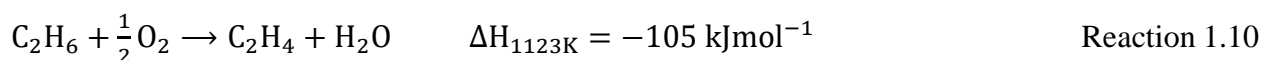
1.4.1.2 Solar Thermal H₂O/CO₂ Splitting

Solar-thermal water or CO₂-splitting represents a potentially attractive and environmentally friendly option^[42,56–62]. Typical solar-thermal splitting schemes involve the cyclic redox reactions 1.8 and 1.9 to obtain separate streams of hydrogen/CO and oxygen^[63]. In this scheme, energy for the reduction reaction is supplied by solar energy without the use of any fuel. By using the sustainable solar energy, H₂ is generated without CO₂ emissions. In the first step, solar energy is used to decompose a metal oxide at high temperature. In the subsequent step, the decomposed metal/metal oxide is reoxidized with water, producing hydrogen.

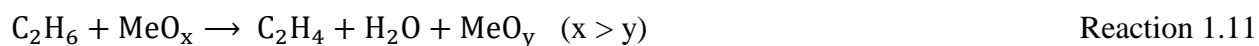


1.4.1.3 Chemical Looping Oxidative Dehydrogenation

The oxidative dehydrogenation (ODH) route for ethane-to-ethylene involves formation of water from hydrogen using an oxidant^[36,64]. ODH is a thermodynamically favorable exothermic reaction (Reaction 1.10) when gaseous oxygen is used as an oxidant. A large number of catalytic systems have been demonstrated for ODH. Being exothermic in nature, the ODH reaction requires an inert atmosphere to keep the reaction mixture out of the flammable zone^[64]. Techno-economic analysis indicates that using the inert gases (e.g., nitrogen, argon, and helium) not only increases the equipment size, thereby increasing the CAPEX, but also increases the risk of safety hazards^[65,66].



To address the potential challenges related to O₂ co-feed, the Chemical Looping ODH (CL-ODH) approach uses lattice oxygen from the redox catalyst to facilitate ethane conversion^[67–69]. The CL-ODH scheme (**Figure 1.9**) is similar to the one described in **Figure 1.8** earlier. Although the overall reaction for CL-ODH (combining Reaction 1.7 and 1.11) is identical to that for conventional ODH (Reaction 1.10), the chemical looping redox catalyst eliminates the needs for air separation and oxygen co-feed. Oxidative conversion of naphtha, also known as oxy-cracking^[38,70], using a chemical looping scheme similar to ethane CL-ODH (**Figure 1.9**) can be an alternative to conventional cracking.



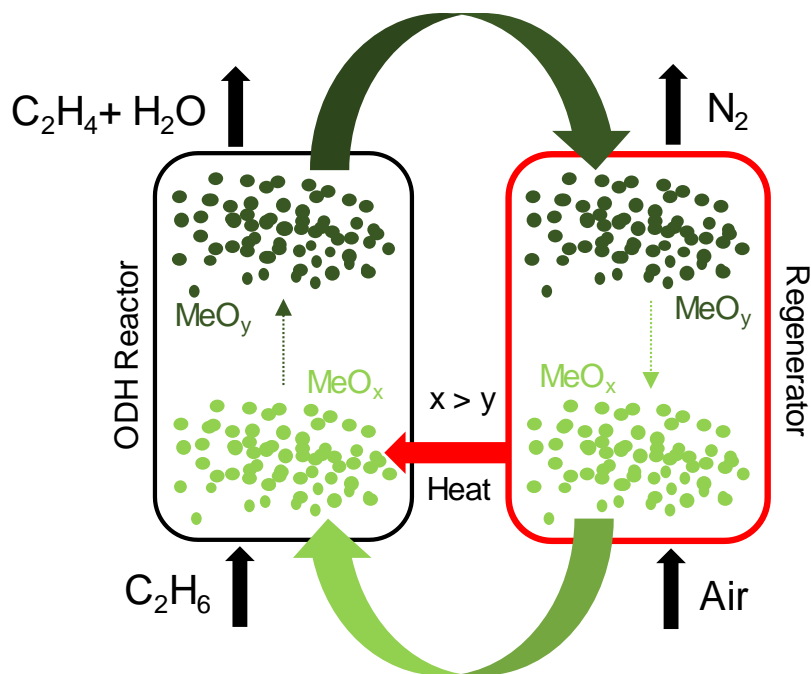


Figure 1.9: Schematic of chemical looping oxidative dehydrogenation (CL-ODH).

1.4.1.4 Oxygen Carrier and Redox Catalyst Design

The oxygen carrier plays a key role in the success of chemical looping processes. Ideal oxygen carriers possess high oxygen capacity (i.e. amount of oxygen that is provided for fuel conversion), reaction kinetics, long term recyclability, mechanical stability, low environmental/health impacts, low cost, and selectivity to the desired products^[18,50,52]. Transition metal oxides have most commonly been studied as oxygen carriers, due to their high oxygen capacities. This has included iron, nickel, cobalt, copper, and manganese oxides. Mixed metal oxides have also been explored because of the synergetic effect that can occur as a result of using more than one metal cation^[50,52,71–73]. Mixed metal oxide design is particularly promising because the oxygen carrier design space is much larger^[18,45,52,72].

1.4.1.4.1 Perovskite-based Oxygen Carriers

Perovskite oxides have emerged as promising mixed metal oxides, due to their unique properties. The general formula of perovskite oxides are $ABO_{3-\delta}$, where A and B are different metal cations and δ is oxygen non-stoichiometry, expressed as oxygen vacancies. Perovskites are highly tunable because they can accept a large number of different cations as well as combination of cations in either the A site of the B site^[74-76]. A semi-empirical factor called the “Goldschmidt tolerance factor” can be used to understand the stability of the oxides with different cations. This is expressed below, in Equation 1.1, where an ideal cubic perovskite gives a tolerance factor of 1. r_a is the ionic radius of A site cation, r_b is the ionic radius of B site cation, and r_o is the ionic radius of oxygen.

$$t = \frac{r_a + r_o}{\sqrt{2}(r_b + r_o)} \quad (\text{Equation 1.1})$$

Perovskites can also donate oxygen, without phase decomposition. For these reasons, perovskite oxides are very attractive for all chemical looping applications and are gaining^[52,77-80].

1.4.1.4.2 Redox Catalyst Development

With redox catalysts requiring high product selectivity and high activity, redox catalyst success has been limited. Supported Ni based redox catalysts have shown the most success for CLR^[18,52,81-83], with other Fe, Mn, and Cu-based redox catalysts suffering from poor selectivity^[81]. These Ni based catalysts include SiO_2 supported NiO ^[81] and MgAl_2O_4 supported NiO ^[84]. However, the issues of carbon formation, toxicity, and cost are present. Perovskites have been investigated as redox catalysts and there has been success with perovskites such as LaFeO_3 , $\text{La}_{1-x}\text{Sr}_x\text{FeO}_3$ ^[80,85,86]. However, these perovskites are costly and do not exhibit high oxygen capacities.

1.4.1.4.3 Surface Promotion for Enhanced Selectivity and Activity

Oxygen carrier activity and selectivity can be enhanced by surface promotion with a catalytically active metal. Shafiefarhood et.al. reported that impregnation of 0.5 wt. % Rh on CaMnO_3 and LaCeO_3 significantly enhanced their activity and syngas selectivity for methane partial oxidation^[87]. Over 300°C decrease in the onset temperature for methane oxidation was observed. Moreover, Rh enriched on the oxide surface and decreased the apparent surface activation energy of methane by 95% for CaMnO_3 based oxygen carriers. The enhanced surface activity also led to significantly increased oxygen donation rate, resulting from the increased driving force for O^{2-} conduction. Rh promoted CaMnO_3 exhibited high activity and selectivity for methane POx for 100 cycles at 600°C^[87,88]. Palchelva et. al. showed that Rh promotion on $\text{La}_{0.8}\text{Sr}_{0.2}(\text{Fe}_{0.8}\text{Co}_{0.2})_{1-x}\text{Ga}_x\text{O}_3$ led to 40% enhancement in CO selectivity under 10% CH_4 pulses at 600°C^[89]. Ni as a promoter for WO_3 based oxygen carriers for methane partial oxidation was reported by Chen et. al^[86]. Methane conversion and syngas yield increased by 2.7 fold upon Ni promotion within the region of high syngas selectivity at 800°C^[86]. Doping low levels (~1%) of heteroatoms such as La on iron oxide was also reported to significantly improve the redox activity of the oxygen carrier^[90].

1.4.1.4.4 Density Functional Theory (DFT) for Oxygen Carrier Design

With a high number of possible oxygen carriers/redox catalysts existing, design principles are desired to guide the selection of the oxygen carrier/redox catalyst in a predictive manner. Describing properties of oxygen carriers and redox catalysts through quantum mechanical modeling is an attractive route to guide the selection of oxygen carriers and redox catalysts. Density functional theory (DFT) has become a popular method, within quantum mechanical modeling to describe metals and metal oxides. Perovskites, as mentioned earlier, along with fluorite-structured materials, are a promising class of materials for chemical-looping applications.

Oxygen donation, in this process, is governed by oxygen vacancy creation. As such, calculating the energy of oxygen vacancy creation in these materials serve as a promising route to predict their performance for chemical looping processes. Using DFT to predict energies of oxygen vacancy creation is most traditionally used for semiconductor applications^[91–96]. More recently, there are studies on guiding the selection of materials using vacancy calculations for thermochemical applications, oxidation of hydrocarbons, or water splitting^[97–105]. While these studies have used a number of approximations to explore a large material space, they have had promising results and can serve as inspiration for designing oxygen carriers for chemical looping processes.

1.5 Summary

With an increasing population, the demand for chemical production is on a rise. Chemical looping processes are promising candidates for sustainable chemical synthesis routes. They possess the potential to selectively oxidize methane to syngas or ethane/naphtha to ethylene. They can also efficiently split CO₂ or H₂O to yield valorized products like CO or H₂ respectively. This ability of chemical looping to produce a valorized output using cheap, abundant and environment-friendly feed-stocks makes it an attractive choice for intensifying chemical production. In this work, development of the redox catalysts for these fuel and CO₂-utilization schemes will be presented. Along with the development of efficient and stable materials, thorough process analyses of these schemes are also carried out, which help in looking at the bigger picture when compared with respective state-of-the-art processes.

In Chapter 2, the chemical looping approach will be explored to selectively oxidize methane to syngas and also convert H₂O (steam) to hydrogen gas while utilizing solar energy. A rationalized strategy will be developed to optimize the redox catalyst for this hybrid solar-redox process. Experiments will support the DFT predictions to demonstrate the ability of BaMn_{0.5}Fe_{0.5}O_{3-δ} to

convert 90% of methane to syngas and provide a steam-to-hydrogen conversion of 90% at 900°C. Process simulations will help in showing the potential of this process to reduce CO₂ emissions by 70% when compared with the state-of-the-art hydrogen and liquid fuel production processes.

Chapter 3 explores the low temperature CO₂ utilization along with methane partial oxidation using the chemical looping scheme, with the integration of industrial waste heat. A Hybrid Redox Process will be reported with the capability of efficiently converting CO₂ to CO and methane to syngas at <700 °C. The ability to integrate industrial waste heat for chemical production, leading to negligible CO₂ emissions, will be explored in this chapter. With lanthanum substitution and rhodium promotion, ceria will be shown to be highly effective for the process with the potential for chemical production using CO₂.

Chapter 4 talks about the potential utilization of a chemical looping process to intensify ethylene production from ethane. Detailed AspenPlus[®] process simulations and analyses of chemical looping oxidative dehydrogenation (CL-ODH) using experimental data on a Mn-based redox catalyst will help in exploring its promising benefits over the traditional steam cracking process. The chapter shows the 82% reduction for CL-ODH, in the overall energy demand and CO₂ emissions with a discussion about the section wise analyses. In the last part of the chapter, a comprehensive second law analysis, in conjunction with refined process models, helps in further elaborating on the ability of CL-ODH to out-perform the near-perfect thermally efficient steam cracker.

In Chapter 5, CL-ODH is further expanded to operate in a modular set-up and convert ethane first to olefins and eventually to gasoline. It addresses the difficulties in liquefaction and transportation of ethane and provides a promising solution. Using experimental proof-of concept data and process

simulations, a simple, single-pass configuration of the modular ethane-to-liquids (M-ETL) scheme will be shown to be economically viable at distributed sites. The end of the chapter identifies the economic factors which have strong effects on the selling price of the final products.

Chapter 6 deals with a naphtha redox oxy-cracking (ROC) process for intensified ethylene/propylene production. Based on experimental data on a redox catalyst, it presents an AspenPlus[®] analysis of the ROC process, demonstrating up to 52% energy and CO₂ savings with respect to the traditional naphtha cracking process. The chapter indicates the promise of the ROC to be an attractive and environmental-friendly option for ethylene and propylene production from naphtha.

1.6 References

- [1] “Fossil Fuels | EESI,” can be found under <https://www.eesi.org/topics/fossil-fuels/description>, **n.d.**
- [2] E. E. Stangland, *Annu. Rev. Chem. Biomol. Eng.* **2018**, 9, 341.
- [3] “EIA: Fossil fuels continue to dominate U.S. energy consumption,” can be found under <https://www.worldoil.com/news/2019/7/3/eia-fossil-fuels-continue-to-dominate-us-energy-consumption>, **n.d.**
- [4] *US Energy Inf. Adm.* **n.d.**, 83.
- [5] “Energy Flow Charts,” can be found under <https://flowcharts.llnl.gov/commodities/energy>, **2018**.
- [6] “U.S. Energy Information Administration (EIA),” can be found under <https://www.eia.gov/environment/emissions/carbon/>, **n.d.**
- [7] “U.S. Energy Information Administration - EIA - Independent Statistics and Analysis,” can be found under <https://www.eia.gov/outlooks/aeo/data/browser/#/?id=22-AEO2019&cases=ref2019&sourcekey=0>, **n.d.**
- [8] “Short-Term Energy Outlook - EIA,” can be found under <https://www.eia.gov/outlooks/steo/report/natgas.php>, **n.d.**
- [9] J. Friedrich, “Greenhouse Gas Emissions Over 165 Years,” can be found under <https://www.wri.org/resources/data-visualizations/greenhouse-gas-emissions-over-165-years>, **2019**.
- [10] H.-J. Leimkühler, in *Manag. CO2 Emiss. Chem. Ind.*, John Wiley & Sons, Ltd, **2010**, pp. 1–30.
- [11] Committee on Developing a Research Agenda for Utilization of Gaseous Carbon Waste Streams, Board on Chemical Sciences and Technology, Division on Earth and Life Studies, National Academies of Sciences, Engineering, and Medicine, *Gaseous Carbon Waste Streams Utilization: Status and Research Needs*, National Academies Press, Washington, D.C., **2019**.
- [12] H. Kharas, *Glob. Econ. Dev. Brook.* **2017**, 32.
- [13] M. Roser, *Our World Data* **2013**.
- [14] R. A. Kerr, *Science* **2010**, 328, 1624.

- [15] J. D. Hughes, *Nature* **2013**, *494*, 307.
- [16] John B. Curtis¹, *AAPG Bull.* **2002**, *86*, DOI 10.1306/61EEDDBE-173E-11D7-8645000102C1865D.
- [17] J. J. Siirola, *AIChE J.* **2014**, *60*, 810.
- [18] L.-S. Fan, *Chemical Looping Systems for Fossil Energy Conversions*, Wiley-AIChE, Hoboken, NJ, **2010**.
- [19] A. Iulianelli, S. Liguori, J. Wilcox, A. Basile, *Catal. Rev.* **2016**, *58*, 1.
- [20] J. A. Moulijn, A. van Diepen, M. Makkee, *Chemical Process Technology*, John Wiley & Sons Inc., Chichester, West Sussex, United Kingdom, **2013**.
- [21] J. G. Speight, in *Handb. Ind. Hydrocarb. Process.* (Ed.: J.G. Speight), Gulf Professional Publishing, Boston, **2011**, pp. 127–162.
- [22] D. Li, Y. Nakagawa, K. Tomishige, *Appl. Catal. Gen.* **2011**, *408*, 1.
- [23] J. H. Edwards, A. M. Maitra, *Fuel Process. Technol.* **1995**, *42*, 269.
- [24] M. A. Nieva, M. M. Villaverde, A. Monzón, T. F. Garetto, A. J. Marchi, *Chem. Eng. J.* **2014**, *235*, 158.
- [25] D. Pakhare, J. Spivey, *Chem. Soc. Rev.* **2014**, *43*, 7813.
- [26] C. Wang, N. Sun, N. Zhao, W. Wei, Y. Sun, C. Sun, H. Liu, C. E. Snape, *Fuel* **2015**, *143*, 527.
- [27] F. F. de Sousa, H. S. A. de Sousa, A. C. Oliveira, M. C. C. Junior, A. P. Ayala, E. B. Barros, B. C. Viana, J. M. Filho, A. C. Oliveira, *Int. J. Hydrog. Energy* **2012**, *37*, 3201.
- [28] M. E. Dry, *Appl. Catal. Gen.* **1999**, *189*, 185.
- [29] M. E. Dry, *Catal. Today* **2002**, *71*, 227.
- [30] K. Otsuka, Y. Wang, I. Yamanaka, A. Morikawa, *J. Chem. Soc. Faraday Trans.* **1993**, *89*, 4225.
- [31] J. A. Labinger, *J. Mol. Catal. Chem.* **2004**, *220*, 27.
- [32] C. Mesters, *Annu. Rev. Chem. Biomol. Eng.* **2016**, *7*, 223.

- [33] H. Zimmermann, R. Walzl, in *Ullmanns Encycl. Ind. Chem.*, Wiley-VCH Verlag GmbH & Co. KGaA, **2000**.
- [34] T. Ren, M. Patel, K. Blok, *Energy* **2006**, *31*, 425.
- [35] “Ethylene Global Supply Demand Analytics Service,” can be found under <https://www.woodmac.com/news/editorial/ethylene-global-supply-demand-analytics-service/>, **2018**.
- [36] F. Cavani, N. Ballarini, A. Cericola, *Catal. Today* **2007**, *127*, 113.
- [37] M. Masoumi, M. Shahrokhi, M. Sadrameli, J. Towfighi, *Ind. Eng. Chem. Res.* **2006**, *45*, 3574.
- [38] V. P. Haribal, Y. Chen, L. Neal, F. Li, *Engineering* **2018**, *4*, 714.
- [39] E. Alper, O. Yuksel Orhan, *Petroleum* **2017**, *3*, 109.
- [40] Z. Sun, T. Ma, H. Tao, Q. Fan, B. Han, *Chem* **2017**, *3*, 560.
- [41] O. K. Varghese, M. Paulose, T. J. LaTempa, C. A. Grimes, *Nano Lett.* **2009**, *9*, 731.
- [42] W. C. Chueh, C. Falter, M. Abbott, D. Scipio, P. Furler, S. M. Haile, A. Steinfeld, *Science* **2010**, *330*, 1797.
- [43] A. H. Bork, E. Povoden-Karadeniz, J. L. M. Rupp, *Adv. Energy Mater.* **2017**, *7*, 1601086.
- [44] J.-B. Peng, H.-Q. Geng, X.-F. Wu, *Chem* **2018**, *0*, DOI 10.1016/j.chempr.2018.11.006.
- [45] A. Mishra, F. Li, *Curr. Opin. Chem. Eng.* **2018**, *20*, 143.
- [46] V. Spallina, F. Gallucci, M. van S. Annaland, in *Handb. Chem. Looping Technol.*, John Wiley & Sons, Ltd, **2018**, pp. 61–92.
- [47] S. Bhavsar, G. Veser, *RSC Adv.* **2014**, *4*, 47254.
- [48] A. Lyngfelt, *Appl. Energy* **2014**, *113*, 1869.
- [49] M. Tang, L. Xu, M. Fan, *Appl. Energy* **2015**, *151*, 143.
- [50] J. Adanez, A. Abad, F. Garcia-Labiano, P. Gayan, L. F. de Diego, *Prog. Energy Combust. Sci.* **2012**, *38*, 215.
- [51] J. Adánez, A. Abad, T. Mendiara, P. Gayán, L. F. de Diego, F. García-Labiano, *Prog. Energy Combust. Sci.* **2018**, *65*, 6.

- [52] F. Li, N. Galinsky, A. Shafieifarhood, in *Handb. Chem. Looping Technol.*, John Wiley & Sons, Ltd, **2018**, pp. 229–261.
- [53] Q. Imtiaz, D. Hosseini, C. R. Müller, *Energy Technol.* **2013**, *1*, 633.
- [54] L. F. de Diego, M. Ortiz, J. Adánez, F. García-Labiano, A. Abad, P. Gayán, *Chem. Eng. J.* **2008**, *144*, 289.
- [55] M. Rydén, A. Lyngfelt, T. Mattisson, *Fuel* **2006**, *85*, 1631.
- [56] J. Luo, J.-H. Im, M. T. Mayer, M. Schreier, M. K. Nazeeruddin, N.-G. Park, S. D. Tilley, H. J. Fan, M. Grätzel, *Science* **2014**, *345*, 1593.
- [57] M. G. Walter, E. L. Warren, J. R. McKone, S. W. Boettcher, Q. Mi, E. A. Santori, N. S. Lewis, *Chem. Rev.* **2010**, *110*, 6446.
- [58] M. Roeb, C. Sattler, *Science* **2013**, *341*, 470.
- [59] M. Romero, A. Steinfeld, *Energy Environ. Sci.* **2012**, *5*, 9234.
- [60] N. S. Lewis, *Science* **2016**, *351*, aad1920.
- [61] T. Nakamura, *Sol. Energy* **1977**, *19*, 467.
- [62] F. Sibieude, M. Ducarroir, A. Tofighi, J. Ambriz, *Int. J. Hydrog. Energy* **1982**, *7*, 79.
- [63] C. Perkins, A. W. Weimer, *AIChE J.* **2009**, *55*, 286.
- [64] C. A. Gärtner, A. C. van Veen, J. A. Lercher, *ChemCatChem* **2013**, *5*, 3196.
- [65] C. Baroi, A. M. Gaffney, R. Fushimi, *Catal. Today* **2017**, *298*, 138.
- [66] G. J. Maffia, A. M. Gaffney, O. M. Mason, *Top. Catal.* **2016**, *59*, 1573.
- [67] L. M. Neal, S. Yusuf, J. A. Sofranko, F. Li, *Energy Technol.* **2016**, *4*, 1200.
- [68] S. Yusuf, L. M. Neal, F. Li, *ACS Catal.* **2017**, *7*, 5163.
- [69] V. P. Haribal, L. M. Neal, F. Li, *Energy* **2017**, *119*, 1024.
- [70] C. Boyadjian, L. Lefferts, K. Seshan, *Appl. Catal. Gen.* **2010**, *2*, 167.
- [71] J. Adánez, L. F. de Diego, F. García-Labiano, P. Gayán, A. Abad, J. M. Palacios, *Energy Fuels* **2004**, *18*, 371.

- [72] C. Yuan, H. B. Wu, Y. Xie, X. W. (David) Lou, *Angew. Chem. Int. Ed.* **2014**, *53*, 1488.
- [73] M. B. Gawande, R. K. Pandey, R. V. Jayaram, *Catal. Sci. Technol.* **2012**, *2*, 1113.
- [74] G. Kieslich, S. Sun, A. K. Cheetham, *Chem. Sci.* **2015**, *6*, 3430.
- [75] M. Kubicek, A. H. Bork, J. L. M. Rupp, *J. Mater. Chem. A* **2017**, *5*, 11983.
- [76] J. Zhu, H. Li, L. Zhong, P. Xiao, X. Xu, X. Yang, Z. Zhao, J. Li, *ACS Catal.* **2014**, *4*, 2917.
- [77] N. Galinsky, A. Mishra, J. Zhang, F. Li, *Appl. Energy* **2015**, *157*, 358.
- [78] N. L. Galinsky, Y. Huang, A. Shafiefarhood, F. Li, *ACS Sustain. Chem. Eng.* **2013**, *1*, 364.
- [79] A. Shafiefarhood, N. Galinsky, Y. Huang, Y. Chen, F. Li, *ChemCatChem* **2014**, *6*, 790.
- [80] F. He, F. Li, *Energy Environ. Sci.* **2015**, *8*, 535.
- [81] M. Ortiz, L. F. de Diego, A. Abad, F. García-Labiano, P. Gayán, J. Adánez, *Int. J. Hydrog. Energy* **2010**, *35*, 151.
- [82] M. Rydén, M. Johansson, A. Lyngfelt, T. Mattisson, *Energy Environ. Sci.* **2009**, *2*, 970.
- [83] M. Rydén, A. Lyngfelt, T. Mattisson, *Energy Fuels* **2008**, *22*, 2585.
- [84] Y. Zheng, K. Li, H. Wang, D. Tian, Y. Wang, X. Zhu, Y. Wei, M. Zheng, Y. Luo, *Appl. Catal. B Environ.* **2017**, *202*, 51.
- [85] M. Rydén, A. Lyngfelt, T. Mattisson, D. Chen, A. Holmen, E. Bjørgum, *Int. J. Greenh. Gas Control* **2008**, *2*, 21.
- [86] S. Chen, L. Zeng, H. Tian, X. Li, J. Gong, *ACS Catal.* **2017**, *7*, 3548.
- [87] A. Shafiefarhood, J. Zhang, L. M. Neal, F. Li, *J. Mater. Chem. A* **2017**, *5*, 11930.
- [88] A. Mishra, A. Shafiefarhood, J. Dou, F. Li, *Catal. Today* **2019**, DOI 10.1016/j.cattod.2019.05.036.
- [89] R. Palcheva, U. Olsbye, M. Palcut, P. Rauwel, G. Tyuliev, N. Velinov, H. H. Fjellvåg, *Appl. Surf. Sci.* **2015**, *357*, 45.
- [90] L. Qin, Z. Cheng, M. Guo, M. Xu, J. A. Fan, L.-S. Fan, *ACS Energy Lett.* **2017**, *2*, 70.
- [91] J.-J. Tang, B. Liu, *J. Phys. Chem. C* **2016**, *120*, 6642.

- [92] A. F. Kohan, G. Ceder, D. Morgan, C. G. Van de Walle, *Phys. Rev. B* **2000**, *61*, 15019.
- [93] C. G. Van de Walle, J. Neugebauer, *J. Appl. Phys.* **2004**, *95*, 3851.
- [94] Z. Yang, G. Luo, Z. Lu, K. Hermansson, *J. Chem. Phys.* **2007**, *127*, 074704.
- [95] A. Janotti, C. G. Van de Walle, *Appl. Phys. Lett.* **2005**, *87*, 122102.
- [96] C. W. M. Castleton, A. Hoglund, S. Mirbt, *Phys. Rev. B* **2006**, *73*, 035215.
- [97] C. L. Muhich, B. D. Ehrhart, V. A. Witte, S. L. Miller, E. N. Coker, C. B. Musgrave, A. W. Weimer, *Energy Environ. Sci.* **2015**, *8*, 3687.
- [98] E. A. Kotomin, Yu. A. Mastrikov, M. M. Kuklja, R. Merkle, A. Roytburd, J. Maier, *Solid State Ion.* **2011**, *188*, 1.
- [99] J. Greeley, T. F. Jaramillo, J. Bonde, I. Chorkendorff, J. K. Nørskov, *Nat. Mater.* **2006**, *5*, 909.
- [100] H.-Y. Su, K. Sun, *J. Mater. Sci.* **2015**, *50*, 1701.
- [101] D. Maiti, B. J. Hare, Y. A. Daza, A. E. Ramos, J. N. Kuhn, V. R. Bhethanabotla, *Energy Environ. Sci.* **2018**, *11*, 648.
- [102] A. Mishra, N. Galinsky, F. He, E. E. Santiso, F. Li, *Catal. Sci. Technol.* **2016**, *6*, 4535.
- [103] V. P. Haribal, F. He, A. Mishra, F. Li, *ChemSusChem* **2017**, *10*, 3402.
- [104] D. Maiti, Y. A. Daza, M. M. Yung, J. N. Kuhn, V. R. Bhethanabotla, *J. Mater. Chem. A* **2016**, *4*, 5137.
- [105] A. Mishra, T. Li, F. Li, E. E. Santiso, *Chem. Mater.* **2019**, *31*, 689.

**CHAPTER 2: IRON-DOPED BaMnO₃ FOR HYBRID WATER-SPLITTING AND
SYNGAS GENERATION WITH EXCEPTIONAL CONVERSIONS**

is a reprint of a manuscript published in *ChemSusChem* 2017, 10, 3402 – 3408.

The supplementary information is in Appendix A.

2.1 Abstract

A rationalized strategy to optimize transition metal oxide-based redox catalysts for water-splitting and syngas generation via a hybrid solar-redox scheme is proposed and validated. While monometallic transition metal oxides do not possess desirable properties, Density Functional Theory calculations indicate that redox properties of perovskite-structured $\text{BaMn}_x\text{Fe}_{1-x}\text{O}_{3-\delta}$ can be varied by changing the B-site cation compositions. Specifically, $\text{BaMn}_{0.5}\text{Fe}_{0.5}\text{O}_{3-\delta}$ is projected to be suitable for the hybrid solar-redox scheme. Experimental studies confirm such predictions, demonstrating 90% steam-to-hydrogen conversion in water-splitting and over 90% syngas yield in the methane partial oxidation step under repeated redox cycles. Compared to state-of-the-art solar-thermal water-splitting, the rationally designed redox catalyst reported is capable of splitting water at a significantly lower temperature with 10-fold increase in steam-to-hydrogen conversion. Process simulations indicate the potential to operate the hybrid solar-redox scheme at a higher efficiency than state-of-the-art hydrogen and liquid fuel production processes with 70% lower CO_2 emissions for hydrogen production.

2.2 Introduction

Hydrogen is an important feedstock for petroleum refining and ammonia synthesis. As a fuel, hydrogen is attractive with zero-emission upon combustion and a high weight-based energy density^[1,2]. To date, most of the hydrogen is produced from fossil fuels, resulting in significant CO_2 and NO_x emissions. Significant efforts have been made in recent years to develop environmental-friendly hydrogen production technologies^[3-7]. Unlike direct water-thermolysis, which operates at elevated temperatures ($>3000^\circ\text{C}$), solar-thermal water-splitting is carried out at lower temperatures and has the potential for hydrogen production with minimal carbon emissions

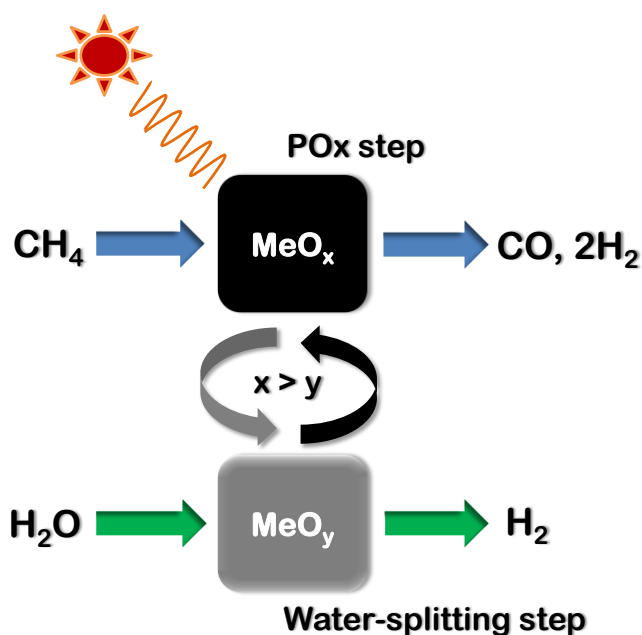
[5,8–14]. Solar-thermal water-splitting uses a two-step reduction and oxidation (redox) scheme of metal oxides, where a reducible metal oxide is first partially reduced at high temperatures to release a fraction of its lattice oxygen into the gas phase. The reduced metal oxide is then regenerated with steam for H₂ production. The heat required in such a high temperature process is provided by concentrated solar energy. While a number of promising redox oxides have been developed, the relatively high decomposition temperatures (>1200°C) and low steam conversion in the water-splitting step limit the efficiency and economic attractiveness of this process [9–11,13–15]

Similar to solar-thermal water-splitting, the chemical-looping reforming (CLR) process also utilizes the redox properties of metal oxides for energy conversion [13,16–24]. In such a process, a transition metal oxide-based oxygen carrier (also known as redox catalyst) is used to partially oxidize (POx) methane to syngas in the first step and the consumed lattice oxygen is subsequently replenished with air via the following reactions:



Multiple downstream processing and separation steps are required to convert the syngas, from CLR, to H₂. Moreover, low efficiency and poor syngas yields are often experienced for most redox catalysts investigated to date [18,19,25]. To address the abovementioned limitations in solar-thermal water-splitting and CLR, we proposed a hybrid solar-redox scheme for liquid fuel and hydrogen co-production from methane and solar energy [26–28], based on the open-loop thermochemical cycle concept [29–32]. As illustrated in **Scheme 2.1**, the process uses a metal oxide based redox catalyst to partially oxidize methane into syngas. The reduced redox catalyst is then regenerated with steam, producing hydrogen. The heat required in such a two-step process is provided by solar energy.

Using $\text{La}_{0.8}\text{Sr}_{0.2}\text{FeO}_{3-\delta}$ (LSF) supported Fe_3O_4 as the redox catalyst, over 25% increase in efficiency and 30% reduction in CO_2 emissions, relative to conventional methane reforming-based liquid fuel and hydrogen generation processes, can be achieved [26,27]. The high energy conversion efficiency results from: (i) significantly lowered water-splitting temperature and increased steam-to-hydrogen conversion; (ii) simultaneous production of Fischer-Tropsch (F-T)-ready syngas and high purity hydrogen without the need for separation; (iii) strategic integration of solar-thermal energy.



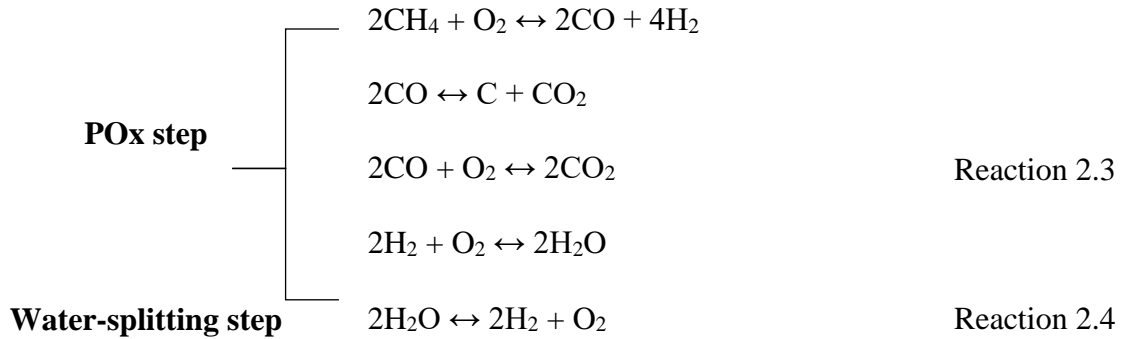
Scheme 2.1: Hybrid solar-redox scheme for syngas and hydrogen co-production.

Our previous studies indicated that the LSF support facilitates O^{2-} and electron conduction in the redox catalyst, thereby enhancing the activity and syngas selectivity of iron oxide for methane conversion [33]. Moreover, a small amount of oxygen vacancies, formed in LSF during the reduction step, participate in the water-splitting reaction and are highly effective. Over 95% methane conversion in the POx step and 77% steam-to-hydrogen conversion in the water-splitting step were achieved. Although the LSF-supported Fe_3O_4 performs significantly better than earlier

work, the syngas yield in the PO_x step was still limited to 67% [27]. Moreover, further improvements in steam-to-hydrogen conversion are desirable to obtain high process efficiency with lower CO₂ emissions. La and Ce-based redox catalysts have been tested for CLR with steam-regeneration as well [34, 35]. A low syngas yield of roughly 45% and average steam to hydrogen conversion close to 90% were reported. CeO₂ has a high oxygen-storage capacity and the interaction with La-containing oxides favors the removal and replenishment of lattice oxygen [35]. Ceria suppresses coke formation during CLR but the deactivation of Ce-containing materials under redox conditions has also been reported previously [36]. It is also desirable to minimize the utilization of rare earth elements like La and Ce, which are in limited supply. The current study investigates the optimization strategy for redox catalysts with the assistance of thermodynamic analysis and Density Functional Theory (DFT) calculations. Thermodynamic analysis of the redox reactions indicates an “optimal region” in the Ellingham diagram for high syngas yield and steam conversion. It was determined, however, that none of the known monometallic metal oxides possess desirable redox properties, to practically fit in such a region. DFT calculations indicated that the redox properties of multi-valent transition metals can be tuned by incorporating them into a mixed metal oxide structure. For instance, equilibrium oxygen partial pressure (P_{O₂}) and oxygen vacancy formation energy ($\Delta E_{\text{vacancy}}$) of perovskite-structured BaMn_xFe_{1-x}O_{3- δ} are significantly different from those of monometallic iron or manganese oxides. Moreover, these redox properties vary with a change in the B-site composition of the perovskite. Based on such principles, a rationally developed, perovskite based redox catalyst, i.e. BaMn_{0.5}Fe_{0.5}O₃, was discovered to be capable of achieving ~90% steam-to-hydrogen conversion and syngas yield.

2.3 Rational Strategy for Redox Catalyst Optimization

Similar to other redox processes, the hybrid solar-redox scheme involves indirect and cyclic exchange of oxygen with a fuel (CH₄) and an oxidant (H₂O). Although such exchange is facilitated by a metal oxide based redox catalyst, a generalized thermodynamic analysis can be carried out by investigating the (independent) reactions below:



Redox reactions of metal oxides can be omitted from the general analysis since they are merely used as the oxygen source (MeO_x in **Scheme 2.1**) and sink (MeO_y) from a thermodynamic standpoint (assuming negligible carbides or carbonates formation). It is apparent that water-splitting is favored under a low oxygen partial pressure (P_{O₂}) environment, thus pushing the reaction towards hydrogen; whereas syngas yield from methane POx is favored within a limited P_{O₂} range at any specific reaction temperature. That is, low P_{O₂} can lead to inadequate methane conversion whereas high P_{O₂} can lead to over oxidation of syngas to CO₂ and H₂O. The optimal P_{O₂} range for methane POx and water-splitting can thus be determined by analyzing the above reactions via Gibbs free energy minimization. Graphical representations of the analysis are shown in **Figure 2.1 and A1. Figure 2.1a**, which shows the favored reactions at a given set of temperature and P_{O₂}, can be used to evaluate the ease of reduction/oxidation of the metal oxides and their applicability for the proposed redox reactions.

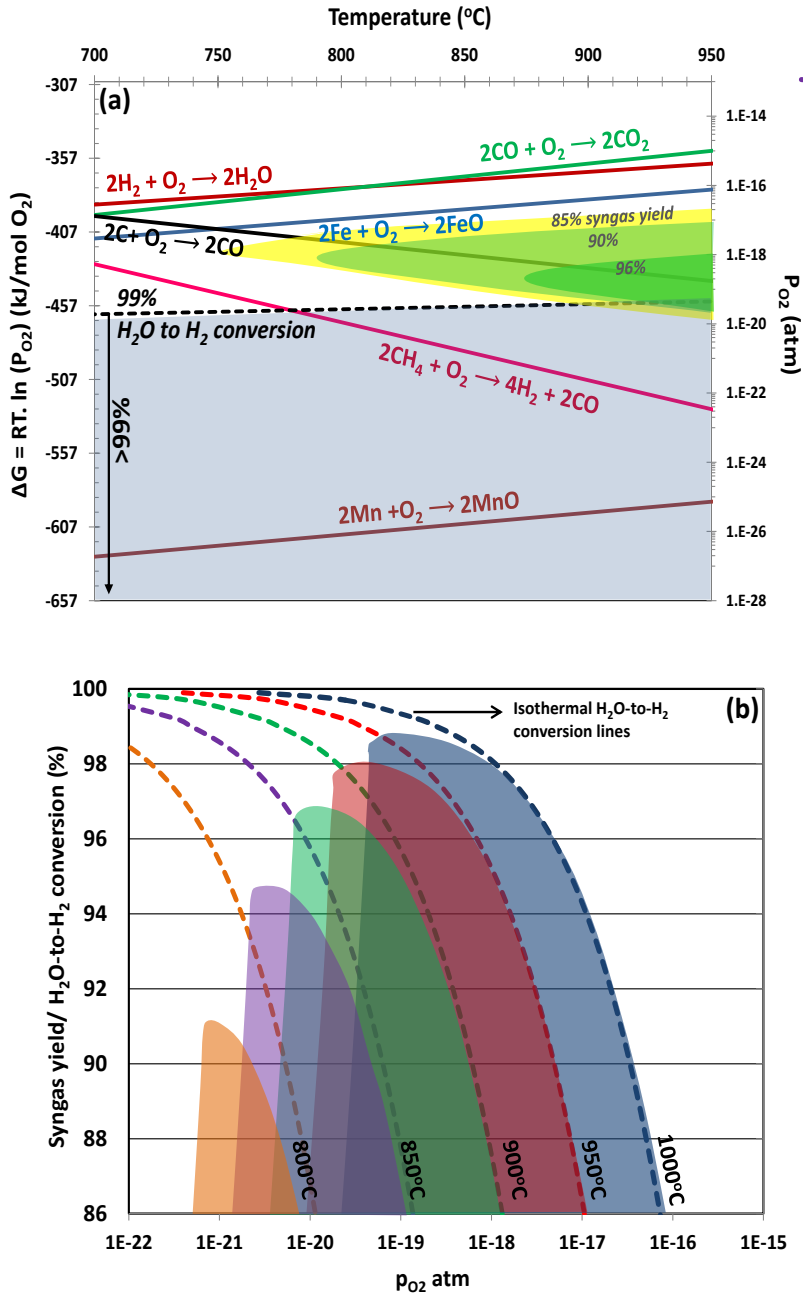
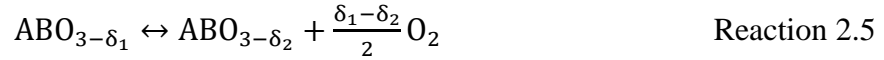


Figure 2.1: (a) Ellingham diagram for the hybrid solar-redox reactions (the P_{O_2} axis is at 950°C); (b) Equilibrium syngas yield (in methane PO_x) and steam conversion (in water-splitting) at different P_{O_2} and temperatures (the boundaries of the shaded regions map the syngas yields at the specified temperatures; the corresponding colored dashed lines define the isothermal steam conversion lines).

It is evident from **Figure 2.1a** that metal oxides with properties that intersect the dark green region are desired for the proposed hybrid solar-redox process from a thermodynamic standpoint. For instance, >96% syngas yield and >99% steam conversion can be achieved in the POx and water-splitting steps, respectively, provided that a metal oxide has redox properties that reside in this region: e.g. $2/(x-y) \text{ MeO}_y + \text{O}_2 \leftrightarrow 2/(x-y) \text{ MeO}_x$ has $-\Delta G = 430\text{-}480 \text{ kJ mol}^{-1}$ or $P_{\text{O}_2} = 4 \times 10^{-21} - 7 \times 10^{-20} \text{ atm}$ at 900°C . **Figure 2.1b** further illustrates the equilibrium steam conversion (in the water-splitting step) and syngas yield (in the methane POx step) at different temperatures and P_{O_2} . While **Figure 2.1** provides a useful guide for optimizing metal oxide based redox catalysts, most, if not all, monometallic metal oxides do not possess such desired properties. Rather, their equilibrium P_{O_2} is either too high or too low. Take MnO and FeO as the examples: the equilibrium P_{O_2} of FeO/Fe ($2\text{FeO} \leftrightarrow 2\text{Fe} + \text{O}_2$) ($7.2 \times 10^{-18} \text{ atm}$, with ~70% syngas-yield and steam conversion @ 900°C) is roughly three orders of magnitude higher than the desired region, limiting its ability to achieve high syngas selectivity in POx and high steam conversion in the water-splitting step. MnO/Mn, on the other hand, can achieve nearly 100% steam conversion ($\text{Mn} + \text{H}_2\text{O} \leftrightarrow \text{MnO} + \text{H}_2$). However, methane oxidation by MnO is not thermodynamically feasible due to the extremely low P_{O_2} ($2.5 \times 10^{-27} \text{ atm}$ with negligible syngas-yield @ 900°C). To identify metal oxides within the desirable P_{O_2} range, perovskite-structured oxide materials are investigated.

Perovskites are a series of mixed oxides with a general formula of $\text{ABO}_{3-\delta}$, where *A* can be a lanthanide and/or alkaline earth cation and *B* is often a transition metal cation. Such metal oxides can accommodate significant oxygen non-stoichiometry, resulting from acceptor-doping in its A-site cations and/or the variable valence states of its B-site cations. The proposed hybrid solar-redox reactions can proceed through the creation (POx step) and elimination (water-splitting step) of oxygen vacancies in such perovskite materials. We further note that the energy cost to create an

oxygen vacancy in perovskite materials is related to their efficacy for the proposed POx and water-splitting reactions:



This indicates that the redox properties and performance of a material can be evaluated based on the tendency of the material to form oxygen vacancies. While FeO and MnO are outside of the optimal region for the proposed redox reactions, one potential strategy to obtain a redox catalyst with desired properties is to integrate Fe and/or Mn into a perovskite structure, which will change the coordination environments for Fe or Mn cations. Moreover, Fe and Mn can co-occupy the perovskite B-site with different compositions, resulting in perovskite materials with tunable redox properties. To validate the abovementioned hypothesis, vacancy formation energy ($\Delta E_{\text{vacancy}}$) of four materials, i.e. FeO, MnO, BaMnO₃ (BMO), and BaMn_{0.5}Fe_{0.5}O₃ (BMFO), are calculated using Density Functional Theory (DFT). The redox properties of these oxides can be ranked based on $\Delta E_{\text{vacancy}}$. Oxide materials with lower vacancy formation energy are anticipated to have a higher equilibrium P_{O2} and a higher ΔG in the Ellingham diagram. While a more rigorous method to estimate equilibrium P_{O2} involves calculating the energy for phase transition of the metal oxides and accounting for the entropy contributions from the solids, vacancy formation energy comparison provides a simpler and more efficient approach to compare relative redox properties among various oxides.

Since equilibrium P_{O2} for a metal oxide is directly related to the strength of metal oxygen bonds in the crystal lattice, oxygen vacancy formation energies of metal oxides should correlate with their equilibrium P_{O2}, i.e. metal oxides with higher oxygen vacancy formation energy should have lower equilibrium P_{O2} due to the decreased tendency for decomposition. Equilibrium P_{O2} differences

among the various oxide systems can be determined by the relative DFT energies using the following relationship:

$$\frac{(p_{O_2})_1}{(p_{O_2})_2} = \exp \left[\frac{(\Delta E_{\text{vacancy}})_2 - (\Delta E_{\text{vacancy}})_1}{k_B T} \right] \quad \text{Equation 1}$$

Using the P_{O_2} value of FeO at 950°C, from thermodynamic database as a reference point, the P_{O_2} values for BaMnO₃, BaMn₅Fe₅O₃, and MnO at 950°C can be estimated using the corresponding values of $\Delta E_{\text{vacancy}}$ in the above equation. These results are illustrated on the Ellingham diagram in **Figure 2.2**.

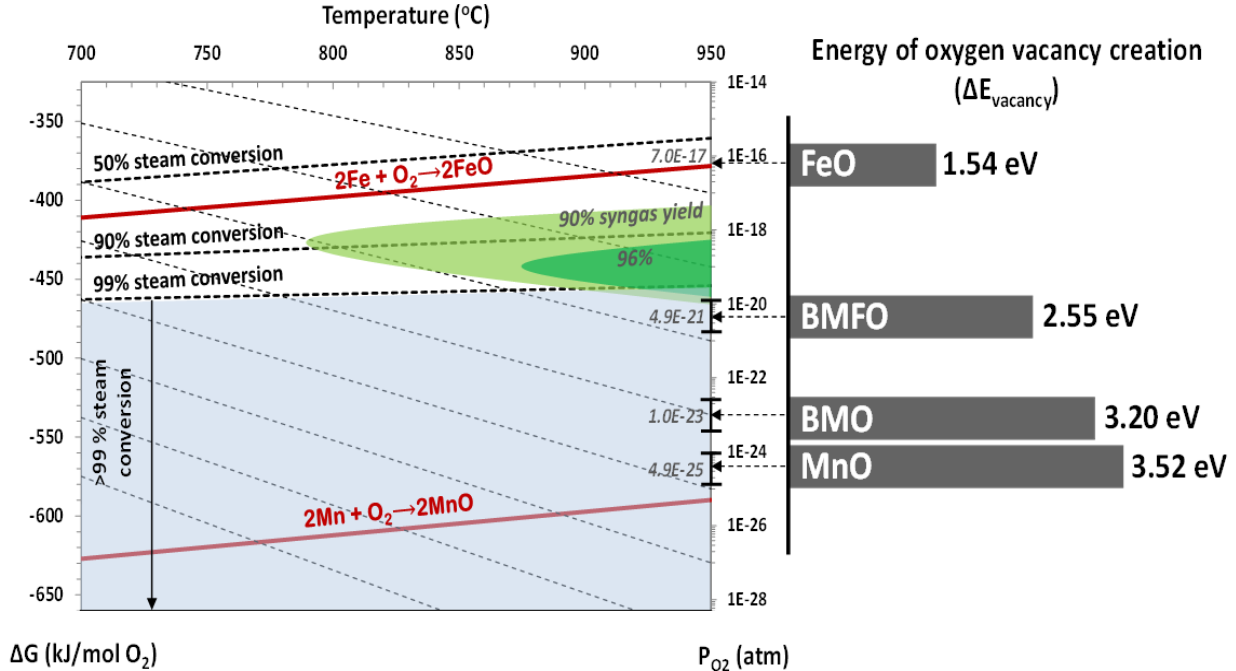


Figure 2.2: DFT-calculated $\Delta E_{\text{vacancy}}$ for the materials and the corresponding equilibrium P_{O_2} at 900°C. The grey dotted lines denote constant P_{O_2} lines.

As can be seen, the results predict the equilibrium P_{O_2} for MnO/Mn with good accuracy. It is apparent from **Figure 2.2** that while MnO and FeO are not ideal for the hybrid solar-redox process, BaMnO₃ and BaMn₅Fe₅O₃ exhibit intermediate redox properties between those of MnO and FeO.

Compared to BaMnO_3 , $\text{BaMn}_5\text{Fe}_5\text{O}_3$ exhibits more suitable redox properties for the proposed redox reactions. At 950°C , the DFT predicted equilibrium syngas yield and steam conversion for the proposed redox reactions are $>90\%$ and $>99\%$ respectively for $\text{BaMn}_5\text{Fe}_5\text{O}_3$.

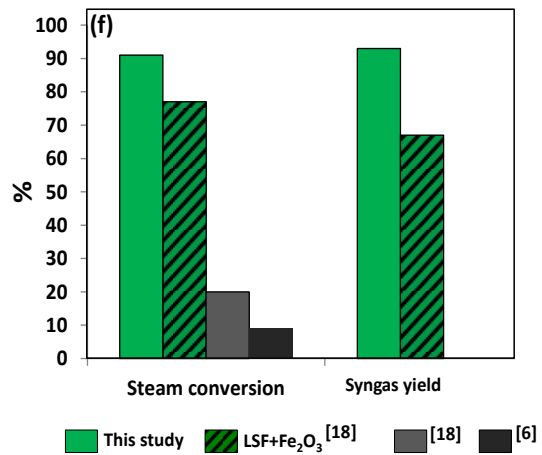
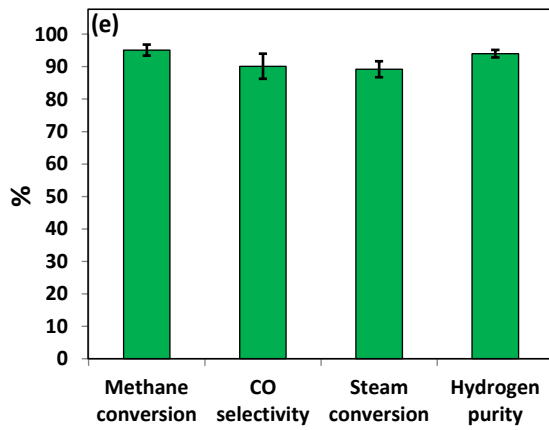
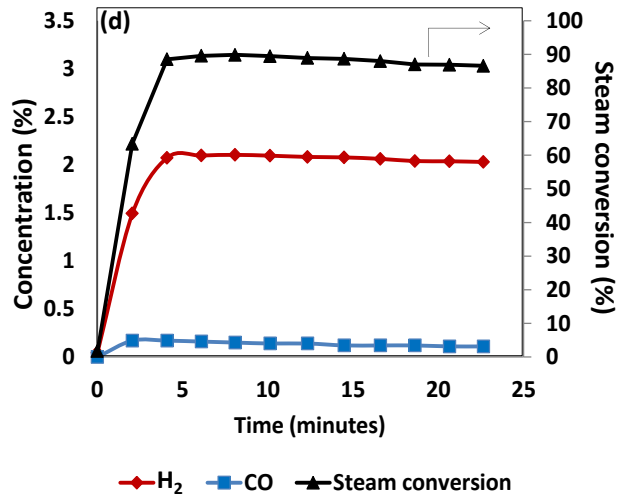
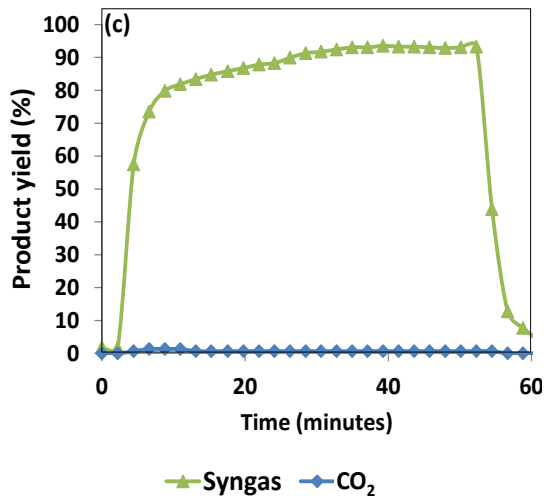
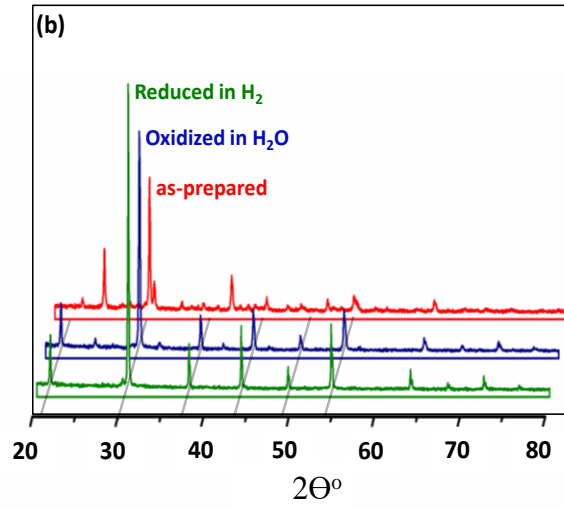
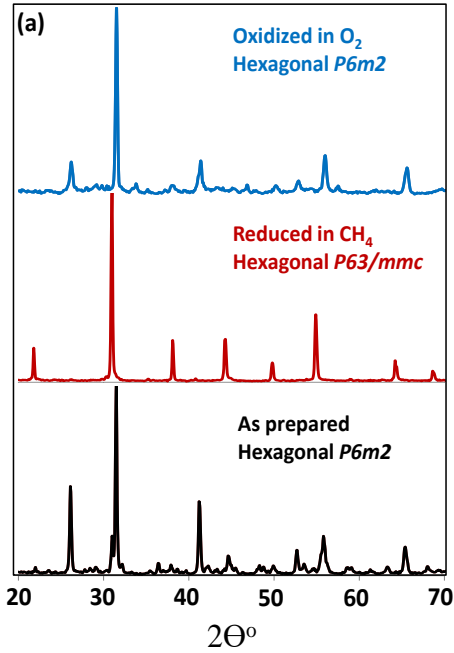
2.4 Experimental Validation of the Redox Catalyst Performance

In order to verify the above analyses, a $\text{BaMn}_5\text{Fe}_5\text{O}_3$ redox catalyst sample was synthesized, characterized and tested for the proposed cyclic redox operations. The changes in the XRD pattern indicate a structural/phase change during methane POx and water-splitting as shown in **Figure 2.3a**. All the samples shown in **Figure 2.3a** contain a perovskite phase indicating a process driven by formation and elimination of oxygen vacancies. Based on the structure of the as-prepared and the oxidized sample, the redox catalyst is shown to be regenerable. *In-situ* XRD spectra of the sample under H_2 - H_2O -redox reactions at 900°C are also performed (**Figure 2.3b**). Introduction of steam into the partially reduced sample leads to regeneration of the original hexagonal structure. The *in-situ* XRD experiments also confirm the regenerability of the redox catalyst. The $\text{BaMn}_5\text{Fe}_5\text{O}_3$ based redox catalysts were also tested in a fluidized bed reactor. The product distributions during the methane POx and water-splitting steps are shown in **Figure 2.3c and d**. The redox catalyst demonstrated excellent stability over 18 redox cycles with a slight increase in syngas conversion during cycles 14 - 18 resulting from an adjustment in inlet gas flow rates (**Table A3**). Maximum methane conversion of over 94% (95% average) was achieved during the POx step with $>90\%$ syngas-yield (88% average). Steam conversion of $\sim 90\%$ (89% average) was also observed in the water-splitting step with up to 95% H_2 purity (94% average). During cycles 14-18, up to 6% carbon monoxide was observed during the water-splitting step due to the removal of coke deposited during the methane POx step.

Figure 2.3: (a) XRD patterns of as-prepared, reduced and oxidized BMFO; (b) in-situ XRD patterns under redox conditions; (c) Typical syngas yield profile during the methane POx step ($H_2:CO = 2.1:1$); (d) Instantaneous product distribution (N_2 and H_2O -free basis) and steam conversion during the water splitting step as a function of time at $900\text{ }^\circ\text{C}$ (cycle 15 data shown here); (e) Methane conversion, CO selectivity, steam conversion, and hydrogen purity (average value of the last five redox cycles with the error bars denoting 95% confidence interval); (f)

Reported steam conversion and syngas yield:

■ *This study (average during cycles 14-18)*, ■ *LSF+Fe₂O₃ in hybrid solar-redox²⁷*, ■ *maximum conversion for open-loop thermochemical cycle²⁷*, ■ *a high-end conversion in solar thermochemical processes⁹.*



Further comparisons of the $\text{BaMn}_5\text{Fe}_5\text{O}_3$ redox performance relative to state-of-the-art redox catalysts confirm significant enhancement in the efficacy of both POx and water-splitting steps for this rationally designed redox catalyst (**Figure 2.3e and f**). As compared to LSF-supported Fe_3O_4 which exhibited the best performance for water-splitting reported so far, the syngas-yield and steam-conversion were 30% and 33% higher, respectively ^[26]. To our knowledge, the $\text{BaMn}_5\text{Fe}_5\text{O}_3$ redox catalyst is the only thermochemical redox material that exhibited 90% water-splitting-conversion based on literature reported to date. **Table A4** summarizes the performance of $\text{BaMn}_5\text{Fe}_5\text{O}_3$, during the redox reactions. The superior performance of the redox catalyst during methane POx and water-splitting leads to an excellent energy conversion efficiency in the hybrid solar-redox scheme. Using our previously reported ASPEN Plus® model ^[28] and experimental data obtained in the fluidized bed experiments, we estimate the methane-to-fuel conversion efficiency to be 83% (HHV), which includes liquid-fuel and H_2 co-production. Compared to conventional approaches such as indirect gas-to-liquids (GTL) technology and reforming-based hydrogen production processes, the newly developed $\text{BaMn}_5\text{Fe}_5\text{O}_3$ redox catalyst has the potential to be 38% more efficient with over 70% reduction in CO_2 emissions for the H_2 product.

2.5 Conclusions

In summary, we proposed and validated a rational strategy to optimize transition metal oxide-based redox catalysts for water-splitting and syngas generation via a hybrid solar redox scheme. Thermodynamic analysis suggests an optimal region on the Ellingham diagram for the proposed methane POx and water-splitting reactions. While few, if any, monometallic metal oxides possess redox properties that reside in this optimal region, DFT calculations reveal the potential of changing the redox properties of Mn and Fe containing oxides by incorporating Mn/Fe cations into

a perovskite structure. For instance, the equilibrium oxygen partial pressure (P_{O_2}) and oxygen vacancy formation energy ($\Delta E_{\text{vacancy}}$) of perovskite-structured $\text{BaMn}_x\text{Fe}_{1-x}\text{O}_{3-\delta}$ are significantly different from those of FeO and MnO. Changing the B-site composition of Barium-containing perovskites can help in adjusting the equilibrium P_{O_2} of the resulting oxides. DFT studies indicate that $\text{BaMn}_{0.5}\text{Fe}_{0.5}\text{O}_{3-\delta}$ possesses desirable properties for the hybrid solar-redox scheme. Such findings were further confirmed by experimental studies. Fluidized bed experiments demonstrated 90% steam conversion in the water-splitting step, compared to a typical conversion of <9% in solar-thermal water-splitting. Over 90% yield in F-T ready syngas was also achieved in the methane POx step. The redox catalyst was shown to be active and regenerable under redox conditions. ASPEN Plus® simulation indicates that the rationally optimized $\text{BaMn}_{0.5}\text{Fe}_{0.5}\text{O}_{3-\delta}$ has the potential to increase the methane-to-fuel efficiencies of state-of-the-art hydrogen and liquid fuel production processes by 38% (relative basis) with 70% lower CO_2 emissions for hydrogen production.

2.6 Experimental Section

2.6.1 Material synthesis

A solid-state reaction (SSR) method was used for sample preparation. Stoichiometric amounts of precursors, i.e. iron oxide (Fe_2O_3 , 99.9%, Noah Chemicals), BaO_2 (99.9%, Noah Chemicals), and Mn_2O_3 (99.9%, Noah Chemicals) were weighed. This was followed by ball-milling, pelletization and sintering at 1200°C for 12 hours. The resulting pellets were subsequently crushed and sieved into 90 to 300 μm .

2.6.2 Characterizations

Crystallite phases of the redox catalysts were confirmed using X-ray powder diffraction (XRD) (Rigaku SmartLab), analyzed using HighScore Plus^[37]. *In-situ* powder XRD studies were performed by PANalytical Empyrean XRD with XRK 900 reaction stage. The 100 mg powder sample was supported on a porous silica disk of 2 cm in diameter. The reaction stage was first heated up to 900 °C with Ar as the inert gas. After that, 3% H₂ (balanced with Ar) was passed through the catalyst sample as the reducing gas at a flowrate of 50 ml/min. After 30 min of reduction or when there is no change of the XRD spectrum, H₂ flow was switched to an Ar-purge for 15 minutes. This was followed by the injection of the oxidizing gas i.e. Ar saturated with steam (~2%) at 20°C.

2.6.3 DFT Calculations

The spin polarized generalized gradient approximations (GGA) and the projector augmented wave (PAW)^[38,39] approach with the PBE^[37] exchange correlation functional, as implemented in VASP^[38-41] were used for the geometry optimizations. A 2x2x2 gamma centered k-point mesh was used for a 2x2x2 unit cell (80 atoms) for BaMnO₃ and BaMn_{0.5}Fe_{0.5}O₃ whereas for MnO and FeO, a 4x4x4 monkhorst-pack mesh was used for a 2x2x2 unit cell (64 atoms). The mesh density was kept constant at larger supercell sizes and an energy cutoff of 450 eV was used for all calculations. Both mesh density and energy cutoff were tested for convergence and system energies were converged within 0.1 eV. Since we are interested in the relative differences of vacancy formation energies, the Hubbard U parameter was not implemented in these calculations.

2.6.4 Fluidized bed experiments

Redox experiments were carried out in a stainless steel tubular reactor with an inner diameter of 19 mm. The reactor was externally heated with a tube furnace (MTI OTF-1200X-S-VT) with K

type thermocouple measuring the temperature. A gas mixing panel with multiple Brooks mass flow controllers (MFCs) was used to deliver gaseous mixtures, e.g. nitrogen and methane, to the reactor. In each experiment, 20 grams of redox catalyst particles was added on top of a SiC layer which served as a gas distributor. In order to mimic the hybrid redox scheme, the tests were carried out in two consecutive steps, i.e. methane POx (redox catalyst reduction) and water-splitting (redox catalyst oxidation). The redox reaction temperature was set at 900 °C. 200 mL min⁻¹ (STP: standard temperature of 0°C and pressure of 1 atm) N₂ was used as the fluidization gas in both reduction and oxidation steps, as well as the purge gas between these two steps. 3.2 ml min⁻¹ (STP) CH₄ was introduced along with N₂ during the reduction step. Water-splitting reaction was carried out after the residue gas from the POx step was completely purged with N₂. For the oxidation step, the N₂ stream was saturated with water at 20 °C to create a gaseous stream that contains 2.34 mol% steam prior to entering the reactor. Compositions of the gases exiting the reactor were determined using a gas chromatograph (Agilent Micro GC 490) and a multi-gas analyzer (Emerson X-Stream gas analyzer). Parameters for evaluating the redox experiments are summarized in **Table A2**.

2.7 References

- [1] J. M. Ogden, *Annu. Rev. Energy Environ.* **1999**, *24*, 227.
- [2] A. Züttel, A. Borgschulte, L. Schlapbach, *Hydrogen as a Future Energy Carrier*, John Wiley & Sons, **2011**.
- [3] J. Turner, G. Sverdrup, M. K. Mann, P.-C. Maness, B. Kroposki, M. Ghirardi, R. J. Evans, D. Blake, *Int. J. Energy Res.* **2008**, *32*, 379.
- [4] K. Maeda, K. Domen, *J. Phys. Chem. Lett.* **2010**, *1*, 2655.
- [5] J. Luo, J.-H. Im, M. T. Mayer, M. Schreier, M. K. Nazeeruddin, N.-G. Park, S. D. Tilley, H. J. Fan, M. Grätzel, *Science* **2014**, *345*, 1593.
- [6] M. Broda, A. M. Kierzkowska, C. R. Müller, *Chem. Eng. Technol.* **2013**, *36*, 1496.
- [7] M. Broda, V. Manovic, Q. Imtiaz, A. M. Kierzkowska, E. J. Anthony, C. R. Müller, *Environ. Sci. Technol.* **2013**, *47*, 6007.
- [8] M. G. Walter, E. L. Warren, J. R. McKone, S. W. Boettcher, Q. Mi, E. A. Santori, N. S. Lewis, *Chem. Rev.* **2010**, *110*, 6446.
- [9] W. C. Chueh, C. Falter, M. Abbott, D. Scipio, P. Furler, S. M. Haile, A. Steinfeld, *Science* **2010**, *330*, 1797.
- [10] M. Roeb, C. Sattler, *Science* **2013**, *341*, 470.
- [11] M. Romero, A. Steinfeld, *Energy Environ. Sci.* **2012**, *5*, 9234.
- [12] N. S. Lewis, *Science* **2016**, *351*, aad1920.
- [13] E. Rytter, K. Soušková, M. K. Lundgren, W. Ge, Å. D. Nannestad, H. J. Venvik, M. Hillestad, *Fuel Process. Technol.* **2016**, *145*, 1.
- [14] I. Ermanoski, J. E. Miller, M. D. Allendorf, *Phys. Chem. Chem. Phys.* **2014**, *16*, 8418.
- [15] K. Go, S. Son, S. Kim, K. Kang, C. Park, *Int. J. Hydrog. Energy* **2009**, *34*, 1301.
- [16] L.-S. Fan, *Chemical Looping Systems for Fossil Energy Conversions*, John Wiley & Sons, **2011**.
- [17] M. Tang, L. Xu, M. Fan, *Appl. Energy* **2015**, *151*, 143.

- [18] C. Dueso, M. Ortiz, A. Abad, F. García-Labiano, L. F. de Diego, P. Gayán, J. Adánez, *Chem. Eng. J.* **2012**, *188*, 142.
- [19] M. Ortiz, A. Abad, L. F. de Diego, F. García-Labiano, P. Gayán, J. Adánez, *Int. J. Hydrog. Energy* **2011**, *36*, 9663.
- [20] M. Rydén, A. Lyngfelt, T. Mattisson, *Fuel* **2006**, *85*, 1631.
- [21] A. Tsoukalou, Q. Imtiaz, S. M. Kim, P. M. Abdala, S. Yoon, C. R. Müller, *J. Catal.* **2016**, *343*, 208.
- [22] J. Adanez, A. Abad, F. Garcia-Labiano, P. Gayan, L. F. de Diego, *Prog. Energy Combust. Sci.* **2012**, *38*, 215.
- [23] Q. Imtiaz, N. S. Yüzbaşı, P. M. Abdala, A. M. Kierzkowska, W. van Beek, M. Broda, C. R. Müller, *J Mater Chem A* **2016**, *4*, 113.
- [24] C. Agrafiotis, M. Roeb, C. Sattler, *Renew. Sustain. Energy Rev.* **2015**, *42*, 254.
- [25] M. Rydén, A. Lyngfelt, T. Mattisson, *Energy Fuels* **2008**, *22*, 2585.
- [26] F. He, J. Trainham, G. Parsons, J. S. Newman, F. Li, *Energy Env. Sci* **2014**, *7*, 2033.
- [27] F. He, F. Li, *Energy Env. Sci* **2015**, *8*, 535.
- [28] F. He, F. Li, *Int. J. Hydrog. Energy* **2014**, *39*, 18092.
- [29] W. L. Conger, *Int. J. Hydrog. Energy* **1979**, *4*, 517.
- [30] A. Steinfeld, P. Kuhn, J. Karni, *Energy* **1993**, *18*, 239.
- [31] A. Steinfeld, *Energy* **1997**, *22*, 311.
- [32] A. Steinfeld, *Sol. Energy* **2005**, *78*, 603.
- [33] N. L. Galinsky, Y. Huang, A. Shafieifarhood, F. Li, *ACS Sustain. Chem. Eng.* **2013**, *1*, 364.
- [34] Y. Zheng, K. Li, H. Wang, D. Tian, Y. Wang, X. Zhu, Y. Wei, M. Zheng, Y. Luo, *Appl. Catal. B Environ.* **2017**, *202*, 51.
- [35] Y. Zheng, Y. Wei, K. Li, X. Zhu, H. Wang, Y. Wang, *Int. J. Hydrog. Energy* **2014**, *39*, 13361
- [36] N. L. Galinsky, A. Shafieifarhood, Y. Chen, L. Neal, F. Li, *Appl. Catal. B Environ.* **2015**, *164*, 371.

- [37] T. Degen, M. Sadki, E. Bron, U. König, G. Nénert, *Powder Diffr.* **2014**, 29, S13
- [38] G. Kresse, D. Joubert, *Phys. Rev. B* **1999**, 59, 1758.
- [39] P. E. Blöchl, *Phys. Rev. B* **1994**, 50, 17953.
- [40] J. P. Perdew, K. Burke, M. Ernzerhof, *Phys. Rev. Lett.* **1996**, 77, 3865.
- [41] G. Kresse, J. Furthmüller, *Phys. Rev. B* **1996**, 54, 11169.

**CHAPTER 3: MODIFIED CERIA FOR LOW-TEMPERATURE CO₂ UTILIZATION: A
CHEMICAL LOOPING ROUTE TO EXPLOIT INDUSTRIAL WASTE HEAT**

is a reprint of a manuscript accepted for publication in *Advanced Energy Materials* 2019.

The supplementary information is in Appendix B.

3.1 Abstract

Efficient CO₂ utilization is key to limit global climate change. Carbon monoxide, which is a crucial feedstock for chemical synthesis, can be produced by splitting CO₂. However, existing thermochemical routes are energy-intensive requiring high operating temperatures. We report a Hybrid Redox Process (HRP) involving CO₂-to-CO conversion using a lattice oxygen-deprived redox catalyst at relatively low temperatures (<700 °C). The lattice oxygen of the redox catalyst, restored during CO₂ splitting, is subsequently used to convert methane to syngas. Operated at temperatures significantly lower than a number of industrial waste heat sources, this cyclic redox process allows for efficient waste heat-utilization to convert CO₂. To enable the low-temperature operation, we report lanthanum-modified ceria (1:1 Ce: La) promoted by rhodium (0.5 wt. %) as an effective redox catalyst. Near-complete CO₂ conversion with a syngas yield of up to 83% at low temperatures were achieved using Rh-promoted LaCeO_{4-x}. While La improves low-temperature bulk redox properties of ceria, Rh considerably enhances the surface catalytic properties for methane activation. Density Functional Theory calculations further illustrate the underlying functions of La substitution. The highly effective redox catalyst and HRP scheme provide a potentially attractive route for chemical production using CO₂, industrial waste heat, and methane, with appreciably lowered CO₂ emissions.

3.2 Introduction

Fossil fuel utilization through human activities lead to over 35,000 teragrams (Tg) global emissions of greenhouse gases each year, with CO₂ being the primary component^[1]. With the aim to limit global warming below a 2°C increase, efficient usage of CO₂ is a pressing issue. CO₂ utilization is a broad term covering a range of technologies that involves the consumption of CO₂

to provide products or services with the main objective of an economic benefit, ideally with additional environmental and social benefits^[2,3]. CO₂ is viewed as a waste product in the context of flue gases, but it has the potential to be a valuable commodity. Productive utilization of CO₂ via conversion to valuable chemicals, is an attractive avenue^[1,2,4]. With a growing global population, cost-effective chemical synthesis *via* CO₂-utilization is highly desired^[5].

For the C₁ molecules, Gibbs free energies of formation (ΔG_f) are in the following order: CH₄ > CH₃OH > HCHO > CO > HCOOH > CO₂^[6,7]. Strong double bonds with oxygen make carbon dioxide stable and difficult to convert from a thermodynamic viewpoint. Geological CO₂ sequestration represents one of the few CO₂ conversion processes that are energetically favored. However, it is technically challenging and can be cost-intensive^[1]. Some CO₂ conversion reactions such as carboxylation do not require significant energy input. However, the production of the carboxylation reactants such as alcohols and alkenes can be quite energy intensive. Reactions producing reduced forms of CO₂ like formaldehyde or carbon monoxide also demand hefty energy input. The required energy, which is thermodynamically unavoidable, can be supplied thermally, electrochemically or photo-chemically^[7]. Electrochemical routes face challenges of low energetic efficiency (or large over-potential), slow electron transfer kinetics, low selectivity and poor long-term stability causing a major hurdle towards commercialization^[8]. Similarly, high operating temperatures and low photon efficiencies hinder the practical operation of the thermo-chemical and photo-chemical processes, respectively^[9-13]. From a sustainability standpoint, the required external energy should be supplied by a renewable source. While such resources can supply the required energy, they still face challenges related to available capacity, intermittency, and/or cost. Industrial waste heat, on the other hand, is an abundant (5-13 quadrillion BTU/year, in the US) and low cost energy source. Discharged industrial waste contains 20-50% of the consumed

industrial energy^[14]. For instance, the oxy-fuel glass furnace can produce 1,427°C-exhaust containing 1.22 GJ of sensible waste heat per metric ton of glass product, which is currently wasted^[1,15]. Recovering this waste heat for CO₂ utilization can result in significant net reduction of greenhouse gas emissions. The challenge for industrial waste heat integration, however, resides in its significantly lower quality (exergy-wise) compared to electric power, chemicals, or fuels. As such, thermochemical CO₂ utilization processes operated at low temperatures are necessary to enable efficient utilization of industrial waste heat.

Commercially, carbon monoxide (CO) is an indispensable raw material for chemical production^[16], being the starting point for a plethora of carbonyl compounds. CO₂-to-CO is a CO₂-utilization scheme which can help produce valuable chemicals sustainably. We propose a Hybrid Redox Process (HRP), shown in **Figure 3.1a**, which not only utilizes the CO₂ to produce CO, but also has the potential to exploit the industrial waste heat, due to its low-temperature operation. Additionally, it uses the abundant methane^[17] to produce methanol-ready syngas. HRP involves a two-step, open thermochemical loop facilitated by a redox catalyst (Reactions 3.1 and 3.2). In the first step, a reduced redox catalyst (generically denoted as MeO_y) reacts with CO₂ to produce high purity CO while being oxidized in the process. The oxidized redox catalyst (MeO_x, x>y) subsequently reacts with methane to yield synthesis gas (syngas, which is CO+H₂) with a H₂: CO ratio (~2:1), ideal for methanol and Fischer-Tropsch synthesis^[6,18,19]. Both syngas and CO are important industrial feed-stocks for chemical production. Transformation of CO₂, CH₄, and industrial waste heat *via* HRP thus offers various opportunities for chemical synthesis, as shown in **Figure 3.1b**.

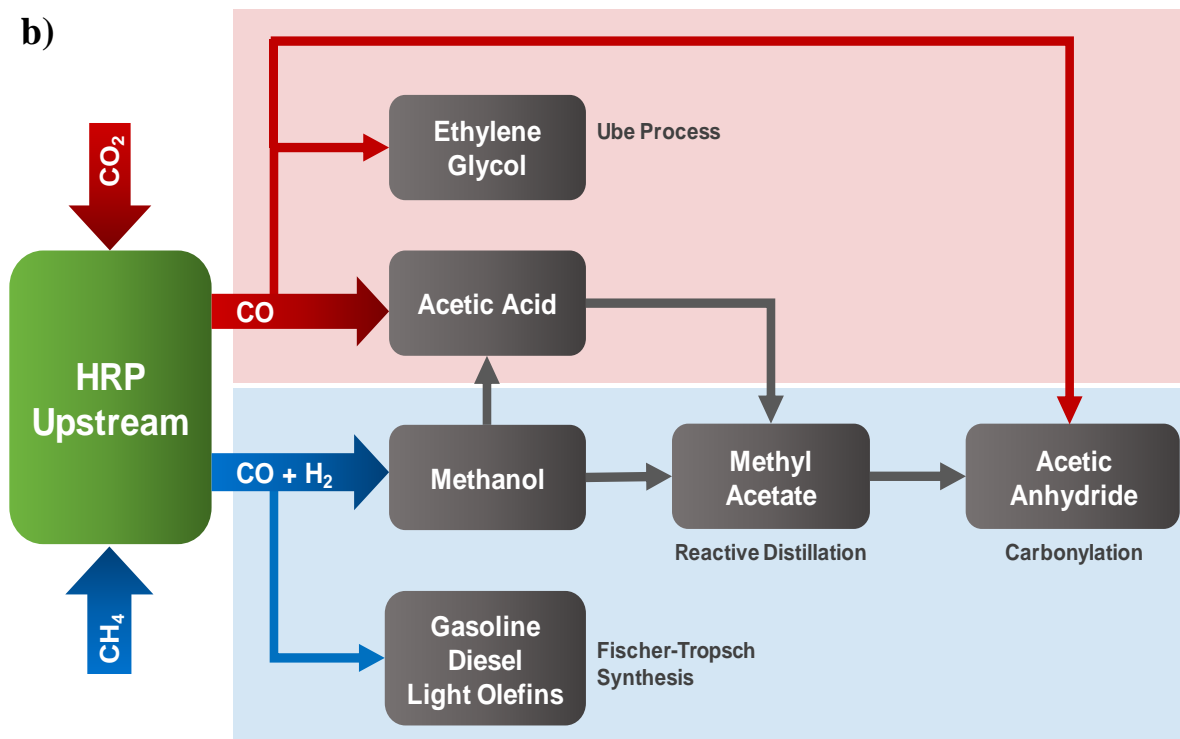
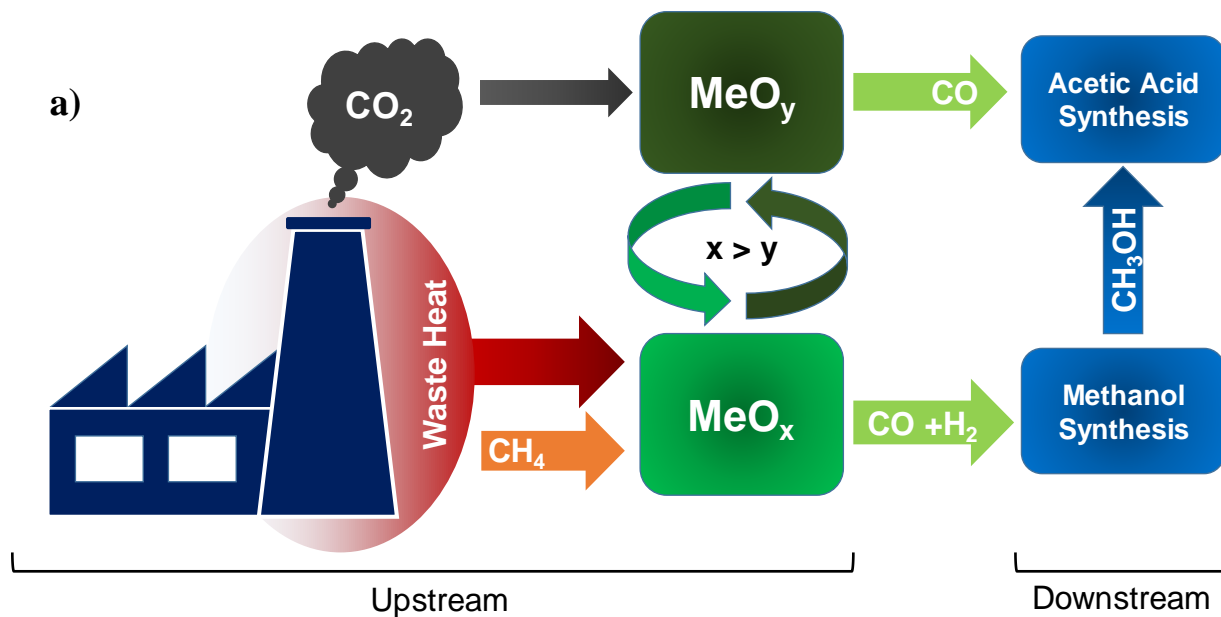


Figure 3.1: a) Schematic of HRP (considering acetic acid as the final product); b) Paths to synthesize chemicals from CO and syngas, obtained via HRP.

As an example, the syngas products from HRP can readily be converted into methanol using Reaction 3.3. By combining this methanol product with the CO product, generated from HRP, acetic acid can be produced by the commercial carbonylation reaction (Reaction 3.4)^[6,16,20]. Other potential products from HRP include methyl acetate, acetic anhydride, etc.



The main challenge for HRP resides in efficient conversion of both methane and CO₂ at relatively low temperatures. The C-H bond in methane has a dissociation energy of 439.3 kJ/mol, making its activation non-trivial, especially when lattice oxygen is used as the oxidant^[21–24]. On the other hand, existing thermochemical approaches for CO₂-splitting require high temperatures and are often subjected to limited CO₂-to-CO conversion^[10,25–29]. Sr and Fe-containing perovskite nanocomposites have exhibited exceptional efficacy for both CO₂-splitting and methane partial oxidation (POx), with >98% CO yield and 96% syngas selectivity in respective steps^[30]. However, these materials require high operating temperatures (>950°C), which do not allow for efficient use of the waste heat. Ceria (CeO₂) is another promising candidate for the two reaction steps, owing to its ability to accommodate oxygen non-stoichiometry and fast oxygen diffusion kinetics. But, it requires temperatures >900°C for high methane conversions^[10,31–33]. The substitution in ceria and surface promotion with platinum group metals have been attempted in previous studies to enhance the activity of ceria-based redox catalysts^[26,32]. However, effective redox catalysts for methane conversion and CO₂-splitting at low operating temperatures have yet to be reported.

For the HRP process, an ideal redox catalyst should possess (i) high oxygen release and storage capacity; (ii) fast oxygen exchange rates; (iii) good stability over redox cycles;^[21] and (iv) ability to operate at low temperatures ($< 700^{\circ}\text{C}$). In the current study, we report 0.5 wt. % Rh-promoted LaCeO_{4-x} (Rh/LCO) as a superior redox catalyst for HRP. High CO_2 conversion ($>95\%$) and CH_4 -to-syngas yield (83%) are demonstrated at low temperatures ($\sim 650^{\circ}\text{C}$). It was determined that La-substitution decreases both the surface and bulk oxygen vacancy formation energies in CeO_2 . Moreover, energy barriers for vacancy migration are also significantly lowered. The low temperature methane activity is further enhanced by Rh-promotion on the oxide surface. When operated at $<700^{\circ}\text{C}$, a majority of the exergy (available work) in the waste heat from a typical glass plant can be utilized. At this rate, waste heat from the U.S. glass industry (2.9 million metric tons of glass/year) alone would be adequate to convert 2.3 million metric tons of CO_2 each year, producing 2.71 million metric tons of acetic acid annually^[1,14,15,34]. Integration of the waste heat and low cost natural gas to convert CO_2 can reduce the net CO_2 emission for acetic acid production by 99%. Through CO_2 utilization and waste heat recovery, HRP and the low temperature redox catalyst reported in this study also has the potential to produce value-added chemicals well beyond acetic acid.

3.3 Results and Discussion

3.3.1 HRP Redox Catalyst Design

Cerium-based oxides, with high oxygen anion (O^{2-}) conductivity, are promising redox catalysts^[26,35–37]. At low temperatures, the concentration of oxygen vacancy and its energy barrier for migration are particularly important since they determine the rate at which lattice oxygen can participate in the redox reactions. It is noted that unmodified CeO_2 has relatively low O^{2-}

conductivity and poor redox kinetics at the temperatures of interest for HRP. However, the fluorite structure can accommodate cation dopants for improved O^{2-} conductivity and/or structural stability^[35,38]. Among a variety of cations, trivalent lanthanum cation is a good candidate due to its similarity in mass and size when compared to Ce^{4+} . Meanwhile, addition of lanthanum can also hinder coke formation by increasing the surface basicity. $LaCeO_{4-x}$ (or LCO) is chosen in the current study since substitution of more than 50% Ce in CeO_2 with La was reported to cause phase segregation whereas LCO forms a stable structure^[33,35].

3.3.2 Effect of La^{3+} substitution: DFT Calculation

To determine the effect of La-substitution, Density Functional Theory (DFT) calculations were performed on (i) the bulk and surface oxygen vacancy formation energies (ΔE_V) and (ii) energy barriers for oxygen vacancy migration of both pure and La-substituted ceria (CeO_2 and LCO, respectively). The former quantifies the thermodynamic energy required for lattice oxygen removal whereas the latter depicts the ease of vacancy migration from a kinetics-viewpoint. Both are important factors for the oxygen conductivity that is required for macroscopic lattice oxygen removal and re-deposition in redox reactions. LCO unit cell was constructed by replacing two Ce atoms of the pristine CeO_2 unit cell by La atoms, and then removing one O atom to form an oxygen vacancy (V_O) as shown in **Figure B1**. As depicted in **Figure 3.2a**, the computed ΔE_V for LCO bulk is 2.26 eV, which is notably lower than that for pristine CeO_2 (2.99 eV^[39]). The ease of O^{2-} migration in LCO bulk can be correlated with a lower oxygen migration barrier of 0.30 eV (vs. 0.46 eV for pure CeO_2 ^[35]) (**Figure 3.2b**), computed through transition-state calculations. In terms of vacancy creation and migration on the surface, (111) surface was selected for both CeO_2 and LCO since it is reported as the most stable ceria surface^[40].

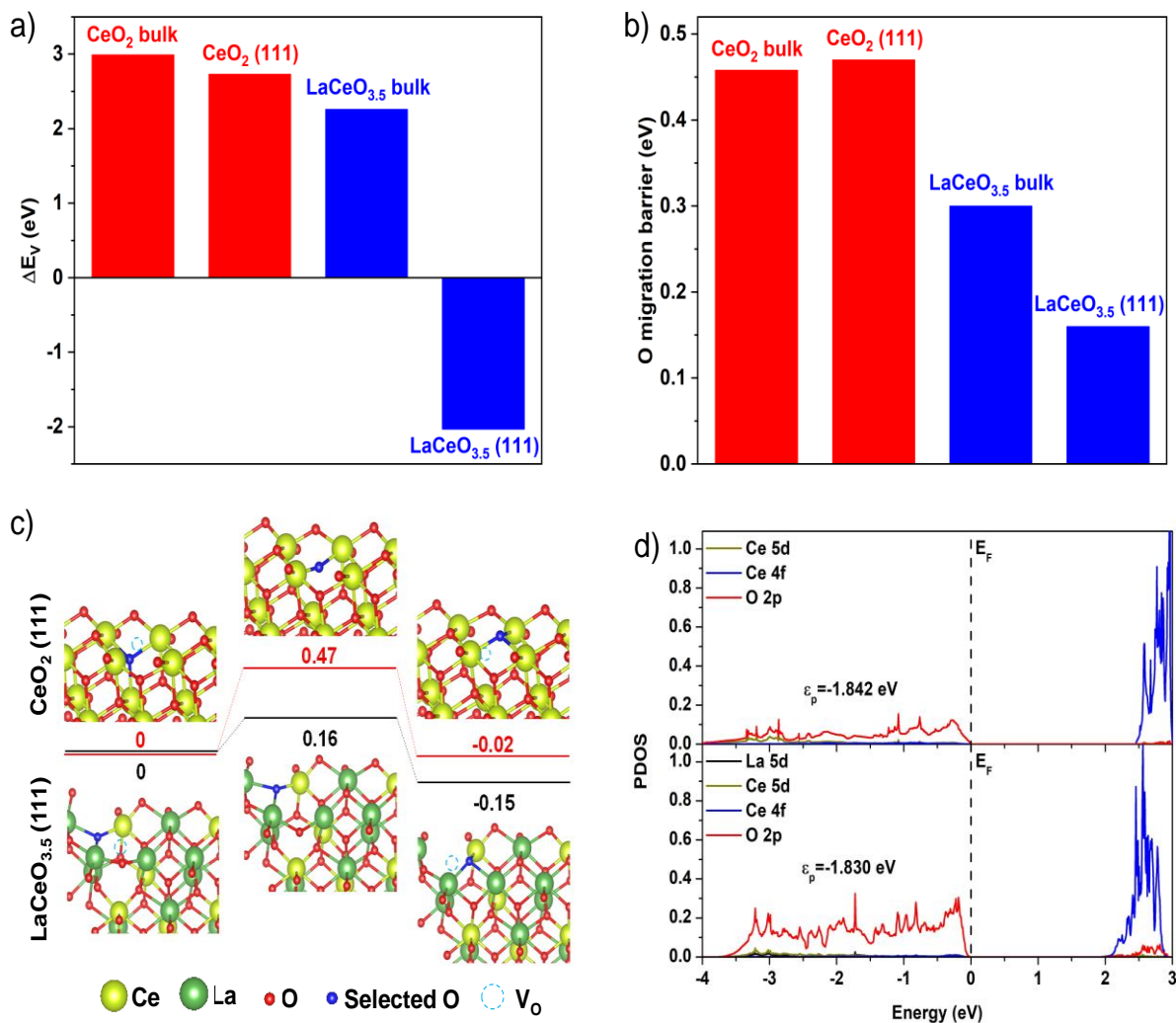


Figure 3.2: a) Computed energies of oxygen vacancy formation (ΔE_V); b) Energy barriers for oxygen vacancy migration for bulk and (111) surface of CeO₂ and LaCeO_{3.5}; c) Energy potential profile along the most favorable oxygen migration pathway on the (111) surfaces of CeO₂ and LaCeO_{3.5}; d) Electronic projected density of states (PDOS) of CeO₂ and LaCeO_{3.5}.

Based on the X-ray photoelectron spectroscopy (XPS) results listed in **Table 3.1**, significant enrichment of La (~2:1 La:Ce atomic ratio) was observed near the oxide surface. As such, the surface was constructed with a similar La: Ce ratio in DFT, as shown in **Figure 3.2c**. A negative

value of ΔE_V was computed for LCO (111) surface, indicating a higher surface oxygen vacancy concentration than the initially assumed $\text{LaCeO}_{3.5}$ stoichiometry. The migration pathway of the sub-surface oxygen to the vacancy site has a very low barrier of 0.16 eV, which is much lower than that of CeO_2 (111) surface (0.47 eV). Overall, the DFT results indicate significantly easier oxygen migration and release, in La-substituted ceria.

Table 3.1: : Near surface atomic compositions of the redox catalysts (oxygen free basis, numbers shown in parentheses correspond to expected compositions based on bulk stoichiometry).

Sample	La 3d (%)	Ce 3d (%)	Rh 3d (%)
CeO₂		100.0	
LCO	64.1 (50)	35.9 (50)	
Rh/LCO	61.0 (49.6)	34.7 (49.6)	4.3 (0.8)

To further elucidate the effect of La-substitution, charge distributions of CeO_2 and $\text{LaCeO}_{3.5}$ were studied. Lanthanum, a p-type dopant, can effectively reduce the electron donation by the cations compared to CeO_2 , thereby decreasing the number of valence electrons (from 1.23 e^- per O for pristine ceria to 1.19 e^-) on oxygen anions. The decrease in electron density can weaken the strength of the metal-oxygen (M-O) ionic bond. This effect of La-substitution, combined with existing oxygen vacancies, reorganize the electronic states for LCO when compared to CeO_2 . Such a reorganization of oxygen electronic states can be well described by the oxygen p-band center (ϵ_p), which is related to the hybridization of metal and oxygen orbitals and has been used as an effective descriptor for the activity of lattice oxygen^[41,42]. **Figure 3.2d** shows an upward-shift of ϵ_p after La-substitution, indicating stronger coupling between the electronic orbitals of oxygen and metal atoms^[43]. This leads to a higher activity of lattice oxygen in LCO. Hence, La-substitution in

ceria can be an effective approach to improve the oxide's redox performance through the lowering of the energy costs for both oxygen vacancy formation and migration.

3.3.3 Effect of Rh-promotion

Redox catalyst performance can be further enhanced by increasing the rate of surface oxygen removal, which can be facilitated by catalytically active sites for methane activation. Our previous studies indicate that the relative rates of lattice oxygen (O^{2-}) conduction to the surface and the surface oxygen removal by the gas–solid reactions determine the selectivity and activity of the redox catalysts for methane POx ^[44]. In the present study, Rh is selected as the active metal to enhance the catalytic activity for methane activation due to its high activity and resistance towards oxidation under the cyclic redox conditions. **Figure 3.3a** illustrates the X-ray Diffraction (XRD) patterns of the as-prepared samples (0.5 wt. % Rh promotion on both CeO_2 and LCO), confirming the fluorite structure of ceria being maintained after both the La-addition and Rh-promotion. Introduction of La in ceria leads to a shift in the position of the ceria peaks to smaller 2θ values. This is consistent with the anticipated lattice parameter increase, resulting from the increased number of oxygen vacancies and larger cation diameter of La^{3+} . The patterns also indicate that Rh is unlikely to be incorporated into the bulk structure (**Figure B13b**), based on absence of lattice parameter change between the reference and Rh-promoted ceria samples. This is consistent with the XPS results (**Table 3.1**), which indicate more than 5 fold increase in near-surface Rh-content, when compared to the average atomic composition of the bulk material. The significant surface enrichment of Rh is desirable for enhanced methane activation.

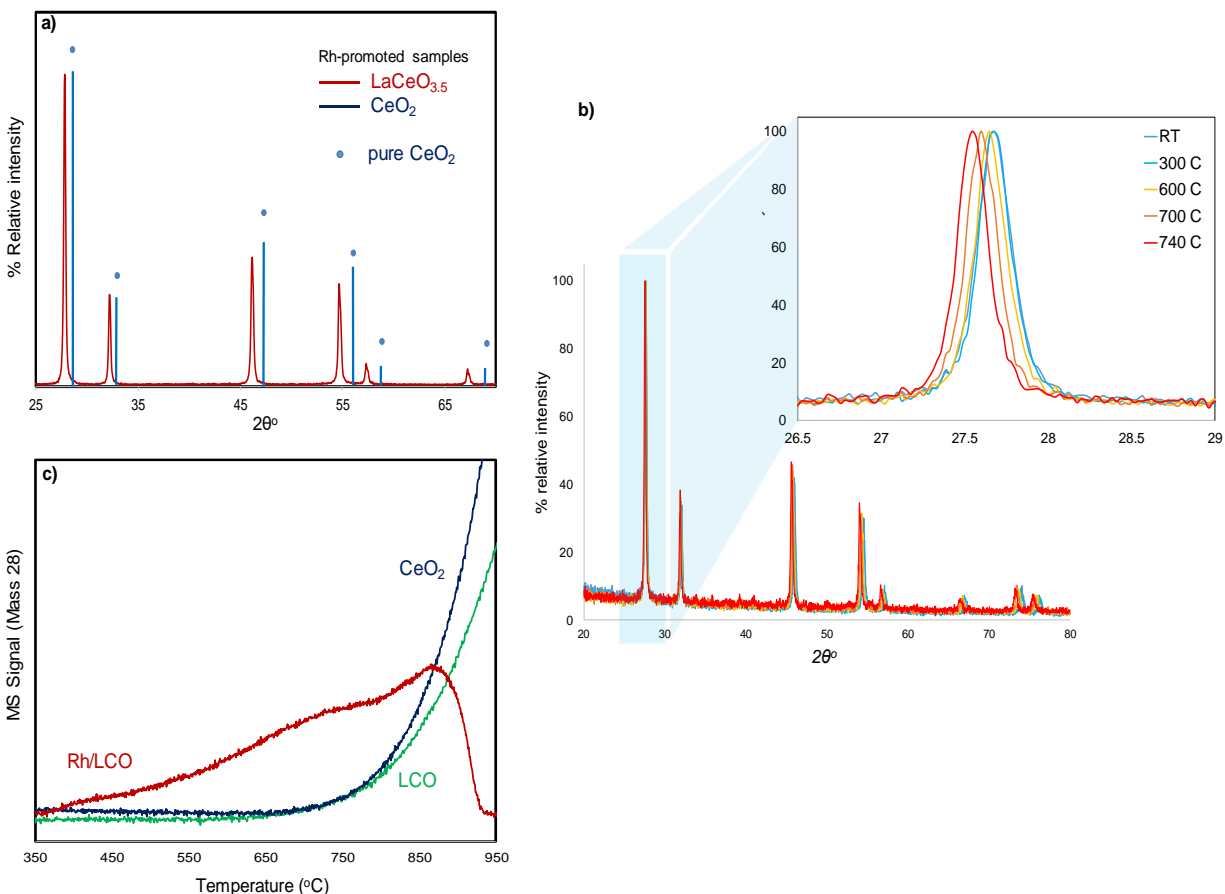


Figure 3.3: a) X-ray diffractogram for Rh-promoted ceria and LCO; b) CH₄ TPR + *in-situ* XRD on Rh/LCO; c) CH₄ TPR of Rh/LCO, LCO and ceria.

Methane temperature programmed reduction (TPR) experiments were conducted to determine the effect of promoting LCO with Rh. As shown in **Figure 3.3b**, Rh/LCO maintained the fluorite structure throughout the reduction reaction in the presence of methane. Lattice oxygen removal resulted in increased oxygen non-stoichiometry as opposed to the collapse of the fluorite structure, as indicated by the systematic shift in peak positions towards smaller angles. **Figure 3.3c** shows that Rh/LCO activates methane at temperatures considerably lower (300°C lower) than both unpromoted LCO and CeO₂. Compared to Rh/CeO₂, the onset temperature for methane activation on Rh/LCO was also approximately 100 °C lower (**Figure B14**). Although the cumulative oxygen

release from Rh/CeO₂ was higher than that for Rh/LCO at higher temperatures due to the higher Ce content in Rh/CeO₂, the superior activity at low temperatures for Rh/LCO represents a distinct advantage for HRP. The ability to maintain phase stability while accommodating significant oxygen vacancy formation under reducing conditions at relatively low temperatures (~ 350 °C onset temperature) makes Rh/LCO a promising material for HRP.

3.3.4 Redox Catalyst Performance in HRP

For HRP, the desired redox catalyst should be able to produce high yields of syngas and CO at low temperatures (<700°C). This would enable efficient waste heat integration. To that end, the activity and selectivity of the redox catalysts during both the reduction and oxidation steps were tested in a quartz U-tube reactor. **Figure 3.4a** compares the performance of Rh/LCO and Rh/CeO₂ at various temperatures. As can be seen, Rh/CeO₂ exhibited comparable methane conversions at 700 °C and above (up to 99% at 900 °C). In comparison, Rh/LCO is significantly more active at lower temperatures (500 and 600 °C). For instance, methane conversion on Rh/LCO more than tripled that on Rh/CeO₂ at 500 °C, highlighting the superior low-temperature performance of the La-substituted ceria sample. Based on the TPR results of Rh/LCO (**Figure 3.3b**) and the requirement of HRP, a standard operating temperature of 650°C was selected for redox performance evaluations. The reactor-feeds were switched between methane (reduction or PO_x step) and CO₂ (oxidation step), with an intermediate purge step. The calculated performance parameters include methane conversion (%), CO selectivity (%) and syngas yield (during reduction) (mmol/g redox catalyst) along with CO₂ conversion (%), during oxidation). **Figure 3.4b** is a representative product distribution during one redox cycle using Rh/LCO at 650°C, with **Figure 3.4c** compiling the results of the two half-cycles over 25 complete redox cycles. Rh/LCO shows a stable methane conversion of ~90% and a high CO selectivity of 90%. CO₂ conversion during the CO₂-splitting step was also

near complete. This stable performance is also observed in **Figure 3.4d**, with the phases being maintained intact after repeated cycles. At a low temperature of 650°C, a syngas yield of roughly 0.5 mmol/g material was observed for each of the redox cycles. **Figure 3.4d** also confirms the stability of the LCO phase, as indicated by the relatively small shifts in diffraction peaks for the reduced Rh/LCO compared to the oxidized sample.

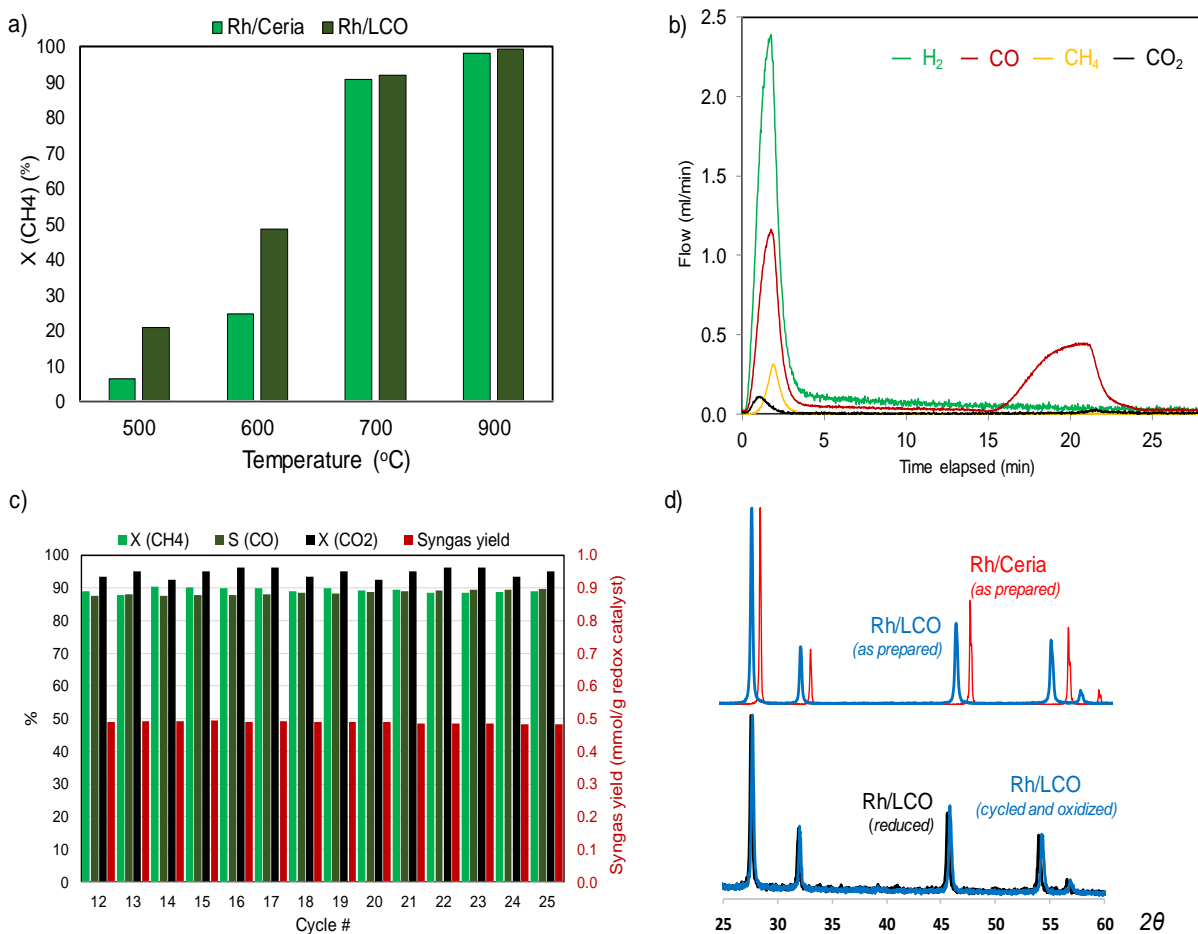


Figure 3.4: a) Performance comparison of Rh/LCO with Rh/Ceria for methane conversion; b) Representative product distribution for Rh/LCO under the HRP scheme at 650°C; c) Redox cycle results of Rh/LCO at 650°C: CH₄ and CO₂ conversion (X), CO selectivity (S) and Syngas yield; d) Phases of as-prepared and cycled Rh/LCO, showing stability over multiple redox cycles.

3.3.5 Process Analysis

As shown in **Figure 3.1a**, the overall HRP has three main sections: (i) upstream HRP section, where syngas and CO are produced; (ii) methanol synthesis section, that converts syngas into methanol; and (iii) acetic acid synthesis section in which methanol and CO are converted to acetic acid by the Cativa™ process. A variety of downstream chemicals can be manufactured with this scheme (**Figure 3.1b**). We first focus on acetic acid considering its growing market. Coal-based acetic acid synthesis, as an established commercial process, is an ideal reference process for comparison. Production of syngas and CO *via* coal gasification and chemical looping are broadly depicted in **Figure 3.5a**. We note that the downstream chemical production section of the two processes, i.e. coal gasification (CG) and HRP, are identical. The main difference of the two approaches resides in the upstream section, where syngas and CO are generated. In CG, water gas shift is necessary, followed by CO₂ removal to obtain methanol-ready syngas and pure CO. Energy required for the CO₂ separation is accounted for without further compression. Methane combustion is assumed to be the energy source for the CG route, with H₂ separation, CO₂-separation and Air Separation Unit (ASU) contributing to the overall process^[21]. Based on the material performance shown of **Figure 3.4c**, HRP provides a carbon efficiency of roughly 87% (**Figure 3.5b**) implying conversion of 87% of carbon in the feeds (CH₄ and CO₂) to acetic acid, which is 51% higher than that of the CG.

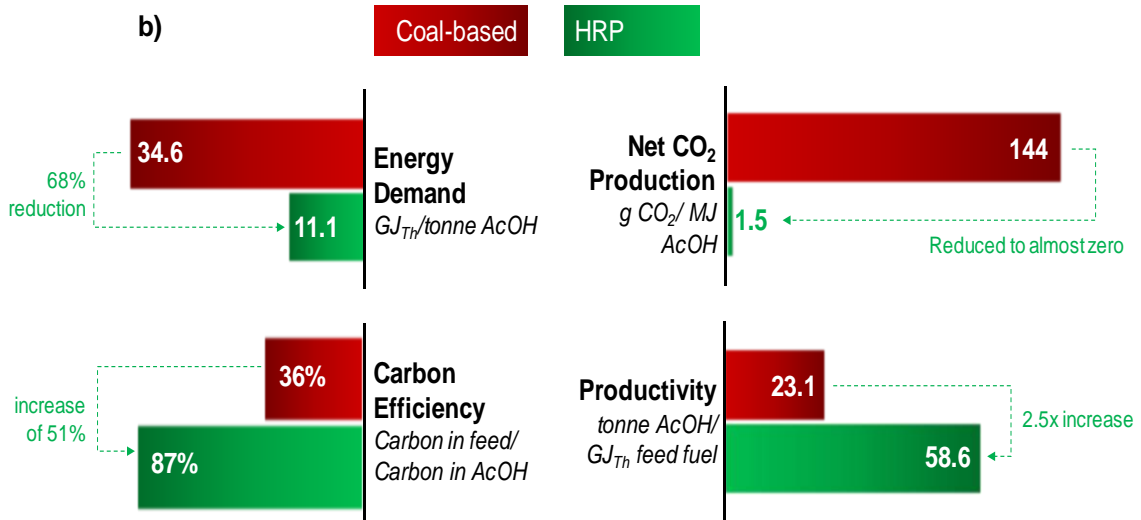
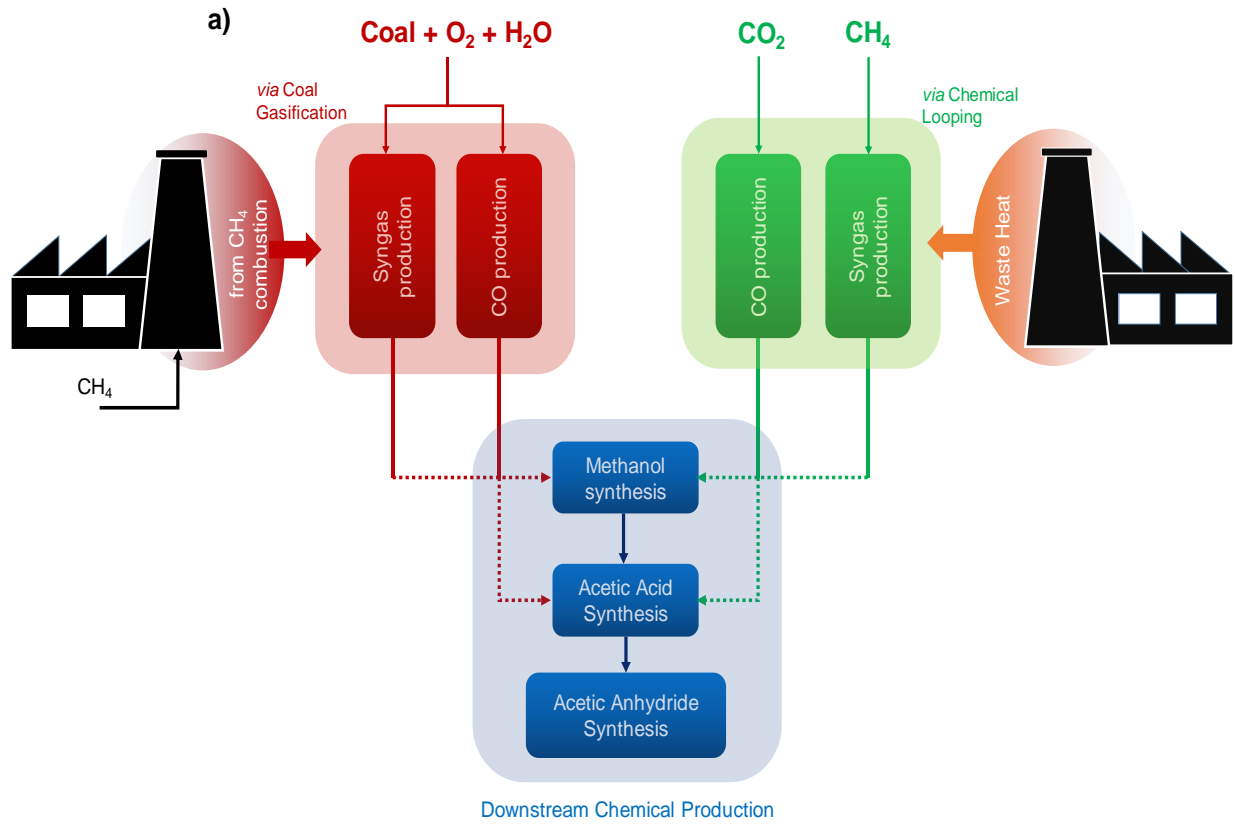


Figure 3.5: a) Schematic of HRP and CG (coal gasification), with similar downstream units [CG route requires H₂ and CO₂ removal to obtain syngas and pure CO]; b) Comparison of HRP with CG, using various parameters.

Using AspenPlus[®][30], the overall energy required for HRP and CG were calculated. After the integration of the industrial waste heat, HRP demands 11.1 GJ_{thermal} for every metric ton of acetic acid produced. This is 68% lower than the CG demand, which includes 8 GJ_{thermal} for CO₂ separation. The high carbon efficiency of HRP manifests in high productivity, where it produces 2.5 times as much acetic acid as CG, per GJ of feed fuel. After accounting for HRP carbon credit for CO₂ utilization, simulation results suggest that production of 1 metric ton of acetic acid results in a negligible net CO₂ production (0.022 metric tons) in the HRP case. In contrast, CG leads to 2.1 metric tons of CO₂ emission for each ton of acetic acid produced.

3.3.6 Potential Impacts

The U.S. industrial sector accounts for approximately one third of all energy used in the country; consuming approximately 32 quadrillion Btu of energy every year^[1,14]. Industrial waste heat refers to energy that is generated in industrial processes without being put to practical use. This accounts for roughly 40% of total annual industrial energy consumption^[14]. Capturing and reusing this waste heat is an effective approach to improve the overall energy efficiency and lowering CO₂ emissions, as it is an emission-free substitute for fossil fuels or electricity. The high temperature waste heat sources (1200-1700°C range)^[1,14], which are listed in **Table 3.2**, are exploitable considering their high quality from a thermodynamic second-law standpoint. These major industrial processes consume a combined total of 120 TBtu of energy every year, out of which approximately 30% ends up in waste heat. Assuming 50% of the sensible heat in the waste heat stream is utilized, there is an annual supply of 18.6 TBtu of energy, efficiently exploitable at an operating temperature of 650°C for HRP. The upstream reactor configuration of HRP demands 5.33 MBtu of energy for every metric ton of produced acetic acid, which can be sufficed by supplying the available waste heat. Considering the carbon efficiency of the process, 0.85 kg of CO₂ is utilized for the production

of 1 kg of acetic acid. This makes HRP capable of utilizing roughly 3 million metric tons of CO₂ to manufacture 3.5 million metric tons of acetic acid each year *via* waste heat integration. The combined usage of the abundant (i) high temperature industrial waste heat, (ii) methane and (iii) CO₂ offers an excellent opportunity for a sustainable process. The superior low temperature redox performance of Rh/LCO enables efficient waste heat integration, making HRP an attractive route for sustainable CO₂-utilization and chemical production.

Table 3.2: Exploitable High Temperature Waste Heat sources^[14] and CO₂-utilization capacity.

Industry	Furnace	Temperature (°C)	Waste Heat ^a (TBtu/year)	CO ₂ utilizable (tonne/year)
Steel	Basic Oxygen Furnace (BOF)	1700	13.6	2,162,207
Glass	Oxy-fuel	1427	2.1	335,102
Steel	Electric Arc Furnace (EAF)	1200	2.9	462,760

^autilizable for an operation at 650°C

3.4 Conclusion

We report a hybrid redox process (HRP) that performs CO₂-splitting and methane partial oxidation (POx) in a synergistic two-step, thermochemical redox scheme. Ceria, being a promising material for such a redox cycle, is modified by La-substitution and Rh-promotion. DFT calculations indicate that La substitution can decrease the oxygen vacancy formation energy and migration barriers in both the bulk and surface of the fluorite structured oxide. The reduced Rh/LaCeO_{3.5-x} is capable of converting almost 100% of the CO₂ to CO at temperatures below 700°C. In the subsequent step, it converts 90% of methane selectively to syngas with a 2:1 H₂: CO ratio that is ideal for methanol synthesis, thus demonstrating superior methane partial oxidation at low

temperatures. The ability to operate redox cycles at low temperatures allows for efficient integration of the industrial waste heat, which is an excellent emission-free energy source. Syngas and CO are crucial feedstocks, for the production of methanol followed by a variety of carbonyl-containing products like mono-ethylene glycol, acetic anhydride or acetic acid. When compared with the conventional coal-based route, HRP offers a 68% reduction in the overall energy demand and 99% reduction in net CO₂ emission for acetic acid production. Moreover, HRP has the potential to produce a variety of high-value chemicals *via* carbonlyation. The ability to produce chemicals with high market volume and important industrial applications makes HRP a promising avenue for efficient and economical CO₂ utilization. At the same time, conversion of low-cost natural gas, along with integration of the waste heat, can reduce the cost of producing acetic acid and the associated CO₂ production. HRP has the potential to utilize roughly 3 million metric tons of CO₂ every year from the three major industrial waste heat sources, making it a potentially suitable choice for sustainable CO₂ fixation.

3.5 Experimental Procedures

3.5.1 Material synthesis

Two redox catalysts are synthesized for this study: CeO₂ and LaCeO_{4-x}. Samples are prepared using a modified Pechini method. Stoichiometric amounts of nitrate salts of lanthanum [La(NO₃)₃, 6H₂O] and cerium [Ce(NO₃)₃, 6H₂O] are dissolved in deionized water and stirred for 30 minutes at room temperature to form a homogeneous solution. Citric acid, with 2.5 times the total moles of cations, is added and the solution is kept under stirring for another half an hour at 40°C. Ethylene glycol with a molar ratio of 1.5: 1 with respect to citric acid is then added to the solution, and the temperature of the solution is increased to 80°C under stirring, until a homogeneous gel is formed.

The gel is then dried overnight at 100°C and annealed at 1000°C for 8 hours. The surface of the synthesized redox catalysts is also promoted with rhodium using a wetness impregnation method (0.5 wt. % Rh). Rhodium nitrate salt is dissolved in deionized water and appropriate stoichiometric amounts of the solution are added to the samples in multiple steps. The impregnated samples are then dried at 100°C for 4 hours and sintered at 1000°C for 6 hours. The prepared redox material is crushed and sieved in the particle range of 90-225µm.

3.5.2 Material characterization

Powder X-ray diffraction (XRD) experiments are done to confirm the formation of the desired crystal phases. XRD patterns are obtained using a Rigaku SmartLab X-ray diffractometer with Cu-K α ($\lambda=0.1542$) radiation operating at 40 kV and 44 mA. A stepwise approach with a step size of 0.1° and residence time of 2.5 seconds at each step in 20-80 angle range (2θ) is used to generate the XRD patterns. The phase identification is done using the HighScorePlus software from PANalytical. Fresh (as-prepared) and spent (cycled) samples are analyzed.

To examine phase properties, *in-situ* XRD is conducted during methane temperature programmed reduction (TPR) using an Empyrean PANalytical XRD using a similar Cu-K α radiation operating at 45 kV and 40 mA. A 2θ range of 20–80° is used at a ramp rate of 0.1° holding each step for 0.1 s. A TPR experiment is conducted in the *in-situ* XRD by heating the oxidized sample at 5 °C/min in 5% CH₄ (balance N₂). XRD scans are conducted the entire length of the ramp from room temperature to 750°C.

X-ray photoelectron spectroscopy (XPS, Thermo Fisher Scientific Inc.) with an Al-K α X-ray source at an operating voltage of 20 kV and a current of 10 mA is used to analyze near surface

elemental compositions. Survey spectra and the single element spectra were collected with 20 eV and 100 eV pass energy.

3.5.3 Redox experiments

Redox experiments are performed in a fixed-bed configuration using a quartz U-tube reactor (1/8" ID) with 500 mg sample loading. Total flow rate is 25 ml min⁻¹ with 10 vol% CH₄ (reduction for 2 min), 2% CO₂ (oxidation) and balance Ar. For the material comparison (**Figure 3.4a**), total flow is 50 ml min⁻¹. The reactor is purged with Ar after each half cycle to prevent mixing of the reactive gases. The samples are held in place using quartz wool to prevent fluidization of the particles. The reactor effluent is analyzed using a quadrupole mass spectrometer (Cirrus 2, MKS). To ensure the accuracy of the qualitative analysis, a single point calibration is performed using a standard calibration gas (1% H₂, 1% CH₄, 1% CO, and 1% CO₂, balance Ar) before each experiment.

The reducibility of the samples in methane is characterized and tested through TPR experiments. The experiments are performed in a quartz U-tube reactor in 10 vol% methane (balance Ar). The temperature is increased from 350°C to 950°C with a 10°C min⁻¹ ramping rate and kept isothermal at 950°C for 15 minutes. The samples are oxidized at 950°C in 20% oxygen (ultra-dry, balance Ar) prior to reduction to keep them completely oxidized.

3.5.4 DFT Computation Methods

All Density Functional Theory (DFT) calculations were implemented by the Vienna ab initio Simulation package (VASP)^[45] with the frozen-core all-electron projector augmented wave (PAW) model^[46] and Perdew-Burke-Ernzerhof (PBE) functions^[47]. A kinetic-energy cutoff for the plane-wave expansion of the electronic wave function is set to be 450 eV. The force and energy convergence criterion are set to be 0.01 eV/Å and 10⁻⁵ eV respectively. A Gaussian smearing of 0.1 eV is applied for optimization. A k-point grid with 7 × 7 × 7 Gamma-centered mesh is chosen

for the CeO₂ and LaCeO_{3.5} bulk unit cell. For all the supercells, a corresponding number of k-points is used to keep the k-mesh spacing constant across different structures. The effect of Ce (4f) electron correlation is corrected by considering on-site Coulomb (U) and exchange (J) interactions following the GGA + U approach^[48] with U_{eff} = 5 eV^[49]. Charge distribution analysis is examined with the DDEC06 method, which is a refinement of the Density Derived Electrostatic and Chemical (DDEC) approach^[50]. The climbing image nudged elastic band (CI-NEB) method is applied to search the transition state structures^[51]. To avoid artificial interactions between adjacent slabs for the surface models, a vacuum spacing of ~15Å is used.

Atomic model of pristine CeO₂ unit cell (**Figure B1a and b**) is built with the optimized lattice constant of 5.418 Å, which is very close to the experimental reports (5.411 Å)^[52]. LaCeO_{3.5} unit cell is built by replacing two Ce atoms by La atoms, and then removing one O atom to form an oxygen vacancy (V_O). Due to symmetry, the selection of the La doping and V_O sites in the CeO₂ unit cell is unique. Subsequently, a 2 × 2 × 2 supercell of LaCeO_{3.5} bulk structure is built to avoid artificial interactions induced by the periodic boundary condition. To calculate ΔE_v, all 7 non-equivalent sites depicted in **Figure B2** are considered and the most stable one (O1 site) is chosen for subsequent calculations. Upon the formation of the vacancy, all adjacent 6 O atoms are allowed to migrate to the vacancy site, and the corresponding reaction energies are calculated (**Table B2**). Among these possible oxygen mobility pathways, the migration of O4 and O6 are no longer considered due to their very large reaction energies, which indicate even larger barriers. Transition state calculations of the migration of the rest oxygen atoms (O2, O3, O4 and O6) are performed (**Figure B3**). For the surfaces, to closely reproduce the experimental La:Ce ratio (64.1:35.9 ≈ 1.79) obtained through XPS, one of the outermost Ce atoms is modified to La artificially, making the La:Ce ratio of the first 6 layers to be 5:3 ≈ 1.67. Then a 2 × 1 × 1 supercell surface model is built,

which shows only two non-equivalent surface oxygen atom sites (A and B, **Figure B4**). For the migration of adjacent sub-surface oxygen to the two vacancy sites (**Figure B5**), the corresponding reaction energies of all possible O migration pathways are calculated (**Table B3**), in which the migrations of O2 or O4 to B site are no longer considered due to the very large reaction energies. The transition state calculations of the rest oxygen migration pathways are calculated as shown in **Figure B6**.

3.5.5 Process simulations

Overall, the process is split into three sections: syngas generation, methanol (MeOH) synthesis, and acetic acid (AcOH) reactor. For the overall process, methane and CO₂ are the feed and the product is AcOH.

Methanol is synthesized with syngas (with CO₂) using a commercial Cu/Zn/Al₂O₃ catalyst. A packed tubular reactor approximated using an RStoic model in AspenPlus[®], is used. The MeOH reactor operates at 265°C and 105 bar, with a 64% yield of CO → MeOH and 17% yield of CO₂ → MeOH. The synthesis of AcOH using MeOH and CO is done using the Cativa[™] process. This commercial process produces AcOH by the carbonylation of MeOH, *via* an iridium-containing complex and hydrogen iodide (HI). A two reactor scheme has been used for modeling the process. The reactors are set at 190°C and 22 barg and modeled as RStoic reactors. The first reactor involves reactions of MeOH with HI to give AcOH *via* AcI (methyl iodide). HI is replenished and is not consumed in the process. The second reactor assumes the formation of byproducts like propionic acid and CO₂ *via* WGS reaction, from the remaining MeOH.

HRP is compared with the traditional coal-slurry gasifier (CG) process to obtain syngas, followed by MeOH synthesis with subsequent AcOH synthesis. Coal is assumed to be composed of pure

carbon (C) with feed-water to be 40% more than the feed coal (by moles). An efficiency of 96% is assumed for the air separation unit (ASU), with the final O₂: C = 0.5. An adiabatic RGibbs reactor model is used for the entrained bed gasifier, operating at 30 bar. All the following units are similar to the HRP process. The end-product is AcOH. H₂ and CO₂ removal are required to produce syngas and CO streams. CO₂ removal demands additional energy, which is accounted for. The separated H₂ is used as a fuel for the process energy requirements. Key assumptions for these AspenPlus[®] models are based on a previous work and are presented in the *supplementary information*^[30]. Net CO₂ production considers the contributions from natural gas/coal upstream and energy conversion facility. The estimated upstream natural gas emission based on a US-DOE report is 9.1 g CO₂/MJ for CH₄ and 10 g CO₂/MJ for coal. The emission analysis from the two processes is based on AspenPlus[®] model results. For both the processes, it is assumed that the thermal energy requirements are met by burning the necessary amount of methane. While CO₂ separated from coal gasification syngas could be further purified and compressed for sequestration, this would incur significant additional cost and energy consumptions. In the present study, we did not include these additional steps and incorporated the CO₂ in syngas into the net CO₂ production calculations. For HRP, CO₂ usage as a feed leads to a CO₂ credit.

3.6 Acknowledgements

This work was supported by the U.S. Department of Energy (Awards DE-FE0031703), National Science Foundation (NSF CBET-1510900), and the North Carolina State University Kenan Institute for Engineering, Technology and Science. The authors acknowledge the use of the Analytical Instrumentation Facility (AIF) at North Carolina State University, which is supported by State of North Carolina and the National Science Foundation (Award ECCS-1542015).

3.7 References

- [1] Committee on Developing a Research Agenda for Utilization of Gaseous Carbon Waste Streams, Board on Chemical Sciences and Technology, Division on Earth and Life Studies, National Academies of Sciences, Engineering, and Medicine, *Gaseous Carbon Waste Streams Utilization: Status and Research Needs*, National Academies Press, Washington, D.C., **2019**.
- [2] A. W. Zimmermann, R. Schomäcker, *Energy Technology* **2017**, 5, 850.
- [3] A. Zimmermann, M. Kant, CO₂ Utilization Today: Report 2017
- [4] B. Smit, A.-H. A. Park, G. Gadikota, *Frontiers in Energy Research* **2014**, 2, DOI 10.3389/fenrg.2014.00055.
- [5] E. E. Stangland, *Annual Review of Chemical and Biomolecular Engineering* **2018**, 9, 341.
- [6] C. Mesters, *Annual Review of Chemical and Biomolecular Engineering* **2016**, 7, 223.
- [7] E. Alper, O. Yuksel Orhan, *Petroleum* **2017**, 3, 109.
- [8] Z. Sun, T. Ma, H. Tao, Q. Fan, B. Han, *Chem* **2017**, 3, 560.
- [9] O. K. Varghese, M. Paulose, T. J. LaTempa, C. A. Grimes, *Nano Letters* **2009**, 9, 731.
- [10] W. C. Chueh, C. Falter, M. Abbott, D. Scipio, P. Furler, S. M. Haile, A. Steinfeld, *Science* **2010**, 330, 1797.
- [11] D. Arifin, V. J. Aston, X. Liang, A. H. McDaniel, A. W. Weimer, *Energy & Environmental Science* **2012**, 5, 9438.
- [12] A. H. Bork, E. Povoden-Karadeniz, J. L. M. Rupp, *Advanced Energy Materials* **2017**, 7, 1601086.
- [13] C. Muhich, A. Steinfeld, *J. Mater. Chem. A* **2017**, 5, 15578.
- [14] I. Johnson, W. T. Choate, A. Davidson, *Waste Heat Recovery. Technology and Opportunities in U.S. Industry*, BCS, Inc., Laurel, MD (United States), **2008**.
- [15] S. U. Nimbalkar, A. Thekdi, B. M. Rogers, O. L. Kafka, T. J. Wenning, *Technologies and Materials for Recovering Waste Heat in Harsh Environments*, **2014**.
- [16] J.-B. Peng, H.-Q. Geng, X.-F. Wu, *Chem* **2018**, 0, DOI 10.1016/j.chempr.2018.11.006.

- [17] R. A. Kerr, *Science* **2010**, 328, 1624.
- [18] J. A. Moulijn, A. van Diepen, M. Makkee, *Chemical Process Technology*, John Wiley & Sons Inc., Chichester, West Sussex, United Kingdom, **2013**.
- [19] K. C. Waugh, *Catalysis Letters* **2012**, 142, 1153.
- [20] J. H. Jones, *Platinum Metals Review* 2000, 44, 94
- [21] L.-S. Fan, *Chemical Looping Systems for Fossil Energy Conversions*, Wiley-AIChE, Hoboken, NJ, **2010**.
- [22] M. Tang, L. Xu, M. Fan, *Applied Energy* **2015**, 151, 143.
- [23] M. Rydén, A. Lyngfelt, T. Mattisson, *Fuel* **2006**, 85, 1631.
- [24] J. Adánez, A. Abad, T. Mendiara, P. Gayán, L. F. de Diego, F. García-Labiano, *Progress in Energy and Combustion Science* **2018**, 65, 6.
- [25] P. Furler, J. Scheffe, M. Gorbar, L. Moes, U. Vogt, A. Steinfeld, *Energy & Fuels* **2012**, 26, 7051.
- [26] P. T. Krenzke, J. R. Fosheim, J. H. Davidson, *Solar Energy* **2017**, 156, 48.
- [27] P. G. Loutzenhiser, A. Meier, A. Steinfeld, *Materials; Basel* **2010**, 3, 4922.
- [28] S. Bhavsar, M. Najera, G. Veser, *Chemical Engineering & Technology* **2012**, 35, 1281.
- [29] M. Najera, R. Solunke, T. Gardner, G. Veser, *Chemical Engineering Research and Design* **2011**, 89, 1533.
- [30] J. Zhang, V. Haribal, F. Li, *Science Advances* **2017**, 3, e1701184.
- [31] K. Otsuka, T. Ushiyama, I. Yamanaka, *Chem. Lett.* **1993**, 22, 1517.
- [32] K. Otsuka, Y. Wang, E. Sunada, I. Yamanaka, *Journal of Catalysis* **1998**, 175, 152.
- [33] V. Bellière, G. Joorst, O. Stephan, **n.d.**, 7.
- [34] “Global Acetic Acid Market 2018-2022| Increasing Demand for Methanol to Drive Growth| Technavio,” can be found under <https://www.businesswire.com/news/home/20181003005834/en/Global-Acetic-Acid-Market-2018-2022-Increasing-Demand>, **2018**.

- [35] L. Zhang, J. Meng, F. Yao, W. Zhang, X. Liu, J. Meng, H. Zhang, *Inorganic Chemistry* **2018**, *57*, 12690.
- [36] X. Zhu, K. Li, Y. Wei, H. Wang, L. Sun, *Energy Fuels* **2014**, *28*, 754.
- [37] X. Zhu, H. Wang, Y. Wei, K. Li, X. Cheng, *Mendeleev Communications* **2011**, *21*, 221.
- [38] R. T. Dirstine, *Journal of The Electrochemical Society* **1979**, *126*, 264.
- [39] Z. Yang, G. Luo, Z. Lu, K. Hermansson, *J. Chem. Phys.* **2007**, *127*, 074704.
- [40] H.-Y. Li, H.-F. Wang, Y.-L. Guo, G.-Z. Lu, P. Hu, *Chemical Communications* **2011**, *47*, 6105.
- [41] Y.-L. Lee, J. Kleis, J. Rossmeisl, Y. Shao-Horn, D. Morgan, *Energy Environ. Sci.* **2011**, *4*, 3966.
- [42] W. T. Hong, M. Risch, K. A. Stoerzinger, A. Grimaud, J. Suntivich, Y. Shao-Horn, *Energy Environ. Sci.* **2015**, *8*, 1404.
- [43] Z. Liu, Y. Sun, X. Wu, C. Hou, Z. Geng, J. Wu, K. Huang, L. Gao, S. Feng, *CrystEngComm* **2019**, *21*, 1534.
- [44] A. Shafieifarhood, J. Zhang, L. M. Neal, F. Li, *Journal of Materials Chemistry A* **2017**, *5*, 11930.
- [45] G. Kresse, J. Furthmüller, *Phys. Rev. B* **1996**, *54*, 11169.
- [46] P. E. Blöchl, *Phys. Rev. B* **1994**, *50*, 17953.
- [47] J. P. Perdew, K. Burke, M. Ernzerhof, *Phys. Rev. Lett.* **1996**, *77*, 3865.
- [48] S. L. Dudarev, G. A. Botton, S. Y. Savrasov, C. J. Humphreys, A. P. Sutton, *Phys. Rev. B* **1998**, *57*, 1505.
- [49] C. W. M. Castleton, J. Kullgren, K. Hermansson, *The Journal of Chemical Physics* **2007**, *127*, 244704.
- [50] T. A. Manz, N. G. Limas, *RSC Adv.* **2016**, *6*, 47771.
- [51] G. Henkelman, B. P. Uberuaga, H. Jónsson, *The Journal of Chemical Physics* **2000**, *113*, 9901.
- [52] L. Gerward, J. Staun Olsen, L. Petit, G. Vaitheeswaran, V. Kanchana, A. Svane, *Journal of Alloys and Compounds* **2005**, *400*, 56.

**CHAPTER 4: OXIDATIVE DEHYDROGENATION OF ETHANE UNDER A CYCLIC
REDOX SCHEME – PROCESS SIMULATIONS AND ANALYSIS**

is based on manuscripts published in *Energy* 119 (2017), 1024e1035 and *iScience* 19 (2019),

894–904

The supplementary information is in Appendix C.

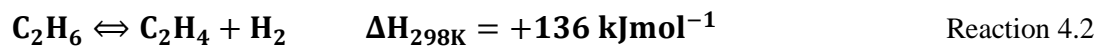
4.1 Abstract

Steam cracking of ethane is an energy intensive process (15-25 GJ_{th}/tonne ethylene) involving significant coke formation and CO₂/NO_x emissions. Decades of optimization has led to a thermally efficient, near “perfect” process with ~95% first law-energy efficiency, indicating little room for further reduction in energy consumption and CO₂ emissions. We propose an alternative two-step redox (or chemical looping) oxidative dehydrogenation (CL-ODH) scheme where hydrogen, produced from ethane cracking, is selectively oxidized by lattice oxygen from a redox catalyst, in the first step. Regeneration of the lattice oxygen in a subsequent step heats the redox catalyst, with the sensible heat providing the thermal energy needed for the cracking reaction. The overall process provides minimal parasitic energy loss and significantly reduced CO₂/NO_x formation, while favoring ethylene formation through the removal of hydrogen. In the current study, the CL-ODH process is simulated with ASPEN Plus® using experimental data on a Mn-based redox catalyst. The CL-ODH is compared with steam cracking for an ethylene production capacity of 1 million tonne/year. Results indicate that the CL-ODH process, with 85% single-pass ethane conversion, provides 82% reduction in overall energy demand and 82% reduction in CO₂ emissions. The overall downstream section consumes approximately 23.5% less energy, with 32.1% less compression work. Increase in the ethane conversion further reduces the energy demand downstream. For every tonne of ethylene, the process has 7.35 GJ_{th} excess fuel energy whereas cracking requires an external fuel input of 1.42 GJ_{th}. Through detailed exergy analyses, we show CL-ODH leads to exergy savings of up to 58% in the upstream reactors and 26% in downstream separations.

4.2 Introduction

Ethylene is an important building block for the petrochemical industry and has the largest production volume among important base petrochemicals ^[1,2]. At present, ethylene is mainly used to manufacture polyethylene (>50%), followed by vinyl chloride, ethylene oxide and ethyl benzene ^[3]. The global ethylene production capacity was at 143 million tonnes per annum (MTA) in 2013, a 27% increase compared to the 2005 production capacity. A compound annual growth rate of 6% is further anticipated till 2020 and beyond ^[4-7].

A significant fraction of ethylene is commercially produced via high-temperature pyrolysis of hydrocarbon feedstocks in the presence of diluting steam, also known as steam cracking ^[3,8]. Typical feedstocks for steam cracking include those derived from crude oil, such as naphtha, gas oil, etc. and those derived from natural gas, such as ethane and propane. ^[6,8] While naphtha accounts for 55% of global ethylene production capacity, ethane is the primary feedstock in regions such as the United States and Middle East. The increasing availability of shale gas in the U.S. is also making ethane cracking more favorable from a process-economic standpoint ^[3,8,9]. When ethane is used as the feedstock, the desired (overall) reaction (Reaction 4.1) involves decomposing ethane into ethylene and hydrogen, which is achieved via a complex network of gas phase radical reactions.



In such a process, a mixed stream of ethane feed and steam is preheated to the initial cracking temperature (500°-680°C) and is fed into a high-temperature reactor (750°-875°C) to complete the cracking reaction, with residence times of 0.1-0.5 s. Key operating parameters that affect the performance of the process and the product distributions include the gas residence time, the partial pressures of the feedstock and steam, and the temperature profile in the reactor, ^[3,9].

Despite being practiced and optimized for more than 50 years, steam cracking has a number of limitations from chemical equilibrium, energy utilization, and environmental viewpoints. Firstly, ethane cracking is limited to a practical single-pass ethane-conversion of 67-70% and an ethylene yield of around 55% ^[6] due to equilibrium limitation and coke formation. Although steam dilution reduces the rate of coke formation, steam cracking furnaces nevertheless need to be periodically shut down and regenerated with air to avoid coke build-up. The use of diluting steam increases the parasitic energy consumption whereas the need for periodic regeneration leads to an increase in the capital investment (for parallel units) and operating costs ^[7,9,10]. The total energy demand of ethane cracking ranges between 15 and 25 GJ/tonne ethylene ^[8,9] which is satisfied by combustion of carbonaceous fuels such as methane. This leads to the production of 1-1.2 ton CO₂/tonne ethylene and considerable amount of NO_x ^[8]. Therefore, new technologies that overcome these limitations are highly desirable.

The oxidative dehydrogenation (ODH) of ethane, in the presence of a heterogeneous catalyst, is an attractive alternative to steam cracking. ODH has the potential to provide higher olefin yields since the formation of water as opposed to hydrogen (Reaction 4.2) effectively removes the equilibrium constraints on ethane conversion. Moreover, the required energy is supplied by hydrogen oxidation ^[11,12].



Despite these advantages, oxygen co-feed ODH has significant limitations. The requirement of pure oxygen or oxygen-enriched air requires an air separation unit (ASU), which adds to the capital and operating costs. The high reactivity of the olefins poses another challenge in developing a suitably selective catalyst. Moreover, the oxygenate byproducts are difficult to separate ^[9]. The

flammability of the gas mixture containing oxygen and fuels in the single step ODH imposes additional safety concerns. Over-oxidation of the alkanes and olefins to CO and CO₂ can cause hot spots in the reactor and reduce product selectivity.^[8,13,14] The current study investigates a two-step, redox based process for ethane chemical looping-oxidative dehydrogenation (CL-ODH) in an O₂-free environment. The first step involves selective oxidation of the hydrogen produced from ethane cracking using the lattice oxygen from a redox catalyst at a high temperature. The sensible heat of such catalyst provides the thermal energy needed for the cracking reaction. This is accompanied by simultaneous reduction of the catalyst. The reduced catalyst is subsequently regenerated (and reheated) in air to complete the redox loop. In such a CL-ODH process, the absence of gas phase oxygen a) inhibits the non-selective reaction pathways, b) reduces the explosion hazard^[14–16], and c) decreases parasitic energy losses by eliminating ASU and providing tighter temperature control^[17]. The overall process also provides significant reduction in NO_x and CO₂ emissions. However, despite of the advantages of CL-ODH over both steam cracking and oxygen co-feed experiments, this novel process, has not been analyzed to date.

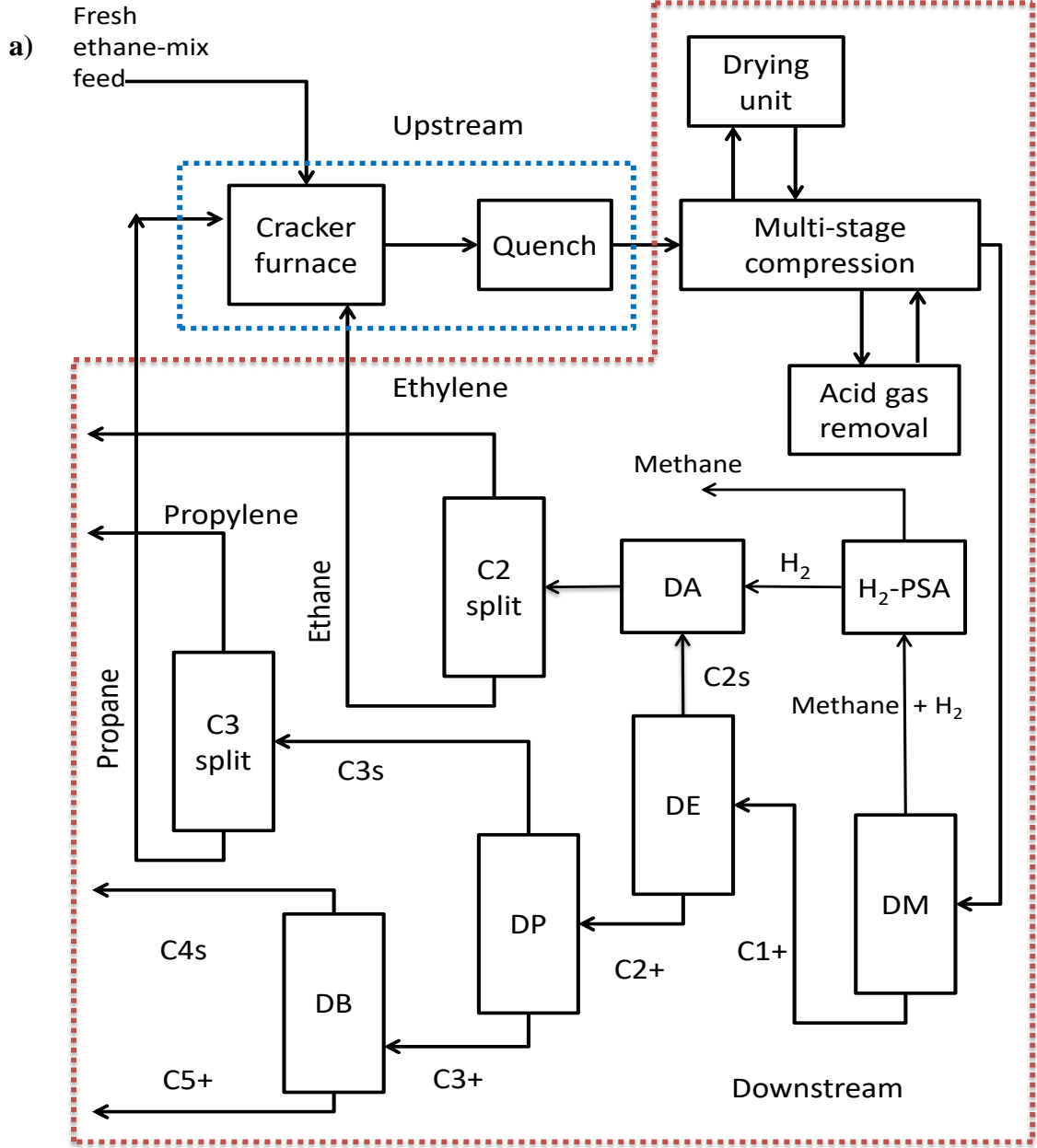
In a previous work, we have reported a highly effective, alkali doped MnO_x-MgO redox catalyst for the abovementioned CL-ODH scheme^[17,18]. High ethane conversion and ethylene selectivity as well as satisfactory redox stability and oxygen carrying capacity are achieved using such a redox catalyst. The current study investigates the performance of the CL-ODH process by conducting comprehensive process simulation and analyses based upon preliminary experimental yield data from an alkali doped MnO_x-MgO. Single-pass ethane conversions of 66%, 85% and 90% are analyzed and the results are compared with a state-of-the-art ethane steam cracking process. Sensitivity analyses are performed on key process parameters such as ethane conversion, product distribution, unit-wise and total energy requirement of the process. Using ASPEN Plus[®], the

reactor and process conditions are optimized and the potential advantages of the redox-based ODH process are also validated based on comprehensive process analyses. For a single-pass ethane conversion of 85%, as compared to the steam cracking process, the overall downstream section energy demands of the ODH case are shown to drop by 23.5% with 32.1% less compression work. This leads to 82% drop in the overall energy demand and 82% reduction in CO₂ emissions. The energy demand for ODH decreases with increasing single-pass ethane conversion.

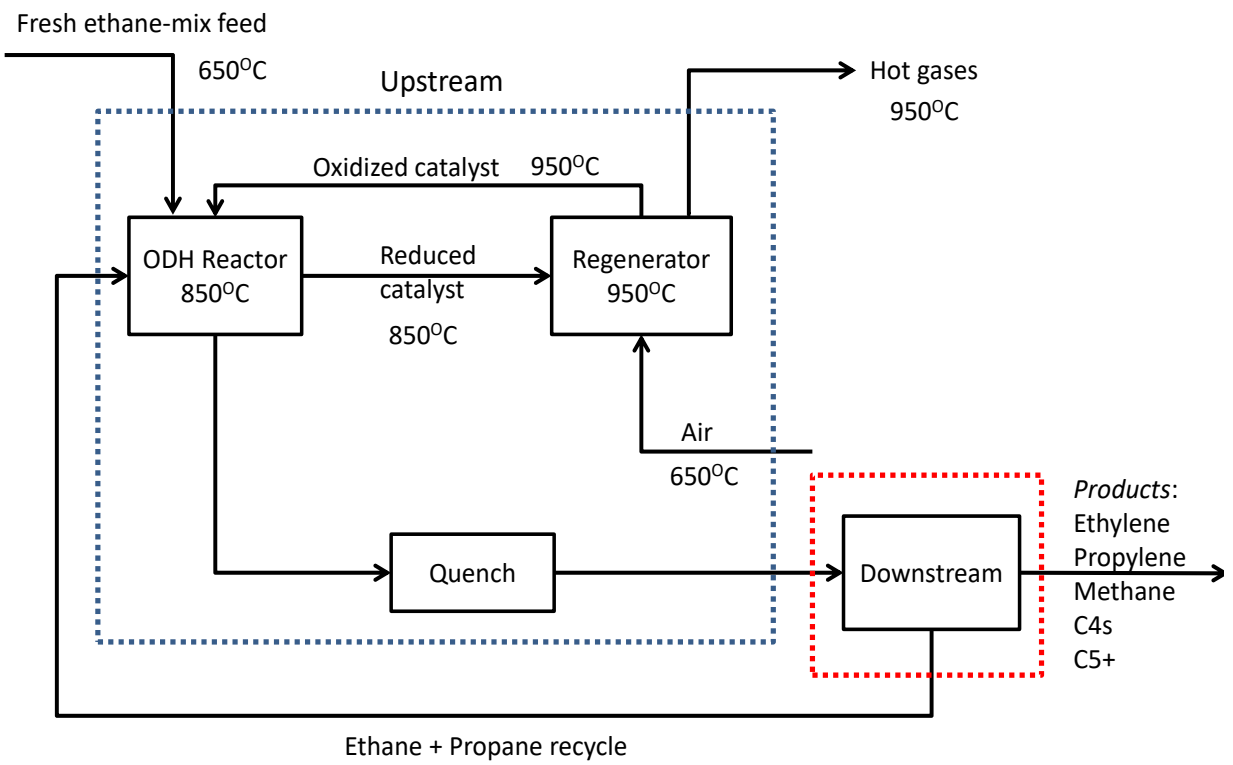
4.3 Process descriptions

Figure 4.1a is a simplified process flow diagram of a state-of-the-art ethane steam cracking process. Pre-heated ethane is thermally cracked in the presence of steam, which functions as a diluent for higher conversions and as a coke-retardant. The feed mixture is passed through the tubes of up to twelve cracker furnaces, which are heated by combustion of fuels to provide considerable heat input at high temperatures (~1,000°C). The hot product stream from the furnace, at approximately 850°C, is first rapidly cooled to 300°-400°C using transfer line heat exchangers to avoid further cracking and preserve the composition. It is further quenched to near ambient temperature using water or oil ^[3,6]. The stream is then compressed to a pressure of around 40 bar with a multi-stage compressor. Drying and acid gas removal units are located at the intermediate compressor stages. The drying unit consists of an adsorption column of molecular sieves and precedes the acid gas removal units to avoid formation of hydrates ^[6]. The stream is then caustic washed to remove the acid gases such as CO₂.

Figure 4.1: a) Simplified process flow diagram of ethane cracking process [DM: Demethanizer, DA: Deacetylenizer, DE: Deethanizer, DP: Depropanizer, DB: Debutanizer, C2 split: C2-splitter, C3 split: C3-splitter, PSA: Pressure Swing Adsorption] b) Simplified schematic of the cyclic redox ODH (CL-ODH) process (temperatures for key units and streams are listed for the reference case).



b)

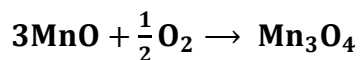


The compression stages are followed by a train of distillation columns which sequentially separate the light components from the heavy fraction, yielding high purity ethylene. The sequence begins with the removal of methane and lighter components, primarily hydrogen, from higher molecular mass components, using a demethanizer. The bottom product is routed to a deethanizer column where acetylene, ethane, and ethylene are separated and C3+ components exit as the bottom-product. The overhead mixture is subsequently treated with hydrogen to remove acetylene and then fractionated in the C2-splitter to give ethylene product and ethane-recycle. The bottom product from the deethanizer is depropanized to separate C4+ components. Depropanizer bottoms are sent to a debutanizer for separation of the C4 materials, raw pyrolysis gasoline, C5 materials and aromatics ^[6]. In the C3-splitter, propylene is recovered as a valuable product and propane is recycled. Traditionally, the front-end demethanizer process sequence was used in cracking process. In alternative configurations, a front-end deethanizer or depropanizer can be used. While the front-end deethanizer option can be advantageous in certain cases ^[6], it is not investigated in the current study for the purpose of direct comparison with the ODH process.

The ethane ODH process is depicted in **Figure 4.1b**. The major difference from steam cracking is the absence of the energy-intensive furnaces, which are replaced by a reactor-regenerator configuration. The hydrocarbon and CO_x yields used in the current work are based upon experimental results of an alkali doped Mn-Mg oxide similar to that reported in previous work ^[17,18]. As this system involves mixed oxides ^[18] that are not available in the ASPEN Plus[®] database, the system is simplified to a MgO-supported MnO_x. Mn₃O₄ (Mn at 8/3+ average valence state) is used as the simulated oxygen-carrier phase, which donates its lattice oxygen during the ODH reaction. Meanwhile, the Mn cation is reduced to a 2+ average valence state (MnO), as shown in Reaction 4.3. The reaction involves the combustion of hydrogen to water. The reduced redox

catalyst, (also known as an oxygen carrier), is subsequently regenerated using air in the regenerator, following a highly exothermic Reaction 4.4. While slow reduction kinetics ^[19] and propensity for deep oxidation ^[20,21] would make undoped Mn₃O₄ unsuitable as a practical oxygen carrier, the thermodynamics of MnO_x/MgO give satisfactory simulation results. Comparing the ASPEN Plus[®] database values for such a surrogate catalyst with our experimental data indicates that the surrogate catalyst exhibits similar heat of reaction and heat capacity values when compared to actual redox catalysts. In the current study, the reducer is operated at 850°C and the regenerator at 950°C, both at near-atmospheric pressure. The re-oxidized redox catalyst particles are recirculated to the reducer to complete the redox loop. It is noted that the redox catalyst not only provides its lattice oxygen but also carries heat required for ODH reactions. Unconverted ethane and propane from the downstream separation block are recirculated to achieve higher overall conversion. Heat loss for the redox process is assumed to be 1% of the total thermal output whereas redox catalyst loss is assumed to be negligible. The hot, oxygen-depleted air from the regenerator is used to generate high pressure steam. The gaseous output from the reducer is treated through a chain of downstream separation units which are nearly identical to the steam cracking. All of the ethane and propane are recycled to the reducer, the heat requirements of which are met entirely via the heat stored in the re-oxidized solids, owing to their high heat capacity and suitable temperature difference (ΔT) between the reducer and regenerator. The heat needed by the cracking furnaces represents a major energy requirement for steam cracking. In contrast, exothermicity of the regenerator is used to compensate the heat needed for the ODH reactor, thereby lowering the upstream energy demand in ODH. In the following sections, the overall energy requirement for the ODH process is evaluated and compared with that of ethane cracking.





$$\Delta H_{1123\text{K}} = -223 \text{ kJ/mol}$$

Reaction 4.4

Table 4.1: ASPEN Plus® modules, property methods and databanks.

Stream class	MIXCISLD
Databank	PURE, AQUEOUS, SOLIDS, INORGANIC
Solid components	Mn ₃ O ₄ , MnO, MgO
Property method	PR-BM and STEAM –TA for steam cycles
Unit operation models	
Regenerator, Reducer and Deacetylenizer	RStoic
Pressure changers	MCompr
Heat exchangers	Heater
Distillation columns	DSTWU
Separators/Flash columns	Sep/Flash2

4.4 Simulation assumptions

ASPEN Plus® simulator ^[22] is used to determine the process performance of ethane CL-ODH and compare it with steam cracking. The processes are simulated for an ethylene production capacity of 1 million tonnes per year. The cracking process (Case I) and the ODH reference case (Case II) with an ethane single-pass conversion of 85% are simulated. ASPEN Plus® modules, property methods, and physical property databanks are summarized in **Table 4.1**. The carbon yields for the various processes are listed in **Table 4.2**.

Table 4.2: Carbon yield for the two cases.

	Case I: Cracker	Case II: ODH reference
Ethane conversion	65%	85%
Carbon yield (%)		
Ethane	35.0%	15.0%
Methane	3.4%	6.0%
Acetylene	0.5%	0.2%
Ethylene	56.1%	65.0%
Propylene	1.2%	2.4%
Propane	0.1%	0.3%
Butadiene	2.1%	2.4%
Butenes	0.2%	2.4%
Butanes	0.2%	0.0%
C ₅ 's	0.6%	0.5%
Benzene	0.5%	2.4%
Toluene	0.1%	0.5%
CO	0.0%	1.5%
CO ₂	0.0%	1.5%

These are based on the experimental results as given in previous work ^[17,18]. Although small amount of CO_x from coke burning can be observed during redox catalyst regeneration, the yield is negligible, and is thus excluded from the simulation. The yields assumed for propane (recycled) cracking ^[6] as well as for propane ODH are given in the supplementary document. The drying unit is modeled as a flash column, where almost all of the water is condensed, and the acid gas removal (AGR) unit is placed at the exit of the compressor. A Sep block is used to simulate the AGR with the energy consumption accounted for. The solids used in the simulation include Mn₃O₄ and MnO

with MgO added as an inert to mimic the actual catalyst ^[18]. The key operating assumptions and parameters used in the simulations are listed in **Table 4.3**.

4.5 Process modeling

The feed is considered as a mixture of 95% ethane and 2.5% of propane and methane, by volume, at a preheated temperature of 650°C. Such a gaseous mixture is also known as ethane-mix and is normally used as a feedstock in industrial practice ^[23]. In the case of a cracking furnace, steam is also fed at 650°C (0.3 kg steam per kg fresh feed). As mentioned earlier, Mn₃O₄ is used as the oxygen carrier in the ODH case. In the process simulation, the Mn₃O₄ particles are initially fed into the reducer, from the exit of which they are transported to the regenerator. There is a ΔT of 100°C, between the reducer and regenerator, with the regenerator being higher at 950°C. In the regenerator, the reduced oxygen carrier is fully oxidized in 10% excess air, preheated to 650°C, via Reaction 4.3, prior to the recirculation to the reducer for another redox loop.

The product gases in both the cases are cooled to a temperature of 30°C, to avoid further cracking. Heat released from the rapid cooling process is assumed to be completely utilized to generate steam and to preheat the ethane and air feeds. The exothermicity of the regenerator can also produce low pressure steam and reduce the upstream energy demand. The cooled gases are flashed to remove the water from the stream. In the present model, this flash column functions as a drying unit and is placed before the compressor, rather than between the initial stages of compression. The dry stream is then compressed to a pressure of 42 atm ^[6], using a 4-stage isentropic compressor, with the exit stream at 25°C. No H₂S is assumed to be in the product stream, with CO₂ being the primary component of acid gas. Negligible energy consumption is assumed for the caustic wash. For ODH, where there is substantially more CO₂ in the product stream, an amine scrubbing process is assumed with an energy consumption of 0.11 MW-hr/tonne CO₂ ^[24]. The

operating conditions of the downstream columns, for the cracking process, are listed in **Table 4.4** [25]. The compressed stream is cooled to -100°C which leads to the separation of hydrogen and CO prior to methane removal. The refrigeration requires a high duty and removes 97% of the hydrogen and 63% of the CO, reducing the load on the demethanizer. The ethane and propane obtained from the C2 and C3-splitters respectively, are completely recycled to the reducer at 650°C . The reflux ratio for each column is fixed as twice that of the R_{\min} . For direct comparison, the C2-splitters in both cases are modeled with the same number of stages and with the same recovery. The concentration of acetylene in the final, polymer-grade ethylene stream needs to be less than 5 ppm. A deacetylenizer is used to hydrogenate the acetylene in the overhead stream of deethanizer. [5][9] Purified hydrogen for acetylene hydrogenation is obtained through pressure swing adsorption (PSA). A 80% hydrogen recovery is assumed, with the purity being 99% and a pressure drop of 1 bar [26]. Operating conditions of the deacetylenizer are based on the study of an industrial cracking unit (**Table C3** of the supplementary document) [27].

Since the process consumes different forms of energy such as thermal energy, steam, and electricity, it is helpful to convert them into a same thermal basis for process comparison. An HHV efficiency of 85% is considered for the thermal to steam energy conversion, whereas 40% (HHV) efficiency is considered for thermal to mechanical energy conversion [8]. Using the condenser and reboiler duties of the columns, as calculated by ASPEN Plus[®], the power needed for refrigeration is calculated using the power-temperature graph as given in literature [28]. The refrigerants chosen for each unit are listed in **Table 4.5**.

Table 4.3: Simulation conditions and assumptions.

Ambient condition	T = 25°C, P = 1 atm
Reaction assumptions	As per the carbon yield distribution in Table 4.2
Heat loss in chemical looping reactors	1% of the total thermal output
Chemical looping reactor operating pressure	1 atm
Deacetylenizer operating pressure	42 atm
Compressor specifications	4 stage with intercooler at 25°C Isentropic efficiency of 0.72
Air feed (to the regenerator)	10% excess
Discharge temperatures to the environment	Temperature: 25°C
Thermal energy to steam efficiency	85%
Thermal energy to electric energy efficiency	40%

Table 4.4: Column details (all columns use a partial condenser with all vapor distillate) ^[25].

Unit	Key component recoveries				Reflux ratio	Pressure (bar)	
	Light key	Recovery	Heavy key	Recovery		Condenser	Reboiler
Demethanizer	Methane	99.90%	Ethylene	0.50%	3	26	27
Deethanizer	Ethylene	99.99%	Propane	0.10%	0.6	10	11
Depropanizer	Propylene	99.99%	Iso-butylene	1.40%	4.6	10	11
C2-splitter	Ethylene	99.00%	Ethane	0.06%	2.7	4	11
C3-splitter	Propylene	99.60%	Propane	0.24%	18	16	18
Debutanizer	Iso-butane	99.90%	Butadiene	0.10%	8.6	4	5

4.6 Results and discussion

4.6.1 Reactor product distributions

The feed and exit gas compositions of the two cases are presented in **Table 4.6**. For ethane cracking, a steam dilution of 0.3 kg/kg fresh feed, is assumed ^[6]. In the ODH case, conversion of

H₂ to H₂O is fixed at 71%, for thermal sufficiency. The energy demand for the columns is accounted for by condenser refrigeration, based on the simulated duty. For the same final ethylene throughput, there is a 64% drop in the amount of hydrogen at the reactor output for ODH when compared to cracking. As a result, the total molar output is reduced by 15%. Owing to higher CO_x and C₃₊ selectivity, the ODH case requires 11.4% more fresh ethane feed. Meanwhile, ODH leads to a 76% increase in the molar output of C₂₊ components from the reactor. Due to the 63% drop in the amount of unreacted ethane flowing through the system, the total mass of the product stream is higher in the case of steam cracking. As a part of the analysis, the High Value Products (HVPs) are considered which include the C₂₊ olefins, C₅ compounds and aromatics.

4.6.2 Energy distribution

ASPEN Plus® simulation of the ethane cracking process indicates an energy consumption of 15.2 GJ/tonne ethylene. This is in agreement with the study of Ren et.al^[8] which states 15-25 GJ/tonne ethylene. Depending on the temperatures in the condensers of the columns, the refrigerants are chosen as shown in **Table 4.5** and the corresponding refrigeration power can be calculated^[28]. For the cracking process, 61% of the upstream energy is required to suffice the endothermicity of the furnace, as shown in **Figure 4.2**. Quenching of the hot gases generates high pressure steam and recovers additional energy. The compression step requires 47% of the downstream energy, while the refrigeration for the demethanizer feed, and the C₂ splitter demand 29% and 14% respectively. The C₂-splitter is the most energy-intensive separation column. **Figure 4.2a** shows the section wise energy distribution in cracking process and the ODH reference case (overall and downstream). The energy distribution for steam cracking is presented in **Table 4.7**.

Table 4.5: Choice of refrigerant^[28].

Unit	T required	Refrigerant
	deg C	
Demethanizer	-95	Ethylene
Deethanizer	-43	Ethane
C2 splitter	-76.3	Ethane
Fractionation	-110	Ethylene
Depropanizer	25	Propylene
C3 splitter	34	Propylene
Debutanizer	32	Propylene

4.6.3 Process comparisons

Unlike steam cracking which requires significant amount of energy for the endothermic cracking reactions and steam generation, the CL-ODH case is operated based on cyclic redox reactions (Reactions 4.3 and 4.4) which are net exothermic. The regenerator replenishes the oxygen in the carrier via the highly exothermic Reaction 4.4. The heat loss in the reactors is assumed to be 1% and is accounted for in the regenerator output. The oxygen-lean hot air leaving the regenerator is used to generate high pressure steam, and is counted as available upstream energy in the ODH case. As a result, the upstream and overall energy requirements for ODH are reduced significantly. The exothermicity of the regenerator and the absence of steam further reduce the upstream energy (thermal) demand and take the upstream section from 218.9 MW_{th} net endothermic for cracking to 115.2 MW_{th} net exothermic for the ODH case, as shown in **Table 4.7**. This accounts for the most significant reduction in energy demand in ODH compared to steam cracking.

The main downstream energy savings in the ODH case are in the compression section, where there is a 32.1% drop, due to a corresponding drop in the total moles of the product gases, on a dry basis. The overall drop in the downstream energy requirement is 23.5%. An overall drop in the total mass flowing downstream reduces the energy for refrigeration prior to the demethanizer. This reflects in the reduced refrigeration duty needed to cool the feed to the demethanizer. The small amounts of CO and CO₂ present in cracking product case do not add significant energy of separation. The amine scrubbing unit is likely to be required for the ODH case, due to the high CO₂ content of 3.2 vol% (dry basis). Overall, 0.11 MW-hr of work/tonne of CO₂ captured is needed for the process [24]. For the simulated plant capacity, this accounts for 1.36 MW (electric)-demand for the ODH case, which assumes a 100% CO₂ removal. There is 3.2 vol% of CO present in the outlet for the ODH case as well, on a dry basis, compared to 300-400 ppm for the cracker output. The PSA unit adds to the energy expense downstream, contributing an energy requirement of 2.2 kW-hr (electric)/kg H₂ separated [26]. Based on the assumptions of the PSA mentioned earlier, this sums up to a requirement of 0.7 and 0.2 MW_{th}(thermal) energy for the cracking and ODH case respectively, owing to lesser amount of hydrogen to be separated in the PSA for the ODH case. Overall, the ODH case provides an 82% drop in the overall energy demand of the plant, compared to cracking, for a 1 million tonne capacity of ethylene per year.

The deacetylenizer in both cases operates at high pressures (~35 bar) and temperatures of 50°-70°C [27]. The reactant gas from the top of a deethanizer is at a very low temperature (-47°C). For ODH, the pre-demethanization refrigeration removes 63% of the CO with the remaining passing on to the demethanizer (DM). Less mass is fed to the DM in the ODH case. The condenser duty of the deethanizer (DE) is reduced due to a considerable drop (~60%) in the amount of ethane flowing

into the DE, owing to the high single-pass ethane conversions. The ODH case showed a 5% drop in the condenser duty.

Table 4.6: Exit gas and solid streams.

Mole flow (kmol/hr)		
	Cracking (Case I)	ODH reference (Case II)
Feed		
Ethane	4807.0	5353.3
Methane	126.5	140.9
Propane	126.5	140.9
Total	5060.0	5635.0
Steam	2500	NA
Final ethylene output (after the downstream purification)	4077	
Output from Cracker or ODH reactor		
Ethane	2580.4	943.1
Methane	704.2	894.9
Acetylene	74.5	14.0
Ethylene	4242.1	4163.9
Propylene	82.6	140.6
Propane	19.5	60.9
Butadiene	80.5	74.8
Butenes	7.5	75.8
Butanes	15.6	1.1
Pentanes	19.9	12.6
Benzene	14.0	49.8
Toluene	2.4	9.0
CO ₂	0.0	279.2
CO	0.0	279.2
H ₂	4441.9	1616.6
H ₂ O	2497.9	3918.4
Total Flow (kmol/hr)	14782.9	12533.9
Total Flow (kg/hr)	276549.0	276442.0

Table 4.6 (continued): Exit gas and solid streams

Solid stream flowrates and compositions (Case II)				
	Solids in		Solids out	
Temperature (°C)	950		850	
Pressure (atm)	1		1	
	million kg/hr	wt%	million kg/hr	wt%
Mn ₃ O ₄	1.26	20.82	0.17	2.85
MnO	0	0	1.01	16.96
MgO	4.79	79.18	4.79	80.19

As shown in **Table 4.6**, the amount of propane + propylene in the ODH case is twice of that in cracking. As a result, the cooling duty of the ODH-C3 splitter is twice that of cracking. Key comparisons between the energy demands are shown in **Figures 4.3 and 4.4**.

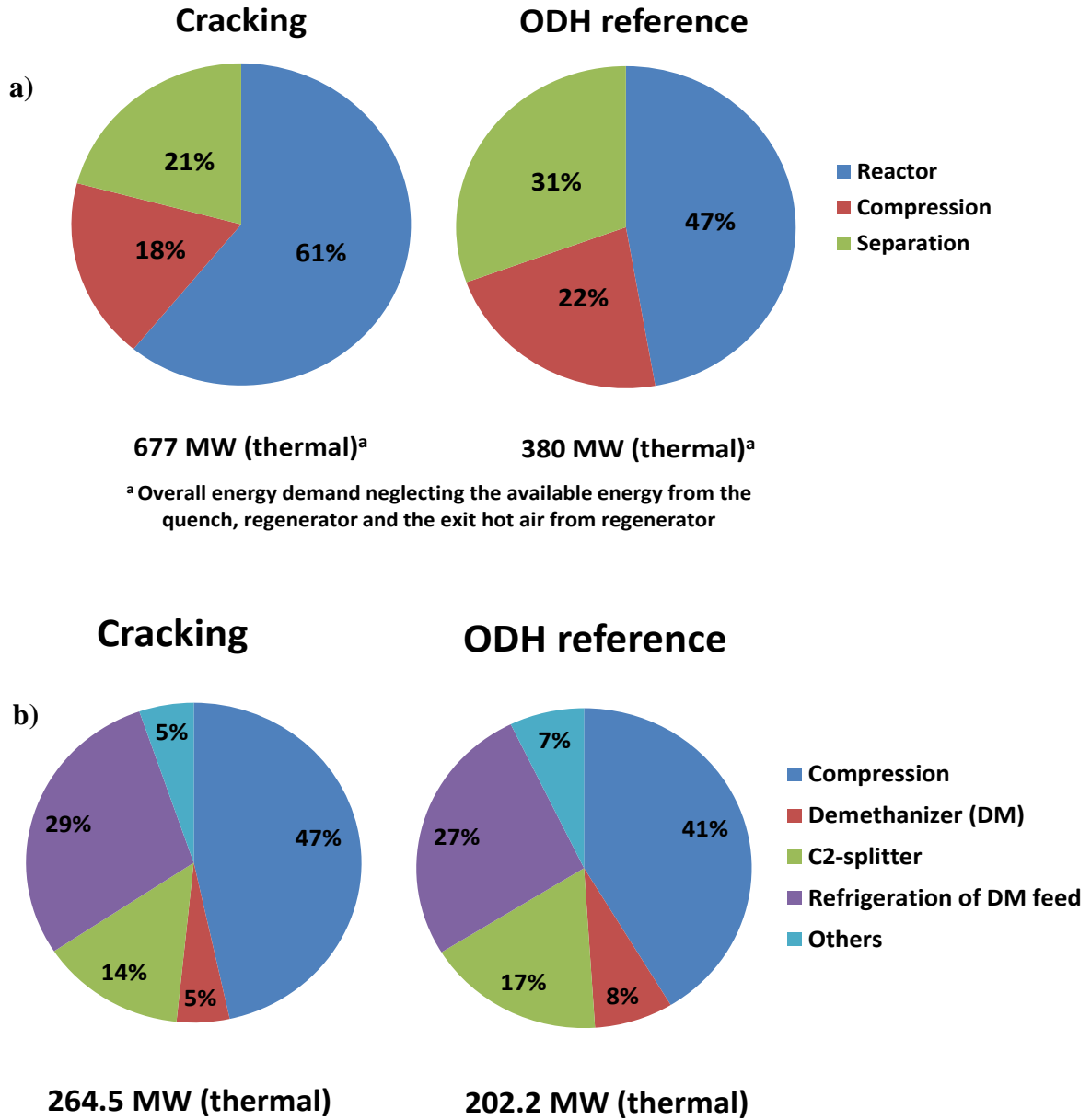


Figure 4.2: a) Section wise energy distribution and b) overall energy distribution for a steam cracking process.

Table 4.7: Comparison of the energy consumption.

Comparison			
	Cracking	ODH reference	
Ethane conversion		65.0	85.0
Flow (tonne/hr)	Ethylene	114.2	114.2
	Fresh Feed	152.2	168.8
Upstream (MW _{th})	Reactor (Endothermicity)	235.9	0.0
	Regenerator ¹	n/a	-33.2
	Ethane recycle	50.0	18.6
	Propane recycle	1.2	1.2
	Feed pretreatment	77.9	86.0
	Steam heat	47.6	n/a
	Air preheat	n/a	72.0
	Exit gas cool ¹	n/a	-76.1
	Quench ¹	-193.6	-183.7
	Downstream ² (MW _{th})	Compressor	123.2
Demethanizer		13.5	15.4
Deethanizer		5.4	2.7
Depropanizer		1.2	1.2
C2-splitter		37.1	34.8
C3-splitter		1.2	2.4
Debutanizer		0.0	0.1
Deacetylenizer		5.5	4.6
CO ₂ scrubbing		0.0	3.4
PSA		0.7	0.2
Fractionation	76.9	53.8	
Upstream Subtotal (MW _{th})		218.9	-115.2
Downstream Subtotal (MW _{th})		264.5	202.2
Net (MW _{th})		483.4	87.0
Net (GJ _{th} /tonne ethylene)		15.2	2.7
¹ Steam energy from thermal with 85% conversion ² Converted to thermal assuming 40% conversion			

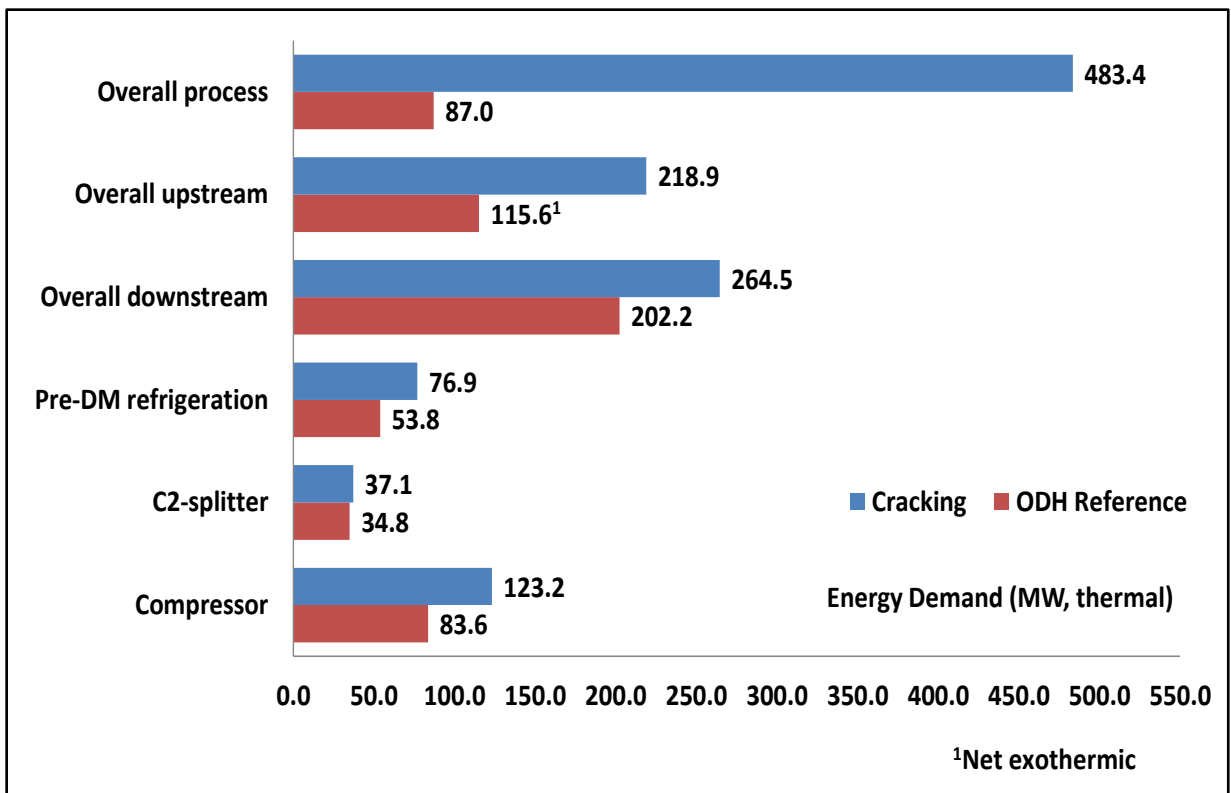


Figure 4.3: Comparison of the energy distributions.

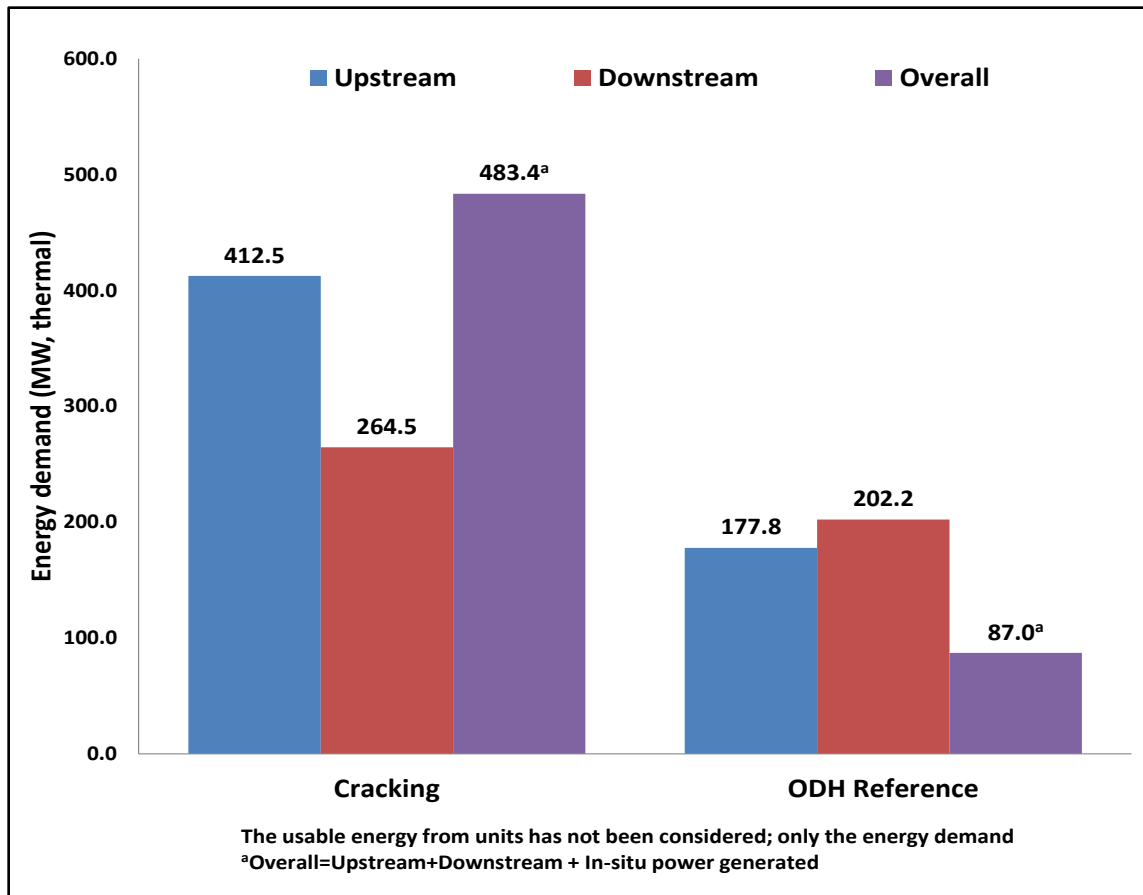


Figure 4.4: Relative energy demand (section wise and overall).

4.6.4 Emission comparisons

The fuel gases produced during the process, which include CO, CH₄ and H₂, can be burned to (partially) satisfy the energy requirements. In **Figure 4.5** it is assumed that all of the fuels are combusted to extract their energy value. Using the $\Delta H_{\text{reaction}}$ as given in **Table 4.8** and the available fuel, as given by ASPEN Plus[®], the total available energy from the fuels is calculated. **Figure 4.5** compares the available energy from the fuels, energy demand from the process, and the net energy production/consumption. For the ODH case, there is 7.35 GJ_{th} excess as compared to the cracking process, which has a 1.42 GJ_{th} deficit for every tonne of ethylene produced.

However, for the same amount of ethylene, the ODH case requires more ethane in the feed than cracking, which translates to an energy-penalty for the system. On the other hand, it also gains an energy-credit in the form of C3+ compounds. If these are taken into account, using the lower heating values (LHV) of ethane and C3+ compounds ^[29], the ODH case has an overall energy-penalty of 3 GJ_{th} for every tonne of ethylene produced.

Table 4.8: $\Delta H_{\text{reaction}}$ and molar flow rate of the fuel.

Heat release (LHV)		
$CO + \frac{1}{2}O_2 \rightarrow CO_2$	282	kJ/mole
$CH_4 + 2O_2 \rightarrow CO_2 + 2H_2O$	800	kJ/mole
$H_2 + \frac{1}{2}O_2 \rightarrow H_2O$	239	kJ/mole
Molar flowrate (kmol/hr)		
	Cracking	ODH
CO	0	279.1
CH ₄	703.8	894.0
H ₂	4247.9	1496.0

In the case of cracking, negligible amount of CO₂ is present in the product gases. Based on the total energy demand and available CO and CH₄, as given in **Table 4.8** and **Figure 4.5**, 2176.3 kmol/hr of CH₄ is required to meet the demand of 483.4 MW_{th}. In the case of the ODH, after burning the CO, combustion of 292.7 kmol/hr of CH₄ is required for energy consumption. By assuming an emission factor of 60 kg CO₂/GJ electricity, the cracking process leads to an emission of 1.2 tonne CO₂/tonne ethylene ^[8] as compared to 0.22 tonne CO₂/tonne ethylene for the ODH case. Therefore CL-ODH provides 82% drop in CO₂ emissions. Unlike cracking which generates

significant amount of NO_x from fuel burning^[30], ODH case has significantly lower NO_x emissions as well.

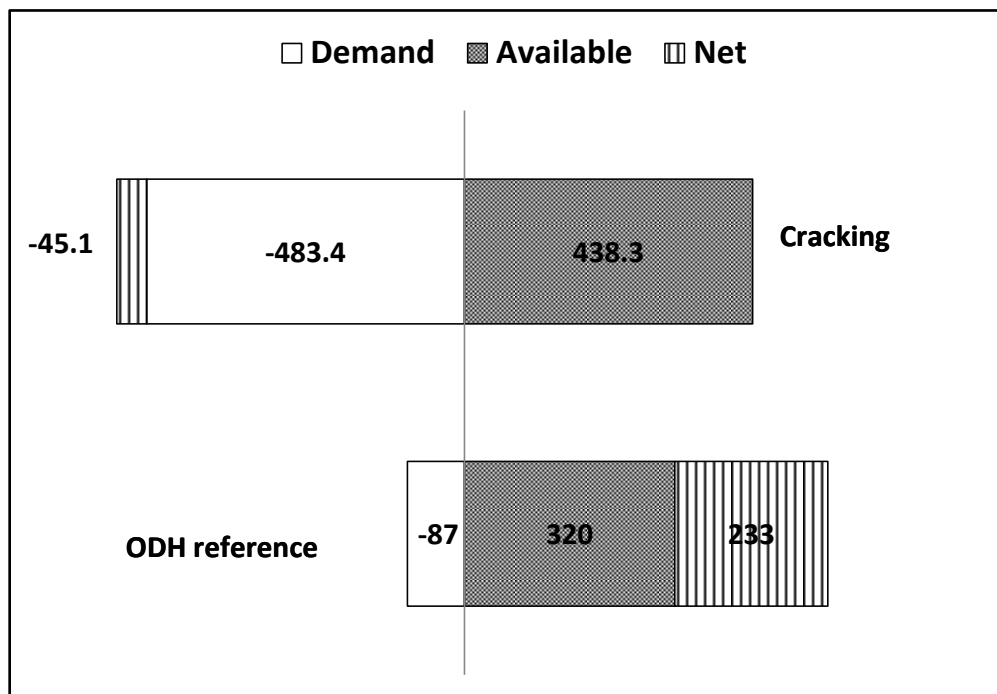


Figure 4.5: (Thermal) Energy surplus and emissions.

4.7 Sensitivity analysis

4.7.1 Ethylene yield

The effect of ethane single-pass conversion is also studied. Two additional cases are considered for the redox ODH process; one at 66% single-pass ethane conversion (similar carbon yield as cracking) and one at 90%. The carbon yields of the various products are listed in **Table 4.9**. The exit gas composition and the energy distribution and demand-reduction, relative to the reference and cracking case, are analyzed.

As shown in **Table 4.10**, with an increase in the ethane conversion, there is a corresponding increase in the amount of heavier hydrocarbons (C3+) produced. The total molar flow-rate on a dry basis decreases at higher conversions, which corresponds to a drop in the compression work. As the heavier hydrocarbon content increases, the mass throughput increases.

Table 4.9: Carbon yield for the different ethane ODH cases considered.

%Carbon yield			
Component	Case III	Case II	Case IV
	ODH low	ODH reference	ODH high
Ethane conversion	66%	85%	90%
Ethane	34.10%	15.00%	10.00%
Methane	3.30%	6.00%	7.00%
Acetylene	0.50%	0.19%	0.19%
Ethylene	56.10%	65.00%	65.03%
Propylene	1.20%	2.38%	2.50%
Propane	0.10%	0.25%	0.25%
Butadiene	2.10%	2.38%	2.50%
Butenes	0.20%	2.38%	2.50%
Butanes	0.20%	0.03%	0.03%
C ₅ 's	0.60%	0.50%	0.80%
Benzene	0.50%	2.38%	5.00%
Toluene	0.10%	0.50%	1.00%
CO	0.50%	1.50%	1.60%
CO ₂	0.50%	1.50%	1.60%

Table 4.10: Exit gas composition of the ethane ODH cases

Mole flow (kmol/hr)			
	Case III	Case II	Case IV
Feed			
Ethane	4774.7	5353.3	5606.9
Methane	125.65	140.9	147.6
Propane	125.65	140.9	147.6
Total	5026	5635.0	5902.0
Final ethylene output (after the downstream purification)	4077		
Output			
Ethane	2457.1	943.1	691.7
Methane	601.2	894.9	902.2
Acetylene	42.3	14.0	14.0
Ethylene	4111.6	4163.9	4172.5
Propylene	92.8	140.6	147.5
Propane	48.2	60.9	63.1
Butadiene	75.7	74.8	78.6
Butenes	7.3	75.8	79.7
Butanes	10.1	1.1	1.1
Pentanes	17.3	12.6	20.1
Benzene	12.0	49.8	104.8
Toluene	2.1	9.0	18.0
CO	150.2	279.2	295.9
CO ₂	150.2	279.2	295.9
H ₂	1411.3	1616.6	1703.3
H ₂ O	3417.1	3918.4	4315.9
Total Flow (kmol/hr)	12606.5	12533.9	12904.3
Total Flow (kmol/hr)(Dry)	9189.4	8635.5	8588.4
Total Flow (kg/hr)	288697.0	276442.0	284259.0
Total Flow (kg/hr) (Dry)	227189.2	205910.8	206572.8

The effect of the change in the ethane conversion on the section wise and overall energy (thermal) demand can be seen in **Figures 4.6 and 4.7**. With an increase in the ethylene yield, the overall energy demand of the process drops from 154 to 87 to 54 MW_{th} as the single pass ethane conversion increases from 66% to 85% to 90%. The available energy from the regenerator, quench, and the hot exit-air, increases with an increase in the single-pass ethane conversion, which thereby reduces the overall energy demand. A better way of comparison among the processes is by using the output of the HVPs, as shown in **Figures 4.8 and 4.9**, where each value is expressed per tonne of HVP. From **Figure 4.9**, it can be seen that as the ethane single-pass conversion increases from 66% to 90%, the CO_2 emissions decrease from 0.31 to 0.17 tonne CO_2 /tonne ethylene. This translates to 0.27 and 0.13 tonne CO_2 /tonne HVP respectively. With respect to the cracking case, which emits 1.2 tonne CO_2 /tonne ethylene ^[8], the increase in ethane conversion from 66% to 90% leads to a reduction in CO_2 emissions from 74% to 87%.

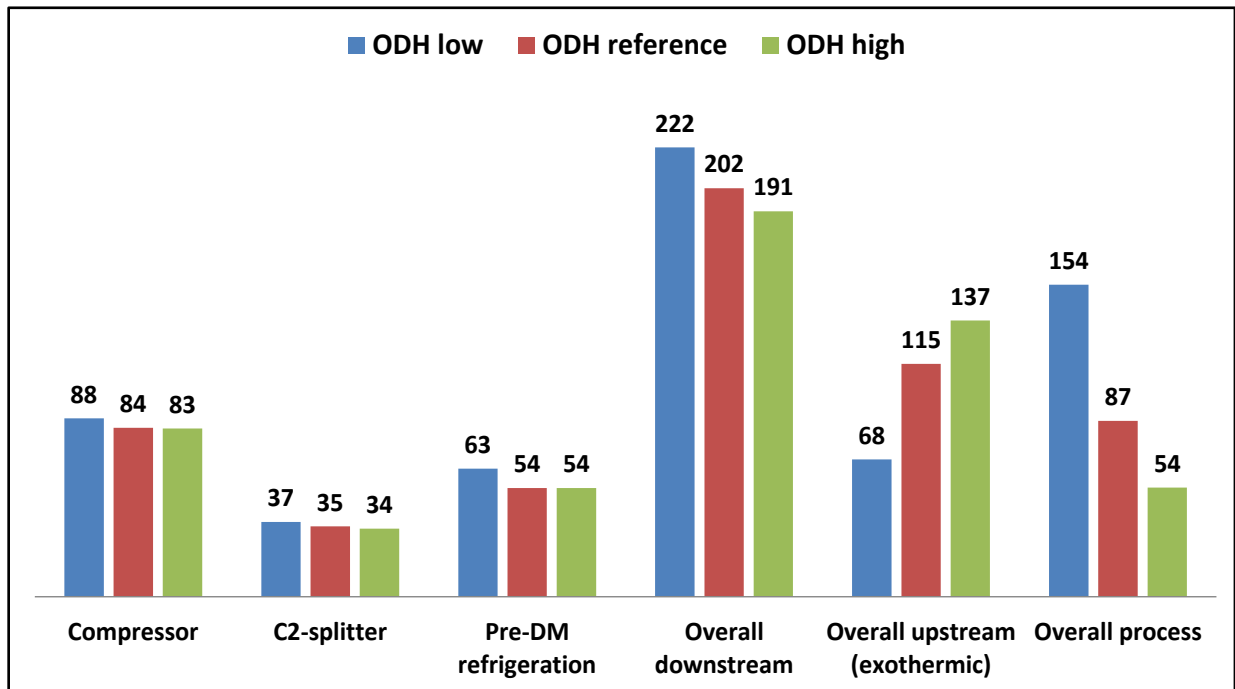


Figure 4.6: Thermal energy (MW_{th}) comparison for the ethane ODH cases.

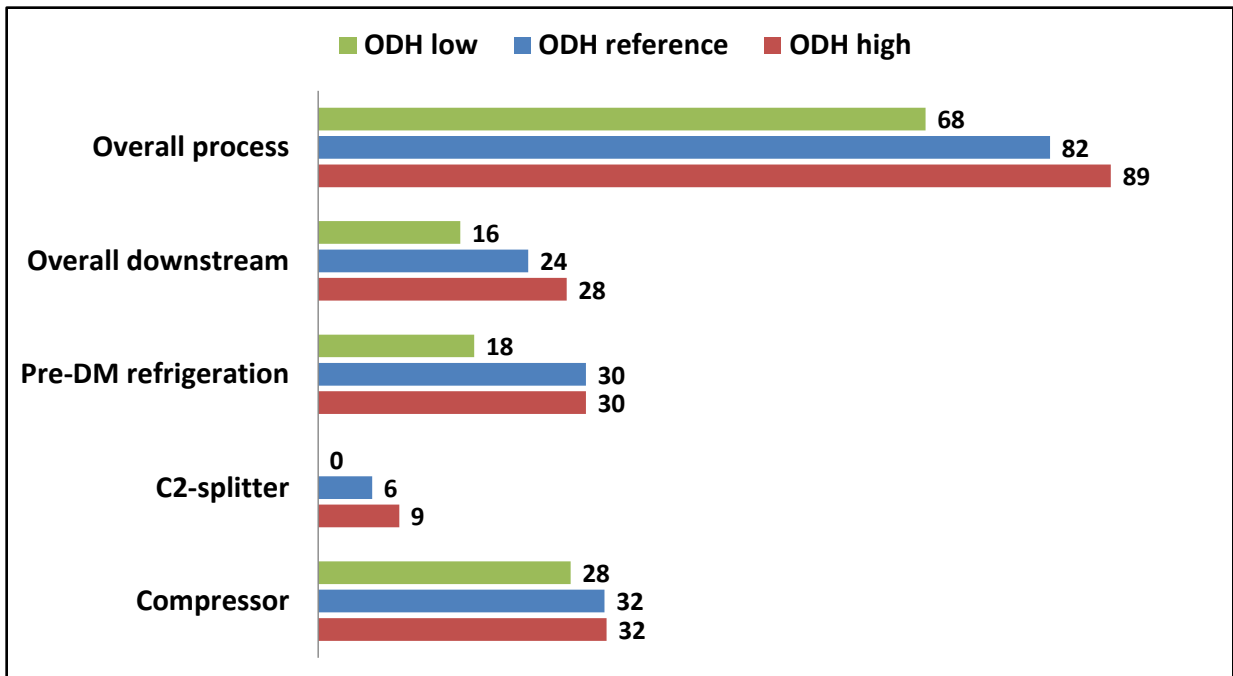


Figure 4.7: % Reduction in the energy demand.

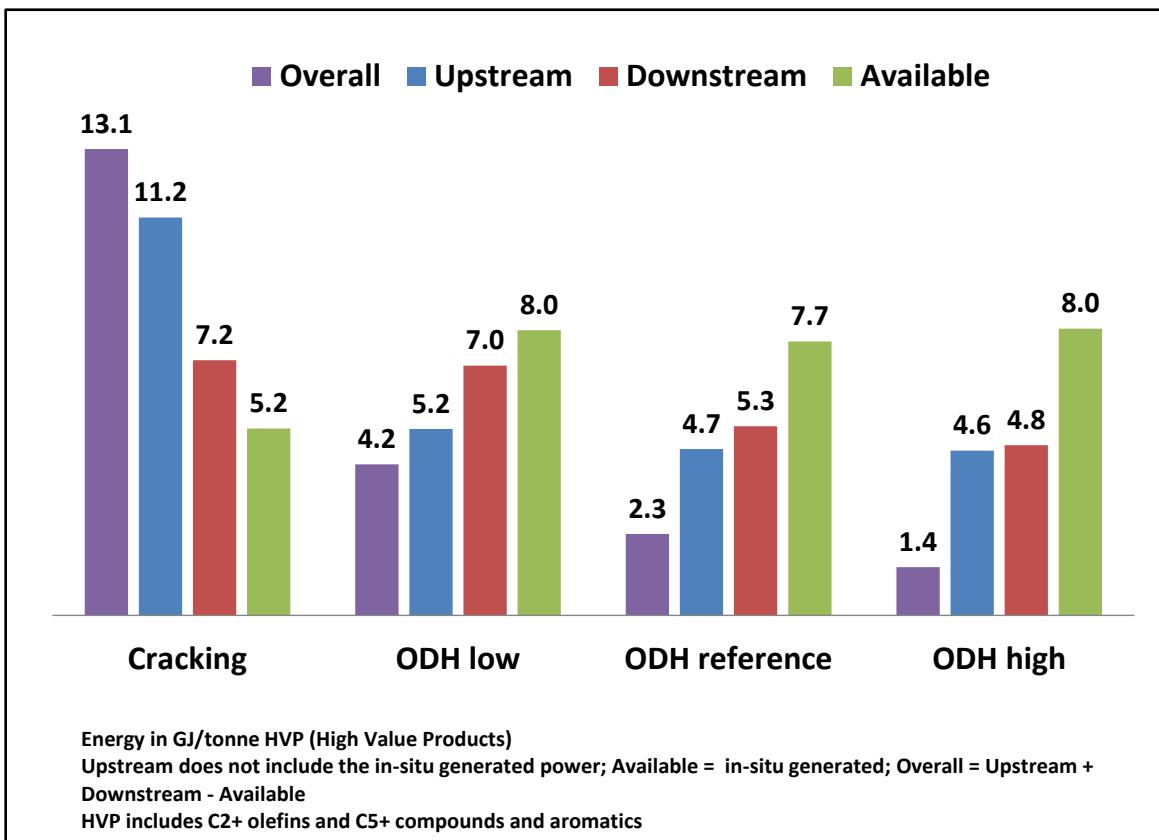


Figure 4.8: Thermal energy distribution comparison.

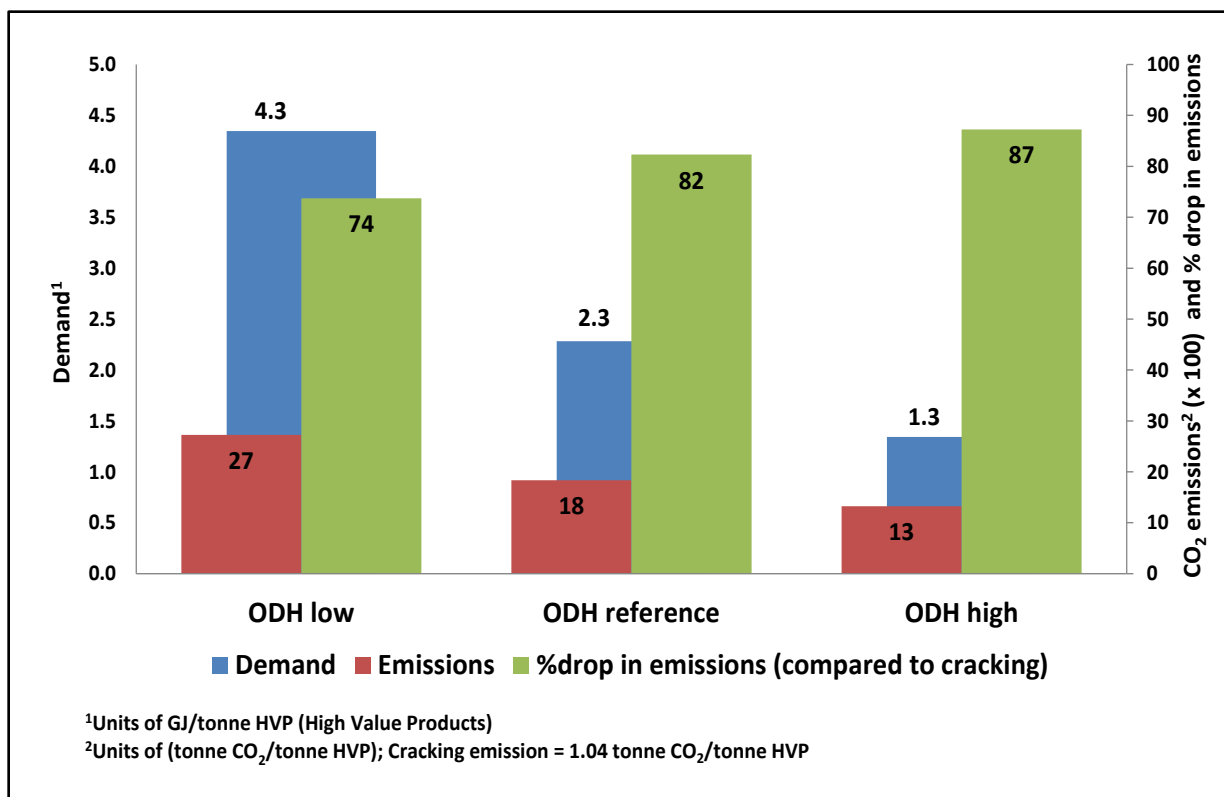


Figure 4.9: Thermal energy demand and emission comparison.

4.7.2 Effect of pressure drop

Solid circulation in the CL-ODH process leads to a pressure drop, which requires additional compression work [27]. The following analysis calculates the amount of work needed to negate the pressure drop in the ODH reactors. Pressure drops of 0.1, 0.2, 0.3 and 0.4 atm are studied and the corresponding energy requirements are presented in **Figure 4.10**. Although the reactor pressure drop related to solids circulation can increase the overall energy demand for ODH, the energy related to solids circulation is anticipated to be small. Even with a conservative assumption of 0.4 atm pressure drop for each reactor, the energy loss adds up to 0.43 GJ/tonne HVP. Under such a scenario, ODH is still 79.2% less energy intensive than cracking.

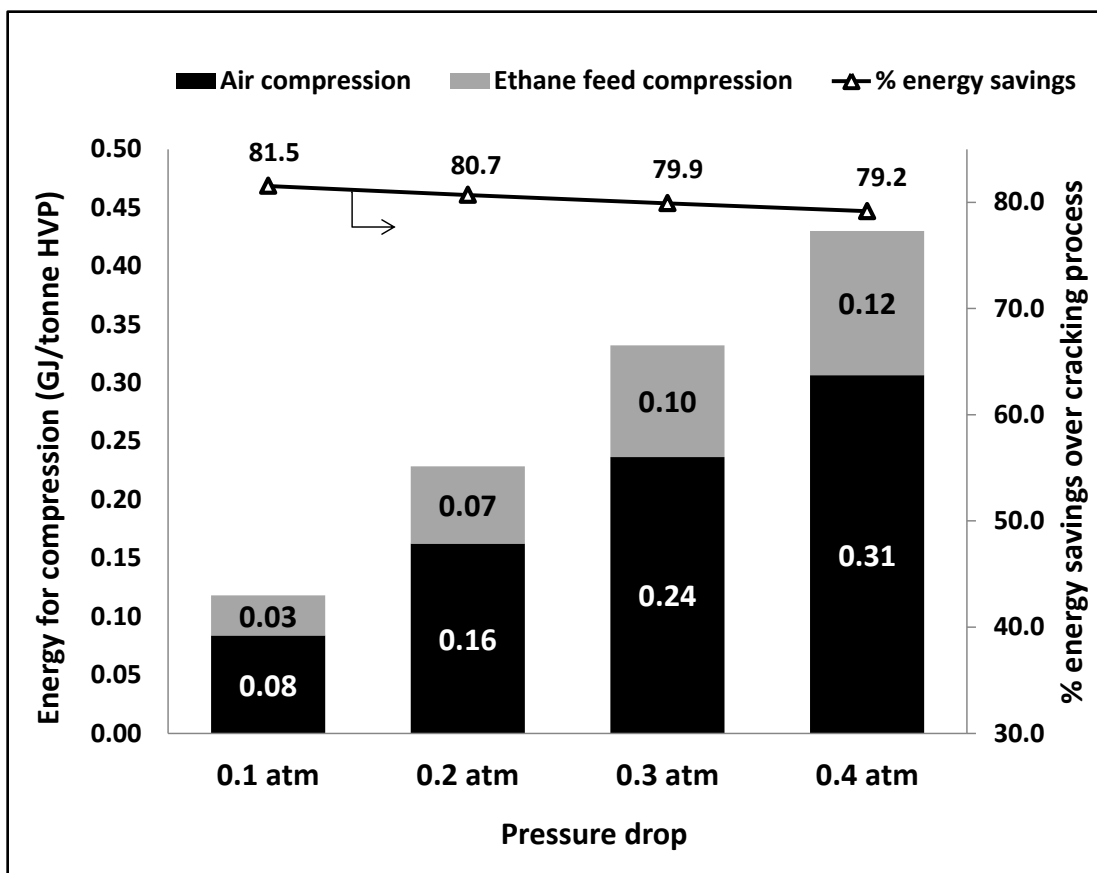


Figure 4.10: Effect of pressure drop.

4.7.3 Regenerator air requirements

The effect of increasing the amount of air in the regenerator is studied in this section for the ODH reference case. As shown in **Figure 4.11**, excess air in the regenerator decreases the exothermicity of the regenerator and demands more heat input to preheat the air to 650°C, but there is more available heat from the hot exit air. Overall, there is a decrease in the net available energy from the regenerator section, with an increase in the amount of air. Excess air would result in unnecessary energy expenditure to heat the input air and then extract heat from it at the outlet. The overall energy demand (MW_{th}) of the process increases with an increase in the amount of air fed. This is shown in **Figure 4.11**. The optimum is likely to be $\leq 20\%$ excess air, which can be achievable using the Mn-based redox catalysts.

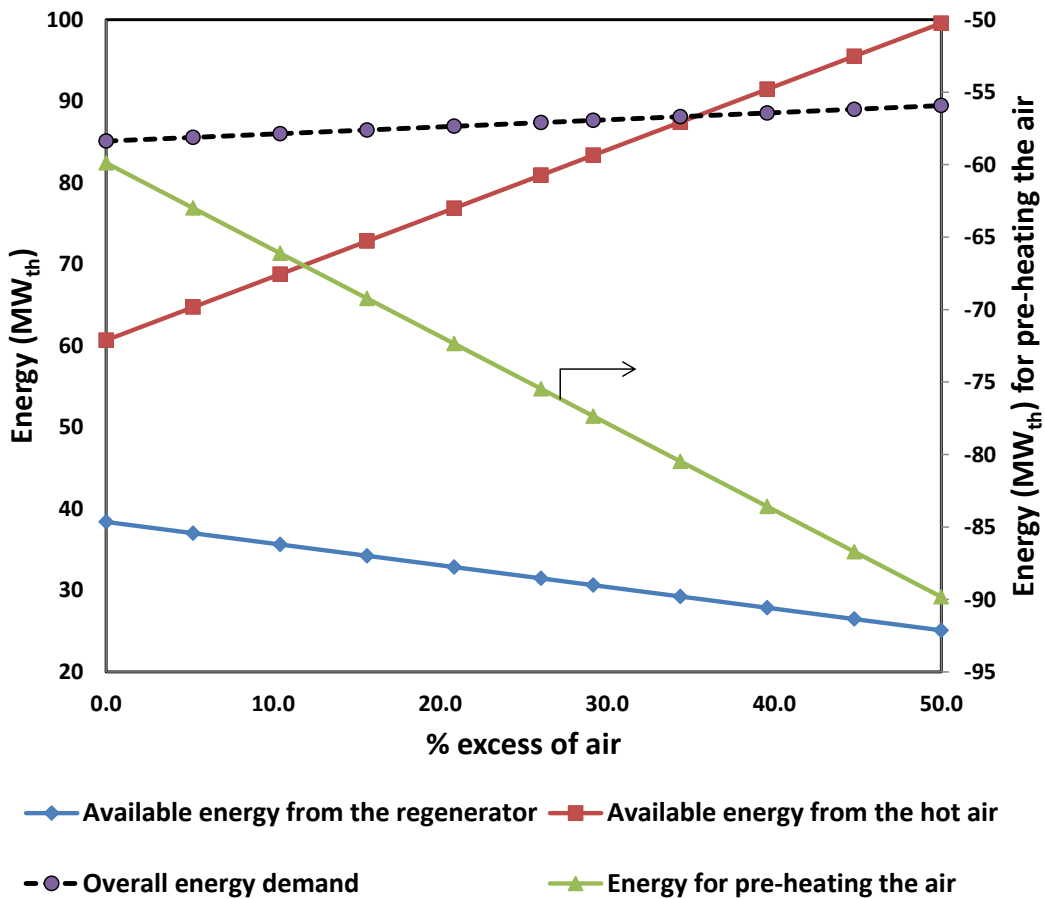


Figure 4.11: Effect of excess air on the thermal energy demand (MW_{th}).

4.8 Further modifications in energy analyses

Modifications, to capture significantly greater details with respect to heat integration and downstream separations, are performed. The furnace is modeled as a series of stacked heat exchangers, as shown in **Figure 4.12** below^[32]. **Figure 4.12a** shows the upstream section of steam cracking which involves the furnace, dilution steam, feed pre-heating and steam-generation from the quench system using Transverse Line Exchangers (TLE). The operating conditions of the separation columns are modified. As shown in **Table C6**, the condenser and reboiler of the columns are assumed to be at higher pressures than earlier. Similar to the earlier analyses, three

chemical looping ODH (CL-ODH) cases have been considered (ODH 67, ODH 85 and ODH 99). Here, ODH 99 is the hypothetical upper-end case to explore the extent of advantages, obtained by extrapolating the data obtained for ODH 85. The modified product distributions for this section are listed in **Table C7**.

Table 4.11 provides a section-wise comparison of the modified energy consumption. The simulation indicates energy demands of 21.13 GJ/tonne HVP for steam cracking vs 5.09 for ODH 85. This corresponds to a net decrease of 15.7 GJ/tonne HVP or 76% in primary energy consumption. It is noted that both CL-ODH and steam cracking co-produce H₂ and CH₄. For CL-ODH, notable amount of CO is also produced. They can either be credited to the process as fuels or purified and sold as byproducts. Accounting for these byproducts as fuel (LHV) produces a credit of 11.38 and 7.30 GJ/tonne HVP for steam cracking and ODH 85, respectively. The fuel credit for ODH 85 is partially offset by an additional ethane demand due to lower C₂₊ selectivity. On accounting for these credits, ODH 85 produces a net reduction in fuel demand of 81%.

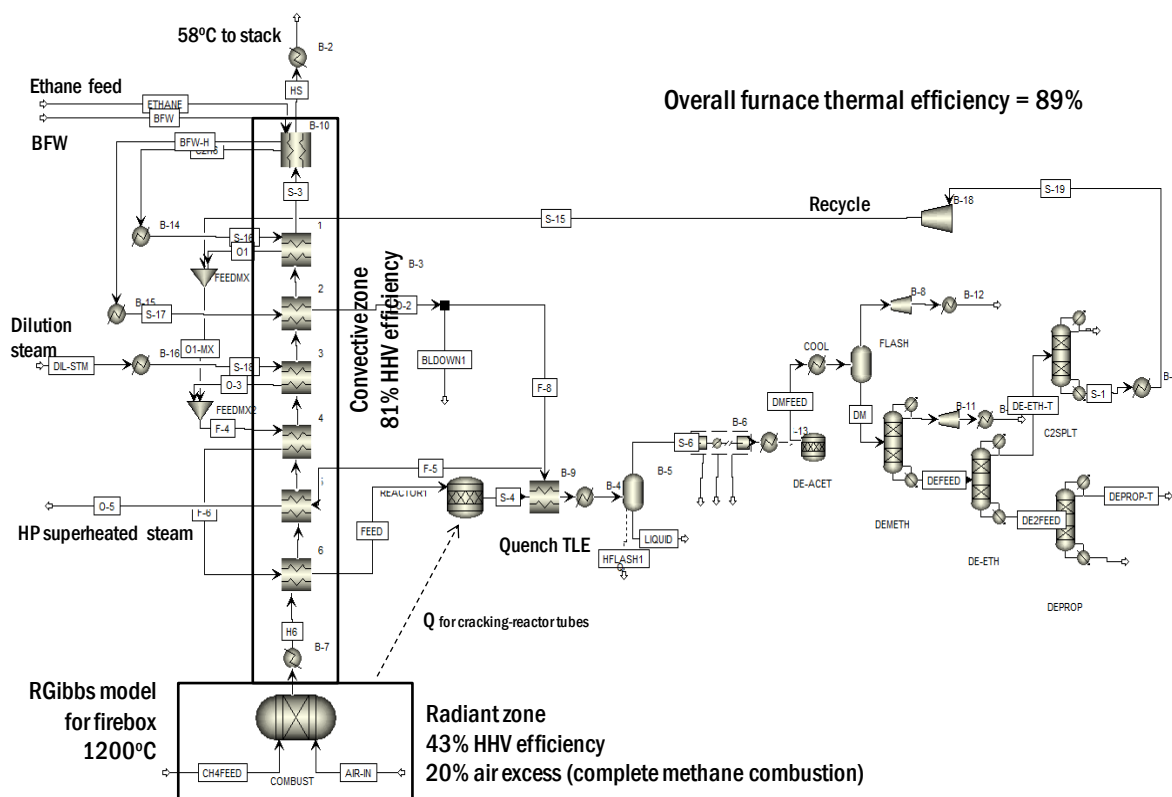
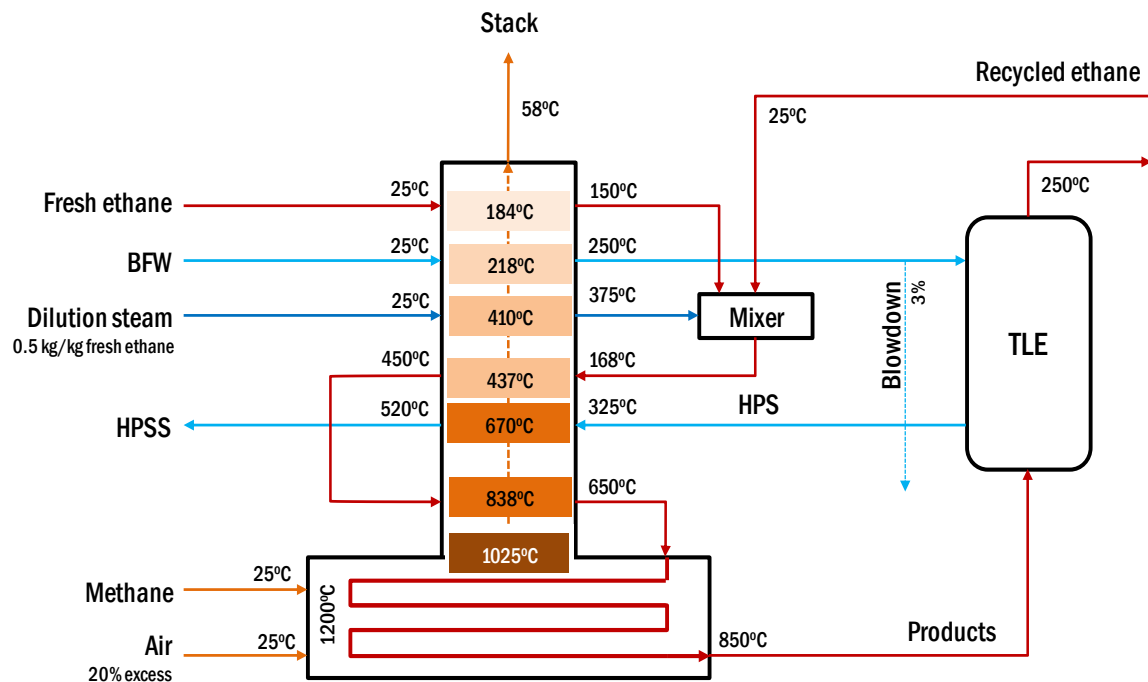


Figure 4.12: a) Modeling the ethane steam cracking furnace^[32]; b) AspenPlus® flowsheet for steam cracking with the furnace^[6,32,33].

Table 4.11: Section wise Energy/Fuel Demand of Steam Cracking and ODH 85.

		<i>Net Energy Demand/Recovery [GJ_{TH}/tonne HVP]</i>	
		<i>Steam Cracking</i>	<i>ODH 85</i>
<i>Demand</i>	<i>Radiant Zone of the Cracking Furnace</i>	6.63	
	<i>ODH Reactor-Regenerator Pair</i>	N/A	-1.3
	<i>Preheating & Heat Recovery</i>	9.55	2.62
	<i>Quench*</i>	-3.92	-2.93
	<i>Compression</i>	3.31	2.04
	<i>Refrigeration</i>	2.37	1.31
	<i>Hydrocarbon Separation</i>	3.19	2.85
	<i>CO₂ recovery & Acetylene Removal</i>	0	0.5
	<i>Total Demand</i>	21.13	5.09
<i>Fuel Credits and Penalties</i>	<i>Fuel Gas Byproduct (CO, H₂ and CH₄) (LHV)</i>	-11.38	-7.3
	<i>Extra Ethane Feed</i>	0 (by definition)	4.04
<i>Net Demand</i>		9.75	1.83

*Steam cracking units and the proposed CL-ODH scheme recover a significant amount of heat from reactor furnaces and the product system quench

4.9 Second Law Analysis

Decades of optimization has led to a thermally efficient, near “perfect” steam cracking process with ~95% first law energy efficiency, indicating little room for further reduction in energy consumption and CO₂ emissions. Although the thermodynamic first law efficiency^[6], second law analysis indicates a significant exergy loss, due to fuel combustion (cracking furnaces) and low energy quality from heat recovery. Second law analysis (exergy analysis) helps in understanding the ability of the CL-ODH process to reduce the energy requirement and CO₂ emissions for ethylene through exergy optimization. As illustrated in **Figure 4.13**, conventional cracking would result in an inevitable exergy loss of >1.7 GJ per tonne of produced ethylene, under an ideal scenario of a) 100% ethylene yield, b) perfect heat utilization for cracking, and c) zero steam

dilution. In comparison, even without accounting for its several practical advantages, CL-ODH reduces this minimum exergy loss by 27%. Such an exergy-saving primarily stems from the *in-situ* hydrogen combustion, in CL-ODH, vs. combustion of externally supplied methane, in conventional cracking. The downstream compression and cryogenic separation in conventional cracking leads to additional exergy losses. Pushing the cracking units to higher per-pass ethane conversions could reduce compression/separation loads. However, this is not practical due to reaction equilibrium limitations and the propensity of ethylene to undergo secondary reactions, which eventually forms coke on inner surfaces of cracking tubes. These factors lead to a net energy demand of 9.75 GJ per tonne of HVP from conventional processes with an estimated exergy loss of 13 GJ/tonne HVP.

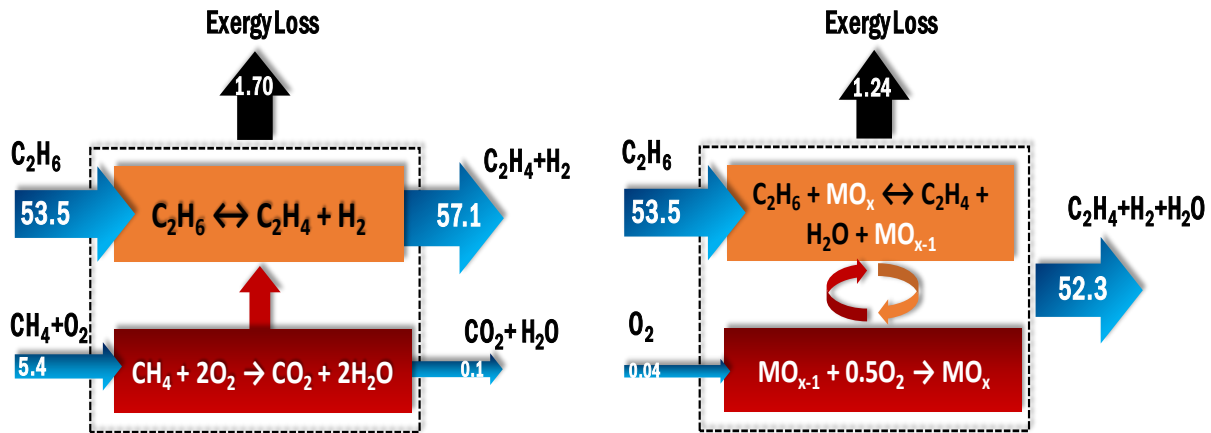


Figure 4.13: Idealized exergy conversion/loss for cracking and CL-ODH schemes at 850°C (GJ/tonne ethylene).

Exergy analysis is particularly useful in light of the different energy qualities associated with the feedstock, fuels, byproducts, and steam. **Table 4.12** compares the section-wise exergy losses in the CL-ODH cases with steam cracking. In the case of ODH 85, a net exergy saving of 4.26 GJ/tonne HVP can be obtained with the prime share occurring in the reactors (2.84 GJ/tonne HVP).

The current simulation indicates little exploitable energy (0.093 GJ/tonne HVP) in the exhaust stream, confirming high thermal (first law) efficiency of steam cracking. However, a large destruction of exergy occurs in the radiant/cracking and convective zones combined, amounting to 7.6 GJ/tonne HVP. As such, even at the reported efficiencies of up to 95% ^[6] (which requires partial condensation in the flue gas stream), sizable exergy losses are inevitable in conventional cracking resulting from irreversibility of fuel combustion and indirect heat transfer as well as the low quality of the heat recovered.

Table 4.12: Section-Wise Exergy Loss Analysis.

Section		Lost work (GJ/tonne HVP)				
		Steam cracking	ODH 67	ODH 85	ODH 99	
Upstream	Radiant Zone		4.90			
	ODH Reactor-Regenerator Pair		N/A	1.64	2.06	2.03
	Power Generation *	Preheating and Heat Recovery	2.73	2.21	2.15	2.11
		Quench	1.54	1.30	1.18	1.06
Downstream	Power Generation Block		1.12	1.44	1.34	1.24
	Compression		0.48	0.34	0.31	0.27
	Refrigeration		0.70	0.45	0.35	0.31
	CO ₂ and Acetylene Removal		0.10	0.18	0.22	0.18
	Separation		1.43	1.44	1.13	1.05
Total		13.00	8.99	8.74	8.26	
% Reduction			30.8	32.7	36.5	

* The Heat Recovery and Quench sections produce steam utilized for power generation

The idealized analysis in **Figure 4.13** indicates potential exergy savings using hydrogen instead of methane as the fuel. Although substitution of fuels cannot be made without changing other process conditions, a direct comparison of the exergy vs. lower heating values of H₂ and methane, indicates that the fuel is responsible for 1.4 GJ/tonne HVP in apparent exergy savings. The remaining 2.1-

2.4 GJ difference in the reactor/preheating sections between the CL-ODH and steam cracking cases is attributed to the significantly improved heat integration and elimination of steam dilution..

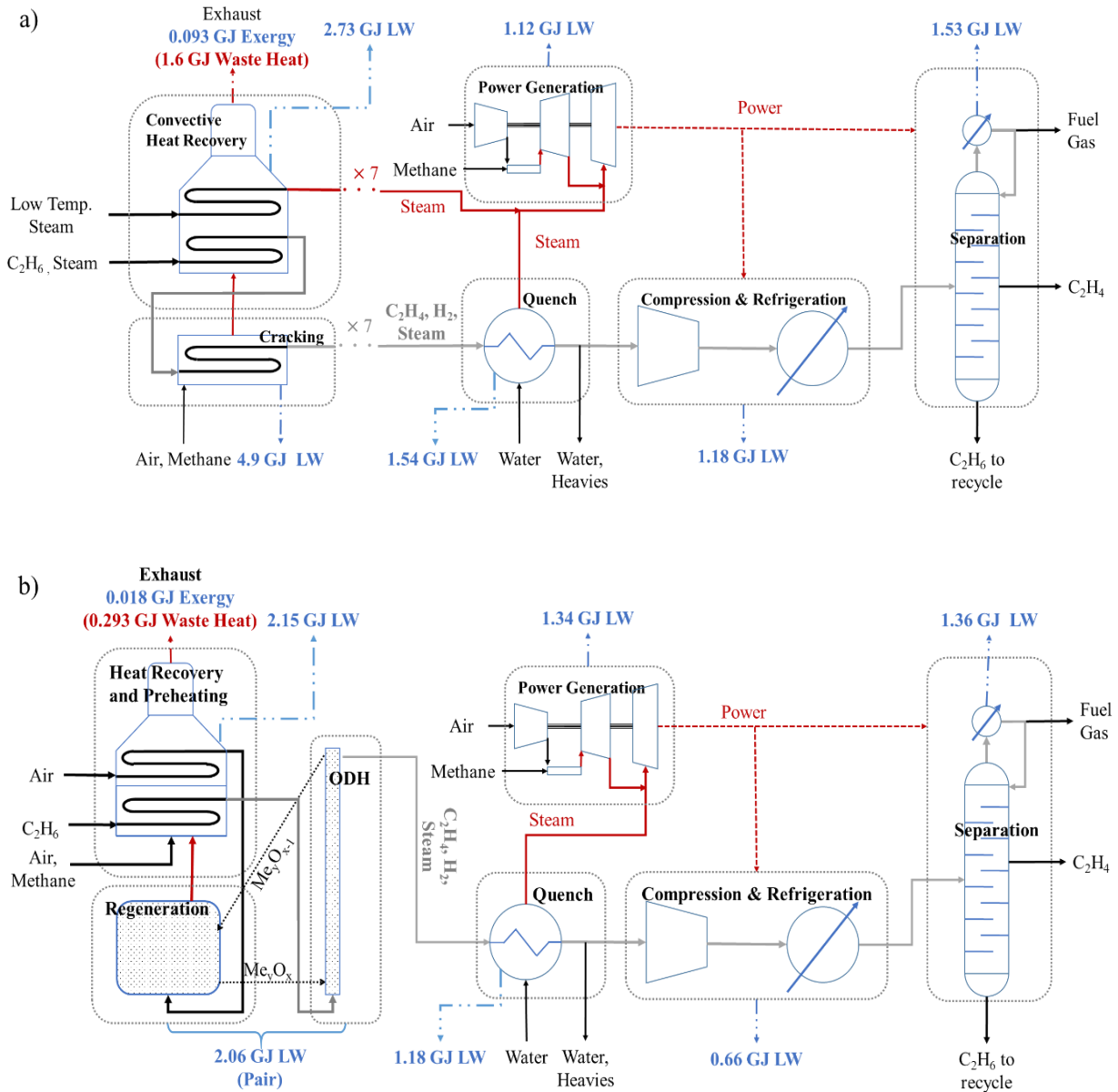


Figure 4.14: Process schematic and exergy/lost work (LW) schematic of a) Steam cracking of ethane and b) CL-ODH of Ethane [Results are in GJ/tonne of high value products (HVP)].

Of particular note is the large temperature differential of 350 °C between the radiant zone of fire box, and the highest temperature inside the cracking coils. This corresponds to a major irreversibility. In contrast, CL-ODH directly utilizes the sensible heat in the oxygen carrier particles to supply the heat required for ethane cracking, thereby minimizing the irreversibility

The exergy savings of CL-ODH in the downstream of the process is relatively straightforward. This is illustrated in **Table 4.12** and **Figure 4.14**. The removal of hydrogen as condensed water in CL-ODH prominently reduces the volume of gas that must be compressed and refrigerated (37 % volume reduction). Combined with a higher per-pass yield, the quench, compression, and refrigeration sections in CL-ODH can result in up to a 0.9 GJ/tonne HVP reduction in exergy loss. It is notable that, in spite of the higher overall downstream power demand, the exergy loss in the power generation section of steam cracking appears to be less than that of the ODH cases. This results from the need to burn more fuel directly for power generation in ODH due to less heat recovery from the CL-ODH reactors. The improved power generation in steam cracking does not offset the large exergy losses in the furnace. When exergy losses in the pre-heating/heat recovery and quench are included in power generation, ODH reduces exergy loss by 0.44-0.97 GJ/tonne HVP (**Table 4.12**) in these sections.

Exergy savings for CL-ODH in the separation sections are more limited than in the upstream. This is attributed to a combination of: a) the need for CO removal prior to acetylene hydrogenation, and b) the inherently heavy separation demands imposed by polymer-grade ethylene. The ODH reaction product contains sufficiently high CO to poison the catalyst used for acetylene removal via selective hydrogenation^[27,34]. This necessitates the placement of acetylene removal (the de-acetylenizer) after the de-ethanizer, requiring an additional heat exchange load. Polymer grade ethylene purity requirements (99.99%) impose a high exergy loss in the C2 splitter (**Table C11**).

This is the case even for the ODH 99 case with 99% ethane conversion (0.487 GJ/tonne HVP). This underscores the potential impact of membranes and other advanced hydrocarbon separation technologies on ethylene production.

4.10 Broader impact

4.10.1 CO₂ emission reduction

CL-ODH's higher exergetic efficiency also leads to substantial reduction in CO₂ emissions. A comparison of CO₂ emissions is given in **Table 4.13** and **Figure 4.15**. If fuel gas byproducts are exported without credit, steam cracking gives CO₂ emissions of 1.26 tonne/tonne HVP, consistent with other simulations in literature^[35].

Table 4.13: CO₂ production by source (tonne/tonne HVP).

		<i>Steam Cracking</i>	<i>ODH 85</i>
CO₂ Source	<i>Fuel Byproducts Burned*</i>	0.17	0.32
	<i>External Fuel Burned</i>	1.09	0.035
	<i>CO₂ from Reactor</i>	<i>N/A</i>	0.093
	<i>CO₂ Produced</i>	1.26	0.45
Credits	<i>H₂ Recovery Penalty</i>	0.094	0.027
	<i>Hydrogen Credit (LHV)⁺</i>	-0.47	-0.14
	<i>CO₂ Capture Credit</i>	<i>N/A</i>	-0.093
	<i>Net CO₂ Emitted</i>	0.88	0.19

**CO and methane, excludes hydrogen, to eliminate fuel effects on heat recovery fuel gasses are treated as a credit against methane, ⁺Calculated as CO₂ from methane vs. the same LHV of hydrogen.*

By comparison, ODH 85 emits only 0.45 tonne/tonne HVP, leading to a 64% reduction, as shown in **Table 4.13**. If the hydrogen is separated and recovered (at the cost of additional energy for pressure swing adsorption), it may be credited as a zero-carbon fuel against methane. Additionally, the ODH cases also capture CO₂ in the product separation section, which, if beneficially utilized or sequestered, reduces the CO₂ emissions of the process. When hydrogen is credited as a byproduct (at LHV) and the 0.093 tonne of captured CO₂/tonne HVP in the ODH cases are credited, the ODH 85 emits 0.19 tonne of CO₂/tonne HVP. This represents a 78% reduction compared to steam cracking (0.88 ton CO₂/ton HVP). On a commercial scale, 1.5 million ton per annum (MTA) plant, this corresponds to a reduction of over 1 million tonnes of CO₂ each year.

Multiple justifiable assumptions can be made about the crediting of hydrogen as either a low carbon fuel or an industrial feedstock. For example, while hydrogen can be utilized as a low carbon fuel in conventional cracking, burning fuel-gas with high hydrogen concentrations can lead to high NO_x emissions,^[36] requiring costlier emissions control. Additionally, in highly integrated areas, hydrogen can be a valuable feedstock, for processes such the production of low sulfur fuel via hydrodesulfurization^[37,38] In this case of integrated chemical use, crediting hydrogen at a rate consistent with displacing steam methane reforming is reasonable (using 9 kg CO₂/kg H₂^[39]). However, while the various values of the hydrogen byproduct credit can affect the absolute value of the overall net CO₂ emissions, it does not change the overall trend between cases. For lower credits, the purification and transportation challenges for hydrogen can make it less carbon intensive to burn the hydrogen as a fuel rather than export it. The trend in CO₂ emissions is consistent with the energy demand and exergy loss trends (CO₂ from Steam Cracking >> ODH 67 > ODH 85 > ODH 99), with the ODH 85 case giving a 60%-87% emission reduction, and the ODH 99 case giving a 65%-94% reduction, depending on the assumptions used (**Figure 4.15**).

This confirms that the CO₂ reduction of CL-ODH is not an artifact of “fuel substitution” (H₂ vs. CH₄). The ability to burn hydrogen without NO_x, while still providing some usable H₂, represents another advantage of CL-ODH.

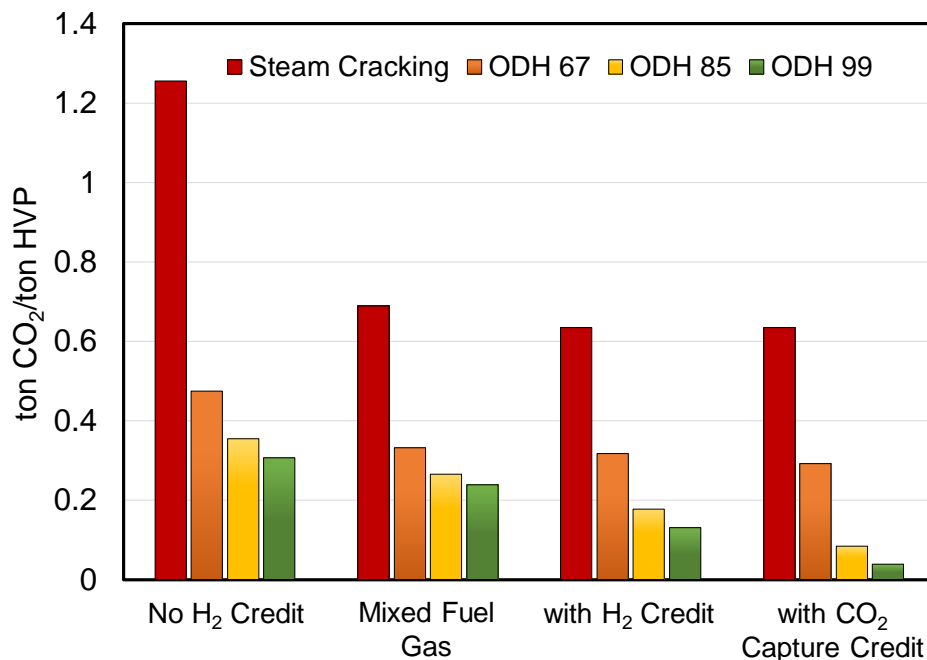


Figure 4.15: CO₂ emissions of Steam Cracking and ODH processes under various assumptions:

- i) **No H₂ Credit:** H₂ is recovered and exported but not credited
- ii) **Mixed Fuel Gas:** H₂ is not recovered and is burned along with CO and CH₄ as fuel
- iii) **with H₂ credit:** H₂ is recovered and credited at 9 kg CO₂/kg H₂ ^[39]
- iv) **CO₂ Capture Credit:** H₂ is recovered and credited at 9 kg CO₂/kg H₂ and CO₂ recovered from ODH product stream is beneficially utilized and not emitted.

Fuel gas and mixed fuel gas are calculated as a credit against methane burned to eliminate fuel composition effects on flue gas heat recovery. The Mixed Fuel Gas, ODH 99 case exports unused fuel gas at no credit.

4.10.2 Transforming ethylene production

Several alternative ethylene production technologies have been investigated to tackle the upstream exergy losses (**Figure 4.16**). Oxidative coupling of methane (OCM) (Reaction 4.5), which

converts methane to ethane, ethylene and water in a set of net-exothermic reactions, has received renewed attention due to the abundance of inexpensive natural gas produced from North American shale.^[40–45] However, the low single pass ethylene yields (< 20% ethylene) and considerable ethane byproduct^[43–45] require intensive downstream separation and recycle of unconverted methane and ethane. **Figure 4.17** maps the performance of these alternative routes with respect to ethane steam cracking, which includes ODH (Reaction 4.2), CL-ODH (Reaction 4.3 and 4.4) along with OCM.



Technology	Industrially Proven	Equilibrium Limited	Steam Dilution	Reaction Endotherm*	Separation Load
Steam Cracking (Reaction 4.1)	Y	Y	Y	143 kJ/mol	High
OCM (Reaction 4.5)	N	N	N	-280.3	Very High
ODH (Reaction 4.2)	N	N	N	-105.5	**
CL-ODH (Reaction 4.3 & 4.4) (This study)	N	N	N	Neutral/ Negative	Low

**per mol ethylene
**Air separation can induce large parasitic losses, and limited single pass conversion at low dilution

Figure 4.16: Comparison of ethylene production techniques (Y is Yes and N is No).

The CL-ODH process eliminates the challenges of traditional ODH and OCM.^[17,33,46] At an industrial scale, this will be carried out in a circulating fluidized bed (CFB) system with continuous circulation of redox catalyst particles. Compared to conventional ODH, CL-ODH can improve the ethylene yield and process safety while eliminating the costly and energy intensive cryogenic air separation step.

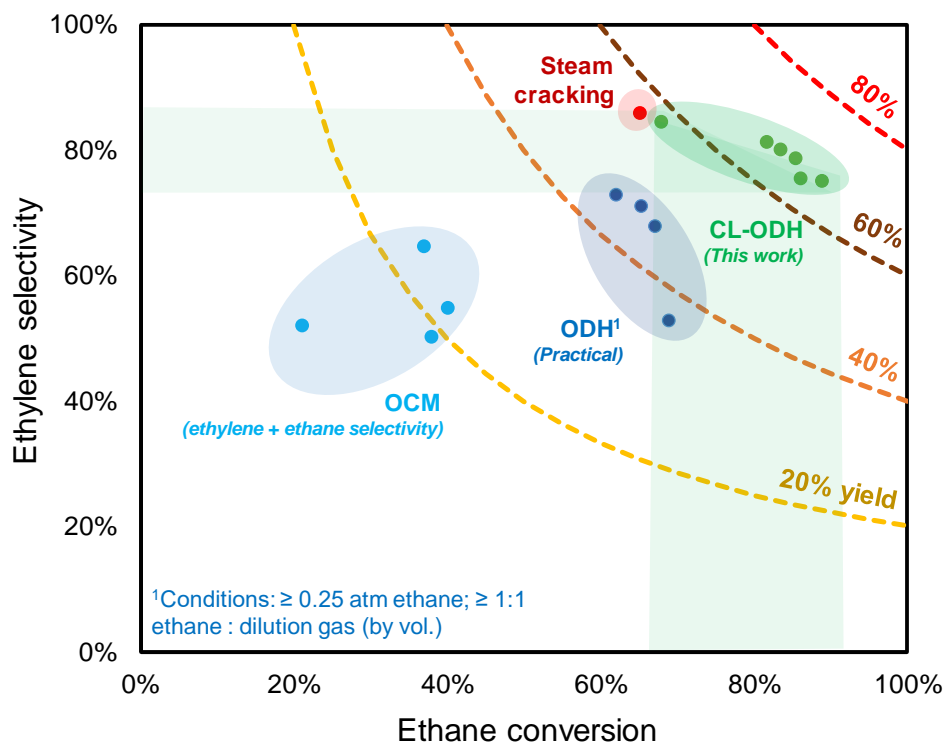


Figure 4.17: Representative ethylene selectivity vs ethane conversion chart.

4.11 Conclusion

In spite of decades of process optimization and high thermal (1st law) efficiency, steam cracking is an energy and carbon intensive process. The present study compares a redox ethane ODH or chemical looping ODH (CL-ODH) process with the traditional steam cracking process. Redox ODH is net exothermic due to selective combustion of H₂ byproduct. The use of Mn based redox catalyst under a cyclic redox scheme eliminates the needs for air separation. The exothermicity of the regenerator and the available energy from the hot regenerator exhaust enable the upstream section of the ODH process to be 115.2 MW_{th} exothermic as compared to 218.9 MW_{th} net endothermic for a cracker. For the same ethylene throughput, ethane ODH with 85% single-pass ethane conversion results in 32% less molar flow. This translates to significant drop in compression work for downstream separations. Overall, the ODH reference case consumes 82% less energy

over cracking, i.e. steam cracking has an energy demand of 15.2 GJ/tonne ethylene whereas the ODH process demands 2.7 GJ/tonne ethylene. By burning all the fuel produced in the process (CO, H₂ and CH₄), the ODH case has 7.35 GJ_{th} excess fuel energy as compared to the cracking process, which has a 1.42 GJ_{th} deficit for every tonne of ethylene produced. The redox ODH process also provides 82% reduction in the CO₂ and NO_x emissions over steam cracking. Increase in single-pass ethane conversion for redox ODH can lead to further reduction in energy demand and less CO₂/NO_x emissions. The energy requirements for solids circulation in redox ODH lead to an energy-penalty of less than 0.6 GJ_{th} per tonne of ethylene produced. Although substantial efficiency improvement of steam cracking, which is already 95% thermally efficient, is not possible based on conventional wisdom, we show that ethylene production can be significantly intensified in CL-ODH via exergy loss minimization. To summarize, redox ODH represents a potentially attractive option for ethylene production with significantly reduced pollutant emissions and energy consumptions. These findings not only support the feasibility of CL-ODH but also provide a useful guidance to design intensified chemical production processes with significantly lowered emissions. If adopted at a global level, this innovative process can reduce annual CO₂ emissions by over 100 million tonnes for ethylene production.

4.12 Acknowledgements

We acknowledge the funding support from Advanced Research Project Agency-Energy (ARPA-E) of the US Department of Energy (Grant DE-AR0000327), Kenan Institute, and EcoCatalytic Technologies LLC.

4.13 References:

- [1] *Res. Mark.* **2015**.
- [2] S. Seifzadeh Haghighi, M. R. Rahimpour, S. Raeissi, O. Dehghani, *Chem. Eng. J.* **2013**, 228, 1158.
- [3] J. A. Moulijn, M. Makkee, A. E. Van Diepen, *Chemical Process Technology*, John Wiley & Sons, **2013**.
- [4] *Forecast of Global Supply and Demand Trends for Petrochemical Products for the Period 2006 to 2019*, Ministry Of Economy, Trade And Industry (METI), Japan, **2015**.
- [5] Brelsford, Robert, *Oil Gas J.* **2014**.
- [6] H. Zimmermann, R. Walzl, in *Ullmanns Encycl. Ind. Chem.*, Wiley & Sons, **2009**.
- [7] *Res. Mark.* **2015**.
- [8] T. Ren, M. Patel, K. Blok, *Energy* **2006**, 31, 425.
- [9] C. A. Gärtner, A. C. van Veen, J. A. Lercher, *ChemCatChem* **2013**, 5, 3196.
- [10] F. Cavani, N. Ballarini, A. Cericola, *Catal. Today* **2007**, 127, 113.
- [11] I. A. Bakare, S. A. Mohamed, S. Al-Ghamdi, S. A. Razzak, M. M. Hossain, H. I. de Lasa, *Chem. Eng. J.* **2015**, 278, 207.
- [12] M. L. Rodríguez, D. E. Ardisson, E. López, M. N. Pedernera, D. O. Borio, *Ind. Eng. Chem. Res.* **2011**, 50, 2690.
- [13] M. M. Bhasin, J. H. McCain, B. V. Vora, T. Imai, P. R. Pujado, *Appl. Catal. Gen.* **2001**, 221, 397.
- [14] E. A. de Graaf, G. Rothenberg, P. J. Kooyman, A. Andreini, A. Bliet, *Appl. Catal. Gen.* **2005**, 278, 187.
- [15] N. Ballarini, F. Cavani, A. Cericola, C. Cortelli, M. Ferrari, F. Trifirò, G. Capannelli, A. Comite, R. Catani, U. Cornaro, *Catal. Today* **2004**, 91–92, 99.
- [16] R. M. Contractor, H. E. Bergna, H. S. Horowitz, C. M. Blackstone, B. Malone, C. C. Torardi, B. Griffiths, U. Chowdhry, A. W. Sleight, *Catal. Today* **1987**, 1, 49.
- [17] L. M. Neal, S. Yusuf, J. A. Sofranko, F. Li, *Energy Technol.* **2016**, 4, 1200.

- [18] L. Neal, S. Yusuf, J. Sofranko, F. Li, in *249th Natl. Meet. Am.-Chem.-Soc. ACS*, **n.d.**
- [19] P. Cho, T. Mattisson, A. Lyngfelt, *Fuel* **2004**, 83, 1215.
- [20] J. Adánez, L. F. de Diego, F. García-Labiano, P. Gayán, A. Abad, J. M. Palacios, *Energy Fuels* **2004**, 18, 371.
- [21] Z.-Y. Tian, P. Mountapmbeme Kouotou, N. Bahlawane, P. H. Tchoua Ngamou, *J. Phys. Chem. C* **2013**, 117, 6218.
- [22] R. Schefflan, *Teach Yourself the Basics of Aspen Plus*, American Institute Of Chemical Engineers, Hoboken, NJ, USA, **2011**.
- [23] A. J. Kidnay, W. R. Parrish, *Fundamentals of Natural Gas Processing*, CRC Press, **2006**.
- [24] G. T. Rochelle, *Science* **2009**, 325, 1652.
- [25] M. Yan, Simulation and Optimization of an Ethylene Plant, Texas Tech University, **2000**.
- [26] M. Ball, A. Basile, T. N. Veziroglu, *Compendium of Hydrogen Energy: Hydrogen Use, Safety and the Hydrogen Economy*, Woodhead Publishing, **2015**.
- [27] G. C. Battiston, L. Dalloro, G. R. Tauszik, *Appl. Catal.* **1982**, 2, 1.
- [28] S. Hall, **n.d.**
- [29] M. A. Fox, J. K. Whitesell, *Organic Chemistry*, Jones & Bartlett Learning, **2004**.
- [30] G. Hassan, M. Pourkashanian, D. Ingham, L. Ma, P. Newman, A. Odedra, *Comput. Chem. Eng.* **2013**, 58, 68.
- [31] L.-S. Fan, *Chemical Looping Systems for Fossil Energy Conversions*, Wiley-AIChE, Hoboken, NJ, **2010**.
- [32] S. M. Sadrameli, *Fuel* **2015**, 140, 102.
- [33] V. P. Haribal, L. M. Neal, F. Li, *Energy* **2017**, 119, 1024.
- [34] N. S. Schbib, M. A. García, C. E. Gígola, A. F. Errazu, *Ind. Eng. Chem. Res.* **1996**, 35, 1496.
- [35] M. P. Tao Ren, *Energy* **2006**, 31, 425.
- [36] M. İlbas, İ. Yılmaz, Y. Kaplan, *Int. J. Hydrog. Energy* **2005**, 30, 1139.
- [37] P. Grange, *Catal. Rev.* **1980**, 21, 135.

- [38] T. A. Pecoraro, R. R. Chianelli, *J. Catal.* **1981**, *67*, 430.
- [39] P. L. Spath, M. K. Mann, *Life Cycle Assessment of Hydrogen Production via Natural Gas Steam Reforming*, National Renewable Energy Lab., Golden, CO (US), **2000**.
- [40] S. Arndt, T. Otremba, U. Simon, M. Yildiz, H. Schubert, R. Schomäcker, *Appl. Catal. Gen.* **2012**, *425–426*, 53.
- [41] Y. T. Chua, A. R. Mohamed, S. Bhatia, *Appl. Catal. Gen.* **2008**, *343*, 142.
- [42] S. Jenkins, *Chem. Eng. N. Y.* **2012**, *119*, 17.
- [43] J. S. Ahari, M. T. Sadeghi, S. Zarrinpashne, *J. Nat. Gas Chem.* **2011**, *20*, 204.
- [44] T. W. Elkins, H. E. Hagelin-Weaver, *Appl. Catal. Gen.* **2013**, *454*, 100.
- [45] T. W. Elkins, H. E. Hagelin-Weaver, *Appl. Catal. Gen.* **2015**, *497*, 96.
- [46] S. Yusuf, L. M. Neal, F. Li, *ACS Catal.* **2017**, *7*, 5163.

**CHAPTER 5: MODULAR SCALE ETHANE TO LIQUIDS VIA CHEMICAL LOOPING
OXIDATIVE DEHYDROGENATION – REDOX CATALYST PERFORMANCE AND
PROCESS ANALYSIS**

is based on a manuscript published in *Journal of Advanced Manufacturing Processes, AIChE*
2019;1:e10015.

The supplementary information is in Appendix D

5.1 Abstract

The difficulties in liquefaction and transportation of ethane in shale gas has led to significant rejection, via reinjection or flaring, of this valuable hydrocarbon resource. Upgrading this low value, isolated ethane into easily transportable liquid fuels is a promising solution to this supply glut. In this study, we present a modular system that can potentially be operated economically at geographically isolated gas processing facilities. The modular ethane-to-liquids (M-ETL) system uses a chemical looping-oxidative dehydrogenation (CL-ODH) technology to convert ethane and natural gas liquids (NGLs) efficiently into olefins (primarily ethylene) via cyclic redox reactions of highly-effective redox catalyst particles. The resulting olefins are then converted to gasoline and mid-distillate products via oligomerization. CL-ODH eliminates air separation and equilibrium limitations for olefin generation. It also simplifies the process scheme and reduces energy consumption. Here we present experimental proof-of-concept data on CL-ODH conversion of ethane to ethylene. Using the CL-ODH performance data at 750 °C, we show that a simple, single-pass configuration can be economically viable at distributed sites. We identify that economic factors such as the capital cost, price of ethane feed, and value of electricity byproduct have strong effects on the required selling price of the liquids. It is also noted that the economic-viability of the M-ETL system is relatively insensitive to the liquids yield under a low ethane price scenario. The demand and value of electricity at distributed locations, on the other hand, can play an important role in the optimal process configuration and economics.

5.2 Introduction

Unlike heavier natural gas liquids, ethane is difficult to transport, and interstate pipeline specifications^[1] can limit the quantity of ethane that can be reinjected into natural gas. This makes the high ethane content of wet shale-gas a liability, leading to over supply at natural gas processing facilities. A typical new shale-oil well in the Bakken (1,500 mcf/day shale gas^[2]) can produce up to 170 bbl./day of ethane, of which a large fraction (50-60%) is rejected through reinjection (as a fuel) or flaring.^[3] Overall, approximately 660 Trillion BTU of ethane is rejected in the U.S. each year, leading to a significant waste of valuable resources.^[4] Considering the significantly higher volume based energy density and the transportability of liquid fuels, technologies that can effectively convert geographically isolated ethane and other natural gas liquids (NGLs) from shale-gas processing into liquid fuels are of great value to US shale-gas producers in geographically-isolated locations.

Unfortunately, ethane-to-liquids (ETL) technologies that are economically viable at a distributed scale have not been developed to date. From a technological standpoint, a conventional indirect gas-to-liquids process, which is based on hydrocarbon reforming and Fischer-Tropsch (F-T) synthesis, can be used for liquid fuel production from ethane or ethane-rich NGLs. However, it is subjected to a number of intrinsic limitations such as high capital cost and limited efficiency due to complex operations including reforming, air separation (for partial oxidation or PO_x), syngas conditioning, F-T, and product refining and upgrading. The process complexity dictates that indirect GTL is unlikely to be economically viable for distributed ethane conversion. Although the extensive attempts on modularization of reforming and F-T synthesis in “microchannel reactors” have led to significant progress to improve the reactor throughputs and reduce the process

footprint,^[5,6] these “small-scale” GTL technologies have yet to demonstrate economic feasibility at scales commensurate with distributed shale gas production/processing sites (150 – 500 BOE/day).^[2] Additionally, most of the GTL work to date focuses on methane-based feedstock. Although ethane would be easier to activate, high temperature C₂ chemistry could also exacerbate coking issues.

In the 1970 and 80’s, an oligomerization-based approach for liquid fuel production was developed. Rather than converting natural gas components to syngas as in F-T, this approach focused on oligomerization of light olefins such as ethylene and propylene into gasoline and mid-distillates.^{[7-}

^{11]} Atlantic Richfield Company (ARCO) explored an oligomerization-based GTL approach that involved oxidative coupling of methane (OCM) to upgrade methane into ethylene and subsequently to liquid fuels.^[7] While this work demonstrated the feasibility of oligomerizing complex ethylene-containing hydrocarbon mixtures from OCM, significant recycling of ethane and unconverted methane into the OCM reactor is necessary to achieve reasonable liquid yields. Recent research effort has focused on the heterogeneous oligomerization of pure ethylene, using ‘immobilised’ versions of the transition metal catalysts found in traditional homogeneous processes, like the Shell Higher Olefin Process.^[12] The most notable are Nickel complexes, supported on crystalline aluminated-silicas such as Al-SBA-15 or Al-MCM-41,^[13] and amorphous or crystalline alumino-silicates, such as Siral-30 and Zeolite Beta, respectively.^[14] Nickel species existing in these catalysts are generally considered to be isolated Ni ions in framework exchange positions. The processes tend to be low temperature (150-200 °C) and high pressure (10-20 atm) in nature. They have proven to be capable of high ethylene conversion (>95%) and favourable selectivity towards fuel-range olefins, at realistic WHSV’s of 0.375 hr⁻¹.^[15] Although

oligomerization of ethylene (and propylene) is relatively well studied, the low ethylene yield from OCM hinders the technical and economic feasibility of the oligomerization-based GTL approach.

Compared to methane, ethane is significantly easier for ethylene production. Steam-cracking, in which ethane is pyrolyzed into ethylene and hydrogen, is a mature technology that can achieve >55% single-pass yield in centralized plants.^[16,17] However, the high endothermicity for cracking reactions, high operating temperatures, tendency to form coke, and the complex cryogenic product separation schemes make it difficult to implement at distributed scales. Oxidative dehydrogenation of ethane (ODH) can be more conducive to small scale implementation than steam cracking. In this approach, the ethane is partially oxidized to ethylene and water. As a result, the ODH system can be exothermic and is no longer subjected to equilibrium limitations. However, gaseous oxygen is required for ethane conversion in traditional catalytic ODH approaches. This raises safety concerns. Moreover, the high cost for air separation would make a small system capital intensive.^[18,19] In this work, we present experimental results and process modeling of a chemical looping-ODH (CL-ODH) approach for modular scale ethane-to-liquids (M-ETL). Operated under a cyclic redox mode, CL-ODH uses lattice oxygen donated from a metal oxide oxygen carrier (also known as a redox catalyst) to efficiently convert ethane or ethane-rich NGLs into olefins (primarily ethylene). The redox catalyst, which functions as both a catalyst and a mass separation agent, significantly intensifies the ethylene production by facilitating: i. ethane conversion; ii. reactive oxygen separation; iii auto-thermal ODH operation with simplified product separation.^[20] We have previously reported multiple high performance CL-ODH oxygen carriers that give excellent selectivity and single pass olefin yield.^[21-24] Modeling work shows that, relative to conventional steam cracking, CL-ODH reduces the energy consumption and CO₂ emissions by up to 82%.^[20]

These studies, however, focus either on redox catalyst characterizations or process analyses for centralized (polymer-grade) ethylene production.

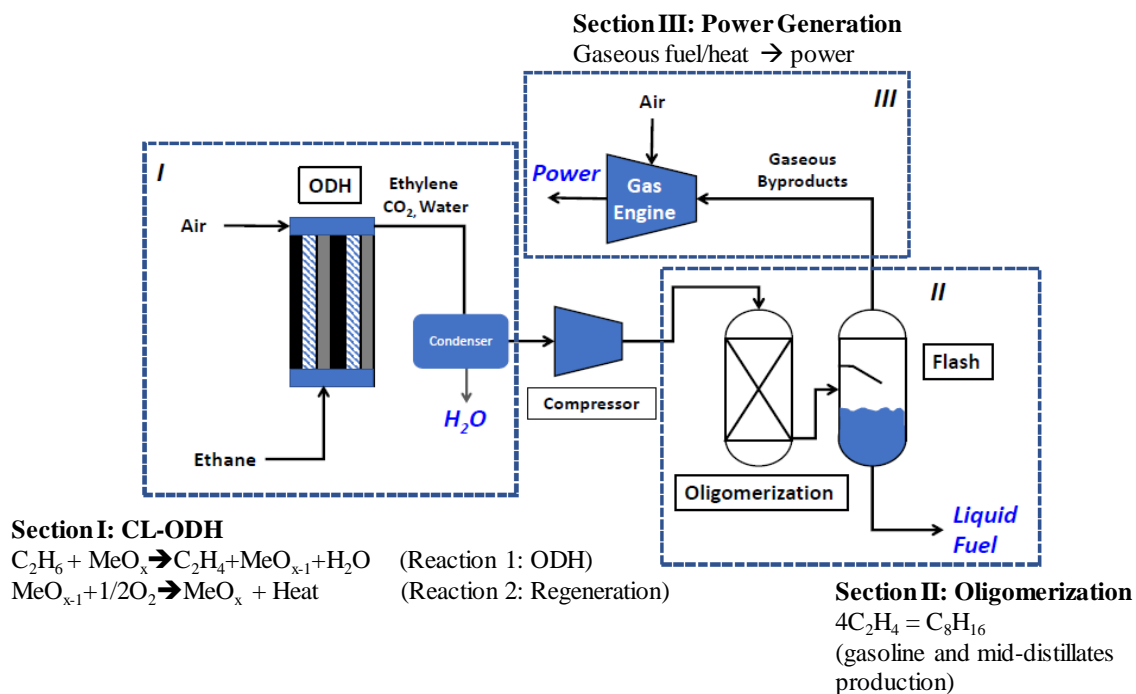


Figure 5.1: Simplified CL-ODH based M-ETL scheme.

Based on our recent progress in redox catalyst development, we propose an M-ETL scheme for distributed liquid fuel production from ethane. As illustrated in **Figure 5.1**, a multi-channel packed bed is used to convert ethane-rich gas into ethylene and water via CL-ODH (Section I). The ethylene is then converted to gasoline and mid-distillate products in an oligomerizer (Section II). A simple flash unit downstream of the oligomerizer is used to separate out the liquids. The gaseous products are subsequently combusted in a gas engine for on-site power generation (Section III). As can be seen, the system produces high-value, easily transportable liquids from the otherwise rejected ethane. Because it operates at relatively low temperatures, and eliminates unit operations such as air separation and/or water gas shift, it offers the potential for reduced cost and easier modular manufacturing than conventional GTL. The system may also be adapted to natural gas

liquids with high C3-C5 components, which are easier to convert to olefins under reaction conditions than ethane and would be more easily obtainable upstream of a gas processing plant. Moreover, both the electricity and water byproducts are very valuable near shale-gas production sites.

Table 5.1: Required selling price of a barrel of liquid product at an initial capital cost of \$100,000/daily barrel capital cost and 25% gross margins.

<i>Electricity Price (\$/MW-hr)</i>	\$0		\$24.00**		\$60.00	
<i>Ethane Price (\$/gal)</i>	\$0.00		\$0.05		\$0.10	
<i>CL-ODH Case</i>	Base	High	Base	High	Base	High
<i>Ethane cost (\$/bbl)</i>	\$0.00	\$0.00	\$10.09	\$8.24	\$20.19	\$16.48
<i>Cost of Capital* (\$/bbl)</i>	\$31.73	\$31.73	\$31.73	\$31.73	\$31.73	\$31.73
<i>25% Gross Margin (\$/bbl)</i>	\$10.58	\$10.58	\$13.94	\$13.32	\$17.31	\$16.07
<i>Electricity Credit (\$/bbl)</i>	\$0.00	\$0.00	-\$11.19	-\$6.02	-\$27.98	-\$15.06
<i>Required selling price of liquids (\$/bbl)</i>	\$42.31	\$42.31	\$44.57	\$47.27	\$41.25	\$49.22

*10% Annual ROI 20-year straight-line depreciation, with monthly compounding and amortization and \$0 residual value. The unit /bbl refers to per barrel of liquid product all cases

** Low end of wholesale pricing [32], 20% of approximate retail price of \$0.12/kW-hr

5.3 Summary of Results

Using experimental CL-ODH performance data, we show that this system can be economically attractive for distributed ethane-to-liquids. The CL-ODH catalyst we reported demonstrated >50% single pass C2+ yield. Coupled with oligomerization, up to 44% liquids yield can be realized without recycle. Preliminary economic analysis indicates that the system is capable of supporting a capital cost of >\$100,000/daily barrel under various ethane and electricity price scenarios and

selling prices of \$1.00-\$1.20/gal (**Table 5.1**). If sold as gasoline, this would be economically viable for the average gasoline prices over the past 5 years.^[25]

5.4 Materials and Methods

5.4.1 CL-ODH Catalyst Testing

To determine the product compositions from CL-ODH, a perovskite-based CL-ODH redox catalyst was tested in cyclic redox mode. Details with respect to the composition and synthesis methods for the perovskite based CL-ODH redox catalysts were reported in our previous publications.^[21,22,26] A summary of the synthesis procedures are is given in the supporting information. The activity and selectivity of the redox catalysts were determined in a quartz U-tube reactor with 1/8'' or 1/4" ID. In a typical experiment, 0.5 or 5.0 g of redox catalyst is loaded into the quartz U-tube, along with inert alumina grit to reduce the dead volume. The U-tube is placed into a benchtop tube furnace and insulated with ceramic fiber. An automated gas switching panel is used to switch between 80 vol.% ethane (balance Ar) and 20 vol.% oxygen (balance Ar). Ar purge is used between the reduction and oxidation steps to prevent the direct mixing between ethane and oxygen. Temperature was varied from 650-750 °C. The products were analyzed with an Agilent Refinery gas GC with FID for hydrocarbon quantification and He and Ar TCDs for permanent gas analysis. Further details with respect to the experimental set up can be found in our previous publications.^[22-24,27] The results at 750 °C and gas hourly space velocity (GHSV) of 600h⁻¹ (WHSV of 0.8 h⁻¹) and 120h⁻¹ (WHSV 0.016 h⁻¹) were used for modeling as base conversions (“Base”) and high conversion (“High”) case respectively.

5.4.2 Oligomerizer Product Distributions

Limited data is available in open literature for oligomerization of complex mixtures, such as those from CL-ODH. However, work by ARCO showed that oligomerization can be used in conjunction with OCM.^[7] Although OCM products consist of similar species, the limited performance data published by ARCO ^[7] cannot be easily extrapolated to the much higher concentrations of C2+ hydrocarbons in CL-ODH. As such, oligomerizer product distributions were estimated from literature data for pure ethylene oligomerization at 10 atm, 200 °C and a WHSV of 0.375 hr⁻¹ over a 4 Wt.% Ni/Siral-30 catalyst.^[15] This case was chosen as it favors C6-C10 hydrocarbons. To account for the dilution of non-ethylene components, our model uses a total pressure of 23 atm to achieve 10 atm partial pressure of ethylene (in the Base Case).

Table 5.2: Estimate of ethylene oligomerization product distributions from literature^[15,28] and Schulz-Flory distribution for C10+.

Data from <i>Lee et al.</i> , 200 °C, 10 atm of pure ethylene	
WHSV (hr ⁻¹)	0.375
Ethylene Conversion (%)	98
Component	Wt. %
1-butene	4.86%
trans-2-butene	10.80%
c-2-butene	11.34%
1-C6	32.00%
1-C8	23.00%
1-C10	10.80%
1-C12	5.40%
1-C14	1.80%

The data reported on Ni/Siral-30 did not indicate the distribution of C4 isomers, so this was estimated using data gained from ethylene oligomerization over a 2.6% Wt.% Ni-ALSBA-15 catalyst,^[28] (10 bar and 150 °C). The Ni/Siral-30 data also did not distinguish between C10+

oligomers. Therefore, a Schulz-Flory distribution was assumed. The resulting estimate is presented in **Table 5.2**. ARCO's work also indicates that some hydrogen will recombine to saturate the olefins, and some CO methanation will occur.^[7] Trace C3+ olefins in the CL-ODH product would also be expected to oligomerize. The treatment of the side reactions with CL-ODH impurities is given in the supplemental document.

5.4.3 Process simulation and Economic Analysis

ASPEN Plus® was used to model the CL-ODH-based M-ETL scheme (**Figure D1** in the supporting information). The various assumptions and models used are provided in **Tables D2 and D3**, and are consistent with our previous work.^[20] The ODH reactor was assumed to be operated adiabatically at 750°C and 1 bar, with the regenerator being at a higher temperature of 800°C, and the oligomerizer was at 150°C and 23 bar. Air was used to regenerate the redox catalyst and was maintained at 10% excess. Feeds (ethane and air) to the two reactors were preheated to 500°C. Heat integration was utilized in the system where the hot outlet from the ODH reactor was used to preheat the feed-ethane along with the oligomerizer-input. The output of the ODH reactor was cooled to 100°C, before compressing it to 23 bar, which results in a $P_{C_2H_4}$ (ethylene partial pressure) of 10 bar for the Base Case. The oligomerizer-output was cooled and flashed to room temperature at 5 bar to separate the liquid fuel from gaseous byproducts. The “vapor” phase from the flash is combusted in a spark ignition engine to generate electrical power (25% fuel-to-electrical efficiency).

For preliminary required selling price analysis, a capital cost target of \$100,000/ per daily barrel production capacity is used. Due to number-up scaling of both CL-ODH reactor tube bundles and the modular system, the capacity cost is assumed to scale linearly. The cost of capital was calculated as amortization of the M-ETL unit price per daily barrel at a 10% annual interest rate

(i.e. 10% ROI) paid monthly over 240 months (20 years) with no residual value. The cost of capital per bbl. was assigned as the total of yearly amortization divided by yearly capacity. The cost of capital and feeds are divided by 0.75 to apply a 25% gross margin. The gross margin on cost of capital is approximated to cover maintenance, labor, and downstream treatment of liquids, and the margin on feed is estimated to cover related financial costs. Electricity credits are applied after the gross margin.

5.5 Discussion

5.5.1 Product distributions of CL-ODH and oligomerizer

Table 5.3 shows two representative product distributions for “low-temperature” (750 °C) CL-ODH with single pass C₂+ olefin yields of >50% (carbon-basis). The “Base” conversion case (600 h⁻¹ GHSV) maintains high C₂+ Selectivity (92%), whereas the “High” conversion case (120 h⁻¹ GHSV) has higher single-pass C₂+ yields (60% vs 52%) at lower olefin selectivity (82%). The decrease in selectivity is mainly attributable to the formation of additional CO₂. The higher conversion does not result in higher C₃+ products, in contrast to our previously reported high temperature (>800 °C) systems.^[20,24] This can be attributed to facile deep oxidation of easier to activate higher hydrocarbons combined with the relatively low operating temperature, which limits C₃+ formation through gas phase reactions. The High Case also has a lower concentration of combusted hydrogen. However, both systems combust enough hydrogen to maintain thermal sufficiency in CL-ODH, as shown by our simulations.

Table 5.3: CL-ODH Product distributions (water free basis).

<i>Percentage</i>	<i>C%</i>		<i>Wt. %</i>	
	<i>Base</i>	<i>High</i>	<i>Base</i>	<i>High</i>
<i>Conversion Case</i>	<i>Base</i>	<i>High</i>	<i>Base</i>	<i>High</i>
GHSV	600 h ⁻¹	120 h ⁻¹	600 h ⁻¹	120 h ⁻¹
Carbon Dioxide	2.16%	9.47%	6.30%	24.21%
Carbon Monoxide	0.00%	0.25%	Trace	0.44%
methane	2.24%	2.89%	2.67%	2.69%
hydrogen	NA	NA	0.55%	0.07%
ethane	43.47%	27.32%	43.27%	23.81%
ethylene	48.52%	56.09%	45.08%	45.63%
acetylene	0.11%	0.00%	0.09%	0.00%
propane	0.14%	0.28%	0.13%	0.24%
propylene	1.06%	1.88%	0.99%	1.53%
methyl acetylene	0.02%	0.06%	0.02%	0.05%
n-butane	0.20%	0.01%	0.19%	0.01%
1-butene	0.11%	0.01%	0.10%	0.01%
trans-2-butene	0.04%	0.12%	0.04%	0.10%
c-2-butene	0.07%	0.00%	0.06%	0.00%
1,3-butadiene	1.60%	0.36%	0.27%	0.28%
C5	0.06%	0.10%	0.05%	0.07%
Benzene	0.20%	1.16%	0.17%	0.88%

5.5.2 Product Analysis and Process Configurations

The inputs and outputs of the M-ETL system, when operated in a single-pass mode, are given in **Figure 5.2a**. In the High Case, which corresponded to 60% C₂+ yield (carbon basis), 44.4% of the feed ethane LHV was captured in the liquid fuel products. Accounting for the inherent ~15% energy degradation in ethane ODH and oligomerization to liquids, it represents >50% of ideal

energy conversion. Considering that this yield number was obtained in a single-pass scheme without the cycle of gaseous products, it can be quite attractive due to the simplicity. The higher CO₂ yield in the High Case partially offsets compressor load decrease due to lowered product volume, giving a similar compression load of 0.9 kWh (electric) /gal. vs. 0.95 kWh/gal. in the Base Case.

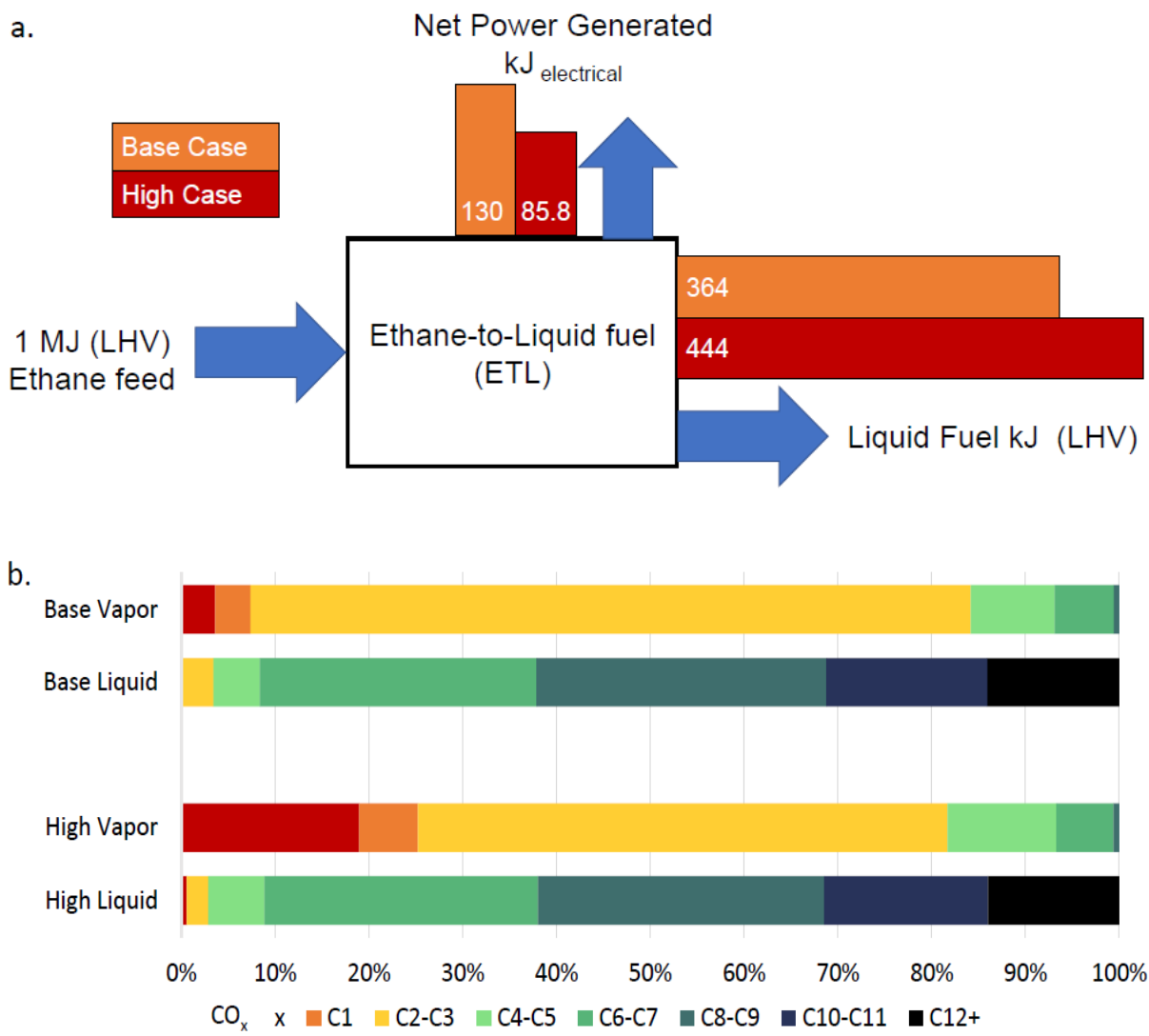


Figure 5.2: a) Product distributions in the single-pass case per 1 MJ of ethane feed for both the Base Conversion Case and High Conversion Case; b) Composition (carbon basis) of gaseous and liquid fractions from the post oligomerization flash.

The products from the oligomerizer were estimated using the CL-ODH product distributions (See **Table D1** in the supporting document). The carbon product distributions from the post flash liquids and vapor streams are provided in **Figure 5.2b**. The product distributions of the liquids are quite similar between the two cases, as ethylene oligomerization was responsible for most liquid products. With flash conditions (5 atm, 25 °C), the liquid fraction contains ~8% C2-C4, which is not practical for conventional liquid transportation fuel. However, the relatively high value and easy liquefaction of C4's could make these products viable, especially if an NGL processing facility is available. Alternatively, these components could be recovered and recycled into either the ODH reactor or into the oligomerizer feed to improve yield of C5+ liquids, at the cost of increased process complexity. The oligomerizer could also be pushed to a higher single-pass conversion, although it would skew the system towards higher C12+ yields and increase the size and/or pressure of the oligomerizer.

Analysis of the “vapor” phase from the flash shows that the “High” conversion case has more methane and CO_x as well as a high ratio of C3+ to Ethane (Fig. 2b). The relatively high CO₂ could create concerns for both recycle and combustion for electricity cogeneration. High CO₂ in gaseous fuels can lower the efficiency of the engine.^[29] While acceptable efficiency can be achieved with 32 vol. % CO₂ of the “High” conversion case, its aggressive recycle ratios (>50%) could require costly CO₂ removal. The lower CO₂ and methane of the Base Case are conducive to recycle. It does, however, have a higher concentration of hydrogen (9.2% vs 0.48 vol% in the “High” case). This could lower the productivity of the CL-ODH reactor if hydrogen combustion is not facile enough.

5.5.3 Preliminary Techno-economic Analysis

The required selling price (RSP) of the liquids is dependent upon capital costs, cost of ethane, and value of electrical cogeneration credit. For low-cost/isolated ethane scenarios, the price is dominated by capital costs, as the economics are relatively insensitive to ethylene selectivity at low ethane costs. Both High and Base Cases can support nearly a \$100,000 per daily barrel capital cost with an RSP of \$1.00/gal. and ethane costs of \$0.05 with a \$24/MWh electricity credit (**Figure 5.3a**).

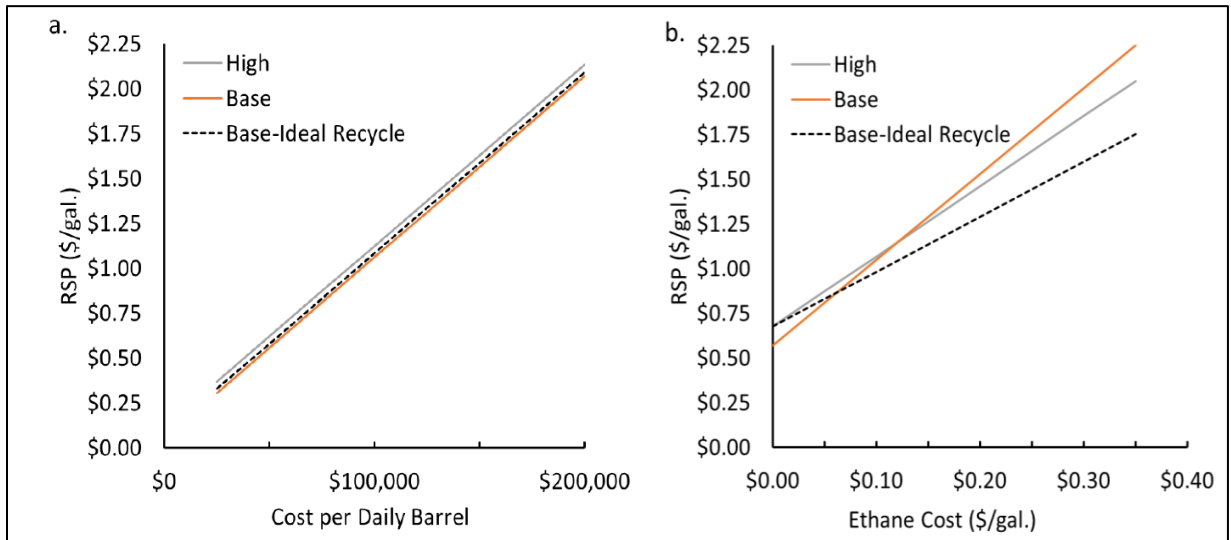


Figure 5.3: Required selling price of liquids assuming \$24/MWh electricity cost, 10% ROI, and 25% gross margins a) vs. capital cost of the system at \$0.05/gal. ethane, and b) vs. the cost of ethane at a capital cost of \$75,000/daily barrel. “Base-Ideal Recycle” case assumes constant conversions a pass of the “vapor” through a second unit.

The ultimate liquid yield has relatively little effect on the RSP even when “ideal recycle” is considered (Fig 3, a 28% increase in yield). The insensitivity to ultimate yield is partially created by the decreased amount of electricity generated in higher liquid yield cases. As will be discussed below, the ability to utilize all electricity produced may not be a reasonable assumption. However,

the low sensitivity to liquids yield indicates that maintaining low capital costs is generally more important than minor increases in liquids yield. While more significant differences in the RSP of the cases is observed at \$0.30/gal. ethane (Mont Belvieu Hub, Jan 2019 ^[30], Fig 3b), such a high price is unlikely at distributed production sites or gas processing plants. For low or zero cost ethane, the systems are likely to be profitable, even an additional cost is incurred for downstream processing to make the liquids marketable (e.g. hydrogenation and/or fractionation). The system economics are also highly dependent upon the value of the electricity credit in the cases presented. Electrical cogeneration creates valuable electricity without lowering the accumulation of methane, hydrogen, CO₂, and/or C3-C6 hydrocarbons in the recycle stream. Both cases export a significant amount of electricity (466 and 251 kWh/bbl. liquids for the Base and High cases respectively). In the Base Case, when the price ratio of electricity to liquid fuel is above 45:1 \$/kWh electricity: \$/gal. liquids, it would be more profitable to produce electricity instead of liquids (see **Figure 5.4a**).

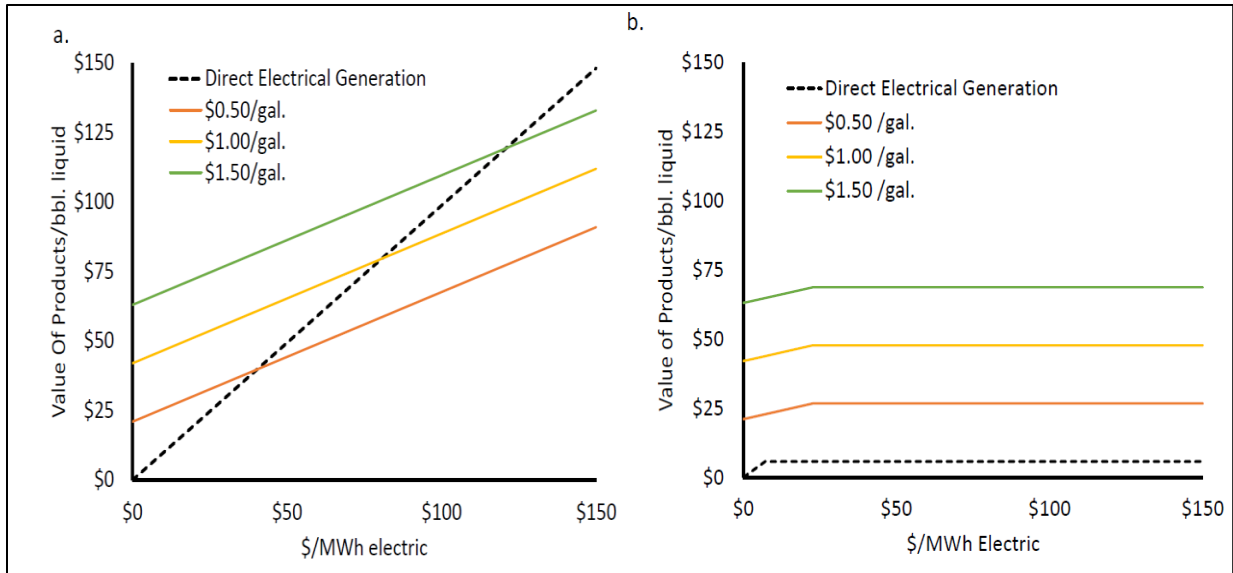


Figure 5.4: a) Value of products per bbl. liquids produced in the “Base” case vs price of electricity credit and liquid fuels price; b) Value of products per bbl. liquids produced vs. liquids vs. value of electricity when the electricity credit is capped at \$5.76/bbl.

Given that a simple generator would likely have much lower capital costs than the modular ethane-to-liquid system, power generation could be justifiable at even lower price ratios. However, this assumes a large, near-site demand, whereas the demand at distributed sites is likely to be strongly inelastic. Although drilling/fracking can entail significant short-term demands, a single well pump may consume only 20 kW of electricity.^[31] For a new well in the Bakken producing ~170 bbl./day of ethylene, the High Case would co-generate 454 kW of electricity (10.9 MWh/day). The output of less than 25 wells would be sufficient to supply the entire power load of a 20 MW^[31] gas-processing plant. Further, detailed analysis of electricity demand and value at isolated sites is needed to fully evaluate the economics of the M-ETL system. However, recycle to achieve higher liquids yields is likely necessary, even with nominally high electricity prices. For example, if we impose an order of magnitude estimate of a maximum demand of 0.5 kW/bbl. ethane per day, and electricity is valued at ~\$0.12/kw kW-hr., the maximum electricity credit obtained would be

\$5.76/bbl. This would limit the value of products to \$47.76/bbl. at \$1/gal (See **Figure 5.4b**), and make the system economics more sensitive to ultimate liquid yields.

5.6 Conclusions

The modular-ethane to liquids (M-ETL) technology presented in this study has the potential to be economically attractive for the intensification of liquids production from isolated ethane and ethane rich LNGs. Based on the experimental results obtained on chemical looping – oxidative dehydrogenation (CL-ODH) of ethane, up to 44% liquid fuel yields (on an LHV basis) can be achieved in a relatively simple, single-pass system. The ability of CL-ODH to achieve high ethylene yields under an auto-thermal operation, via *in-situ* oxygen separation, is a key to simplify ethane conversion. With discounted ethane price at isolated sites, preliminary economic modeling suggests that the M-ETL process can be economically feasible at \$1.00/gallon selling price with capital costs of up to \$100,000/daily barrel. Due to its simplicity and the compatibility of the “low-temperatures” CL-ODH with modular reactors, this capital expenditure is potentially feasible. In addition to capital costs, the value of co-generated electricity has a strong effect on the value of the products, and the required selling price of the liquids. We have also identified that further analysis is needed to determine both the demand and the value of electricity at isolated sites.

5.7 Acknowledgments

We acknowledge the DOE-RAPID Institute for funding this research (DE-EE007888-05-6).

5.8 References

- [1] M. M. Foss, **n.d.**, 52.
- [2] “U.S. Energy Information Administration (EIA),” can be found under <https://www.eia.gov/petroleum/drilling/>, **n.d.**
- [3] “OUTLOOK '16: Exports to boost US ethane,” can be found under <https://www.icis.com/>, **n.d.**
- [4] E. Gue, “Midstream MLPs: The Best Way To Ride The U.S. Petrochemical Wave,” can be found under <https://seekingalpha.com/article/4042473-midstream-mlps-best-way-ride-u-s-petrochemical-wave>, **2017**.
- [5] S. R. Deshmukh, A. L. Y. Tonkovich, K. T. Jarosch, L. Schrader, S. P. Fitzgerald, D. R. Kilanowski, J. J. Lerou, T. J. Mazanec, *Ind. Eng. Chem. Res.* **2010**, *49*, 10883.
- [6] S. LeViness, S. R. Deshmukh, L. A. Richard, H. J. Robota, *Top. Catal.* **2014**, *57*, 518.
- [7] A. M. Gaffney, *Hydrocarbon Production*, **1989**, US4849571A.
- [8] R. J. Quann, L. A. Green, S. A. Tabak, F. J. Krambeck, *Ind. Eng. Chem. Res.* **1988**, *27*, 565.
- [9] H. Owen, S. A. Tabak, B. S. Wright, *Process for Converting Olefins to Gasoline, Distillate and Alkylate Liquid Hydrocarbons*, **1986**, US4633027A.
- [10] S. A. Tabak, *Two Stage System for Catalytic Conversion of Olefins with Distillate and Gasoline Modes*, **1984**, US4433185A.
- [11] H. Owen, P. B. Venuto, *Upgrading Refinery Light Olefins with Hydrogen Contributor*, **1977**, US4012455A.
- [12] W. Keim, *Angew. Chem. Int. Ed.* **2013**, *52*, 12492.
- [13] M. Lallemand, A. Finiels, F. Fajula, V. Hulea, *Appl. Catal. Gen.* **2006**, *301*, 196.
- [14] S. Moussa, P. Concepción, M. A. Arribas, A. Martínez, *ACS Catal.* **2018**, *8*, 3903.
- [15] M. Lee, J. W. Yoon, Y. Kim, J. S. Yoon, H.-J. Chae, Y.-H. Han, D. W. Hwang, *Appl. Catal. Gen.* **2018**, *562*, 87.
- [16] H. Zimmermann, R. Walzl, in *Ullmanns Encycl. Ind. Chem.*, Wiley-VCH Verlag GmbH & Co. KGaA, **2000**.

- [17] M. P. Tao Ren, *Energy* **2006**, *31*, 425.
- [18] W. F. Castle, *Int. J. Refrig.* **2002**, *25*, 158.
- [19] A. R. Smith, J. Klosek, *Fuel Process. Technol.* **2001**, *70*, 115.
- [20] V. P. Haribal, L. M. Neal, F. Li, *Energy* **2017**, *119*, 1024.
- [21] Luke Michael Neal, Fanxing Li, Yunfei Gao, *Oxygen Carrying Materials with Surface Modification for Redox-Based Catalysis and Methods of Making and Uses Thereof*, **n.d.**, PCT/US2018/037570.
- [22] Y. Gao, L. M. Neal, F. Li, *ACS Catal.* **2016**, *6*, 7293.
- [23] L. M. Neal, S. Yusuf, J. A. Sofranko, F. Li, *Energy Technol.* **2016**, n/a.
- [24] S. Yusuf, L. M. Neal, F. Li, *ACS Catal.* **2017**, *7*, 5163.
- [25] CNBC, “@RB.1: 1.3894 0.00 (0.00%) – Stock Quote and News - CNBC,” can be found under <https://www.cnbc.com/quotes/?symbol=@RB.1>, **n.d.**
- [26] Junshe Zhang, Fanxing Li, Luke Michael Neal, *Redox Catalysts for the Oxidative Cracking of Hydrocarbons, Methods of Making, and Methods of Use Thereof*, **n.d.**, PCT/US2017/051157.
- [27] R. B. Dudek, X. Tian, M. Blivin, L. M. Neal, H. Zhao, F. Li, *Appl. Catal. B Environ.* **2019**, *246*, 30.
- [28] R. D. Andrei, M. I. Popa, F. Fajula, V. Hulea, *J. Catal.* **2015**, *323*, 76.
- [29] A. B. Wasiu, Abd. Aziz, M. R. Heikal, *J. Appl. Sci.* **2012**, *12*, 2346.
- [30] “Mont Belvieu Ethane (OPIS) Futures Quotes - CME Group,” can be found under <https://www.cmegroup.com/content/cmegroup/en/trading/energy/petrochemicals/mont-belvieu-ethane-opis-5-decimals-swap.html>, **n.d.**
- [31] KJL Inc., **2012**.
- [32] “Electricity Monthly Update,” can be found under https://www.eia.gov/electricity/monthly/update/wholesale_markets.php, **n.d.**

**CHAPTER 6: INTENSIFICATION OF ETHYLENE PRODUCTION FROM NAPHTHA
VIA A REDOX OXY-CRACKING SCHEME – PROCESS SIMULATIONS AND
ANALYSIS**

is a reprint of a manuscript published in *Engineering 4* (2018) 714–721.

The supplementary information is in Appendix E.

6.1 Abstract

Ethylene production by thermal cracking of naphtha is an energy intensive process (up to 40 GJ_{th}/tonne ethylene), leading to significant formation of coke and NO_x along with 1.8-2 kg of CO₂ emission per kg of ethylene produced. We propose an alternative process for redox oxy-cracking (ROC) of naphtha. In this two-step process, hydrogen from naphtha cracking is selectively combusted by a redox catalyst with its lattice oxygen first. Subsequently, the redox catalyst is re-oxidized by air and releases heat, which is used to satisfy the heat requirement for the cracking reactions. This intensified process reduces parasitic energy consumptions as well as emissions of CO₂ and NO_x. Moreover, formation of ethylene and propylene can be enhanced resulting from selective combustion of hydrogen. In this study, the ROC process is simulated with ASPEN Plus® based on experimental data from recently developed redox catalysts. Compared to traditional naphtha-cracking, the ROC process can provide up to 52% energy and CO₂ savings. The upstream section of the process consumes approximately 67% less energy while producing 28% more ethylene and propylene for every kg of naphtha feedstock.

6.2 Introduction

Ethylene is one of the most important organic materials and a building block to produce fibers, plastics and other chemicals. The world ethylene production capacity was around 148 million tonnes/year in 2014, representing a 32% increase over the past decade ^[1]. At present, ethylene is almost exclusively produced via steam cracking of gaseous and liquid hydrocarbon feedstocks such as ethane, naphtha, and gas oil. Due to its high endothermicity and complex product separations steps, steam-cracking ranks among the most energy-intensive processes in the chemical industry. While ethane is the most common feedstock for cracking in the US and Middle

East, more than 80% ethylene produced in Europe and the Asian-Pacific region is from naphtha [2,3].

Naphtha is a mixture of hydrocarbons in the boiling point range of 30–200°C. In naphtha based steam cracking processes, naphtha is first fed into the convective section of the furnace for preheating and vaporization. At elevated temperatures in the radiant section of the furnace (750–900°C or higher), naphtha is cracked into smaller molecules in absence of catalysts. The gaseous light olefins are formed via reactions involving free radicals [4,5]. Steam cracking is highly endothermic and requires significant external heat input. Coke deposition, which is inevitable in the complex cracking reaction scheme, represents another significant challenge. Diluting the feed with steam lowers the propensity of coke formation. However, the cracking furnaces still need to be periodically shutdown and regenerated with air to avoid the accumulation of coke. The parasitic energy consumption due to steam-usage and the need for periodic shutdown result in an increase in capital and operating costs. [6,7]. From an energy consumption standpoint, the pyrolysis section accounts for approximately 2/3 of the total process energy required in naphtha steam crackers, and it leads to about 3/4 of the total exergy destructions [3]. Furthermore, large amounts of CO₂ is generated in this process due to the needs to combust carbonaceous fuels to satisfy the parasitic energy requirements. Therefore, novel technologies that address these shortcomings of steam cracking are highly desirable.

Oxidative cracking of naphtha in the presence of a heterogeneous catalyst represents a promising option [8–10]. The high reactivity of the olefins; however, poses a challenge in identifying a suitable catalyst with high selectivity [11]. Moreover, the oxygenate byproducts are difficult to separate [6]. The flammability of the gaseous mixture containing oxygen and fuels in a single step also imposes safety concerns. Hot spots can result from over-oxidation of the alkanes and olefins to CO and

CO₂, lowering the product selectivity^[3,12,13]. The current study investigates a two-step, redox oxy-cracking (ROC) process for naphtha conversion in an O₂-free environment. The first step involves selective oxidation of the hydrogen produced from hexane cracking with active lattice oxygen in a mixed-oxide redox catalyst. The redox catalyst particles, which enter the reactor at high temperatures, provide the sensible heat to compensate the endothermicity of the cracking reactions. Meanwhile, the catalyst is reduced in this step. The reduced redox catalyst is subsequently regenerated (and reheated) in air to complete the redox loop. The absence of gas phase oxygen in the naphtha conversion step has the potential to i. inhibit the non-selective reaction pathways; ii. reduce the potential safety hazards^[13-15]; iii. decrease parasitic energy losses by eliminating air separation unit and providing tighter temperature control^[16]. The overall process also significantly decreases the energy consumptions and hence NO_x and CO₂ emissions. Despite of its advantages over steam cracking and conventional oxy-cracking, this novel ROC approach has yet to be investigated in detail.

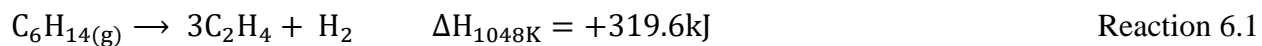
We recently reported a chemical looping – oxidative dehydrogenation (CL-ODH) approach for ethylene production from ethane using operational principles similar to those of ROC^[17,18]. The redox catalyst development, performance, reaction mechanism, and overall process efficiency were investigated^[17-19]. However, these studies were limited to ethane conversion. Oxidative cracking of n-hexane to olefins using lattice oxygen of VO_x/Ce-Al₂O₃ has been investigated, showing up to 60% olefin selectivity at 30% n-hexane conversion^[11]. The performance of sol-gel synthesized Li/MgO for oxidative cracking of hexane in the presence of gaseous oxygen, with 28% hexane conversion and 60% selectivity to light olefins was also shown^[8]. The same authors further studied an integrated plasma-Li/MgO system to improve the oxidative conversion of hexane at a relatively low temperature of 500°C^[9]. Although the integration of plasma was

effective to reduce the operating temperature, light olefin yield was still limited to about 35%. Overall, existing oxy-cracking processes have demonstrated relatively low olefin yields (<35%). Moreover, studies on oxy-cracking of naphtha via the chemical looping scheme are limited. In the current study, a detailed process simulation and analysis is conducted to investigate the performance of the ROC process. Experimental data obtained from a novel redox catalyst composed of alkali doped mixed oxides were used in the simulation [20]. Single-pass hexane conversions of 79% with 61% light olefin selectivity were achieved in a lab scale reactor. The experimental results were used in the process simulation and the performance of the ROC process was compared with a state-of-the-art naphtha steam cracking process. Using ASPEN Plus®, the effect of reactor and process conditions were investigated. The potential advantages of the ROC process were validated using the detailed process analyses. When compared to the steam cracking process, the net energy demand of the upstream section of the ROC reference case (79% naphtha conversion) was shown to drop by 67% along with 25% less compression work. This leads to a 52% drop in the overall energy demand and corresponding reduction in CO₂ emissions when compared with the conventional cracking process.

6.3 Process descriptions

Naphtha is the refinery hydrocarbon fraction with the boiling point range of 35–180°C and can vary in composition depending on source and refinery conditions. It is a complex mixture of hydrocarbons ranging from straight-chain alkanes to aromatics. One of the major components of naphtha is n-hexane, Reaction 6.1 illustrates one of the representative cracking reactions of n-hexane to ethylene. In addition to its high endothermicity, vaporization of naphtha can also be energy consuming – enthalpy of vaporization for hexane at 298K is 359 kJ/kg. A simplified process

flow diagram for the conventional naphtha steam cracking process is shown in **Figure 6.1a**. As the first step, pre-heated naphtha is thermally cracked in the presence of steam. Since naphtha cracking is equilibrium limited and tends to form coke, steam is used as a diluent to enhance naphtha conversions and to inhibit coke formation. In the cracking step, naphtha is passed through the tubes of the cracking furnace. The furnace is operated at high temperatures (~1,000°C), the heat for the endothermic cracking reactions is provided by the combustion of fuels. . The furnace consists of a radiant zone, where the cracking reaction occurs at >750 °C, and the convective zone, where the feed pre-heating takes place at up to 650 °C. The product stream is approximately at 800°C. Using transfer line heat exchangers, the stream is rapidly quenched to 300-400°C. This avoids further cracking and preserves the product compositions. As the product contains significant amounts of heavy hydrocarbons, a primary fractionator is installed to remove tar and oily material (boiling point > 200 °C) from the cracked gases. The product is further quenched to near ambient temperature to remove the heavies. This is followed by a multi-stage compression system to raise the pressure of the lighter gaseous products to around 40 bar. Drying and acid gas removal units are present at the intermediate compressor stages, as they need to be operated at high pressures. An adsorption column of molecular sieves facilitates the drying, followed by a caustic-wash to remove the acid gases such as CO₂. The formation of hydrates is prevented by having the drying unit before the caustic wash ^[2].



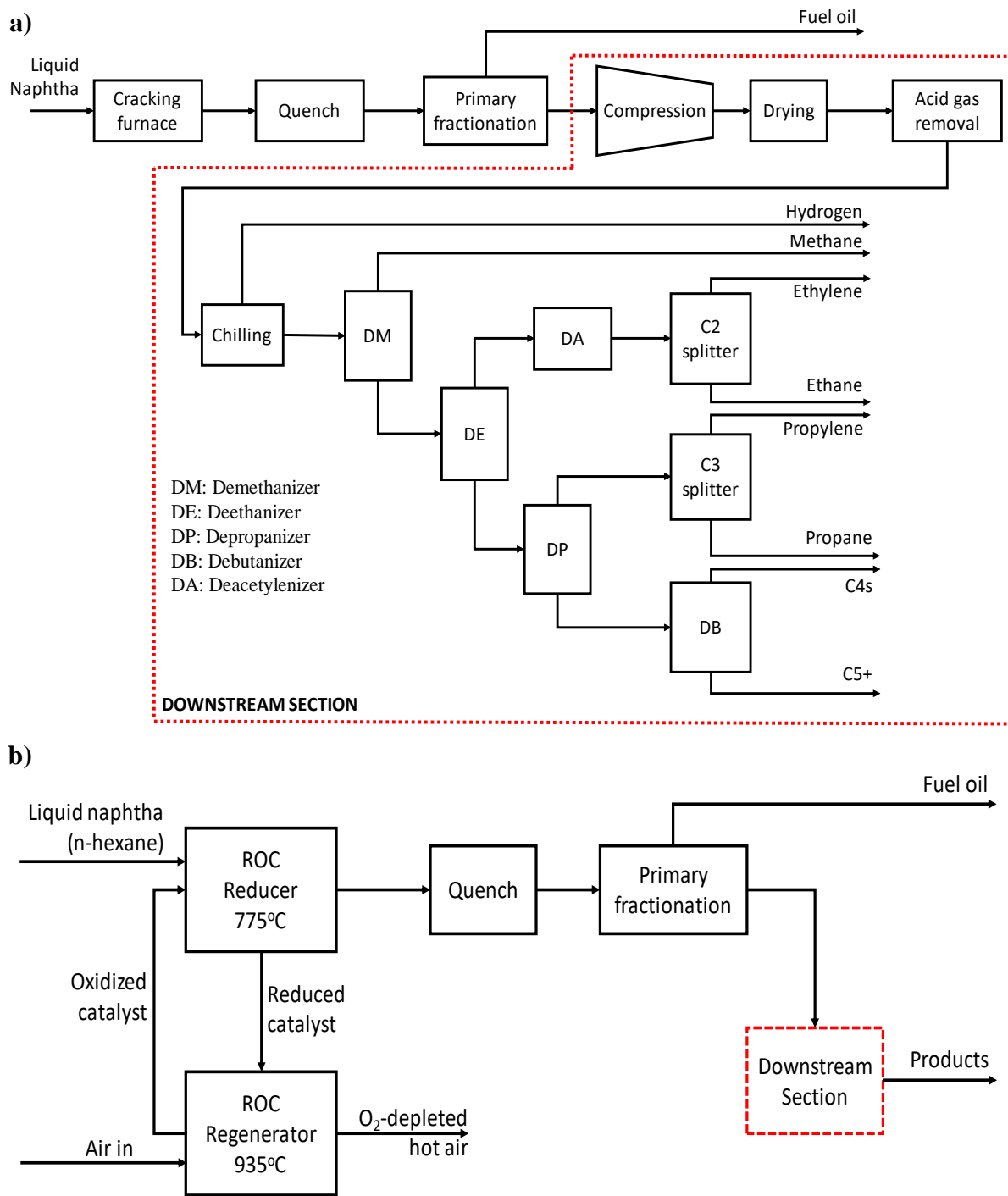
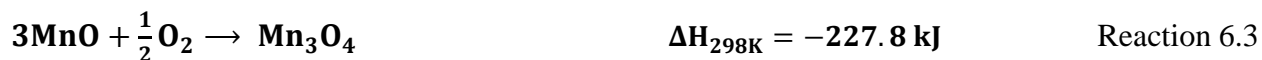


Figure 6.1: a) Simplified process flow diagram of naphtha cracking process b) Simplified schematic of the ROC process.

The light components, from the compressed stream, are sequentially separated from the heavy fractions using a separation train of distillation columns to ultimately yield high purity ethylene and propylene. At the beginning of the sequence, methane and lighter components, primarily hydrogen, are separated from higher molecular mass components, using a demethanizer (DM). A deethanizer (DE) column separates acetylene, ethane, and ethylene from the DM-bottom product. The distillate of the DE is treated with hydrogen to convert acetylene to ethylene, and then fractionated in the C2-splitter to generate the ethylene product. The C3+ components exit at the bottom of the DE, which is further purified in a depropanizer (DP) to separate the C4+ components. The debutanizer (DB) separates the C4 materials, raw pyrolysis gasoline, C5 materials and aromatics from the bottom of a DP^[2]. The C3-splitter follows the DP and recovers propylene as a valuable product.

Figure 6.1b depicts the naphtha ROC process. A reactor-regenerator scheme is used instead of the energy-intensive furnaces. Experimental product distribution for the ROC scheme using an alkali doped Ca-Mn based oxide similar to that reported in our previous work^[20], are used in the current work. For the ASPEN Plus[®] simulations, an oxide mixture containing CaO and MnO_x is used since the specific mixed-oxide is not available in the ASPEN database. Mn₃O₄ is used as the simulated oxygen carrier phase, which donates its lattice oxygen during the ODH reaction. Mn₃O₄ is reduced to MnO following Reaction 6.2. Naphtha gets converted to a variety of products, but for simplicity, Reaction 6.2 uses n-hexane to ethylene as the model reaction, which involves the combustion of hydrogen to water. In a regenerator, the reduced redox catalyst, also known as an oxygen carrier, is replenished with air via Reaction 6.3 (highly exothermic). ASPEN Plus[®] database values indicate that the surrogate catalyst exhibits similar heat of reaction and heat capacity values when compared to the actual redox catalysts. In the current work, the reducer is operated at 775°C and

the regenerator at 935°C, both at near-atmospheric pressure. The re-oxidized redox catalyst particles are recirculated to the reducer to complete the redox loop. The redox catalyst provides both the necessary lattice oxygen and heat required for ROC reactions. The naphtha and the air are pre-heated to 650°C. The hot, oxygen-depleted air from the regenerator is used to generate high pressure steam to compensate parasitic energy requirements. The gaseous output from the reducer passes through a series of downstream separation units similar to steam cracking. For CO₂ removal, an amine scrubbing unit is required for the ROC process as it produces more CO₂ than traditional cracking. The heat requirements of the reducer and naphtha pre-heating are sufficed by the heat stored in the re-oxidized solids, owing to their high heat capacity and temperature difference (ΔT) between the reducer and regenerator. The reducer is endothermic whereas the regenerator is exothermic. The reducer-regenerator system is operated under adiabatic conditions. The cracking furnace constitutes a major share of the total energy requirement, which is replaced by the ROC reactors, thereby reducing the energy demand. In the following sections, the ROC process is compared with naphtha cracking based on the overall energy requirements.



6.4 Simulation assumptions

The performance of ROC is evaluated and compared with naphtha steam cracking using the ASPEN Plus[®] simulator [21]. Two kinds of naphtha feeds are used to model the cracking process: a) a complex naphtha consisting of a variety of hydrocarbons, based on literature data, b) n-hexane. Since n-hexane is a major component of naphtha, the process model can be significantly simplified

provided that results from n-hexane feed provide reasonable representation of those using the complex feed. The composition of the complex naphtha is shown in **Figure 6.2**, which has been optimized to mimic ‘true’ naphtha. For simplicity of the model, pure n-hexane is used as a representative compound for naphtha in the ROC process. ASPEN Plus® modules, property methods, and physical property databanks are summarized in **Table 6.1**, whereas **Table 6.2** lists the carbon yields for the various processes. The cracking results are based on literature data ^[2,22], whereas those of ROC are experimental results were given in our previous work ^[20]. A higher hexane-conversion case has also been considered, where 97% of the hexane is assumed to get converted in the ROC process. Experiments on blank hexane cracking and the ROC case revealed roughly 30% increase in ethylene and propylene yield, for the ROC. Keeping the CO_x yield similar to the base ROC case, the ethylene and propylene yields have been proportionally increased for the high ROC case, with the overall hexane conversion being 97%. The other products were assumed to have yields similar to the base ROC. This hypothetical high ROC case’s product distributions are given in **Table E3**.

The drying unit and the primary fractionator are modeled as flash columns, where almost all of the water is condensed along with the heavy hydrocarbons. To simulate the acid gas removal (AGR) unit, a Sep block is used, with the energy consumption accounted for. It is placed at the exit of the compressor. The solids used in the simulation include Mn₃O₄ and MnO with CaO added as an inert to mimic the actual redox catalyst ^[20]. **Table 6.3** lists the key operating conditions and simulation assumptions.

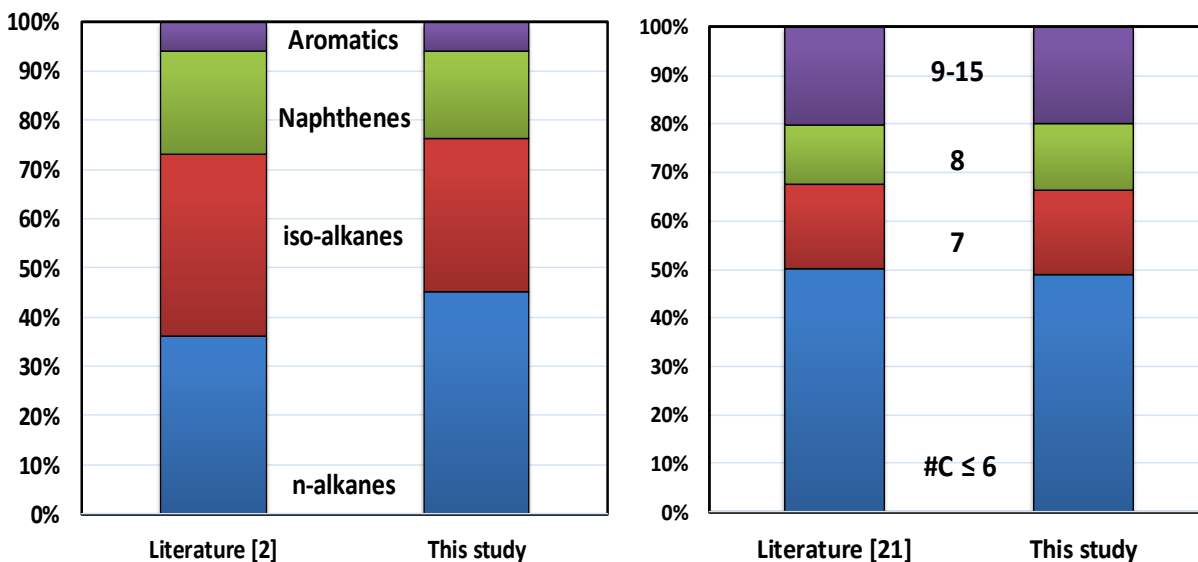


Figure 6.2: Composition to represent complex naphtha, a) based on [2] and b) based on [22].

Table 6.1: ASPEN Plus® modules, property methods and databanks.

Stream class	MIXCISLD
Databank	PURE, AQUEOUS, SOLIDS, INORGANIC
Solid components	Mn ₃ O ₄ , MnO, CaO
Property method	PR-BM and STEAM –TA for steam cycles
Unit operation models	
Regenerator, Reducer and Deacetylenizer	RStoic
Cracking reactor/furnace	RYield
Pressure changers	MCompr
Heat exchangers	Heater
Distillation columns	DSTWU
Separators/Flash columns	Sep/Flash2

Table 6.2: Carbon yields for the cases investigated.

Component	%C yield		
	Complex Feed	Hexane Feed	ROC
Hydrogen	0.0	0.0	0.0
Methane	11.5	9.6	7.7
Acetylene	0.7	0.6	0.3
Ethylene	27.3	27.3	32.0
Ethane	3.3	2.8	2.1
Propadiene	0.8	0.7	0.0
Propylene	12.3	10.3	16.2
Propane	0.3	0.2	0.6
C4s	0.2	0.2	0.0
Butadiene	4.1	3.4	4.0
Butene	2.8	2.4	7.5
Butane	0.2	0.1	0.1
Benzene	13.3	11.2	0.2
Toluene	2.6	2.2	0.0
Xylene	1.0	0.9	0.0
Ethyl benzene	0.4	0.3	1.8
Styrene	1.3	1.1	0.0
Naphthalene	0.0	0.0	0.0
n-pentane	4.4	1.7	1.5
n-hexane	1.1	18.0	21.4
iso-heptane	3.1	1.7	0.0
iso-octane	2.5	0.8	0.0
cyclohexane	3.2	0.8	0.0
TMB	1.1	0.9	0.0
Dodecane	2.5	3.0	0.0
CO	0.0	0.0	1.3
CO ₂	0.0	0.0	3.4
Naphtha conversion	82% ¹	82% ²	79% ²

¹Equal conversions of all the feed components were assumed listed in Table 6.1; ²Conversion of n-hexane

In both the complex and hexane feed cases, the hydrocarbon feedstock is introduced to the cracker furnace after being preheated to 650 °C along with steam. A steam-dilution of 0.5 kg/kg fresh feed is used ^[2]. A same preheating temperature is used in the ROC case without steam dilution. In the process simulation, the Mn₃O₄-containing redox catalyst particles are initially fed into the reducer, from the exit of which they are transported to the regenerator. The regenerator is maintained at 935°C, with the reducer at 160°C lower. In the regenerator, the reduced oxygen carrier is fully oxidized in 10% excess air, preheated to 650°C, via Reaction 6.3, prior to the recirculation to the reducer for another redox loop. Based on the product distribution in **Table 6.2**, the ROC involves the combustion of 75% of H₂ to H₂O.

To prevent further cracking, the product gases in all the cases are quenched to a temperature of 100°C. Heat released from the rapid cooling process is assumed to be completely utilized to generate steam and to preheat the ethane and air feeds. The exothermicity of the reactor-regenerator system can also produce low pressure steam and reduce the upstream energy demand. The cooled gases are compressed to 25 bar and flashed at 100°C, to remove the heavy hydrocarbons and water from the stream. In the present model, this compressor, with the flash column, functions as the primary fractionator. The light stream is further compressed to a pressure of 42 atm ^[2] using a 4-stage isentropic compressor. The primary component of acid gas is assumed to be CO₂, with no H₂S present. Negligible energy consumption is assumed for the caustic wash. For the ROC, where there is substantially more CO₂ in the product stream, an amine scrubbing process is assumed with an energy consumption of 0.11 MW-hr/tonne CO₂ ^[23]. **Table 6.4** lists the operating conditions of the downstream columns, for the cracking process ^[24]. The compressed stream is cooled to -100°C prior to methane removal in the demethanizer. This refrigeration step reduces the load on the demethanizer by removing most of the hydrogen and CO. A single pass is

assumed in all the cases. The reflux ratio for each column is fixed as twice that of the R_{min} . For direct comparison, the C2-splitters in both cases are modeled with the same number of stages and with the same recovery. A deacetylenizer is used to hydrogenate the acetylene in the overhead stream of deethanizer and is integrated after the deethanizer. Purified hydrogen for acetylene hydrogenation is obtained through pressure swing adsorption (PSA). A 80% hydrogen recovery is assumed, with the purity being 99% and a pressure drop of 1 bar ^[25].

For process comparison, the different forms of energy such as thermal energy, steam, and electricity are converted into a same thermal basis. An HHV efficiency of 85% is considered for the thermal to steam energy conversion, whereas 40% (HHV) efficiency is considered for thermal to mechanical energy conversion ^[3]. Using the condenser and reboiler duties of the columns, as calculated by ASPEN Plus[®], the power needed for refrigeration is calculated using the power-temperature graph as given in literature ^[26]. The refrigerants chosen for each unit are listed in

Table 6.4.

Table 6.3: Simulation conditions and assumptions.

Ambient condition	T = 25°C, P = 1 atm
Reaction assumptions	As per the carbon yield distribution in Table 3
Chemical looping reactor operating pressure	1 atm
Deacetylenizer operating pressure	42 atm
Compressor specifications	4 stage with intercooler at 25°C Isentropic efficiency of 0.72
Air feed (to the regenerator)	10% excess
Discharge temperatures to the environment	Temperature: 25°C
Thermal energy to steam efficiency	85%
Thermal energy to electric energy efficiency	40%

Table 6.4: Details of the distillation columns^[24].

Unit	Key component recoveries		Reflux ratio	Pressure (bar)		T°C required /Refrigerant
	Light/ Heavy Key	Recovery Heavy%/ Light%		Condenser	Reboiler	
Demethanizer	Methane/ Ethylene	99.90/ 0.50	3	26	27	-95/ Ethylene
Deethanizer	Ethylene/ Propane	99.99/ 0.10	0.6	10	11	-43/ Ethane
Depropanizer	Propylene/ iso-butylene	99.99/ 1.40	4.6	10	11	25/ Propylene
C2-splitter	Ethylene/ Ethane	99.00/ 0.06	2.7	4	11	-76/ Ethylene
C3-splitter	Propylene/ Propane	99.60/ 0.24	18	16	18	34/ Propylene
Debutanizer	Iso-butane/ Butadiene	99.90/ 0.10	8.6	4	5	32/ Propylene

6.5 Results and discussion

6.5.1 Effect of feed compositions

Using the product distribution shown in **Table 6.2**, both the complex naphtha and pure n-hexane feed were simulated for the conventional steam cracking process. **Figure 6.3** shows the similarities in the properties of the two feeds. Typically, a naphtha cracking unit has an overall energy demand in the range of 20-40 GJ_{Thermal}/tonne ethylene^[3]. **Table 6.5** illustrates the overall and unit-wise energy distribution of the two cases with the complex and n-hexane feeds. As can be seen, the results from pure n-hexane feed are very similar to those with the complex naphtha feed. This indicates that n-hexane can be a suitable model compound for naphtha without compromising the

accuracy of the simulation results. **Figure 6.3** breaks down the energy consumptions for section relative to the overall energy demand for both pure n-hexane and complex feedstocks. Again, close agreement was obtained. For process analysis purpose, we consider both the ethylene product and the High Value Products (HVPs). The latter is consisted of C2+ olefins and aromatics.

Table 6.5: Overall and unit-wise energy distribution for complex naphtha and n-hexane feed.

Unit/Section		Complex feed	n-hexane feed
Upstream (MW)	Reactor (Endothermicity)	8.04	8.72
	Feed pretreatment	7.80	8.27
	Steam heat	6.85	7.19
	Quench	-8.53	-9.17
	Primary fractionation	9.68	10.44
Downstream (MW)	Compressor	3.66	4.03
	Demethanizer	0.40	0.45
	De-ethanizer	0.00	0.00
	Depropanizer	0.16	0.14
	C2-splitter	1.16	1.13
	C3-splitter	0.49	0.40
	Debutanizer	0.01	0.01
	Deacetylenizer	0.08	0.09
	CO ₂ scrubbing	0.00	0.00
	PSA	0.03	0.03
	Chilling	0.79	0.74
Upstream		23.84	25.44
Downstream		6.77	7.02
Total		30.6	32.5
HVPs (kg/kg ethylene)		3.1	3.2

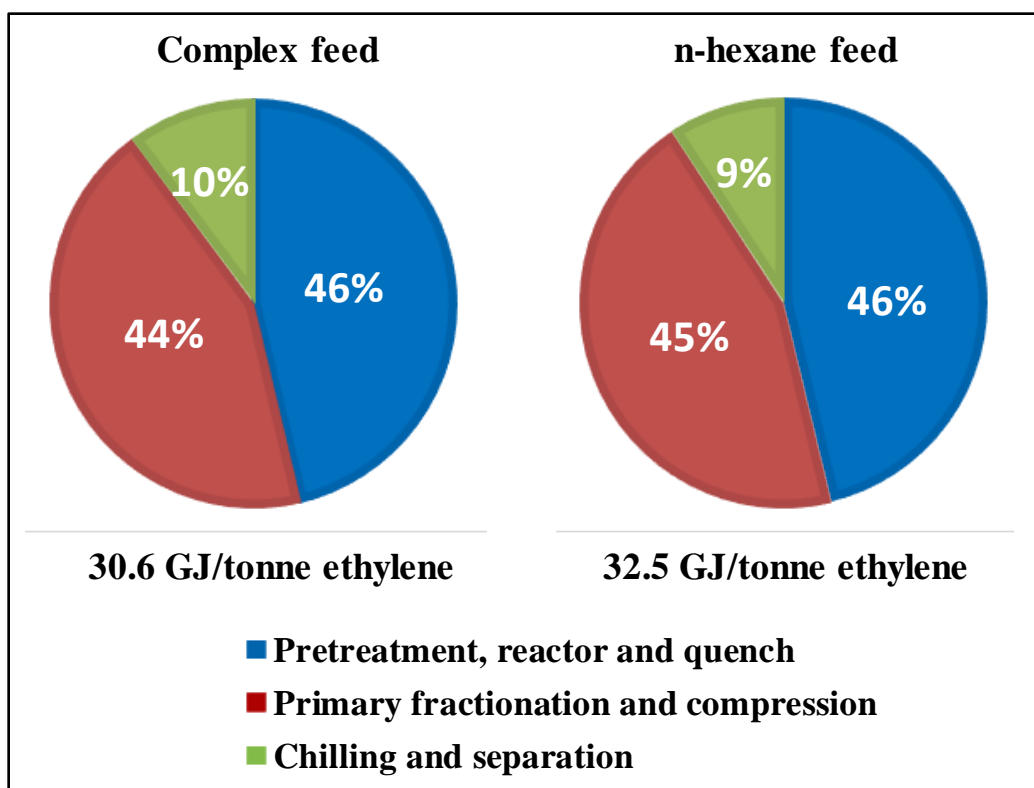


Figure 6.3: Section-wise energy distribution for naphtha cracking.

6.5.2 Energy distributions in steam cracking

Considering the similarities of the results from n-hexane and complex feeds, n-hexane is used to represent naphtha in the rest of the studies. ASPEN Plus® simulation of naphtha cracking process indicates an energy consumption of 32.5 GJ/tonne ethylene. This is in agreement with the study of Ren et.al ^[3] which states an energy consumption range of 20-40 GJ/tonne ethylene. For the cracking process, 78% of the total energy is required in the upstream section of the process. Quenching of the hot gases generates high pressure steam and recovers additional energy. The compression step corresponds to 57% of the overall downstream energy consumption, while the refrigeration for the demethanizer feed and the C2 splitter consume 17% and 16% of the downstream energy respectively with the C2-splitter being the most energy-intensive separation column.

6.5.3 Process comparisons

As shown in **Table 6.3**, the conversions are comparable for the cracking and ROC base cases, but the ROC process offers a 28% increase in the combined ethylene and propylene yield, which are the main products of the process. **Figure 6.4** shows the section wise energy distributions in naphtha cracking process and the ROC case. **Table 6.6** lists the energy distributions for the two processes. The cracking process requires the energy-intensive furnace, which contributes about 27% of the overall energy demand. They are replaced by the reducer-regenerator system in the ROC case, which is operated based on cyclic redox reactions (Reactions 6.2 and 6.3). The regenerator replenishes the oxygen in the carrier via the highly exothermic Reaction 6.3. The oxygen-lean hot air leaving the regenerator is used to generate high pressure steam, and is counted as available upstream energy in the ROC case. As the reactors are operated adiabatically, the upstream and overall energy requirements for the ROC case are reduced significantly. The absence of dilution steam further reduces the upstream energy (thermal) demand and takes the upstream demand from 25.44 GJ_{Th}/tonne ethylene for cracking to 8.32 for the ROC case, as shown in **Table 6.6**. This upstream section leads to the most significant reduction in energy demand in ROC compared to cracking. The compression section offers the main energy savings downstream in the ROC with a 25% reduction compared to cracking, due to a drop in the total moles of the product gases, on a dry basis. The overall downstream energy requirement is roughly the same for the two cases. The refrigeration duty needed to cool the feed to the DM is reduced as less mass is fed to the DM in the ROC case. The amine scrubbing unit is likely to be required for the ROC case, due to the high CO₂ content. Overall, 0.11 MW-hr of work/tonne of CO₂ captured is needed for the ROC process^[23]. Assuming 100% CO₂ removal, this accounts for 0.12 GJ (electric)/tonne ethylene, contributing roughly 4% of the downstream energy demand. The PSA unit adds to the energy expense

downstream, contributing an energy requirement of 2.2 kW-hr (electric)/kg H₂ separated [25]. The ROC involves the separation of lesser amount of hydrogen leading to reduced PSA energy requirements. The deacetylenizer in both cases operates at high pressures (~35 bar) and temperatures of 50°-70°C [27]. The reactant gas from the top of a deethanizer is at a very low temperature (-50°C). Higher ethylene: ethane and propylene: propane ratios lead to higher C2 and C3-splitter energy demands. Overall, the ROC case has a potential to provide a 52% reduction in the overall energy demand of the plant, compared to hexane cracking, as shown in **Figure 6.4**. **Figures 6.5 and 6.6** compare the two cases by normalizing the energy demand in terms of the HVPs.

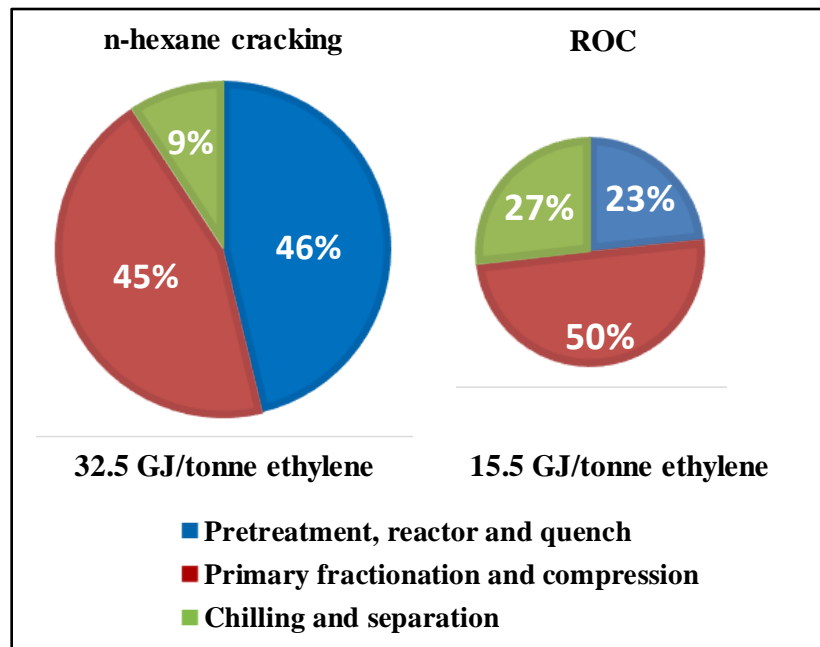


Figure 6.4: Section wise energy distribution for hexane cracking and ROC.

Table 6.6: Comparison of the energy demands.

Unit/Section		GJ/tonne ethylene	
		Hexane cracking	ROC
Upstream (MW)	Reactor (Endothermicity)	8.72	0.00
	Feed pretreatment	8.27	8.56
	Air/Steam preheat	7.19	2.98
	Quench	-9.17	-7.93
	Heat released	0.00	0.00
	Primary fractionation	10.44	4.70
Downstream (MW)	Compressor	4.03	3.02
	Demethanizer	0.45	0.38
	De-ethanizer	0.00	0.05
	Depropanizer	0.14	0.16
	C2-splitter	1.13	1.18
	C3-splitter	0.40	0.53
	Debutanizer	0.01	0.00
	Deacetylenizer	0.09	0.15
	CO ₂ scrubbing	0.00	0.30
	PSA	0.03	0.01
	Chilling	0.74	1.4
Upstream		25.44	8.32
Downstream		7.02	7.17
Total		32.5	15.5
HVPs (kg/kg ethylene)		3.2	2.7

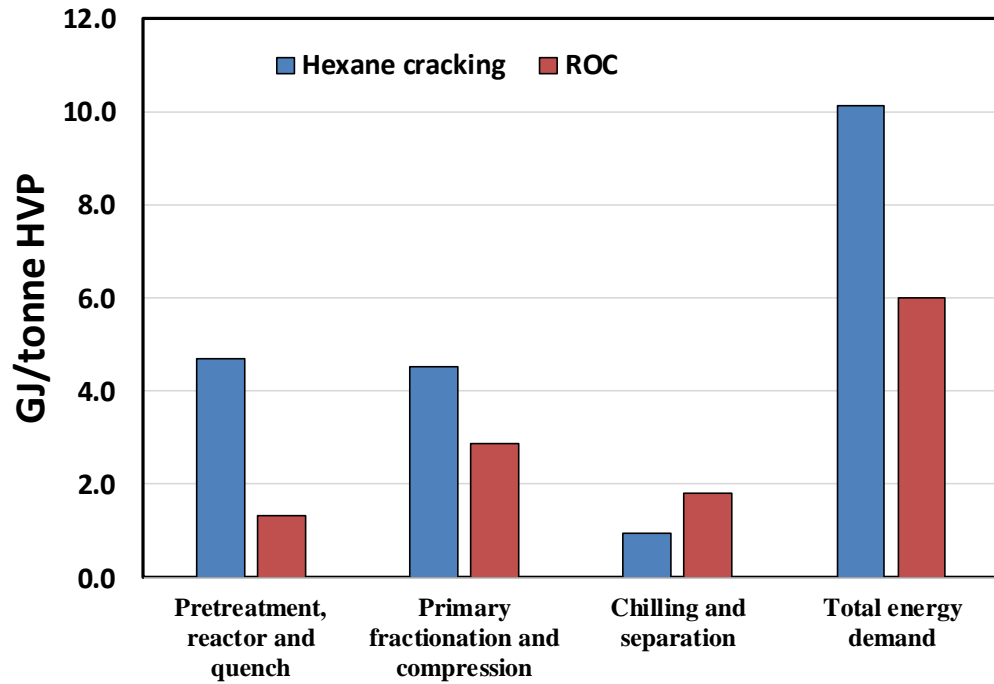


Figure 6.5: Comparison of the energy distributions in steam cracking and ROC processes.

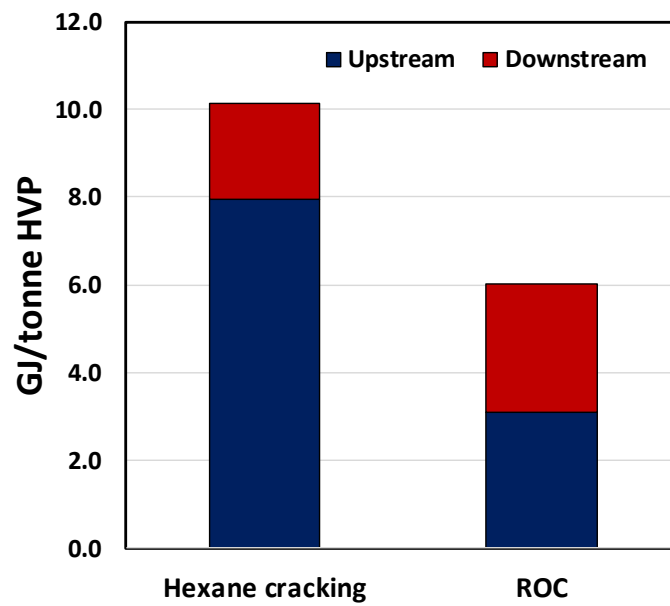
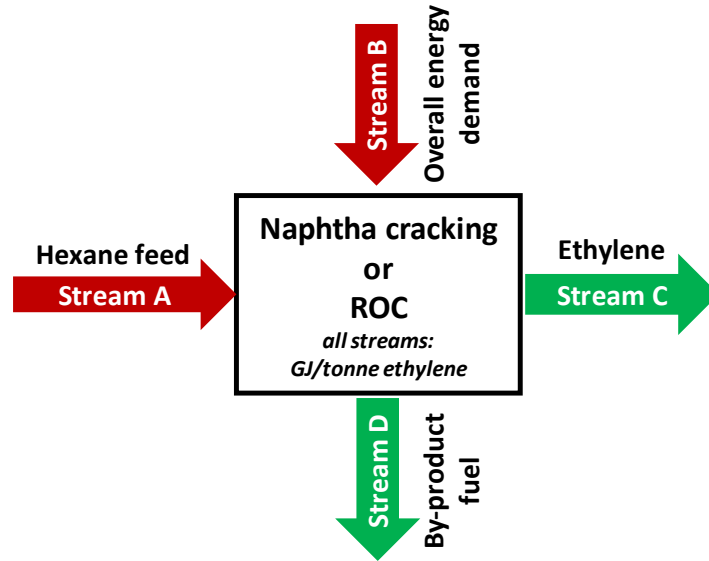


Figure 6.6: Normalized energy demand (section wise and overall) in steam cracking and ROC processes.

6.5.4 Net demand and emission comparisons

The cracking and the ROC process produce fuel gases (CO, CH₄ and H₂) which can be combusted to meet the energy requirements. Assuming all the fuel gases are used, hexane cracking shows a deficit of 5.2 GJ/tonne ethylene, which represents 16% of the total demand. In comparison, the ROC process requires no further fuel input as calculated using the $\Delta H_{\text{reaction}}$ in **Table 6.7** and the amount of available fuel based on ASPEN Plus[®]. In the steam cracking case, a portion of the fuel oil can also be combusted to suffice the energy demands. For simplicity, no recycle of the fuel oil has been considered in this study although it can be used as a feedstock to increase the ethylene and propylene yields.

This section compares the two processes based on the net energy required to produce 1 tonne of ethylene. In this analysis, we used the energy values of the feedstock and products to determine the net energy consumptions for ethylene production. This will allow an impartial comparison of the conventional and ROC process since one could argue that ROC's primary energy "savings" were resulted from indirect combustion of hydrogen and hydrocarbons. As shown in **Figure 6.7**, the entire process is divided into four relevant energy streams: 1) Hexane feed (A); 2) Overall thermal energy demand (B); 3) Ethylene (main product) (C); 4) By-product fuel out (D). Lower heating values (LHVs) are used for the fuel streams and are normalized based on 1 tonne of ethylene produced.



$$\text{Net demand} \left(\frac{\text{GJ}}{\text{tonne ethylene}} \right) = \text{Stream A} + \text{Stream B} - \text{Stream D}$$

Figure 6.7: Schematic for net energy demand analysis.

As shown in **Figure 6.8** below, the ROC process requires 14% less hexane per tonne of ethylene produced owing to higher ethylene yields, along with being less-energy intensive compared to traditional naphtha cracking. For every tonne of ethylene produced, the ROC process requires a net energy feed of 67 GJ, leading to 39% savings in overall process energy consumptions.

Table 6.7: $\Delta H_{\text{reaction}}$ and molar flow rates of the byproduct (fuels).

Heat release (LHV)		
$CO + \frac{1}{2}O_2 \rightarrow CO_2$	282	kJ/mole
$CH_4 + 2O_2 \rightarrow CO_2 + 2H_2O$	800	kJ/mole
$H_2 + \frac{1}{2}O_2 \rightarrow H_2O$	239	kJ/mole
Fuel oil (heavy hydrocarbons)	43.3 (Cracking)	MJ/kg
	45.0 (ROC)	MJ/kg

Table 6.8 (continued): $\Delta H_{\text{reaction}}$ and molar flow rates of the byproduct (fuels).

Component output		
	Cracking	ODH
CO (mol/mol C ₂ H ₄)	0	0.085
CH ₄ (mol/mol C ₂ H ₄)	0.718	0.488
H ₂ (mol/mol C ₂ H ₄)	0.804	0.080

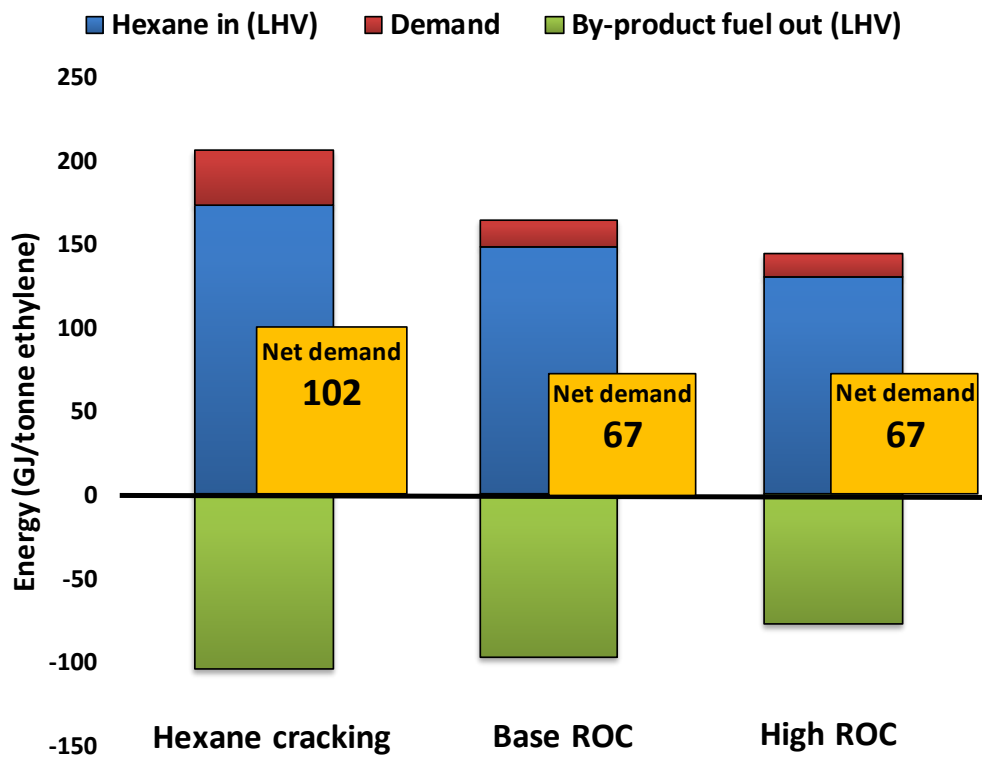


Figure 6.8: Net (Thermal) Energy demand for ethylene production.

In the case of hexane cracking, negligible amount of CO₂ is present in the product gases. Here, it is assumed that methane is used to meet the energy requirements in both the cracking case and ROC. Based on the lower heating value (LHV) of CH₄ and the total energy demand of the two processes, as given in **Table 6.7** and **Figure 6.5**, 40.6 and 19.4 kmol CH₄/tonne ethylene are required for the cracking case and ROC respectively. This leads to an emission of 1.8 and 0.85 kg

CO₂/kg ethylene respectively. Ren et.al ^[3] states an emission of 1.8-2 kg CO₂/kg ethylene for naphtha cracking units. Therefore ROC has the potential to result in 52% reduction in CO₂ emissions. The ROC process does not need high temperature furnaces. Therefore, significantly reduced NO_x emissions can also be anticipated ^[28]. The overall thermal energy demand for the high ROC case is 14 GJ/tonne ethylene which provides 10% and 57% energy reduction compared to the base ROC and cracking cases respectively with proportional reduction in CO₂ emissions. As shown in **Figure 6.8**, although the net demand remains unchanged for the ROC cases, for every tonne of ethylene produced, there is 12.8% and 10% reduction in the hexane feed and overall energy demand for the ROC high conversion case.

6.6 Conclusion

The current study investigates a redox oxy-cracking (ROC) process for light olefin production from naphtha. Based on our recently obtained experimental data using an Mn-based redox catalyst, the ROC process was simulated using ASPEN Plus® and compared with the traditional steam cracking process. Compared with cracking, ROC replaces the energy intensive cracking furnaces with an autothermal reducer-regenerator system. This results in significant energy savings. Moreover, experimental results indicate significantly improved ethylene and propylene yields. For each tonne of ethylene product, the ROC process has the potential to reduce the overall thermal energy demand by 52% when compared to steam cracking. While conventional naphtha cracking process is estimated to consume 32.5 GJ of energy in order to produce one tonne of ethylene, the ROC only requires a net thermal energy input of 15.5 GJ. The ROC can also provide over 50% reduction in the CO₂ emissions. Specifically, the upstream section of the ROC process consumes approximately 67% less energy while producing 28% more ethylene and propylene for every kg

of naphtha feedstock. Absence of the cracking furnaces also leads to considerable reduction in NO_x emissions for the ROC process. Overall, the current study indicates that the novel ROC concept has the potential to be an attractive and environmental-friendly option for ethylene and propylene production from naphtha.

6.7 Acknowledgements

This work was supported by the U.S. National Science Foundation (Award No. CBET-1604605) and the Kenan Institute for Engineering, Technology and Science at NC State University.

6.8 References

- [1] J. V. Moreira, **2015**.
- [2] H. Zimmermann, R. Walzl, in *Ullmanns Encycl. Ind. Chem.*, Wiley-VCH Verlag GmbH & Co. KGaA, **2000**.
- [3] T. Ren, M. Patel, K. Blok, *Energy* **2006**, *31*, 425.
- [4] M. Shahrokhi, M. E. Masoumi, S. M. Sadrameli, J. Towfighi, *Iran. J. Chem. Chem. Eng.* **2003**, *22*, 27.
- [5] M. Masoumi, M. Shahrokhi, M. Sadrameli, J. Towfighi, *Ind. Eng. Chem. Res.* **2006**, *45*, 3574.
- [6] C. A. Gärtner, A. C. van Veen, J. A. Lercher, *ChemCatChem* **2013**, *5*, 3196.
- [7] F. Cavani, N. Ballarini, A. Cericola, *Catal. Today* **2007**, *127*, 113.
- [8] C. Boyadjian, L. Lefferts, K. Seshan, *Appl. Catal. Gen.* **2010**, *2*, 167.
- [9] C. Boyadjian, A. Ağiral, J. G. E. Gardeniers, L. Lefferts, K. Seshan, *Plasma Chem. Plasma Process.* **2011**, *31*, 291.
- [10] C. A. Boyadjian, **2010**, DOI 10.3990/1.9789036530811.
- [11] A. H. Elbadawi, M. Y. Khan, M. R. Quddus, S. A. Razzak, M. M. Hossain, *AIChE J.* **2017**, *63*, 130.
- [12] M. M. Bhasin, J. H. McCain, B. V. Vora, T. Imai, P. R. Pujadó, *Appl. Catal. Gen.* **2001**, *221*, 397.
- [13] E. A. de Graaf, G. Rothenberg, P. J. Kooyman, A. Andreini, A. Bliet, *Appl. Catal. Gen.* **2005**, *278*, 187.
- [14] N. Ballarini, F. Cavani, A. Cericola, C. Cortelli, M. Ferrari, F. Trifirò, G. Capannelli, A. Comite, R. Catani, U. Cornaro, *Catal. Today* **2004**, *91–92*, 99.
- [15] R. M. Contractor, H. E. Bergna, H. S. Horowitz, C. M. Blackstone, B. Malone, C. C. Torardi, B. Griffiths, U. Chowdhry, A. W. Sleight, *Catal. Today* **1987**, *1*, 49.
- [16] L. M. Neal, S. Yusuf, J. A. Sofranko, F. Li, Boston, MA, United States, **2015**.
- [17] V. P. Haribal, L. M. Neal, F. Li, *Energy* **2017**, *119*, 1024.

- [18] S. Yusuf, L. M. Neal, F. Li, *ACS Catal.* **2017**, 7, 5163.
- [19] Y. Gao, L. M. Neal, F. Li, *ACS Catal.* **2016**, 6, 7293.
- [20] F. Li, L. M. Neal, J. Zhang, *Redox Catalysts for the Oxidative Cracking of Light Hydrocarbons*, **n.d.**, PCT/US2017/051157.
- [21] R. Schefflan, *Teach Yourself the Basics of Aspen Plus*, American Institute Of Chemical Engineers, Hoboken, NJ, USA, **2011**.
- [22] J. A. Moulijn, A. van Diepen, M. Makkee, *Chemical Process Technology*, John Wiley & Sons Inc., Chichester, West Sussex, United Kingdom, **2013**.
- [23] G. T. Rochelle, *Science* **2009**, 325, 1652.
- [24] M. Yan, *Simulation and Optimization of an Ethylene Plant*, Texas Tech University, **2000**.
- [25] M. Ball, A. Basile, T. N. Veziroglu, *Compendium of Hydrogen Energy: Hydrogen Use, Safety and the Hydrogen Economy*, Woodhead Publishing, **2015**.
- [26] S. Hall, **n.d.**
- [27] G. C. Battiston, L. Dalloro, G. R. Tauszik, *Appl. Catal.* **1982**, 2, 1.
- [28] G. Hassan, M. Pourkashanian, D. Ingham, L. Ma, P. Newman, A. Odedra, *Comput. Chem. Eng.* **2013**, 58, 68.

CHAPTER 7: CONCLUSION AND FUTURE WORK

7.1 Conclusion

Chemical looping is an attractive process-intensification avenue to utilize shale/natural gas along with $\text{CO}_2/\text{H}_2\text{O}$ for chemical production. Chemical looping reforming (CLR) is a novel redox scheme that uses lattice oxygen to convert methane, a major component of natural gas, to syngas through a simpler and potentially more efficient and cost effective route. Chemical looping oxidative dehydrogenation (CL-ODH) uses a redox scheme to convert ethane to ethylene. This redox approach consists of a metal oxide redox catalyst, which donates its lattice oxygen in order to oxidize the fuel (light alkanes). The reduced redox catalyst is transferred to a separate reactor where it is regenerated with an oxidant. It is during this oxidation that such a redox approach can valorize CO_2 or H_2O to CO or H_2 respectively. Successful development of chemical looping processes is tied with rational design and development of active and selective redox catalysts. An ideal candidate possesses a large enough oxygen capacity, high oxygen mobility, and high selectivity towards the desired. A small fraction of the synthesized and tested oxygen carriers demonstrate reasonable activity, selectivity, oxygen capacity, and long-term stability for these processes. These materials often impose high costs and/or environmental concerns. Modification of cheap and environmentally benign redox catalysts is extremely desirable. These modifications include tuning the thermodynamic and surface properties of the redox catalysts to make them more active and selective. Following the design and development of suitable redox catalysts, the process simulations along with energy and exergy analyses help in gathering a broader perspective and in comparing against existing processes.

Moving towards the development of redox catalysts for methane-to-syngas and CO₂/H₂O-to-CO/H₂ conversions, a rational strategy to optimize transition metal oxide-based candidates for via a hybrid solar redox scheme was proposed and validated. Integration of the solar energy for the endothermicity reduces the carbon footprint. Thermodynamic analyses coupled with DFT calculations revealed the potential of changing the redox properties of Mn and Fe-containing oxides by incorporating Mn/Fe cations into a perovskite structure. The prediction of BaMn_{0.5}Fe_{0.5}O_{3-δ} possessing the desirable properties for the hybrid solar-redox scheme was confirmed by experimental studies. Fluidized bed experiments demonstrated 90% steam conversion in the water-splitting step, compared to a typical conversion of <9% in solar-thermal water-splitting. Over 90% yield of Fischer Tropsch-ready syngas was also achieved in the methane partial oxidation step. The redox catalyst was found to be active and regenerable after multiple redox loops. AspenPlus® simulation indicated the potential of BaMn_{0.5}Fe_{0.5}O_{3-δ} to increase the methane-to-fuel efficiencies of state-of-the-art hydrogen and liquid fuel production processes by 38% (relative basis) with 70% lower CO₂ emissions for hydrogen production.

For low-temperature methane partial oxidation and CO₂ utilization, a hybrid redox process (HRP) that operates in a synergistic two-step, thermochemical redox scheme was presented. Ceria, being a promising material for such redox cycles, was further enhanced by La-substitution and Rh-promotion. DFT calculations indicated a decrease in the oxygen vacancy formation energy and migration barriers in both the bulk and surface of the fluorite structured oxide due to La substitution. The reduced Rh/LaCeO_{3.5-x} is shown to be capable of converting almost 100% of the CO₂ to CO at temperatures below 700°C. In the subsequent step, it converted 90% of methane selectively to syngas with a 2:1 H₂: CO ratio making it ideal for methanol synthesis. This ability to operate redox cycles at low temperatures allows for efficient integration of the industrial waste

heat, which is an excellent emission-free energy source. When compared with the conventional coal-based route, HRP offered a 68% reduction in the overall energy demand and 99% reduction in net CO₂ emission for acetic acid production. The ability to produce chemicals with high market volume and important industrial applications makes HRP a promising avenue for efficient and economical CO₂ utilization. HRP has the potential to utilize roughly 3 million metric tons of CO₂ every year from the three major industrial waste heat sources, making it a potentially suitable choice for sustainable CO₂ fixation.

To explore the intensification of ethylene production from ethane via CL-ODH, the process is compared with the traditional steam cracking process using energy and exergy analyses with the help of AspenPlus®. The selective combustion of hydrogen which aids in pushing towards higher ethylene yields, makes the oxidation reactor or regenerator exothermic. Overall, increased ethylene production along with other high value products was shown to enable CL-ODH (with 85% ethane conversion) to consume 82% less energy over cracking. It was also demonstrated to provide 82% reduction in the CO₂ and NO_x emissions over steam cracking. Although substantial efficiency improvement of steam cracking, which is already 95% thermally efficient, is not possible based on conventional wisdom, CL-ODH was shown to be a transformational route to ethylene via exergy loss minimization. These findings not only support the feasibility of CL-ODH but also provide a useful guidance to design intensified chemical production processes with significantly lowered emissions. If adopted at a global level, this innovative process can reduce annual CO₂ emissions by over 100 million tonnes for ethylene production.

To tackle the concerning issue of stranded low value ethane at isolated sites, the modular-ethane to liquids (M-ETL) technology was presented. It was shown to have the potential to be economically attractive for the intensification of liquid production from isolated ethane and ethane

rich LNGs. Based on the experimental results obtained using CL-ODH of ethane, up to 44% liquid fuel yields (on an LHV basis) was achieved in a relatively simple, single-pass system. The ability of CL-ODH to achieve high ethylene yields under an auto-thermal operation, via *in-situ* oxygen separation, is a key to simplify ethane conversion. With discounted ethane price at isolated sites, preliminary economic modeling suggested that the M-ETL process can be economically feasible at \$1.00/gallon selling price with capital costs of up to \$100,000/daily barrel. Due to its simplicity and the compatibility of the “low-temperatures” CL-ODH with modular reactors, this capital expenditure is potentially feasible. In addition to capital costs, the value of co-generated electricity has a strong effect on the value of the products, and the required selling price of the liquids.

Extending the chemical looping approach as a process intensification route to another major source of global ethylene, a redox oxy-cracking (ROC) process for light olefin production from naphtha was presented. Using experimental results from a Mn-based redox catalyst, the ROC process was simulated using ASPEN Plus® and compared with the traditional steam cracking process. For each tonne of ethylene product, the ROC process was shown to reduce the overall thermal energy demand by 52%, with conventional naphtha cracking process demanding 32.5 GJ of energy. The ROC can also provide over 50% reduction in the CO₂ emissions. Absence of the cracking furnaces also causes considerable reduction in NO_x emissions. Overall, novel ROC concept was demonstrated to have the potential to be an attractive and environmental-friendly option for ethylene and propylene production from naphtha.

7.2 Outlook

- The current study gives a rationale to design redox catalysts for syngas generation from methane. This is a guide for development of efficient redox catalysts. The design approach can be extended to different chemical looping processes.
- Low temperature CO₂ utilization, along with the ability to use the industrial waste heat, is a step towards development of sustainable processes. It has the potential to reduce the greenhouse gas emissions and valorize CO₂ at low temperatures into CO and eventually into chemicals.
- The framework for process analyses of CL-ODH, provides a foundation for a detailed techno-economic analysis (TEA) of various CL-ODH processes using different feed-stocks. Considering the promise of CL-ODH towards intensifying ethylene production, a thorough TEA is crucial for large-scale operations. The simulation models can also be modified to suit any given chemical looping process.
- With large availability of ethane from shale gas, modular systems help in chemical production on-site in a cost-effective and energy-effective way. Analyses of the M-ETL scheme explore the merits in modular systems and provide a starting point for future schemes.

7.3 Future work

7.3.1 *Towards low temperature methane partial oxidation and CO₂-utilization*

As shown in **Chapter 2 and 3**, chemical looping processes can be utilized for efficient methane partial oxidation, coupled with H₂O/CO₂ splitting. Modified ceria (**Chapter 3**) can perform the HRP at a low temperature of 650°C, allowing the integration of industrial waste heat. Although this redox catalyst contains only a small amount of rhodium, the aim is to develop cheaper and

robust materials which can perform the same reactions at lower temperatures. At the same time, high yields of syngas and H₂/CO are desired, which are possible with high oxygen release capacity of these redox catalysts.

In that regard, mixed ionic-electronic conducting oxides (MIEC) have shown to be promising candidates for applications in oxygen supply, mainly as oxygen transport membranes (OTMs)^[1-3]. Oxygen-deficient perovskites like Ba_{0.5}Sr_{0.5}Co_{0.8}Fe_{0.2}O_{3-δ} are well-known but they degrade in presence of CO₂^[4], which is essential in HRP. On the other hand, as discussed in **Chapter 3**, ceria-based oxides possess fast oxygen-ion mobility, good catalytic properties and compatibility with CO₂/H₂O. Lanthanide dopants improve ion conductivity, but not electronic conductivity. A combination of an ionic conductor (IC) and electronic conductor (EC) can be a solution (IC + EC) for effective materials for oxygen supply. IC can be materials like Ce_{0.9}Gd_{0.1}O_{2-δ} or CGO and EC can be La_{0.7}Sr_{0.3}MnO_{3-δ}^[5]. The other way is by expanding the oxygen release area. The oxygen surface-exchange reaction (OSER) is generally thought to be confined at the triple phase boundary^[6] (TPB; **Figure 7.1a**). Replacing pure EC with a predominantly electronic MIEC (La_{0.6}Sr_{0.4}Co_{0.2}Fe_{0.8}O_{3-δ}) for both oxygen ionic and electronic transport (**Figure 7.1b**), can boost oxygen release. By introducing ionic transport to the EC phase, OSER could take place not only at the TPBs, but also over a significant portion of the MIEC surface, thereby extending the size of the active region and increasing the total oxygen release (**Figure 7.1b**). It is an MIEC + MIEC combination, one being a predominant IC MIEC and other one predominant EC MIEC^[7].

An example would be Ce_{0.85}Gd_{0.1}Cu_{0.05}O_{3-δ} (CGCO) + La_{0.6}Ca_{0.4}FeO_{3-δ} (LCF), comprising of an IC MIEC in CGCO, with a fluorite structure, and EC MIEC in LCF with a perovskite structure. As illustrated in **Figure 7.1c**, with this composite strategy, the oxygen ions and electrons are transported in both MIEC phases at the same time, which enables the OSER to be extended to the

overall surface area of the mixed material, thus significantly increasing the rate of OSER and bulk diffusion for oxygen release^[7]. This can provide considerable oxygen release along with excellent stability in the presence of CO₂, exhibiting great potential for chemical looping processes like low temperature HRP.

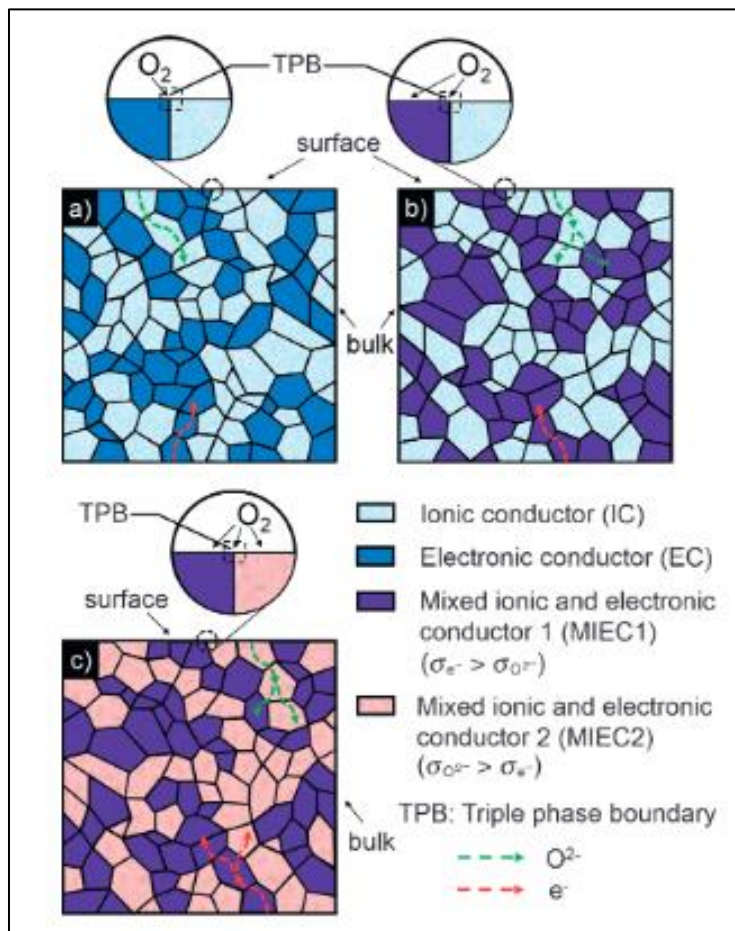


Figure 7.1: Concept of combining materials^[7]: a) IC + EC; b) IC + MIEC; c) MIEC + MIEC [σ is the conductivity, ionic and electronic].

7.3.2 Kinetics of ethane CL-ODH

The CL-ODH AspenPlus® model described in **Chapter 4** simulates steady-state operating conditions and cannot capture the dynamic behaviors of CL-ODH under varying reaction

conditions. The kinetics of the CL-ODH reaction would help in describing the various design variables. This would be helpful in the scale-up of the process. It has been shown earlier that in the case of CL-ODH (Mg-Mn based redox catalyst), ethane cracking (pyrolysis) occurs, followed by the combustion of the formed hydrogen, which pushes the equilibrium towards higher ethane conversions^[8,9]. This is shown in **Figure 7.2**.

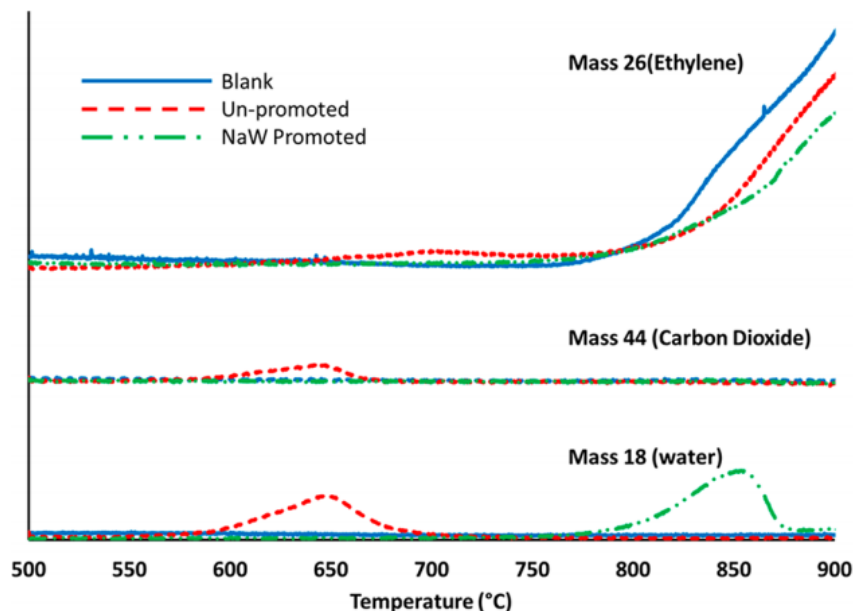


Figure 7.2: Ethane TPR results for mass 26 (ethylene), mass 18 (water) on Mn-Mg based CL-ODH redox catalysts^[8].

To describe the overall reaction, it is essential to first have a model which can predict the ethane cracking product distribution with reasonable accuracy. Following that, the kinetics of the selective hydrogen combustion (or SHC) can be added to capture the overall CL-ODH. This rationale is depicted in **Figure 7.3**.

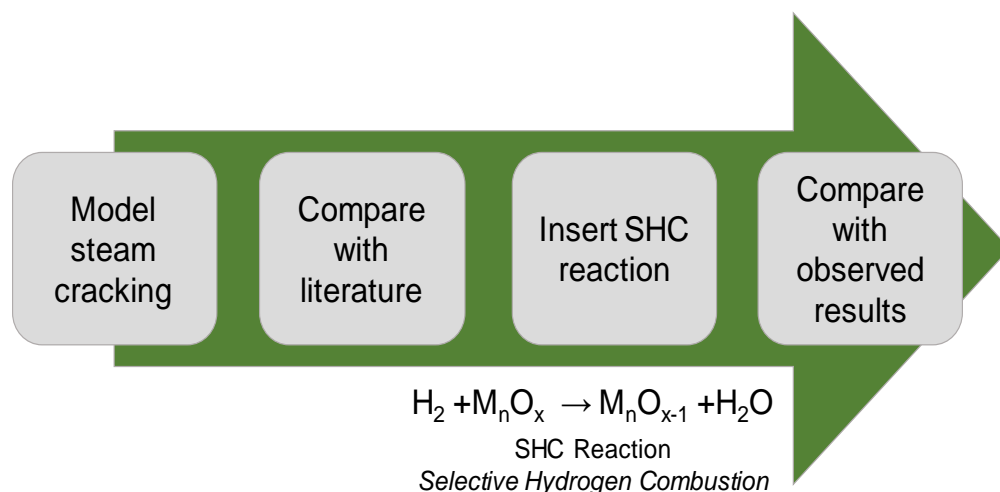


Figure 7.3: Schematic for depicting the overall Cl-ODH reaction through kinetics.

7.3.2.1 Using AspenPlus®

Ethane steam cracking is well studied in literature. Based on the earlier published results^[10–15] a simple AspenPlus® model (**Figure 7.4a**) can be set up to study the reaction. A plug-flow reactor (PFR) is used in the model with Reaction 7.1 ($K_{\text{equilibrium}} = 1.8 \times 10^{-2}$)^[15]. In the overall ethane pyrolysis, this reaction is dominant accounting for roughly 90% of the overall rate^[15]. The results, as shown in **Figure 7.4b**, are close to the industrial value, but slightly higher. This is due to the simplistic nature of the model accounting for a single reaction whereas in reality there are several in action, leading to other products.



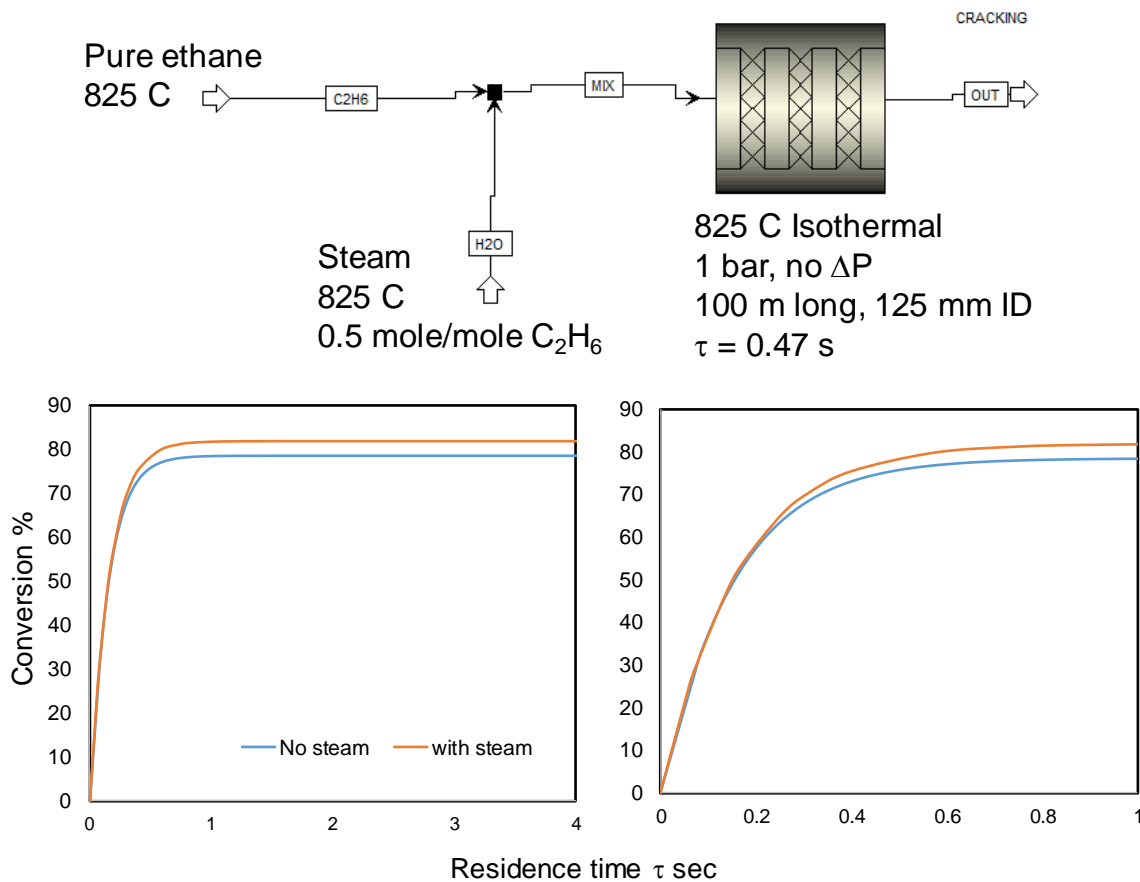


Figure 7.4: Schematic for simulation of ethane cracking in a PFR using AspenPlus® and the corresponding ethane conversion (or ethylene yield, as only one reaction is considered).

7.3.2.2 Using Chemkin®PRO

Chemkin®PRO can be used for modeling and simulating complex gas phase and surface chemistry reactions. It can provide accurate, fast and robust kinetic models and can quickly explore the impact of design variables on performance^[16]. The approach is to model steam cracking process in Chemkin®PRO, using models available in literature and compare with existing industrial data. **Table 7.1a and b** lists a few models, from literature, used for the study. **Figure 7.5** describes the setup of Chemkin®PRO^[16]. An isothermal PFR model was used for the study, with a residence

time of 0.4 - 0.5s^[10]. The ethane conversion and product distribution were monitored for the different models and are presented in **Table 7.2**.

Table 7.1: Models and the sources for kinetic modeling.

a) Model	Source
Reference ^[10]	H. Zimmermann and R. Walzl, "Ethylene," in <i>Ullmann's Encyclopedia of Industrial Chemistry</i> , Wiley & Sons, 2009
Model 1 ^[12]	Gothem et al. "A kinetic modelling study of ethane cracking for optimal ethylene yield," <i>Chem. Eng. Res. Des.</i> , vol. 91, no. 6, pp. 1106–1110, Jun. 2013
Model 2 ^[13]	Ranjan et al. "Modeling of Ethane Thermal Cracking Kinetics in a Pyrocracker," <i>Chem. Eng. Technol.</i> , May 2012
Model 3 ^[11]	Sabbe et al. "First principle-based simulation of ethane steam cracking," <i>AIChE J.</i> , vol. 57, no. 2, pp. 482–496, Feb. 2011
Model 4 ^[14]	Xu, Chen, et al. "Kinetic modeling of ethane pyrolysis at high conversion." <i>The Journal of Physical Chemistry A</i> 115.38 (2011): 10470-10490.

b) Source	Set-up	Length of coil/reactor	Diameter of coil/reactor	L/D	Reported residence time (s)
Reference ^[10]	Industrial	10 m	25 mm	400	0.5
		100 m	180 mm	555	0.5
Sundaram and Froment ^[15]	Industrial	101 m	124 mm	814	not specified
Model 3 ^[11]	Pilot	23 m	10 mm	2300	2.5
Model 4^[14]	Lab-scale	34 cm	6 mm	57	5

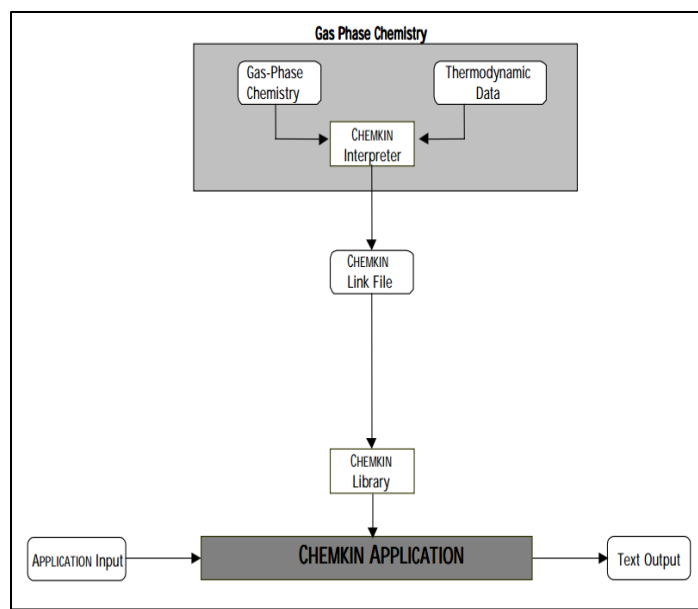


Figure 7.5: Chemkin®PRO set-up.

Table 7.2: Product distribution for various models.

	Model 1 ^[12]	Model 2 ^[13]	Model 3 ^[11]	Model 4 ^[14]	Reference ^[10]
Feed	Ethane				
Temperature (°C)	805	805	805	825	800-850
Ethane Conversion (%)	67.5	66.1	71.4	69.5	65
Residence time (s)	0.44	0.52	0.51	0.5	0.46
Ethane	32.49	33.92	28.59	30.51	35.00
Methane	0.07	1.25	2.92	2.02	3.75
Acetylene	0.00	0.04	1.84	0.64	0.44
Ethylene	62.60	57.53	60.78	57.67	51.88
Propylene	0.12	2.55	0.57	0.31	1.22
Propane	0.00	0.10	0.14	0.01	0.12
Butadiene	0.09	0.15	0.01	2.48	1.80
Butene	0.10	0.14	0.32	0.24	0.19
Butane	0.00	0.00	0.20	-	0.21
Pentane	0.00	0.00	0.00	-	0.69
Benzene	0.00	0.00	0.00	0.59	0.58
Toluene	0.00	0.00	0.00	0.73*	0.08
Hydrogen	4.49	4.26	4.53	4.61	4.04
Ethane steam cracking outlet wt.% distribution					

* Includes all the heavy products, mainly cyclopentadiene

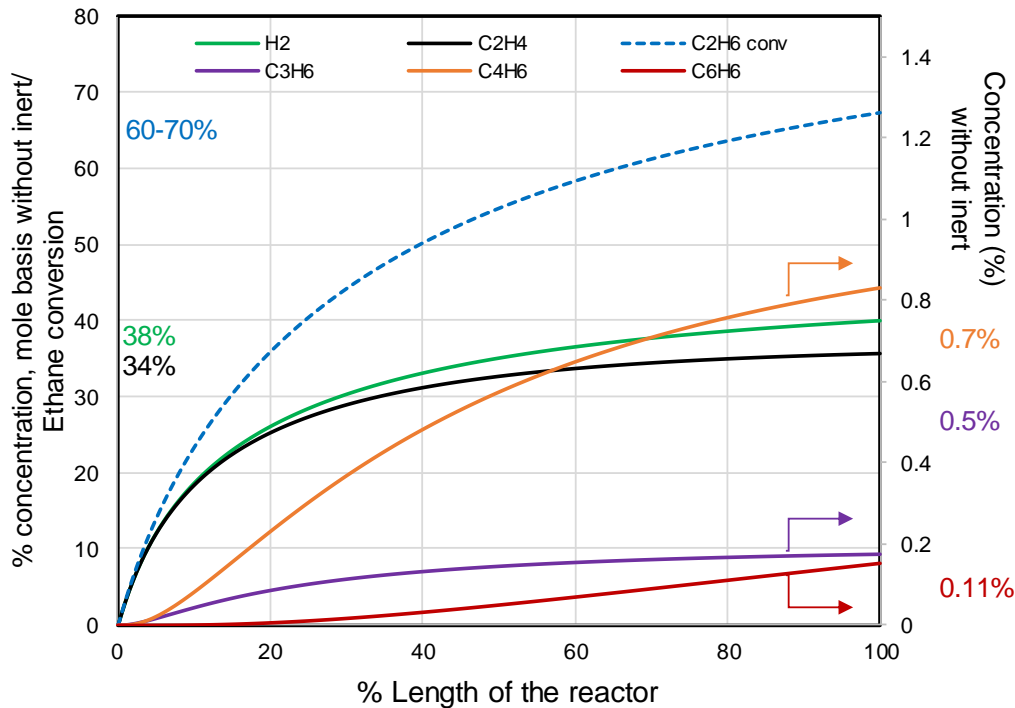


Figure 7.6: Product distribution of Model 4^[7] (isothermal) vs. reference literature values.

All the models, except Model 4, failed to predict the heavy components like butadiene and C4+.

Figure 7.6 compares the results of Model 4 (isothermal at 825°C) with the reference values. A 100 m long reactor, 125 mm ID and a residence time of 0.5s has been used. Model 4^[14], consisting of 513 number of radical reactions, has the prediction closest to the reference and hence can be used as the basis for investigating ODH reactions in the presence of redox catalysts. Product distribution variation along the length of the tube is shown in **Figures 7.7a to h**. In these figures, both isothermal 850°C (a, c, e and g) and a temperature profile (b, d, f and h) (based on **Figure 7.8**^[10]) are used.

Dashed curves represent isothermal conditions at 850°C
 Solid curves represent integration of a T-profile
 Dotted curve shows the T-profile

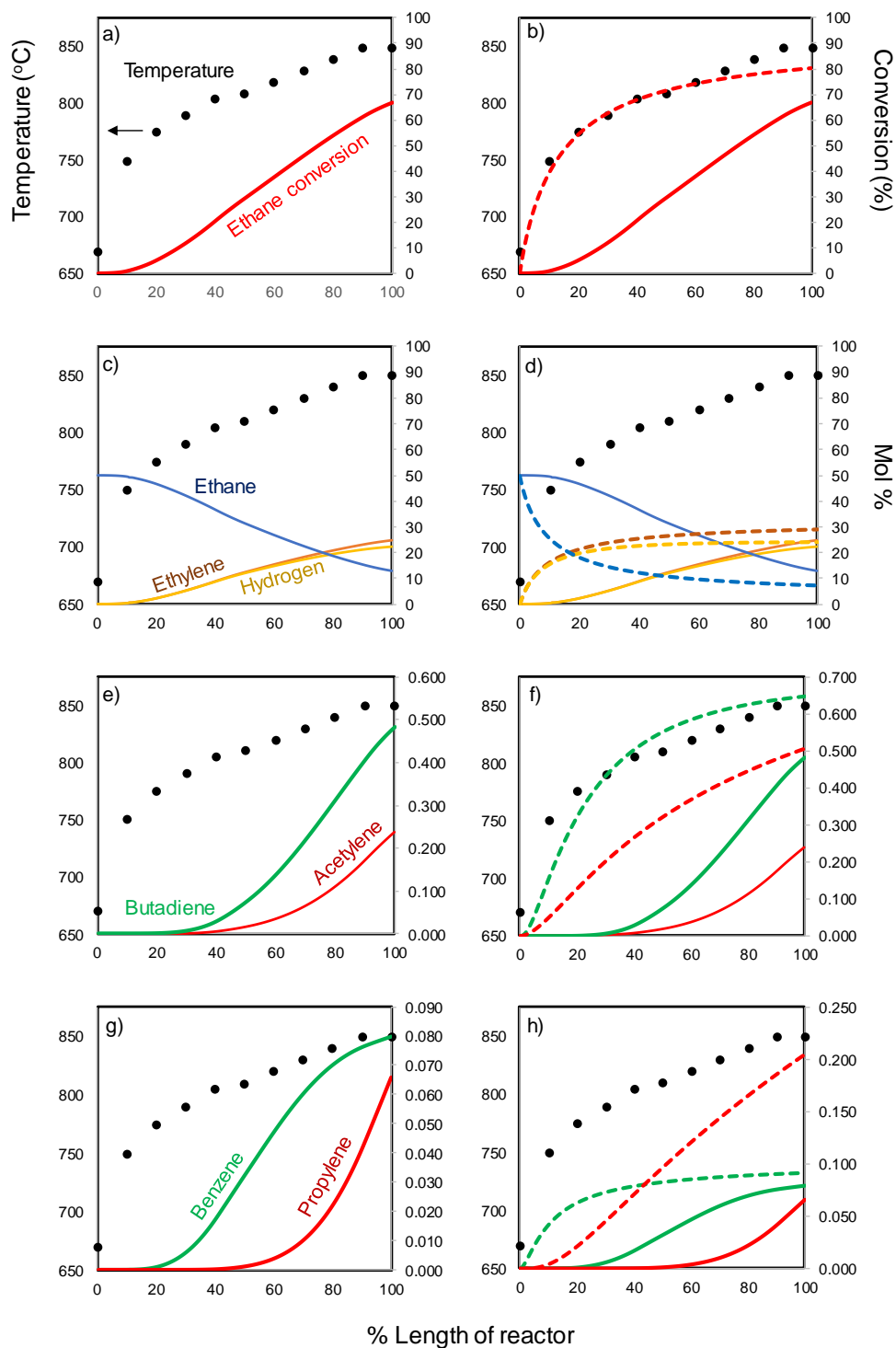


Figure 7.7: Results from Model 4^[7]; both isothermal and with a T-profile.

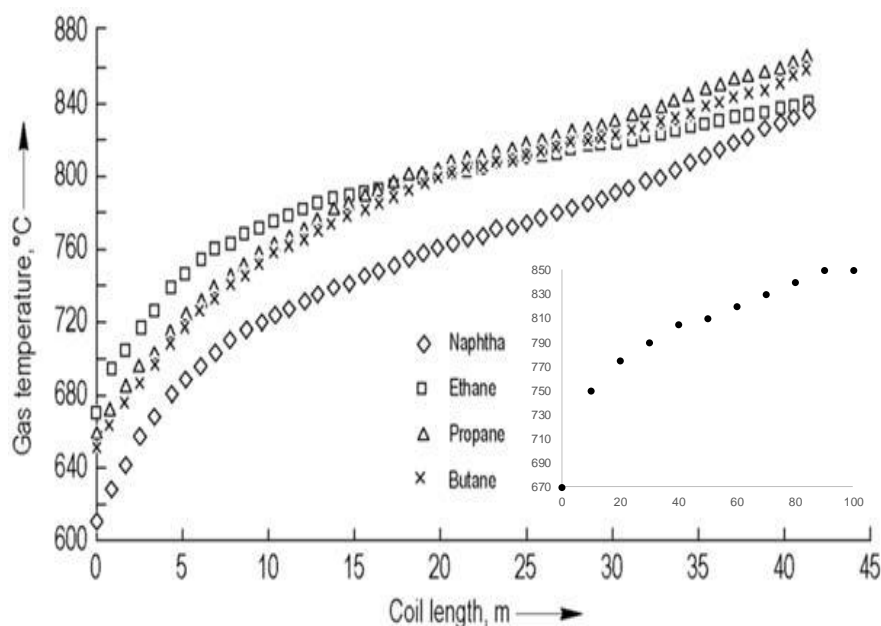


Figure 7.8: Temperature profile in the cracking tube for different feeds [subset is the T-profile for ethane].

Considerations

Accurate prediction of the output requires accurate representation of the high molecular weight compounds. The molecular weight growth (MWG) reactions are crucial in this regard^[14]. At high temperatures, acetylene is key in formation of soot and heavy products, whereas at low temperatures, ethylene is important. Butadiene is an important component for the MWG. As shown in **Figure 7.9**, MWG reactions start with butane around 550°C. As temperature increases (around 800°C), the formed ethylene further participates in MWG, where acetylene does not contribute. H-addition reactions to olefins is not favorable for MWG. This is seen in the results of **Chapter 4 and 5**, where H₂-removal causes an increase in the formation of heavy products. Additionally, depiction of Model 4 has utilized nitrogen as the inert gas, and yields satisfactory results. Practical

operation uses steam as the diluent and presence of H₂O in the reaction network would cause a higher 3rd body collision efficiency and could affect the output.

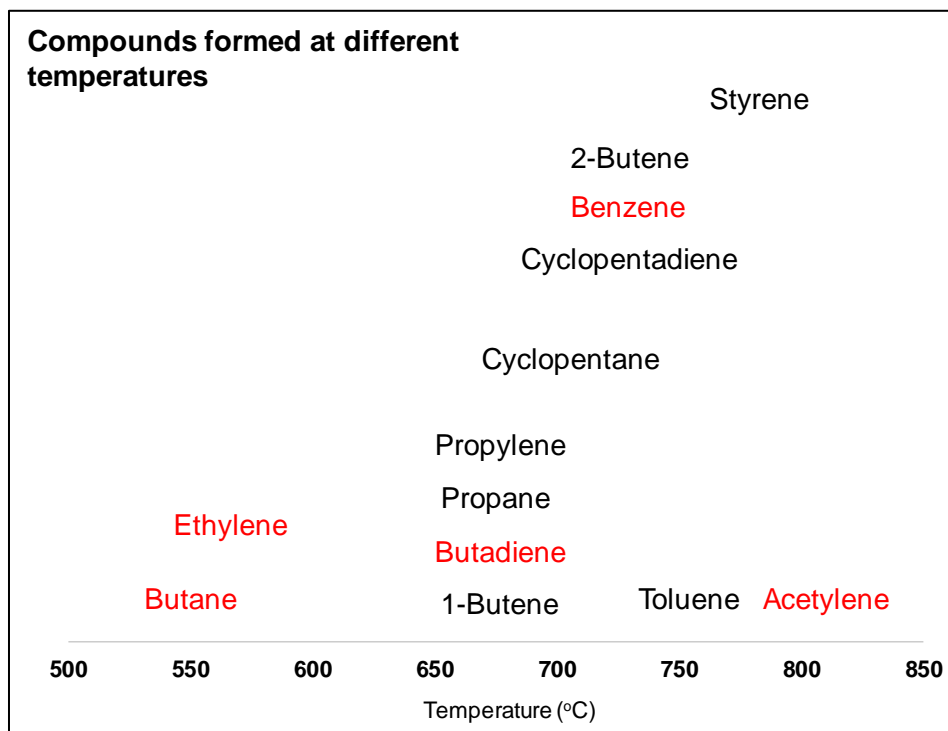


Figure 7.9: Compounds formed at different temperatures^[7] as part of MWG reaction products (highlighted ones are the important products in the CL-ODH study, based on experimental results shown in Chapter 4).

Insertion of the SHC reaction

Once an ethane cracking model in Chemkin[®]PRO gives an output closer to the literature values, the SHC reaction can be incorporated in the model. This would involve the usage of the surface kinetics package of Chemkin[®]PRO, which would be an addition to the Gas Phase Chemistry package shown in **Figure 7.5**^[17]. This can be used to analyze the effect of hydrogen removal on the output, which needs to be then compared with the experimental results. Once a satisfactory

kinetic model is developed for this process, a dynamic model could then be implemented in AspenPlus[®], incorporating the kinetics. To analyze the effect of H₂ removal, pure oxygen is passed to the cracking reactor, in the feed, enough to consume 80% of the formed H₂ (based on the results of **Chapter 4**). The reactor is the one used for Model 4 (**Figure 7.6** and **7.7**). The output is shown in **Figure 7.10**, which shows an increase in the heavy products, as expected on H₂-removal.

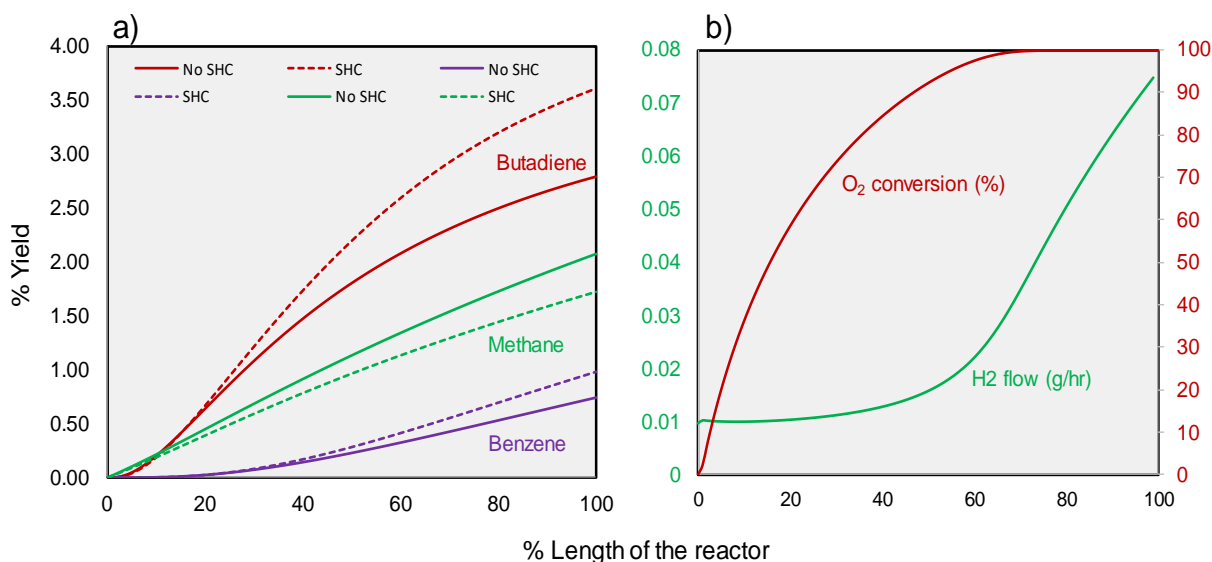


Figure 7.10: Output results with and without the insertion of SHC reaction to Model 4.

A staged O₂-injection can be done, as shown in **Figure 7.11** to mimic the oxygen release from a redox catalyst. The reactor of 100 m in sliced into multiple PFRs in series, all with an ID of 125 mm and 825°C temperature. O₂-feed is equally distributed at three locations to match 80% H₂ combustion. In the thermodynamic file for Chemkin[®]PRO, an irreversible reaction of H₂ combustion to water, is added, with activation energy as zero and no kinetic parameters. This was to check the effect of SHC, but for detailed incorporation of surface reactions, experimentally observed kinetic parameters of the SHC need to be added. The results, from **Table 7.3**, show a small effect of SHC, but shows expected trends in ethane conversion and ethylene selectivity.

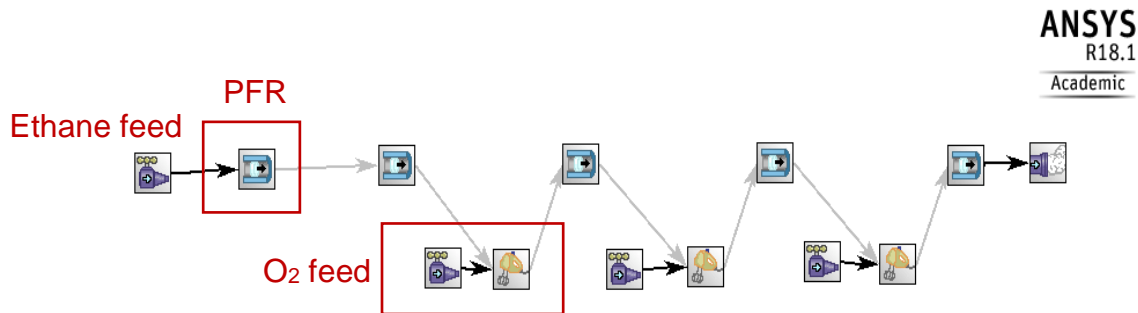


Figure 7.11 Chemkin®PRO set-up for staged O₂ injection to sliced PFR reactor scheme.

Considerations

There are two ways to incorporate the redox catalyst SHC kinetics into the steam cracking model. One is by using the surface Chemkin®PRO package and depicting the surface reactions responsible for the CL-ODH to capture the SHC. This would involve the development of the mechanism for the CL-ODH along with the kinetic parameters of the involved reactions. The other way is to incorporate the SHC of the material *via* a User Defined Function (UDF) in Chemkin®PRO. The UDF is basically a block that inserts the SHC kinetics into the cracking model, which changes along the length of the reactor. This would require the experimental kinetic SHC parameters for the redox catalyst. The SHC UDF can run simultaneously with the current ethane cracking model. The UDF captures the rate of SHC based on experiments and changes as partial pressure of H₂ changes along the length of reactor (or time). With the consumption of H₂, the UDF also adds an equivalent amount of H₂O (steam) in the reactor, to represent the actual CL-ODH reaction. *This scheme, as shown in Figure 7.12, once developed and validated, can provide flexibility to alter the kinetic parameters of the SHC based on different redox catalysts and can eventually provide a general model of CL-ODH.*

Table 7.3: Comparing the output of SHC reaction addition with ethane cracking.

	No SHC	Staged SHC
Ethane conversion	67%	68%
%C yield (mol%, without inert)		
CH4	2.21	2.16
C2H4	59.06	59.12
C3H6	0.435	0.503
C3H8	0.018	0.021
C4H6	2.757	3.325
C6H6	0.758	0.887

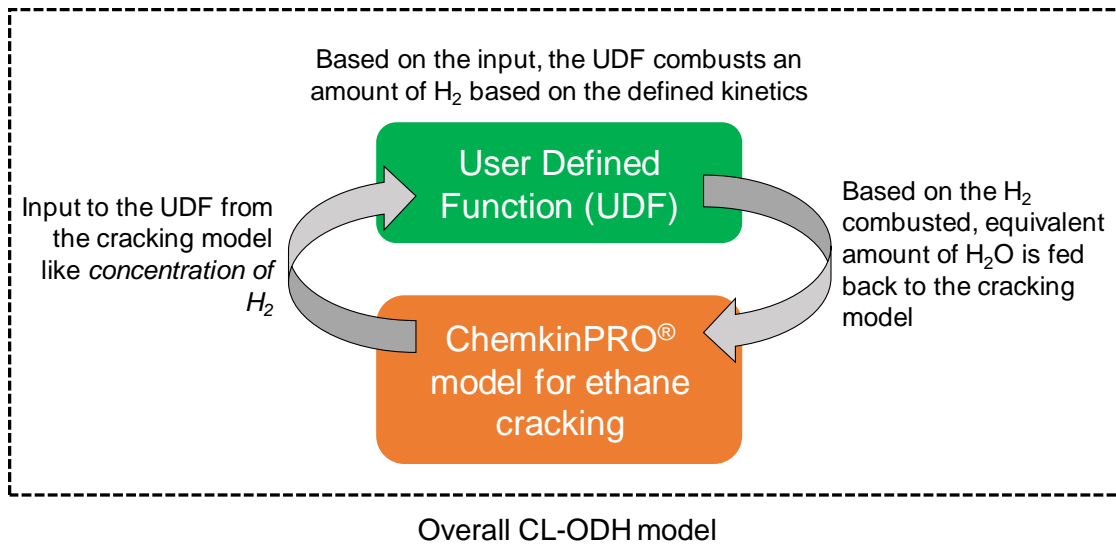


Figure 7.12: Rationale for integration of a UDF for capturing the CL-ODH kinetics.

7.4 References

- [1] A. Aguadero, H. Falcon, J. M. Campos-Martin, S. M. Al-Zahrani, J. L. G. Fierro, J. A. Alonso, *Angew. Chem. Int. Ed.* **2011**, *50*, 6557.
- [2] J. Suntivich, H. A. Gasteiger, N. Yabuuchi, H. Nakanishi, J. B. Goodenough, Y. Shao-Horn, *Nat. Chem.* **2011**, *3*, 546.
- [3] Y. Liu, X. Zhu, M. Li, H. Liu, Y. Cong, W. Yang, *Angew. Chem. Int. Ed.* **2013**, *52*, 3232.
- [4] Z. Shao, W. Yang, Y. Cong, H. Dong, J. Tong, G. Xiong, *J. Membr. Sci.* **2000**, *172*, 177.
- [5] V. V. Kharton, A. V. Kovalevsky, A. P. Viskup, F. M. Figueiredo, A. A. Yaremchenko, E. N. Naumovich, F. M. B. Marques, *J. Electrochem. Soc.* **2000**, *147*, 2814.
- [6] S. B. Adler, *Chem. Rev.* **2004**, *104*, 4791.
- [7] W. Fang, F. Liang, Z. Cao, F. Steinbach, A. Feldhoff, *Angew. Chem. Int. Ed.* **2015**, *54*, 4847.
- [8] S. Yusuf, L. M. Neal, F. Li, *ACS Catal.* **2017**, *7*, 5163.
- [9] L. M. Neal, S. Yusuf, J. A. Sofranko, F. Li, *Energy Technol.* **2016**, *4*, 1200.
- [10] H. Zimmermann, R. Walzl, in *Ullmanns Encycl. Ind. Chem.* (Ed.: Wiley-VCH Verlag GmbH & Co. KGaA), Wiley-VCH Verlag GmbH & Co. KGaA, Weinheim, Germany, **2009**.
- [11] M. K. Sabbe, K. M. V. Geem, M.-F. Reyniers, G. B. Marin, *AIChE J.* **2011**, *57*, 482.
- [12] M. W. M. van Goethem, S. Barendregt, J. Grievink, P. J. T. Verheijen, M. Dente, E. Ranzi, *Chem. Eng. Res. Des.* **2013**, *91*, 1106.
- [13] P. Ranjan, P. Kannan, A. A. Shoaibi, C. Srinivasakannan, *Chem. Eng. Technol.* **2012**, *35*, 1093.

- [14] C. Xu, A. S. Al Shoaibi, C. Wang, H.-H. Carstensen, A. M. Dean, *J. Phys. Chem. A* **2011**, *115*, 10470.
- [15] K. M. Sundaram, G. F. Froment, *Chem. Eng. Sci.* **1977**, *32*, 601.
- [16] R. J. Kee, F. M. Rupley, J. A. Miller, *Chemkin-II: A Fortran Chemical Kinetics Package for the Analysis of Gas-Phase Chemical Kinetics*, Sandia National Labs., Livermore, CA (USA), **1989**.
- [17] M. E. Coltrin, R. J. Kee, F. M. Rupley, *Int. J. Chem. Kinet.* **1991**, *23*, 1111.

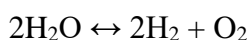
APPENDICES

Appendix A: Supplementary Information for Chapter 2

Thermodynamic analysis of the hybrid solar redox process

H₂O-to-H₂ conversion

Thermodynamic analysis can provide the equilibrium steam-to-hydrogen conversion as a function of temperature and P_{O₂}. Thermodynamic data for the individual components involved in the reaction can be either obtained using handbooks or conveniently calculated using software packages such as HSC Chemistry or ASPEN Plus®. The reaction considered is:



The equilibrium constant for the reaction (K_n) at a given temperature (T_n):

$$K_n|_{T_n} = e^{\frac{-\Delta G}{RT_n}} = \frac{[\text{P}_{\text{H}_2}]_{T_n}^2 \cdot [\text{P}_{\text{O}_2}]_{T_n}}{[\text{P}_{\text{H}_2\text{O}}]_{T_n}^2} = \frac{X}{1 - X}$$

where X is the steam conversion given by the following equation:

$$X = \frac{[\text{P}_{\text{H}_2}]_{T_n}}{[\text{P}_{\text{H}_2\text{O}}]_{T_n} + [\text{P}_{\text{H}_2}]_{T_n}}$$

At a given value of T_n, different values of X require different P_{O₂}. X is varied from 0 to 100%, with T_n varying from 800° to 1000°C. Each set of X and T_n give a value of P_{O₂}. That is plotted in Figure 2.1b and A1. The different steam-conversion lines shown in Figure 2.1a and Figure 2.2 are generated as described above.

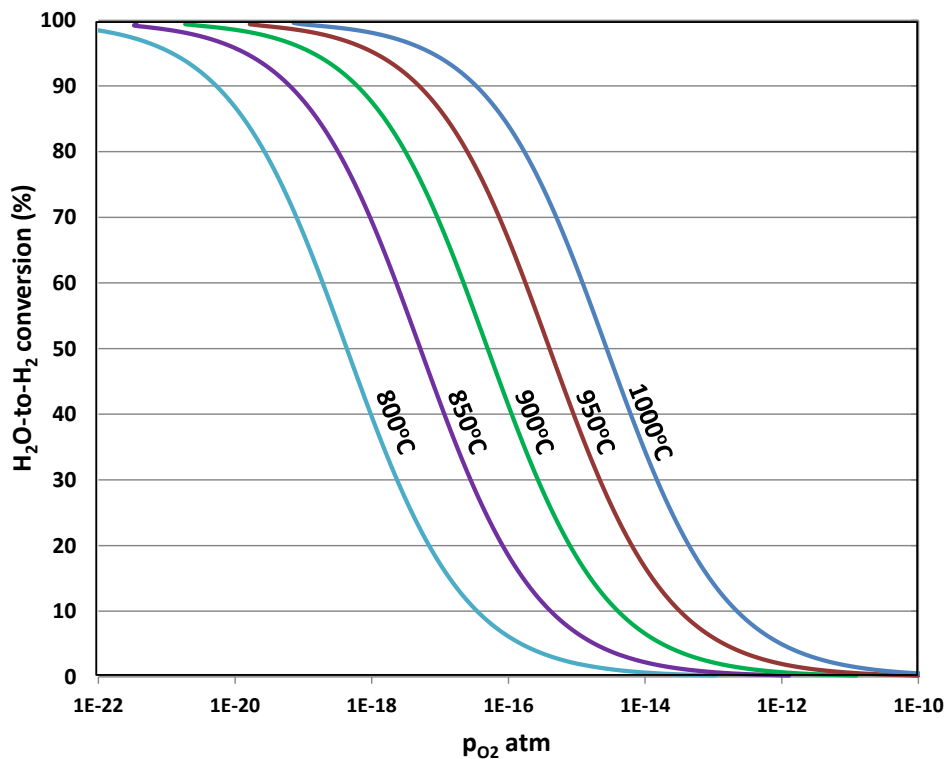


Figure A1: Equilibrium H₂O-to-H₂ conversion at different temperatures and P_{O₂}.

Ellingham diagram

The various reaction lines (ΔG vs T) on the Ellingham diagram in Figure 2.1a and Figure 2.2 are generated using HSC Chemistry v7. The ΔG for the metal oxide/metal system corresponds to the ΔG (kJ mol⁻¹) for the metal oxide decomposition. For example, for the FeO/Fe system: $2\text{Fe} + \text{O}_2 \leftrightarrow 2\text{FeO}$,

$$\Delta G = -R \cdot T \cdot \ln(P_{\text{O}_2})$$

where R is the gas constant. The right Y-axis in Figure 2.1a and Figure 2.2, reads the P_{O_2} (atm) corresponding to the ΔG (applicable for metal/metal oxide system) at 950°C.

Syngas yield

As discussed in the manuscript, high syngas yield for methane PO_x can be achieved only within an intermediate P_{O_2} range. To obtain demarcations between the high yield vs low yield regions,

ASPEN Plus® was used to generate the boundary lines of the regions on the Ellingham diagram based on fixed syngas yields via Gibbs free energy minimizations. The following table lists the conditions of the ASPEN Plus® model used for the sensitivity analysis. The results from such a model are consistent with those obtained from HSC Chemistry v7.

Table A1: : Description of the ASPEN Plus® model.

Reactor model	RGibbs (all possible products)
Property method	PENG-ROB
Databank	PURE32, AQUEOUS, SOLIDS, INORGANIC, NRTL-SAC
Species considered	CH ₄ , C, CO, H ₂ , CO ₂ , H ₂ O
Operating pressure	1 atm
Methane feed	100 kmol hr ⁻¹
Temperature range tested	800° to 1000° C
Oxygen feed range tested	0 to 100 kmol hr ⁻¹

Each set of T and feed O₂ corresponds to a specific equilibrium P_{O₂} value, which was calculated from the product distribution at the reactor outlet (\dot{n} = molar flowrate)

$$P_{O_2} = \frac{\dot{n}_{O_2}}{\dot{n}_{O_2} + \dot{n}_{\text{all other gaseous products}}}$$

The syngas yield was calculated using the following equation:

$$Y_{\text{syngas}} = \frac{\dot{n}_{H_2} + \dot{n}_{CO}}{3 \times \dot{n}_{CH_4, \text{in}}}$$

With the syngas yield obtained at different T and corresponding P_{O₂}, the boundary lines were plotted on the Ellingham as shown in Figure 2.1a for 85%, 90% and 96% syngas yield. Figure 2.1b

was also generated using this method. In Figure 2.2, each of the grey dotted lines represent a constant P_{O_2} , with the corresponding value equal to the point of intersection on the right Y-axis at 950°C. An uncertainty of $\pm 0.1\text{eV}$ was used in calculating the energy of vacancy creation using DFT [1]. This error bar is shown in Figure 2.2, while representing the calculated P_{O_2} values for BMFO, BMO and MnO.

DFT calculations

To determine the oxygen vacancy formation energy ($\Delta E_{\text{vacancy}}$), the energy of three different systems was calculated: bulk crystal, defected crystal, and an isolated diatomic oxygen molecule. Both perfect and defected supercells were relaxed with respect to supercell volume and lattice parameters. BaMnO_3 and $\text{BaMn}_{0.5}\text{Fe}_{0.5}\text{O}_3$ employed g-type antiferromagnetic spin, FeO, employed paramagnetic spin ordering, and MnO employed paramagnetic spin ordering. These were chosen as they corresponded to the lowest energy of the pristine crystals. A-type, g-type, and paramagnetic was simulated for BaMnO_3 and $\text{BaMn}_{0.5}\text{Fe}_{0.5}\text{O}_3$. A-type and paramagnetic was simulated for MnO and FeO. G-type was not simulated as it would have been redundant (the same as a-type given the geometry). Spin ordering for a-type and g-type is demonstrated in the figure below:

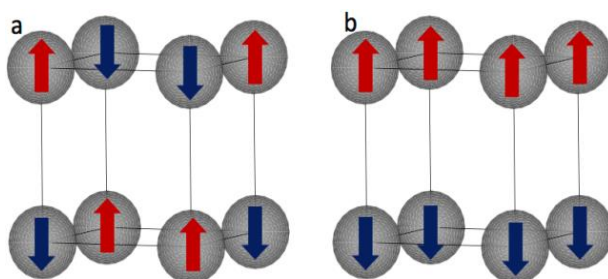


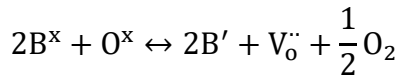
Figure A2: Diagram of spin ordering for a) g-type antiferromagnetic b) a-type antiferromagnetic.

Grey spheres represent sites of spin ordering.

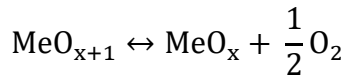
The energy of vacancy formation can be expressed in the following equation:

$$\Delta E_{\text{vacancy}} = E_{\text{defect}} + \frac{1}{2} \mu_{\text{O}_2} - E_{\text{perfect}}$$

It is noted that $(\Delta E_{\text{vacancy}})_2 - (\Delta E_{\text{vacancy}})_1$ is assumed to remain constant with temperature, as the entropy differences of pristine and defected crystals as well as gas-phase oxygen entropy contributions will cancel out when comparing the vacancy formation energy differences of two similar perovskites. The above equation is consistent with the following definition in Kröger-Vink notation, where B is the B-site cation.



Consider the following reaction 1, with a $\Delta G_{\text{reaction}} = \Delta G_{r1}$ (J molecule⁻¹):



$$\Delta G_{r1} = G_{\text{products}} - G_{\text{reactants}}$$

$$= \frac{1}{2} [H - T \cdot S]_{O_2} - [H - T \cdot S]_{x+1} + [H - T \cdot S]_x$$

$$= (H_x - H_{x+1}) + \frac{1}{2} \mu_{O_2} - T \cdot (S_x - S_{x+1})$$

$$= (E_{\text{defect}} - E_{\text{perfect}}) + \frac{1}{2} \mu_{O_2} - T \cdot (S_x - S_{x+1}) \quad (\text{assuming } H=E)$$

$$\Delta G_{r1} = \Delta E_{\text{vacancy}} - T \cdot (S_x - S_{x+1}) = -k_B \cdot T \cdot \ln K$$

where K is equilibrium constant and k_B is the Boltzmann constant)

$$K = [P_{O_2}]^{0.5}$$

$$2 \cdot \Delta G_{r1} = -k_B \cdot T \cdot \ln(P_{O_2})$$

Therefore, for reaction 2: $2\text{MeO}_{x+1} \leftrightarrow 2\text{MeO}_x + O_2$

$$\Delta G_{r2} = -k_B \cdot T \cdot \ln(P_{O_2})$$

For a single metal oxide system:

$$(P_{O_2})_1 = \exp \left[\frac{-(\Delta E_{\text{vacancy}})_1 + [T \cdot (S_x - S_{x+1})]_1}{k_B \cdot T} \right]$$

For the relative differences of two metal oxides (redox pairs) with similar structure:

$$\frac{(P_{O_2})_1}{(P_{O_2})_2} = \exp \left[\frac{(\Delta E_{\text{vacancy}})_2 - (\Delta E_{\text{vacancy}})_1}{k_B \cdot T} \right]$$

where $(S_x - S_{x+1})_1 \approx (S_x - S_{x+1})_2$. That is, the relative differences in configurational and vibrational entropy changes for two metal oxides undergoing a reduction reaction are assumed to be the same, when these two oxides have similar structures before and after the reaction.

The P_{O_2} value of FeO/Fe system at 950°C is assumed to be the reference point. The $\Delta E_{\text{vacancy}}$ values for FeO, BMFO, BMO and MnO are calculated using DFT (described in the Methods section), which are then used to estimate the P_{O_2} values of the other three systems at 950°C. DFT calculates the $\Delta E_{\text{vacancy}}$ values at 0 K. The P_{O_2} values of FeO/Fe and MnO/Mn systems are calculated at various temperatures using HSC Chemistry v7. Using the above equation, the values of $(\Delta E_{\text{vacancy}})_{\text{MnO}} - (\Delta E_{\text{vacancy}})_{\text{FeO}}$ are calculated. These values seem to show negligible change with temperature and are in close agreement with the DFT-calculated value for the same system. This is illustrated in Figure A3.

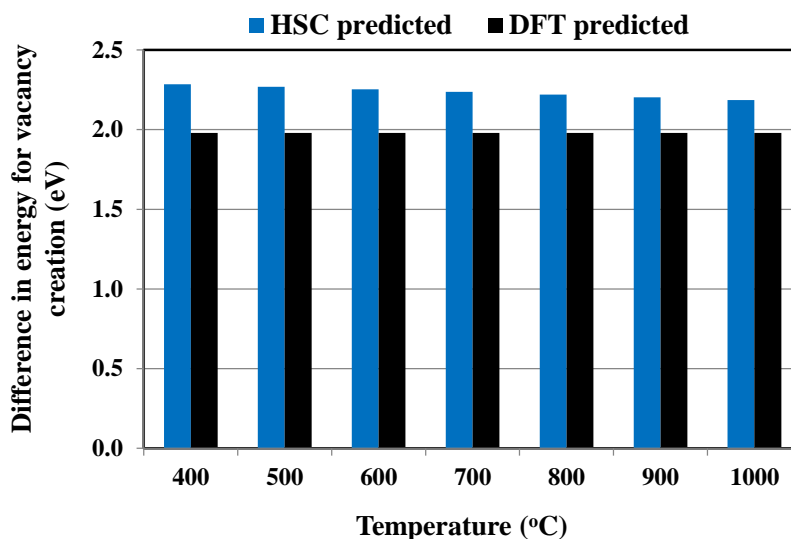


Figure A3: ($\Delta E_{\text{vacancy,MnO}} - \Delta E_{\text{vacancy,FeO}}$) at different temperatures predicted by DFT:

$$\Delta E_{\text{vacancy,MnO}} = 3.52 \text{ eV}, \Delta E_{\text{vacancy,FeO}} = 1.54 \text{ eV}, \Delta E_{\text{vacancy,MnO}} - \Delta E_{\text{vacancy,FeO}} = 1.98 \text{ eV}.$$

Experimental methods

Fluidized bed experiments

The set-up shown below was used for the fluidized bed experiments and the parameters for testing the performance are listed in Table A2. Table A3 lists the different conditions used for the feed gases. While the present study did not include use of direct solar energy an equivalent form of thermal energy was provided by external heating. Design of a solar concentrator/reactor configuration to achieve high solar flux, uniform heating up to $>1000^{\circ}\text{C}$ and efficient heat transfer to the desired location has been shown in literature^[2, 3]. All the reactions, which are proven to be feasible through the above-shown fluidized bed testing, will perform comparably if solar thermal energy is used. The performance of the redox catalyst over different sets of cycles over the entire

18 cycles is shown in Figure A5 and summarized in Table A4. The cycles 14-18 show an overall good performance and could be labelled as the optimized region of operation.

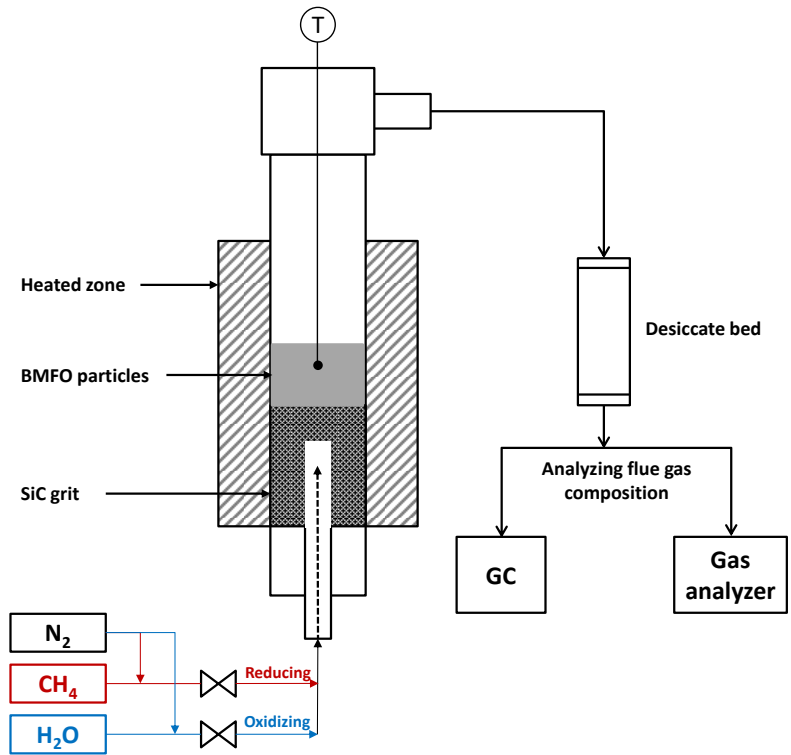


Figure A4: Experimental setup for the fluidized bed experiments.

Table A2: Parameters to test the performance of BMFO.

Syngas yield	as defined earlier
Methane conversion	$\left(1 - \frac{\dot{n}_{\text{CH}_4, \text{out}}}{\dot{n}_{\text{CH}_4, \text{in}}}\right) \times 100\%$
Steam conversion	$\frac{\dot{n}_{\text{H}_2, \text{out}}}{\dot{n}_{\text{H}_2\text{O}, \text{in}}} \times 100\%$
Hydrogen purity	$\frac{\dot{n}_{\text{H}_2, \text{out}}}{\dot{n}_{\text{H}_2, \text{out}} + \dot{n}_{\text{CO}, \text{out}} + \dot{n}_{\text{CO}_2, \text{out}}} \times 100\%$

Table A3: Feed flowrates (mL min^{-1}) and concentrations (vol%) (at 0°C and 1 atm) (N_2 as inert at 200 mL min^{-1}).

Cycles	Methane flowrate/concentration	Steam flowrate/concentration
1-13	3.2/1.6	6.8/3.3
14-18	3.2/1.6	4.7/2.3

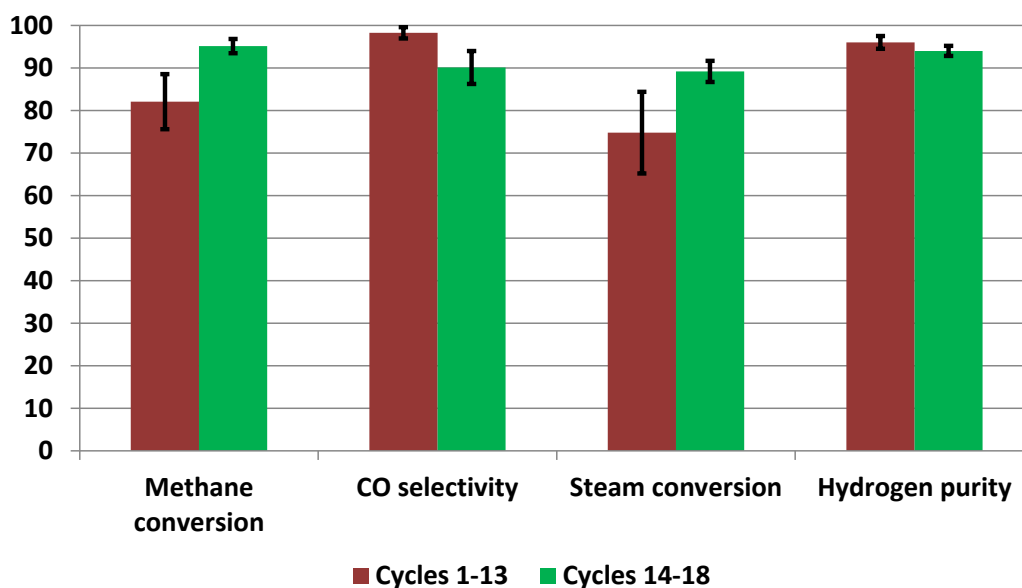


Figure A5: Performance of the redox catalyst during various sets of cycles (Error bars indicate 95% confidence interval).

Table S4: Summary of the performance during redox reactions (cycles 14-18).

Syngas yield (average/maximum)	88%/93%
Methane conversion (average/maximum)	95%/96%
Steam conversion (average/maximum)	89%/91%
Hydrogen purity (average/maximum)	94%/95%
Efficiency (ASPEN Plus) (Methane-to-fuel conversion)	83% (HHV)

Process modeling

Liquid fuel and hydrogen are produced in two redox steps using methane and solar energy in the hybrid solar-redox scheme ^[4-6]. In the first step (reducer), methane is partially oxidized by redox catalyst into CO and H₂, which is then converted into naphtha and diesel in the Fischer-Tropsch (F-T) reactors. In the subsequent step (oxidizer), steam oxidizes the reduced redox catalyst material from the previous step, producing concentrated H₂. Fe₃O₄-to-Fe swing is used for the simulation. As shown in Figure A6, ASPEN Plus® simulation is used to estimate reactor and process performances of the hybrid solar-redox concept. Detailed simulation assumptions with respect to materials, simulation modules, property methods, physical property databanks, and key operating parameters are summarized in our previous publications ^[4-6]. A steam conversion of 90% is used in the oxidizer whereas a methane conversion of 95% with 90% syngas yield is used in the reducer. The temperature of the reducer and oxidizer is set at 900 °C, which matches the experimental conditions. All other simulation assumptions and parameters are assumed to be the same as those in our previous model ^[4-6]. Table A5 shows the molar flow-rates of the key streams, obtained from the ASPEN Plus® simulation. Brief section-wise and overall consumed and generated-energy values are given in Table A6. Solar energy is assumed to be the source of energy for the endothermicity of the reducer. A solar absorption efficiency of 80% has been assumed ^[5]. These simulation results represent realistic estimates of the process performance with solar energy input. The higher heating values (HHV) of the fuels which include methane as the feed, hydrogen and liquid fuel (naphtha and diesel) as products, have been considered based on literature^[7,8]. The conventional steam methane reforming (SMR) process has been considered as the reference case for comparison based on previous analysis ^[7]. Figure A7 shows the energy balance comparison between conventional SMR and the hybrid solar redox process using BMFO.

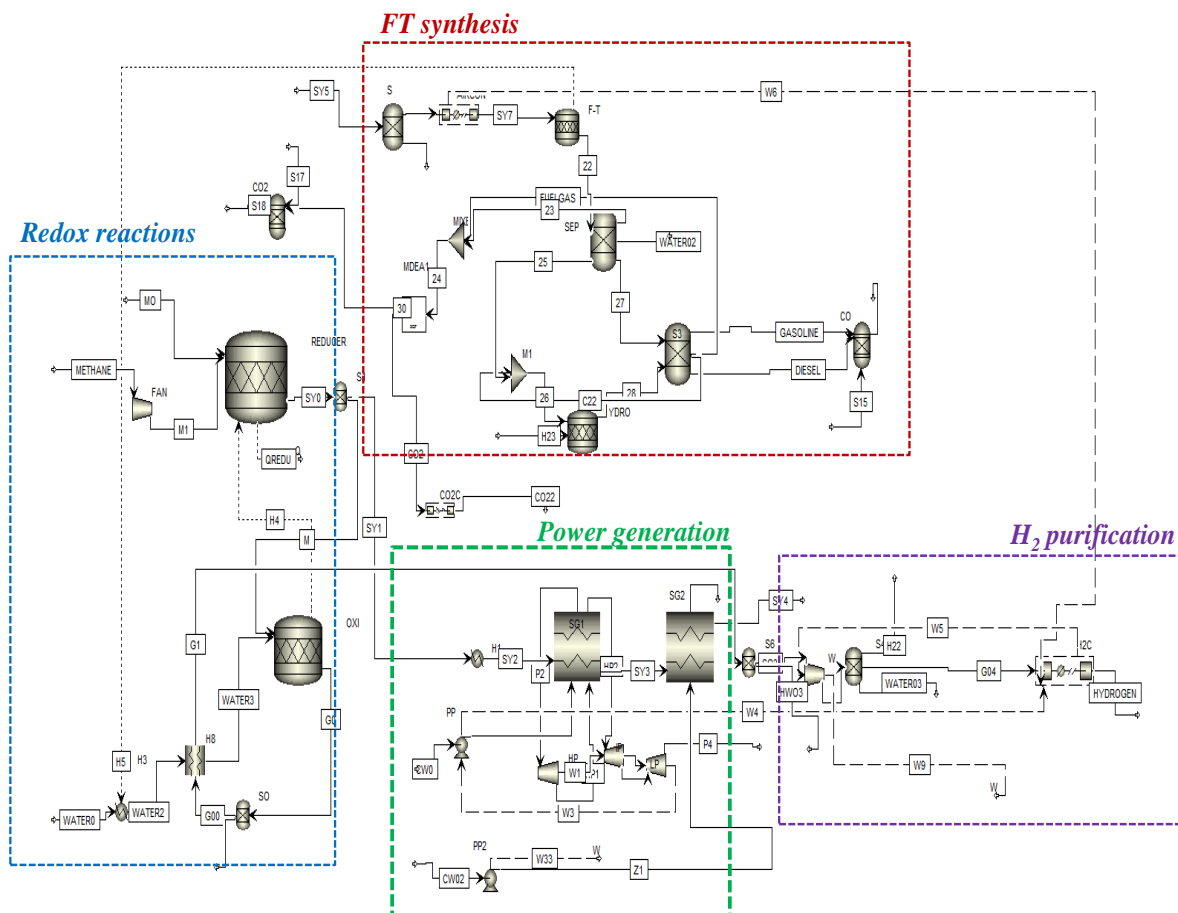


Figure A6: ASPEN Plus simulation of the hybrid solar redox process using BMFO.

Table A5: Flow-rates (kmol hr⁻¹) of key streams.

	Feed to the reducer	Reducer output	Post-F-T fuel gas	Liquid fuel	Oxidizer output	Post-PSA
CO	0	447	89	0	24	0
CO ₂	0	4.5	4.5	0	0	0
H ₂	0	893	154	0	535	509.4
H ₂ O	0	56.5	0	0	148	0
CH ₄	500	25	25.4	0	0	0
C ₂ -C ₄	0	0	2.7	0	0	0
C ₅ -C ₁₁	0	0	0	16.1	0	0
C ₁₂ -C ₁₉	0	0	0	13.9	0	0

Table A6: Energy consumed and generated from key units.

	Energy (MW)
Compressor for syngas	-4.5
PSA ^a	-2.4
H ₂ compressor	-4.2
Total consumption	-11.1
Heat recovery	2.5
Flue gas combustion	12.1
Total generation	14.6
Net power	3.5

^aPSA: Pressure Swing Adsorption

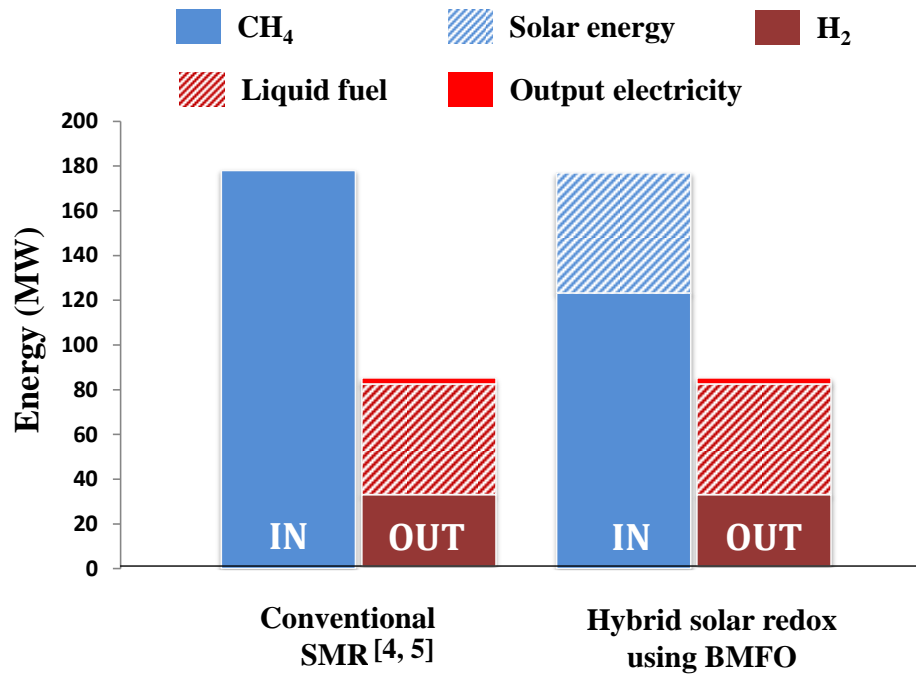


Figure A7: Energy balance comparison of the two cases for the same fuel output.

The following Table A7 lists the various process parameters used for the analysis and comparison (η denotes efficiency and e denotes CO₂ emissions):

Table A7: Process parameters for analysis.

Methane-to-fuel conversion efficiency	$\frac{\text{H}_2(\text{HHV}) + \text{Liquid Fuel (HHV)}}{\text{Methane feed (HHV)}}$
R	$\frac{\text{H}_2(\text{HHV})}{\text{H}_2(\text{HHV}) + \text{Liquid fuel (HHV)}}$
Equivalent efficiency for H₂ and liquid fuel production^[4]	$\left(\frac{R}{\eta_{\text{SMR for H}_2}} + \frac{(1 - R)}{\eta_{\text{SMR for liquid fuel}}} \right)^{-1}$
Equivalent CO₂ emissions for H₂ and liquid fuel production^[4]	$e_{\text{SMR for H}_2} \cdot R + e_{\text{SMR for liquid fuel}} \cdot (1 - R)$

Table A8: Process simulation results of BMFO in a hybrid solar redox scheme.

	This study	Reference case	
Methane feed	8 ton hr ⁻¹ [4,5]		
Methane-to-fuel conversion efficiency	83%	60%	<i>SMR equivalent efficiency for H₂ and liquid fuel production</i> [4,5,6]
CO₂ footprint (g CO₂ per MJ H₂)	25.0	85.5	<i>SMR for H₂ production</i> [4]
CO₂ footprint (g CO₂ per MJ of all fuel products)	64.7	91.3	<i>SMR for H₂ and liquid fuel production</i> [4]

The methane-to-fuel conversion efficiency of 83% is obtained for the process (assuming no CO₂ capture), which is 38% higher than the equivalent efficiency of a conventional SMR process on a relative basis. A life cycle greenhouse gas (GHG) footprint analysis is conducted, which considers the contributions from natural gas upstream and energy conversion facility. Emissions from the upstream natural gas production activities are assumed to be 9.1 kg CO₂ per mm Btu (8.6 g CO₂ MJ⁻¹) [4,9]. The emission analysis from energy conversion facility is based on ASPEN Plus® model

results. While considering only hydrogen production, CO₂-emission quota of 90 g MJ⁻¹ [6] for the liquid fuel products, which is identical to the case of petroleum derived fuels, is subtracted. The CO₂ footprint from the hybrid solar-redox scheme is shown in Table A8.

References

- [1] K. Lejaeghere, V. Van Speybroeck, G. Van Oost, S. Cottenier, *Crit. Rev. Solid State Mater. Sci.* **2014**, 39, 1.
- [2] Y. Tamaura, A. Steinfeld, P. Kuhn, K. Ehrensberger, *Energy* **1995**, 20, 325.
- [3] C. L. Muhich, B. D. Ehrhart, I. Al-Shankiti, B. J. Ward, C. B. Musgrave, A. W. Weimer, *Wiley Interdiscip. Rev. Energy Environ.* **2016**, 5, 261.
- [4] F. He, J. Trainham, G. Parsons, J. S. Newman, F. Li, *Energy Env. Sci* **2014**, 7, 2033.
- [5] F. He, F. Li, *Int. J. Hydrog. Energy* **2014**, 39, 18092.
- [6] F. He, F. Li, *Energy Env. Sci* **2015**, 8, 535.
- [7] U. Bossel, B. Eliasson, **2003**.
- [8] D. Hofstrand, *Iowa State Univ. Ext. Outreach* **2007**.
- [9] P. Jaramillo, W. M. Griffin, H. S. Matthews, *Environ. Sci. Technol.* **2008**, 42, 7559

Appendix B: Supplementary Information for Chapter 3

DFT Computations

Model construction, oxygen formation energy and migration barrier calculations of bulk CeO₂ and LaCeO_{3.5}

The atomic model of pristine CeO₂ unit cell is shown in Figure B1a, the optimized lattice constant is 5.418 Å, which is very close to the experimental reports (5.411 Å)^[1]. The LaCeO_{3.5} unit cell is built by replacing two Ce atoms by two La atoms, and then removing one O atom to form an oxygen vacancy (V_O) as shown in Figure B1b. Due to symmetry, the selection of the La doping and V_O sites in the CeO₂ unit cell is unique. Subsequently, a 2 × 2 × 2 supercell of LaCeO_{3.5} bulk structure is built to avoid artificial interactions induced by the periodic boundary condition. In this model, all 7 non-equivalent sites depicted in Figure B2 are considered to calculate the oxygen vacancy formation energy (ΔE_V) (Table B1) and the most stable one (O1 site) is chosen for subsequent calculations. The computed lowest ΔE_V of LaCeO_{3.5} is 2.26 eV, which is much lower than pristine CeO₂ (2.99 eV^[2]). Upon the formation of one V_O, all adjacent 6 O atoms are considered to migrate to the vacancy site, and the corresponding reaction energies are listed in the Table B2. Among these possible oxygen mobility pathways, the migration of O5 and O7 will no longer be considered due to their very large reaction energies, which indicates their barriers could be even larger. Then the transition state calculations of the migration of the rest oxygen atoms (O2, O3, O4 and O6) are performed as shown in Figure B3. The computed lowest migration barrier (0.30 eV) is lower than it is in CeO₂ (0.46 eV^[3]) (Figure 3.1b), suggesting that the oxygen migration is more likely to occur in LaCeO_{3.5} than in CeO₂. It is found that the O atom initially neighboring to three oxygen vacancies is most likely to migrate (O6 → V_O).

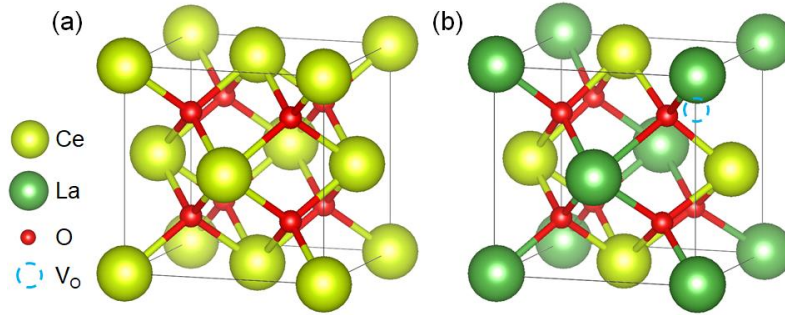


Figure B1: Model structures of (a) CeO_2 and (b) $\text{LaCeO}_{3.5}$.

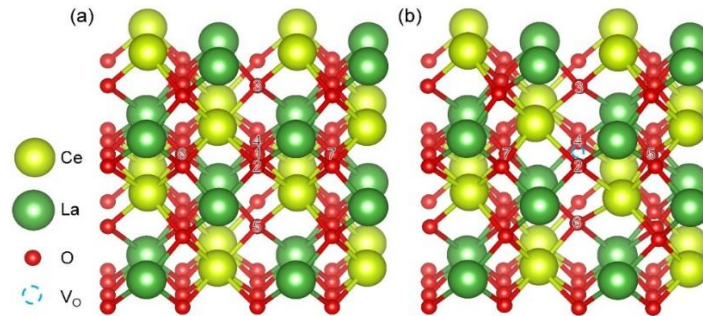


Figure B2: Model structures of (a) $\text{LaCeO}_{3.5}$ bulk $2 \times 2 \times 2$ supercell (b) $\text{LaCeO}_{3.5}$ bulk $2 \times 2 \times 2$ supercell with V_O at the O1 site.

Table B1: Computed ΔE_V of each oxygen site in $\text{LaCeO}_{3.5}$.

Vacancy Site	ΔE_V (eV)
O1	2.26
O2	2.69
O3	2.61
O4	2.57
O5	3.65
O6	2.59
O7	4.25

Table B2: Computed reaction energies of each oxygen migration to the V_O site in $\text{LaCeO}_{3.5}$.

Oxygen migration pathways	Reaction energy (eV)
$O2 \rightarrow V_O$	0.43
$O3 \rightarrow V_O$	0.36
$O4 \rightarrow V_O$	0.31
$O5 \rightarrow V_O$	1.40
$O6 \rightarrow V_O$	0.33
$O7 \rightarrow V_O$	2.00

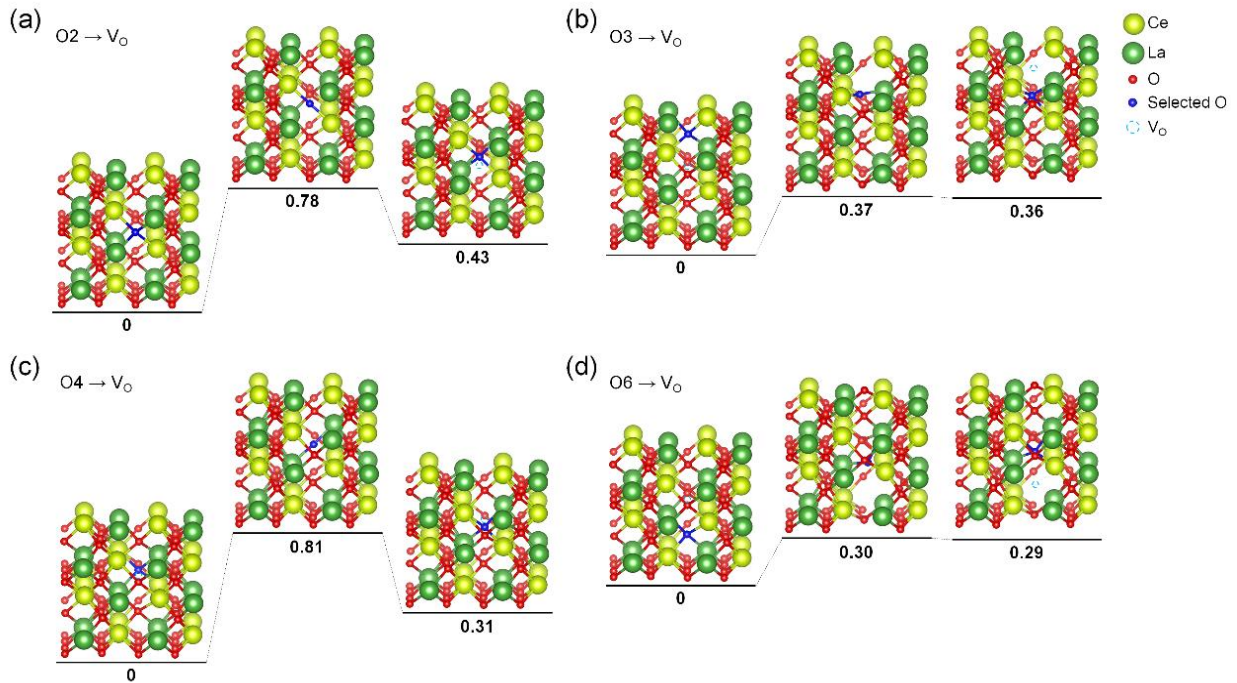


Figure B3: Energy potential profile along the (a) $O2 \rightarrow V_O$, $O3 \rightarrow V_O$, $O4 \rightarrow V_O$ and $O6 \rightarrow V_O$ pathways in $\text{LaCeO}_{3.5}$ bulk. Among these, the $O6 \rightarrow V_O$ is the most favorable one with the lowest barrier of 0.30 eV.

Model construction, oxygen formation energy and migration barrier calculations of CeO_2 and $\text{LaCeO}_{3.5}$ (111) surface

The atomic model of CeO_2 (111) surface can be directly cleaved from the CeO_2 bulk model. While the $\text{LaCeO}_{3.5}$ (111) unit cell is firstly cleaved from the $\text{LaCeO}_{3.5}$ bulk model and then replace one

outermost Ce atom with La atom artificially to reproduce the La: Ce ratio obtained through XPS. Subsequently, the $(2 \times 1 \times 1)$ supercell models of both CeO_2 and $\text{LaCeO}_{3.5}$ (111) are used to avoid artificial interactions induced by the periodic boundary condition as shown in Figure 3.2c in the main text and Figure B4. In this model, there are only two non-equivalent surface oxygen atom sites, namely A and B. The computed ΔE_V of A and B sites are -1.03 and -2.03 eV respectively, both are much lower than pristine CeO_2 (2.73 eV). Negative values of ΔE_V indicate that both A and B oxygen are readily to release. Then we move on to study the migration of adjacent sub-surface oxygens to A or B vacancy sites respectively as shown in Figure B5. The corresponding reaction energies of all possible O migration pathways are listed in Table B3, in which the migration of O2 or O4 to B site will no longer be considered due to the very large reaction energies. The energy potential surfaces of the rest migration pathways are further studied as shown in Figure B6. The most favorable pathway (O1 \rightarrow A) has a very low barrier of 0.16 eV, which is much lower than CeO_2 (111) surface (0.47 eV) (Figure 3.1b and 3.1d).

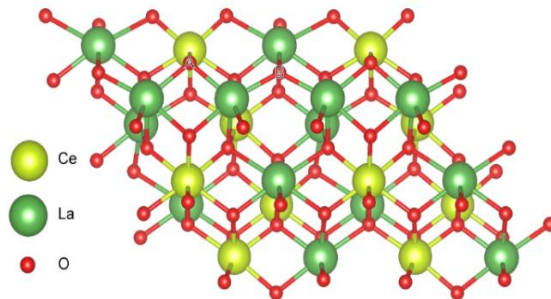


Figure B4: Model structures of $\text{LaCeO}_{3.5}$ (111) surface. A and B sites are the two non-equivalent sites on the surface.

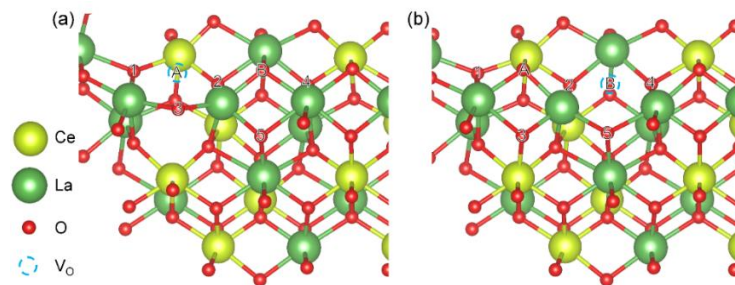


Figure B5: Model structures of $\text{LaCeO}_{3.5}$ (111) surface with (a) A and (b) B site vacancy. Here O1-O5 are all sub-surface lattice oxygen.

Table B3: Computed reaction energies of each oxygen migration to the A or B site in $\text{LaCeO}_{3.5}$ (111).

Oxygen migration pathways	Reaction energy (eV)
O1 → A	-0.15
O2 → A	-0.06
O3 → A	-0.09
O2 → B	0.91
O4 → B	1.16
O5 → B	0.03

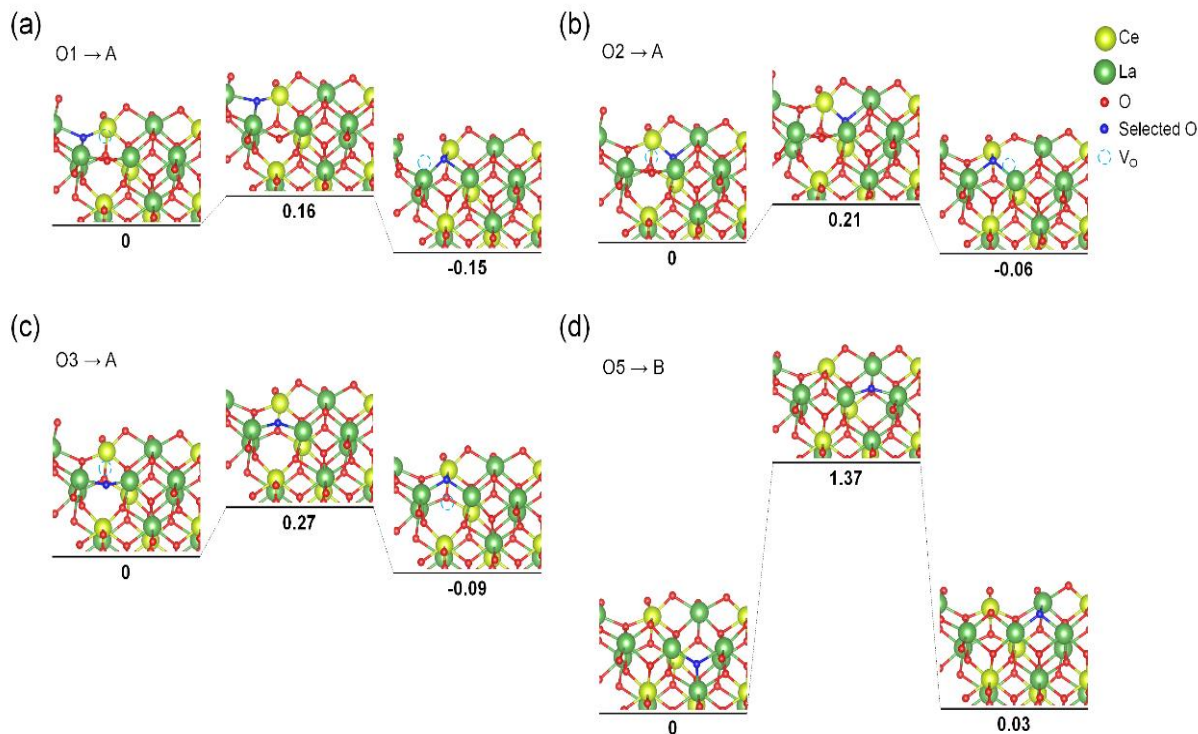


Figure B6: Energy potential profile along the (a) $O1 \rightarrow A$, (b) $O2 \rightarrow A$, (c) $O3 \rightarrow A$ and (d) $O5 \rightarrow B$ pathways on $LaCeO_{3.5}$ (111) surface. Among these, the $O1 \rightarrow A$ is the most favorable one with the lowest barrier of 0.16 eV.

Process Simulations

Acetic acid production

The process for the production of acetic acid (AcOH) using the HRP is shown in Figure B7. This is based on our previous work^[4]. Overall, the process is split into three sections: syngas generation, methanol (MeOH) synthesis, and AcOH reactor. For the overall process, methane and CO_2 are the feed and the product is AcOH. The redox catalyst considered for the process is LCO. Based on the available AspenPlus[®] database, $CeO_2 \leftrightarrow Ce_2O_3$ transition is used. The AspenPlus[®] flowsheet for the entire process is shown in Figure B8.

Hybrid Redox Process (HRP)

Reducer is where methane POx occurs and is assumed to be operated at 650°C and 1 bar. Methane is fed to the reducer at the operating pressure. 90% methane conversion (X_{CH_4}) is assumed with 90% selectivity to CO (S_{CO}). The definitions of these terms are:

$$X_{CH_4} = \frac{\dot{n}_{CH_4,reacted}}{\dot{n}_{CH_4,feed}} \quad (B1)$$

$$S_{CO} = \frac{\dot{n}_{CO}}{\dot{n}_{CO} + \dot{n}_{CO_2}} \quad (B2)$$

CeO_2 is assumed to get reduced to Ce_2O_3 . The product stream from the reducer contains syngas. Ce_2O_3 is oxidized in a separate reactor called a CO_2 -splitter, which is at 650°C and 1 bar. 100% of the feed CO_2 is assumed to get converted to CO with no other byproducts. For the simulation, RStoic reactor models are used for the reducer and CO_2 -splitter. The CO-rich product stream at 650°C is partially used to preheat the CO_2 feed stream. The CO-rich stream is later used as a feedstock for the acetic acid (AcOH) synthesis. Ce_2O_3 is oxidized back to CeO_2 by CO_2 , with the CeO_2 being recycled back to the reducer. The following reactions are assumed in the two reactors:

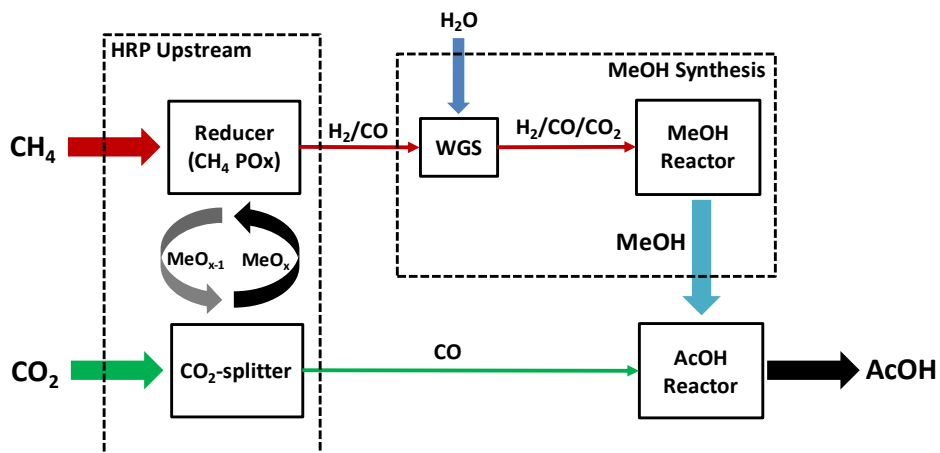
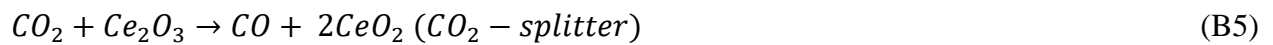
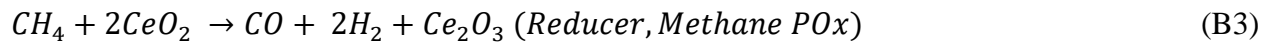


Figure B7: Block diagram of HRP^[4].

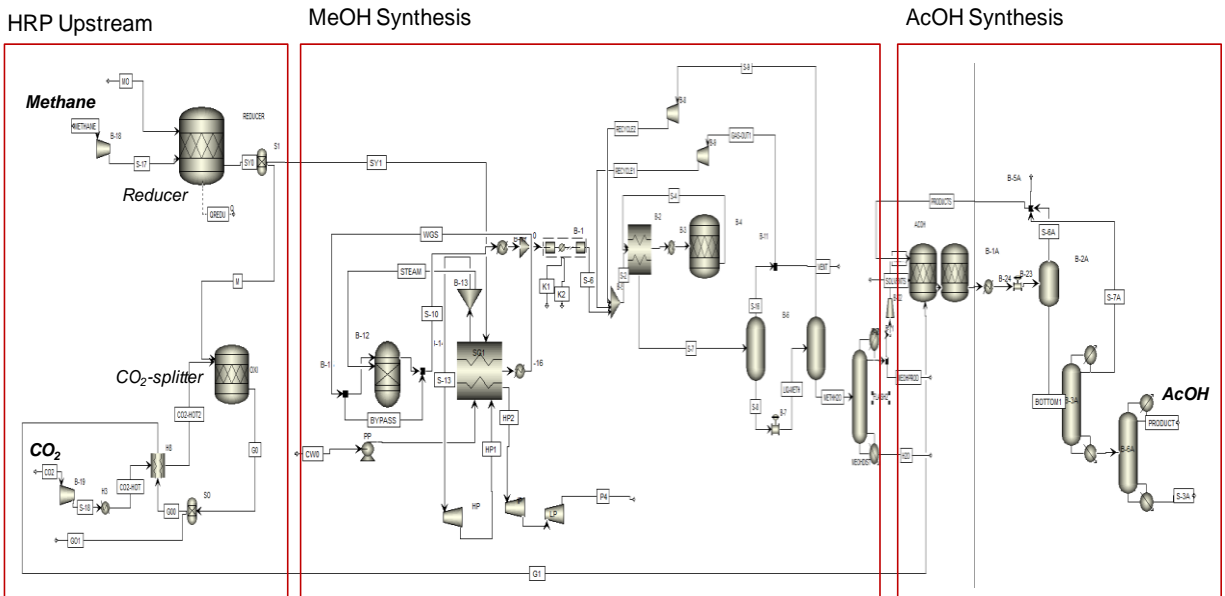


Figure B8: AspenPlus® flow diagram for HRP.

Methanol synthesis

Methanol is synthesized with syngas (with CO₂) using a commercial Cu/Zn/Al₂O₃ catalyst^[5]. A packed tubular reactor is used, which is approximated using an RStoic model in AspenPlus®. The required fresh feed composition for the MeOH reactor is CO: CO₂: H₂ ≈ 23:7:70 (by vol)^[6]. CO₂ along with CO contribute towards the formation of MeOH. CO₂ needs to be added to the stream with a reduction in H₂, so that the CO_x: H₂ ratio remains the same. This can be done using the water gas shift (WGS) reaction. As shown in Figure B7, water is fed to a WGS reactor, modeled as an RGibbs reactor, at 400 °C and 20 bar. A Heat Recovery Steam Generator (HRSG) scheme is also implemented to generate power from steam. The exit stream of the WGS reactor is cooled to around 100°C and then compressed to 105 bar for MeOH synthesis, condensing out the water. The stream has the desired composition of CO/CO₂/H₂. This forms a part of the feed pretreatment for MeOH synthesis.

The MeOH reactor operates at 265 °C and 105 bar, with a 64% yield of $\text{CO} \rightarrow \text{MeOH}$ and 17% yield of $\text{CO}_2 \rightarrow \text{MeOH}$ ^[5,6]. The product is cooled and is flashed in two stages at 35 °C, with a sequential pressure reduction to eventually separate the gases (CH_4 , CO , CO_2 , H_2) from the $\text{MeOH} + \text{H}_2\text{O}$ liquid mixture (4:1, by vol). This mixture is fed to a distillation column to obtain 99% pure MeOH at the top. The gases are recycled, with a small fraction (3%) as vent, such that the feed stream (fresh + recycled) has a composition of $\text{CO} : \text{CO}_2 : \text{H}_2 = 14 : 19 : 67$, with the desired one being 10:10:80. Overall, 95% conversion of CO_x to MeOH has been achieved.

AcOH reactor

The synthesis of AcOH using MeOH and CO is done using the Cativa™ process^[7]. This commercial process produces AcOH by the carbonylation of MeOH, via an iridium-containing complex and hydrogen iodide (HI). A two reactor scheme has been used for modeling the process. Based on the commercial process^[7], the reactors are set at 190 °C and 22 barg and modeled as RStoic reactors. The first reactor involves reactions of MeOH with HI to give AcOH via AcI (methyl iodide). HI is replenished and is not consumed in the process. The second reactor assumes the formation of byproducts like propionic acid and CO_2 via WGS reaction, from the remaining MeOH. As most of the MeOH is consumed towards AcOH, the process leads to negligible amount of these byproducts. The reactions considered are given below where 99.96% of MeOH is assumed to be consumed. The required CO for this process is obtained from the product stream of the CO_2 -splitter. As shown in Figure B8, the AcOH product stream is cooled and flashed at a lower pressure (15 barg), to obtain the unreacted HI, which is recycled. The distillation columns give 99.5% pure AcOH. Based on the overall reaction, almost 100% of the MeOH and 97% of the CO are consumed. This is close to the literature value of >94% CO utilization for the Cativa™ process^[7].





Coal Gasification (CG)

The hybrid solar-redox process is compared with the traditional CG process to obtain syngas^[8], followed by MeOH synthesis with subsequent AcOH synthesis. The process is shown in Figure B9 and B10. Coal is assumed to be composed of pure carbon (C) with feed-water to be 40% more than the feed coal (by moles). An efficiency of 96% is assumed for the air separation unit (ASU), with the final O₂: C = 0.5. An adiabatic RGibbs reactor model is used for the gasifier, operating at 30 bar. The product distribution is found to be CO: CO₂: H₂ = 30:35:35. WGS reaction is done followed by CO₂ removal (by amine scrubbing), to keep the composition to 24:6:70, as required for the MeOH synthesis. H₂ and CO₂ removal is required for CO production, which requires additional power, but the H₂ can be used as a fuel. The separated-CO₂ is not compressed. All the following units are similar to the HRP process. The end-product is AcOH. The CO required for AcOH synthesis is provided by additional gasification of coal followed by CO₂ and H₂ removal. The other key assumptions for these AspenPlus[®] models are listed in Table B4. The overall reaction in this route is as follows:



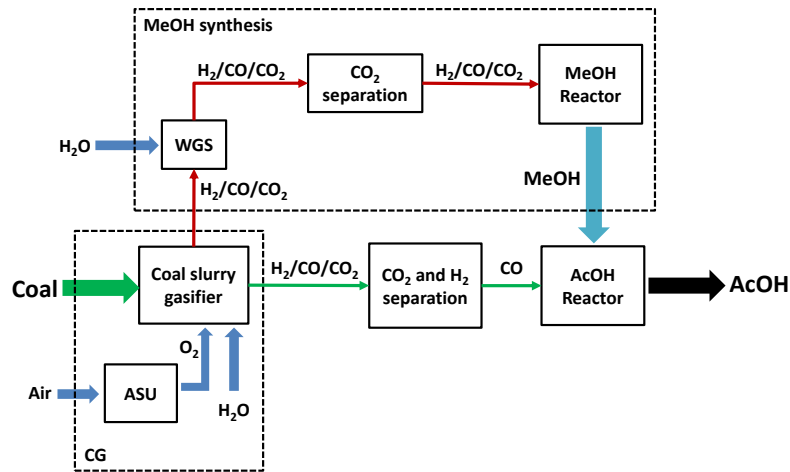


Figure B9: Block diagram of CG route^[4].

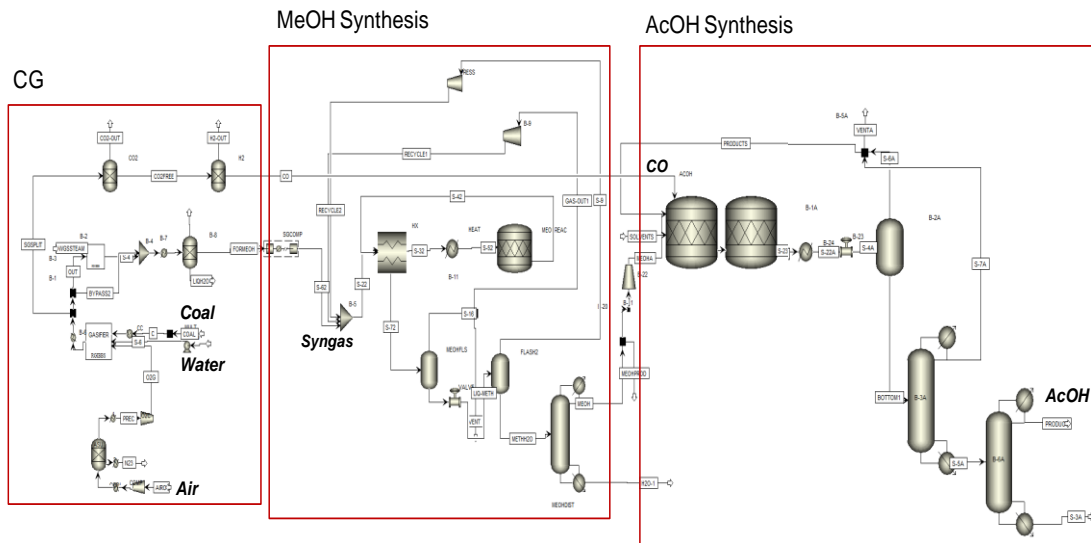


Figure B10: Block diagram of CG route^[4].

Table B4: AspenPlus[®] modules, property methods and databanks.

Stream class	MIXCISLD
Databank	PURE, AQUEOUS, SOLIDS, INORGANIC
Property method	PR-BM and STEAM –TA for steam cycles
Unit operation models	
Pressure changers	MCompr
Heat exchangers	Heater
Distillation columns	DSTWU
Separators/Flash columns	Sep/Flash2

Process analysis

Based on the AspenPlus® model for both the processes, the energy requirements are compared in Table B5. Comparison is done based on the thermal energy demand for each unit of the process. 85% conversion efficiency of thermal to steam energy and 40% for thermal to electricity is assumed. For the ASU, 230 kW-hr demand/ton of O₂ is assumed^[8]; for CO₂ removal, 0.12 MW-hr/tonne of CO₂ is assumed^[9] (for CO₂-separation without the following compression); for H₂-pressure swing adsorption (PSA), 0.2 kW-hr/kg H₂ is assumed^[8].

Table B5: Comparison of HRP with CG.

	HRP	CG
Methanol out (kg/hr)	2507	2594
Acetic acid (AcOH) out (kg/hr)	4678	4831
Methane in (kg/hr)	1440	
Coal in (kg/hr)		5510
Syngas feed to methanol unit (kg/hr)	3137	3075
(MeOH synthesis section)		
Demand in GJ/tonne methanol		
Upstream	2.65	12.94
Reactor	-1.26	-0.83
Downstream	0.06	-0.20
HRP upstream section		
Reducer	13.28	
Oxidizer	-2.77	
Methane compressor	0.00	
CO ₂ feed compressor	0.00	
Cooling water pump	0.03	
Steam cycle	-0.04	
Gasifier upstream section		
ASU		6.10
Oxygen compressor		3.33
Coal preheat		0.24
CO ₂ removal		5.26

Table B5 (continued): Comparison of HRP with CG

HRP AcOH section (GJ/tonne AcOH)		
Upstream	0.65	0.65
Reactor	-1.75	-1.79
Downstream	12.96	21.29
Methanol demand (GJ/tonne methanol)		
Overall	12	27
With waste heat	-1.3	27
AcOH demand (GJ/tonne AcOH)		
Overall	18.3	34.6
With waste heat	11.1	34.6
Production		
Tonne methanol/tonne feed fuel	1.7	0.5
Tonne methanol/GJ feed fuel	31	12
Tonne AcOH/tonne feed fuel	3.2	0.9
Tonne AcOH/GJ feed fuel	58.6	23.1

Net CO₂ Production

Net CO₂ production considers the contributions from natural gas/coal upstream and energy conversion facility. The estimated upstream natural gas emission based on US-DOE report is 9.1 g CO₂/MJ for CH₄ and 10 g CO₂/MJ for coal^[10]. The emission analysis for the two processes is based on AspenPlus[®] model results. For both the processes, it is assumed that the thermal energy requirements are met by burning the necessary amount of methane. 80% efficiency of combustion has been assumed. The CO₂ emissions arising from the energy demand are calculated accordingly. The HHV of coal, methane and AcOH are assumed to be 30.1, 55.5 and 14.6 MJ/kg respectively^[11]. For the HRP, CO₂ usage as a feed leads to a CO₂ credit. In CG, the separated-CO₂ is not compressed. The H₂ separated (0.43 MJ of H₂ per MJ of produced AcOH) is assumed to be used

for process energy requirements, with no associated CO₂ emissions. Figure B11 shows the rationale in this calculation and the comparison. All units in the figure are g CO₂/MJ AcOH, unless specified.

Net CO₂ Production (for CG, after burning the separated H₂) (g CO₂/MJ produced AcOH)

= CO₂ Production due to upstream coal processing + CO₂ Production due to methane combustion to suffice overall energy demand

Net CO₂ Production (for HRP) (g CO₂/MJ produced AcOH)

= CO₂ Production due to upstream methane processing + CO₂ Production due to methane combustion to suffice overall energy demand – CO₂ credit for utilizing CO₂ in the process

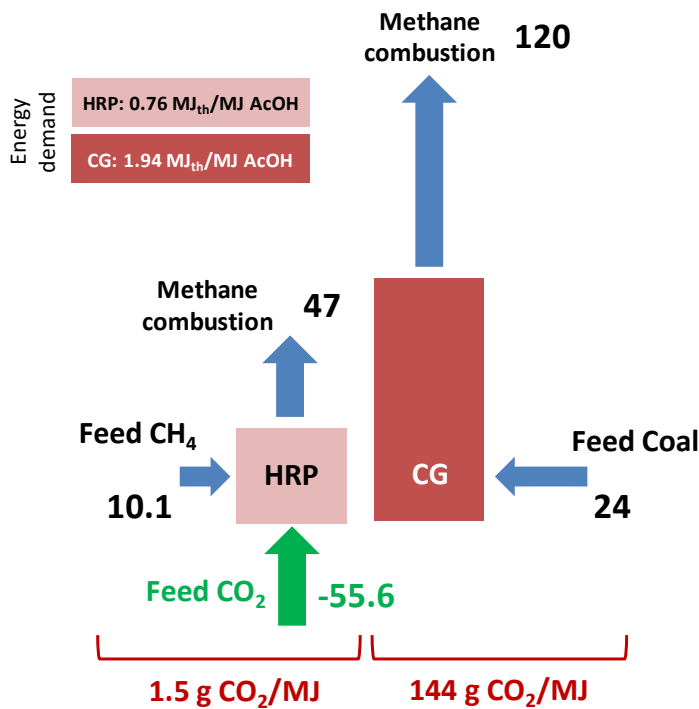
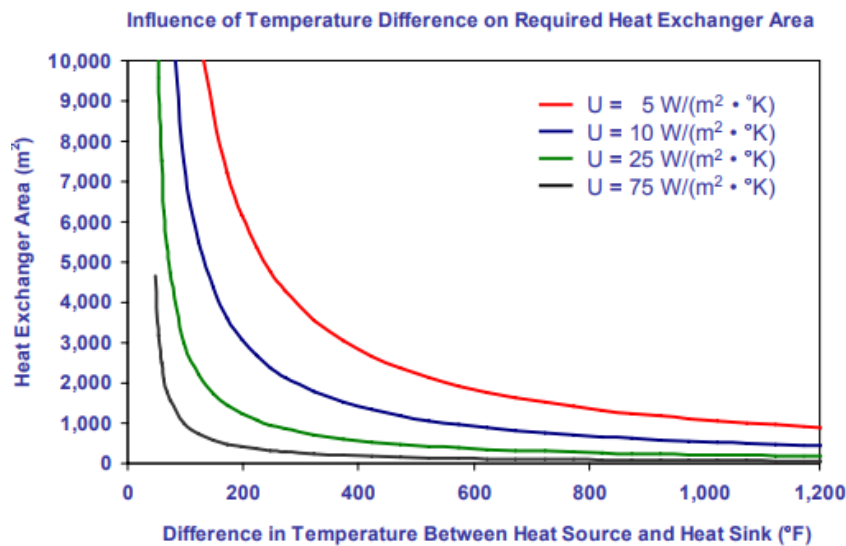


Figure B11: Net CO₂ production of the two processes (all figures are in g CO₂/MJ AcOH, unless defined separately).

Waste Heat

The magnitude of the temperature difference between the heat source and sink determines the utility and quality of the waste heat (or exergy efficiency). The source and sink temperature difference influences (i) the rate at which heat is transferred per unit surface area of heat exchanger, and (ii) the maximum theoretical efficiency of converting thermal from the heat source to another form of energy. Based on the figures below, operating at 650°C (assuming $T_{\text{source}} = 1400^{\circ}\text{C}$, $\Delta T = 750^{\circ}\text{C}$ or 1382°F) enables HRP to efficiently utilize the waste heat and also helps in easier design through lower heat exchange area requirements.



This figure graphs the surface area (m²) required for recovering 10 million Btu/hr from a gaseous exhaust stream with a mass flow rate of 5 million lbs/hr by transfer to liquid water flowing at 1 ft³/s. Calculated from Equation 2 using estimated log mean temperature difference for ΔT .

Figure B12a: Influence of source and sink temperature (ΔT) on required heat exchanger area

(adapted from ^[12]).

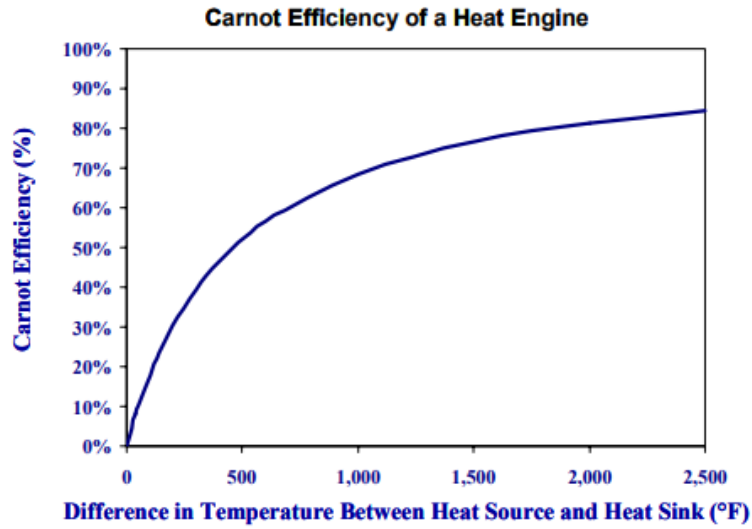


Figure B12b: Variation of heat engine Carnot efficiency as a function of ΔT (adapted from ^[12]).

X-Ray Diffraction

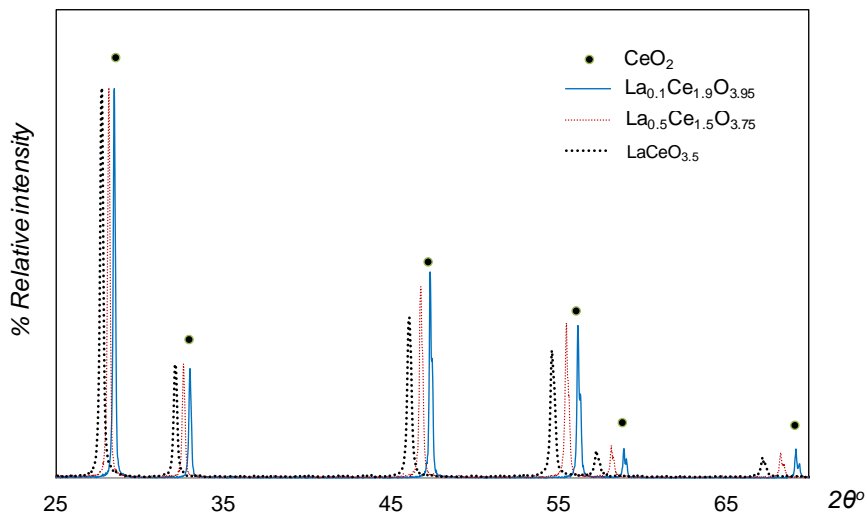


Figure B13a: XRD patterns of pure and La-substituted CeO_2

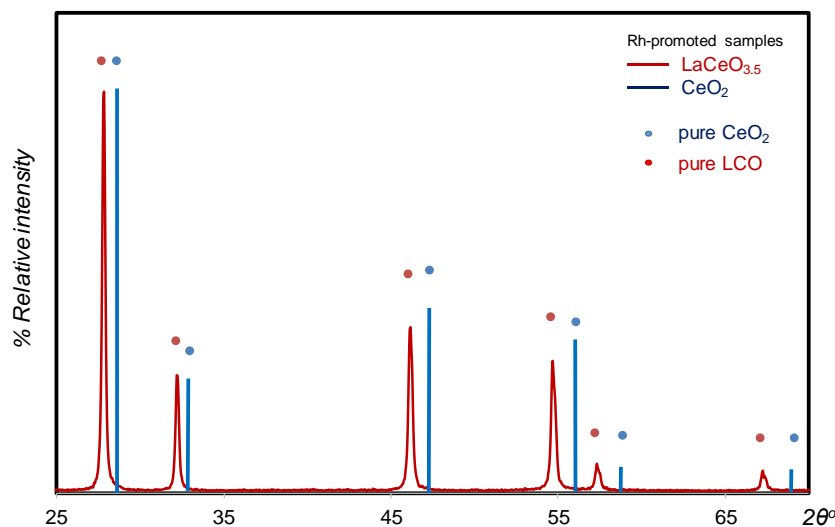


Figure B13b: XRD patterns of CeO₂ and La-substituted CeO₂; with and without Rh-promotion [based on the obtained and matched patterns, the unit cell parameter remained unchanged on Rh-promotion, indicating the absence of Rh in bulk structure. Matched XRD reference codes: CeO₂ is 01-078-3999 and LCO is 04-012-6396].

The following tables contain the peak analysis^[13] for the *in-situ* XRD, to estimate the contribution of thermal expansion to the overall expansion of lattice.

Table B6a: Peak positions (2θ°) of oxidized Rh/LCO: Room temperature (RT) to 740°C.

Peak #	1	2	3	4
RT	27.676	32.061	46.032	54.593
740	27.676	32.009	45.848	54.304

Bragg's equation: $n \cdot \lambda = 2 \cdot d \cdot \sin \theta$; where n is the order of reflection, λ is the wavelength of X-ray, d is the interplanar spacing and θ is the Bragg angle (radians).

For cubic systems: $a = d \cdot \sqrt{h^2 + k^2 + l^2}$, where a is the unit cell parameter and h , k and l are Miller indices. Unit cell parameter after expansion can be estimated^[14] using: $\frac{\Delta d}{d} = \frac{\Delta a}{a}$

In the following calculation, a_1 (Å) is obtained from the Rh/LCO pattern fitted to the literature data (Ref code: 04-012-6396) using the HighScorePlus® software.

Table B6b: Lattice parameter of the expanded lattice at 740°, from RT.

Peak #	θ_1	θ_2	$\sin \theta_1$	$\sin \theta_2$	d1/d2	$\Delta d/d_2$	$\Delta a/a_2$	a1	a2
1	0.483037	0.483037	0.46447113	0.464471	1	0	0	5.5770	5.577
2	0.55957	0.558662	0.53082184	0.530052	0.998551	0.001449	0.00144939	5.5770	5.585095
3	0.80341	0.800199	0.71972766	0.717494	0.996897	0.003103	0.00310291	5.5770	5.594359
4	0.952828	0.947784	0.81505702	0.812124	0.996402	0.003598	0.00359822	5.5770	5.59714
							Average	5.5770	5.5884

Table B6c: Peak positions (2 θ) of Rh/LCO at 740°C: Oxidized to reduced (in methane).

Peak #	1	2	3	4
740 Oxi	27.676	32.009	45.848	54.304
740 Red	27.545	31.904	45.612	54.015

Table B6d: Lattice parameter of the expanded lattice at 740°, from oxidized to reduced (in CH₄).

Peak #	θ_1	θ_2	$\sin \theta_1$	$\sin \theta_2$	d1/d2	$\Delta d/d_2$	$\Delta a/a_2$	a1	a2
1	0.483037	0.480751	0.46447113	0.462445	0.995638	0.004362	0.00436196	5.5884	5.612882
2	0.558662	0.55683	0.53005247	0.528498	0.997067	0.002933	0.00293342	5.5884	5.60484
3	0.800199	0.79608	0.71749441	0.714619	0.995993	0.004007	0.00400729	5.5884	5.610883
4	0.947784	0.94274	0.81212426	0.809171	0.996363	0.003637	0.00363665	5.5884	5.608796
							Average	5.5884	5.6093

Table B6e: Unit cell expansion due to heat and methane reduction.

Parameter	Oxidized		Reduced
	25 C	740 C	740 C
a	5.5770	5.5884	5.6093
Δa (thermal)		0.011	
Δa (reduction)			0.021
Δa (overall)		0.032	
$\% \Delta a$ (thermal)		0.204	
$\% \Delta a$ (reduction)			0.375
$\% \Delta a$ (overall)		0.580	

Methane TPR

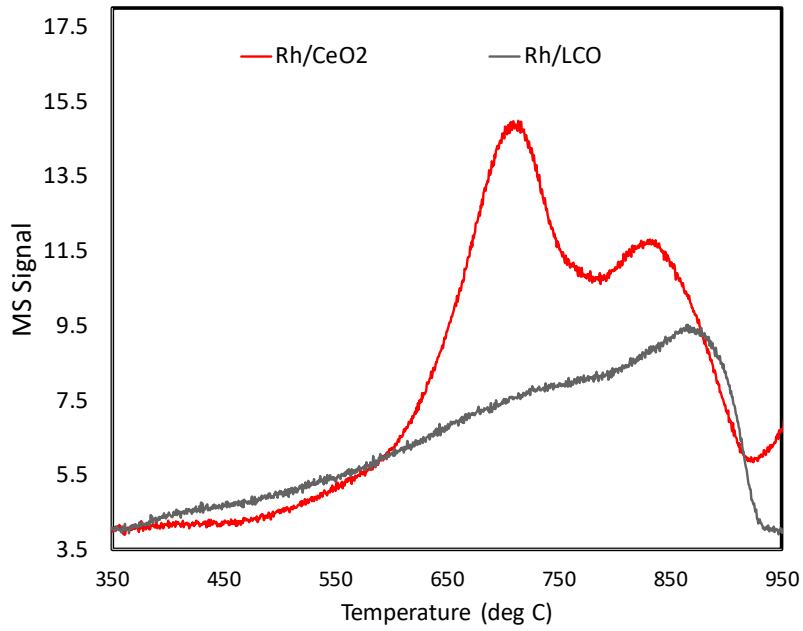


Figure B14a: CH₄ TPR of Rh-promoted CeO₂ and LCO.

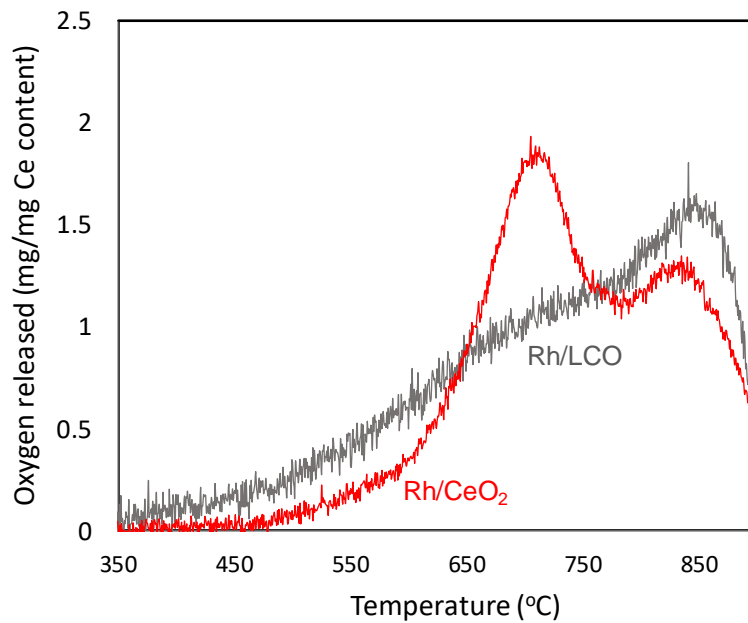


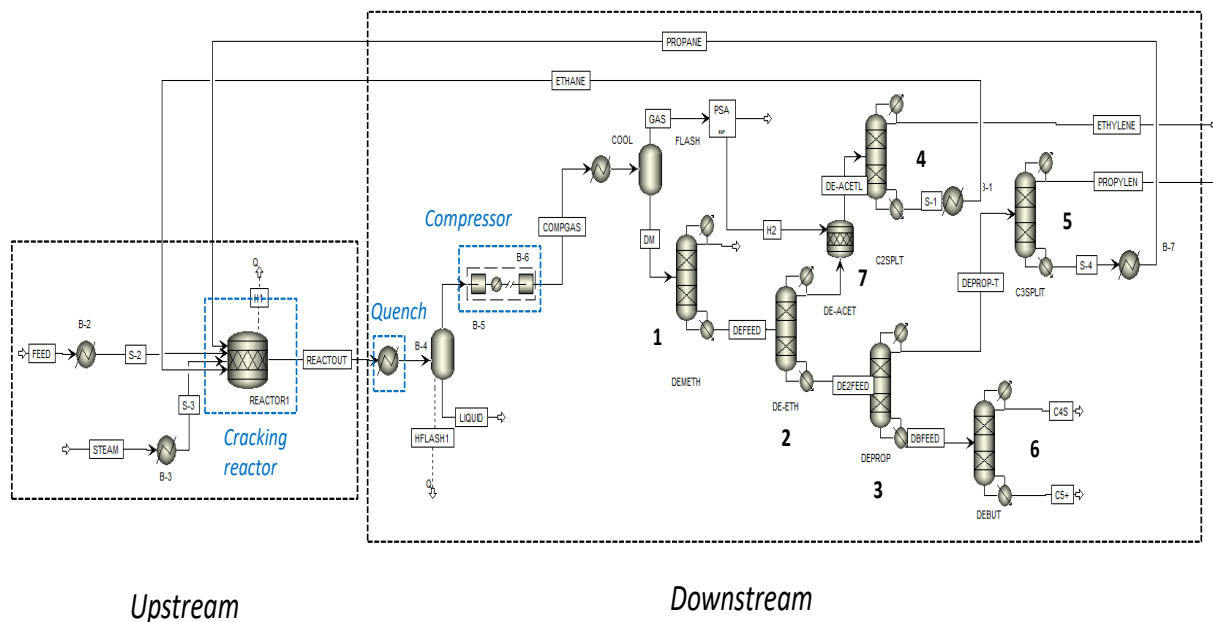
Figure B14b: CH₄ TPR of Rh-promoted CeO₂ and LCO, with oxygen normalized to Ce content.

References

- [1] L. Gerward, J. Staun Olsen, L. Petit, G. Vaitheeswaran, V. Kanchana, A. Svane, *J. Alloys Compd.* **2005**, *400*, 56.
- [2] Z. Yang, G. Luo, Z. Lu, K. Hermansson, *J. Chem. Phys.* **2007**, *127*, 074704.
- [3] L. Zhang, J. Meng, F. Yao, W. Zhang, X. Liu, J. Meng, H. Zhang, *Inorg. Chem.* **2018**, *57*, 12690.
- [4] J. Zhang, V. Haribal, F. Li, *Sci. Adv.* **2017**, *3*, e1701184.
- [5] K. C. Waugh, *Catal. Lett.* **2012**, *142*, 1153.
- [6] W. L. Luyben, *Ind. Eng. Chem. Res.* **2010**, *49*, 6150.
- [7] J. H. Jones, **n.d.**, 12.
- [8] L.-S. Fan, *Chemical Looping Systems for Fossil Energy Conversions*, Wiley-AIChE, Hoboken, NJ, **2010**.
- [9] G. T. Rochelle, *Science* **2009**, *325*, 1652.
- [10] F. He, J. Trainham, G. Parsons, J. S. Newman, F. Li, *Energy Environ. Sci.* **2014**, *7*, 2033.
- [11] F. He, F. Li, *Energy Environ. Sci.* **2015**, *8*, 535.
- [12] I. Johnson, W. T. Choate, A. Davidson, *Waste Heat Recovery. Technology and Opportunities in U.S. Industry*, BCS, Inc., Laurel, MD (United States), **2008**.
- [13] S. Sameshima, M. Kawaminami, Y. Hirata, *J. Ceram. Soc. Jpn.* **2002**, *110*, 597.
- [14] S. Stecura, W. J. Campbell, *THERMAL EXPANSION AND PHASE INVERSION OF RARE-EARTH OXIDES*, **1960**.

Appendix C: Supplementary Information for Chapter 4

ASPEN Plus® process configuration



Column 1: Demethanizer (DM), 2: De-ethanizer (DE), 3: Depropanizer (DP), 4: C2-splitter, 5: C3-splitter, 6: Debutanizer (DB), 7: Deacetylenizer (DA)

Figure C1: ASPEN Plus® flowsheet for ethane cracking.

The ASPEN Plus® simulation model for ethane steam cracking is shown in Figure C1. The upstream and downstream sections have been highlighted and so are the reactor and the compressor. The downstream consists of the quench system, the compressor, the refrigeration unit (cold box), PSA unit and the separation columns. The different columns have been identified in the figure. The pre-heated ethane feed and steam can be seen as the inlet streams to the reactor. The reactor is operated at 850°C. As shown, all of the ethane and propane have been recycled. The major products leaving the system include ethylene and propylene, from the C2 and C3 splitter respectively.

Table C1: Reactions used in the simulations.

Cracking reactor
Ethane cracking
1) $C_2H_6 \rightarrow C_2H_4 + H_2$
2) $C_2H_6 \rightarrow C_2H_2 + 2H_2$
3) $3 C_2H_6 \rightarrow 2 C_3H_6 + 3 H_2$
4) $3 C_2H_6 \rightarrow 2 C_3H_8 + H_2$
5) $2 C_2H_6 \rightarrow C_4H_6 + 3 H_2$
6) $2 C_2H_6 \rightarrow C_4H_8 + 2 H_2$
7) $2 C_2H_6 \rightarrow C_4H_{10} + H_2$
8) $5 C_2H_6 \rightarrow 2 C_5H_{12} + 3 H_2$
9) $3 C_2H_6 \rightarrow C_6H_6 + 6 H_2$
10) $7 C_2H_6 \rightarrow 2 C_7H_8 + 13 H_2$
11) $C_2H_6 + H_2 \rightarrow 2 CH_4$
Propane cracking
12) $C_3H_8 \rightarrow C_3H_6 + 2H_2$
13) $2 C_3H_8 \rightarrow 3 C_2H_4 + 2 H_2$
14) $2 C_3H_8 \rightarrow 3 C_2H_2 + 5 H_2$
15) $4 C_3H_8 \rightarrow 3 C_4H_6 + 7 H_2$
16) $4 C_3H_8 \rightarrow 3 C_4H_8 + 4 H_2$
17) $4 C_3H_8 \rightarrow 3 C_4H_{10} + H_2$
18) $5 C_3H_8 \rightarrow 3 C_5H_{12} + 2 H_2$
19) $2 C_3H_8 \rightarrow C_6H_6 + 5 H_2$
20) $7 C_3H_8 \rightarrow 3 C_7H_8 + 16 H_2$
21) $2 C_3H_8 \rightarrow CH_6 + 5 H_2$
22) $C_3H_8 + 2 H_2 \rightarrow 3 CH_4$
ODH Reactor
Reactions 1 to 11 and the following
23) $C_2H_6 + 5 Mn_3O_4 \rightarrow 2 CO + 3 H_2O + 15 MnO$
24) $C_2H_6 + 7 Mn_3O_4 \rightarrow 2 CO_2 + 3 H_2O + 21 MnO$
25) $H_2 + Mn_3O_4 \rightarrow H_2O + 3 MnO$
26) $C_3H_8 + Mn_3O_4 \rightarrow C_3H_6 + H_2O + 3 MnO$
27) $2 C_3H_8 + 2 Mn_3O_4 \rightarrow 3 C_2H_4 + 2 H_2O + 6 MnO$
28) $C_3H_8 + 10 Mn_3O_4 \rightarrow 3 CO_2 + 4 H_2O + 30 MnO$
29) $C_3H_8 + 7 Mn_3O_4 \rightarrow 3 CO + 4 H_2O + 21 MnO$
Regenerator
30) $6 MnO + O_2 \rightarrow 2 Mn_3O_4$

Table C2: Carbon yield distribution for propane reactions^[1].

	Cracking	ODH
Propane conversion (%)	90	75
% Carbon yield		
Ethane	39.43	
Methane	21.4	
Acetylene	0.58	
Ethylene	2.75	25
Propylene	16.18	20
Propane	10	
Butadiene	3.16	
Butenes	0.04	
Butanes	1.01	
Benzene	2.4	
Toluene	0.45	
CO	0	15
CO ₂	0	15
Others	2.6	

Deacetylenizer conditions

Table C3 provides the conditions used for the deacetylenizer, based on an industrial cracking unit.

For the deacetylenizer, negligible conversion of ethylene to ethane has been assumed ^[2].

Table C3: Deacetylenizer conditions.

Pressure	25 atm
Feed H₂/C₂H₂ ratio	1:1
Feed CO concentration	5-60 ppm (Higher in the ODH case)
Temperature	50-70°C
Feed C₂H₂ concentration	< 0.8 vol%
C₂H₂ to C₂H₄ conversion	80%

Process material flow

Tables C4 and C5 show the molar flow rate of the components in various streams in the process, for the cracking the ODH reference case respectively. The results have been exported from the corresponding Aspen Plus simulations.

Table C4: Material flow in the cracking process.

Cracking process									
	Flowrate in kmol/hr								
			Top stream of the columns						
Component	Feed	Reactor outlet	DM	DE	DP	DA	DB	C2-splitter	C3-splitter
Ethane	4807.0	2580.1	0	2527.9	13.2	2528.0	0	1.5	13.2
Methane	126.5	704.2	435.7	0.4	0	0.7	0	0.7	0
Acetylene	0	47.2	0	46.3	0.3	9.3	0	0	0.3
Ethylene	0	4204.4	20.3	4043.8	0.4	4081.0	0	4077	0.4
Propylene	0	82.6	0	0	82.5	0	0	0	82.1
Propane	126.5	19.5	0	0	19.4	0	0	0	0
Butadiene	0	80.5	0	0	0	0	0.1	0	0
Butenes	0	7.5	0	0	0.1	0	0.6	0	0
Butanes	0	15.4	0	0	6.9	0	8.4	0	0
Pentanes	0	19.9	0	0	0	0	0	0	0
Benzene	0	14.0	0	0	0	0	0	0	0
Toluene	0	2.4	0	0	0	0	0	0	0
CO	0	7.4	1.6	0	0	0	0	0	0
CO ₂	0	0	0	0	0	0	0	0	0
H ₂	0	4441.3	142.2	0	0	14.1	0	14.1	0
H ₂ O	0	2497.9	0	0	0	0	0	0	0

Table C5: Material flow in the ODH reference case.

ODH reference case (85% ethane conversion)									
	Flowrate in kmol/hr								
			Top stream of the columns						
Component	Feed	Reactor outlet	DM	DE	DP	DA	DB	C2-splitter	C3-splitter
Ethane	5353.3	943.1	0	930.8	4.7	930.8	0	0.6	4.7
Methane	140.9	894.9	688.1	0.7	0	0.8	0	0.8	0
Acetylene	0	14.9	0	14.7	0.1	2.9	0	0	0.1
Ethylene	0	4163.9	20.4	4069.1	0.4	4080.9	0	4077	0.4
Propylene	0	140.6	0	0	140.4	0	0	0	139.9
Propane	140.9	60.9	0	0	60.7	0	0	0	0
Butadiene	0	74.8	0	0	0	0	0.1	0	0
Butenes	0	75.8	0	0	1.1	0	4.8	0	0
Butanes	0	1.1	0	0	0.2	0	0.9	0	0
Pentanes	0	12.6	0	0	0	0	0	0	0
Benzene	0	49.8	0	0	0	0	0	0	0
Toluene	0	9.0	0	0	0	0	0	0	0
CO	0	279.2	102.5	0	0	0	0	0	0
CO ₂	0	279	0	0	0	0	0	0	0
H ₂	0	1616.6	104.7	0	0	4.4	0	4.4	0
H ₂ O	0	3918.4	0	0	0	0	0	0	0

Further modifications in energy analyses

Table C6: Modified operating conditions of the separation columns.

Unit	Key component recoveries				Pressure (bar)		Condenser specifications
	Light key	Recovery	Heavy key	Recovery	Condenser	Reboiler	
Demethanizer	Methane	99.90%	Ethylene	0.50%	34	35	Partial with vapor distillate
Deethanizer	Ethylene	99.99%	Propane	0.10%	26	27	Total
Depropanizer	Propylene	99.99%	Iso-butylene	0.1%	10	11	Total
C2-splitter	Ethylene	99.99%	Ethane	0.06%	25	26	Total

Table C7: Modified product distributions used for steam cracking and various ODH cases.

Case	Cracking	ODH		
Component		%C yield		
Ethane conversion (%)	65	67	85	99
Methane	3.40%	3.80%	5.94%	6.83%
Ethane	35.00%	32.20%	13.92%	1.00%
Ethylene	56.10%	57.30%	65.05%	74.81%
Propane	0.10%	0.20%	0.16%	0.19%
Propylene	1.20%	1.20%	2.05%	2.36%
iso-butane	0.20%	0.06%	0.00%	0.00%
n-butane		0.20%	0.07%	0.08%
Propadiene		0.05%	0.04%	0.05%
Acetylene	0.50%	0.46%	1.04%	1.20%
trans-2-butene		0.12%	0.05%	0.06%
1-butene		0.17%	0.12%	0.14%
i-butylene	0.20%	0.08%	0.01%	0.01%
c-2-butene		0.13%	0.05%	0.05%
i-pentane		0.07%	0.00%	0.00%
n-pentane	0.60%	0.07%	0.01%	0.01%
1,3-butadiene	2.10%	2.20%	4.69%	5.39%
Methyl acetylene		0.10%	0.14%	0.16%
trans-2-pentene		0.08%	0.03%	0.04%
2-methyl-2-butene		0.04%	0.01%	0.01%
1-pentene		0.07%	0.02%	0.02%
c-2-pentene		0.06%	0.01%	0.01%
Pentadiene		0.05%	0.21%	0.49%
Cyclopentadiene		0.05%	0.21%	0.00%
Benzene	0.50%	0.05%	1.05%	1.21%
Toluene	0.10%	0.05%	1.05%	1.21%
CO	0.00%	0.70%	1.83%	2.10%
CO2	0.00%	0.50%	2.24%	2.58%

Table C8: Unit-wise distribution of energy demand for all the cases.

Unit	Cracking	ODH 67	ODH 85	ODH 99
Energy Consumed (GJ)/Tonne HVP	0.91	0.91	0.86	0.86
Reactor/Furnace	6.63	0.00	0.00	0.00
Regenerator	0.00	0.00	-1.30	-1.42
Feed and recycle treatment	9.67	3.20	2.55	2.20
Quench	-3.92	-3.38	-2.93	-2.60
Compressor	3.31	2.32	2.04	1.87
Refrigeration steps	2.37	1.63	1.31	1.15
Demethanizer	0.22	0.24	0.23	0.23
De-ethanizer	1.29	1.26	0.94	0.79
C2-splitter	1.53	1.48	1.22	1.22
Depropanizer	0.04	0.02	0.05	0.04
Deacetylenizer	0.00	0.90	0.87	0.69
CO ₂ removal	0	0.02	0.09	0.09
H ₂ purification	0	0.01	0.02	0.02
Total	21.13	7.69	5.09	4.27

Exergy analysis ^[3-5]

Total exergy = Physical exergy + Chemical exergy

- **Physical exergy**, $b_{ph} = (h-h_o) - T_o(s-s_o)$

Quantity X_o stands for the value at the reference state, which is $T_o=298.15K$ and $P_o=1$ atm

- **Chemical exergy**: The environment is the dead (reference) state

Table C9: Chemical exergy of the compounds at reference state.

	X_{ref}(mole fraction)	b_{chem}(kJ/mole)	G (kJ/mole)
N₂	0.765	0.7	0
O₂	0.206	3.9	0
CO₂	0.0003	20.1	-394.4
H₂O	0.019	1.3	-237.1
%RH	60		

For 1 mole $C_xH_yO_z$: $x \cdot CO_2 + a \cdot H_2O = C_xH_yO_z + c \cdot O_2$

- $b_{chem}(C_xH_yO_z) = x \cdot b_{chem}(CO_2) + a \cdot b_{chem}(H_2O) + \Delta G_{(C_xH_yO_z)} - c \cdot b_{chem}(O_2)$
- For change in concentration of reference compounds, subtract the term: $-R.T.ln(x_i \text{ or } RH)$ from the reference value

Table C10: Calculated chemical exergy of the various compounds.

Compound	Formula	ΔG (kJ/mol)	b (kJ/mol)
Ethane	C2H6	1467	1497.5
Methane	CH4	818	832.7
Acetylene	C2H2	1235	1266.8
Ethylene	C2H4	1094	1125.8
Propylene	C3H6	1969	2015.8
Propane	C3H8	2108	2154.2
Butadiene	C4H6	2441	2503.6
Butene	C4H8	2592	2654.1
Butane	C4H10	2749	2810.1
Pentane	C5H12	3386	3462.4
Benzene	C6H6	3202	3297.4
Toluene	C7H8	3820	3930.5
Carbon monoxide	CO	257	275.3
Carbon dioxide	CO2	394	20.1
Hydrogen	H2	237	236.4
Water	H2O	237	1.3
Methyl acetylene	C3H4	1856	1902.8
Propadiene	C3H4	1856	1902.8
Oxygen	O2	0	3.9
Nitrogen	N2	0	0.7
Nitric oxide	NO	181	182.8
Nitrogen dioxide	NO2	66	70.6

Sample exergy calculations

Chemical exergy

Using the values given in Table C9 and ΔG from C10, consider the compound ethane (C_2H_6).

For 1 mole C_2H_6 : $2 \cdot CO_2 + 3 \cdot H_2O = C_2H_6 + 3.5 O_2$

$$\text{➤ } b_{chem(C_2H_6)} = 2. b_{chem(CO_2)} + 3. b_{chem(H_2O)} + \Delta G_{(C_2H_6)} - 3.5. b_{chem(O_2)}$$

$$\text{➤ } b_{chem(C_2H_6)} = 2. (20.1) + 3. (1.3) + 1467 - 3.5. (3.9) = \mathbf{1497.5 \text{ kJ/mol}}$$

Consider the compound carbon monoxide (CO). For 1 mole C₂H₆: $CO_2 = CO + 0.5 O_2$

$$\text{➤ } b_{chem(CO)} = b_{chem(CO_2)} + \Delta G_{(C_2H_6)} - 0.5. b_{chem(O_2)}$$

$$\text{➤ } b_{chem(C_2H_6)} = 20.1 + 257 - 0.5. (3.9) = \mathbf{275.3 \text{ kJ/mol}}$$

- With the calculated chemical exergy of each component, the chemical exergy component of each process stream can be obtained, which along with the physical component, provides the total exergy (of the stream). This is demonstrated in the idealized exergy flow diagram in Figure 4.1.

- With the exergy (or exergy flow in GJ/hr) obtained for each process stream, the exergy loss across each unit can be calculated. It can be normalized per tonne of ethylene product or HVP

$$\text{Exergy loss (across each unit)} = \text{Lost work (GJ/tonne HVP)} = \text{Exergy in} - \text{Exergy out}$$

- With the exergy loss across each unit, the overall exergy loss for the entire process can be calculated and compared with different process schemes

$$\text{Exergy loss (entire process)} = \sum_{(all \ units)} \text{Exergy loss across each unit}$$

Physical exergy

Consider a stream of pure ethane, which has a chemical exergy of 1497.5 kJ/mol as described earlier. Figure C3 shows the change in physical exergy (and total exergy) of the stream with a change in temperature (at 1 atm), which is calculated using the databanks in AspenPlus®. Using a similar method, the exergy loss across each unit is calculated for the processes, which is listed in Table C11. The comparison of the cases is depicted in Figure C4.

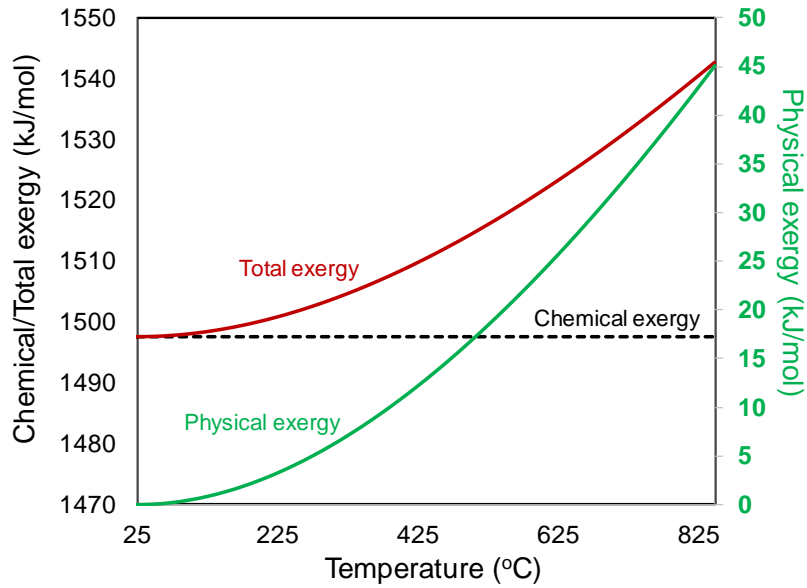


Figure C3: Exergy of an ethane stream with change in temperature.

Table C11: Exergy losses (GJ/tonne HVP) calculated using AspenPlus® functions (excluding chemical exergy).

Separation Unit	Cracking	ODH 67	ODH 85	ODH 99
CO2 scrub	0.000	0.010	0.032	0.034
De-acetylenizer	0.101	0.167	0.189	0.149
PSA	0.000	0.005	0.005	0.008
Demethanizer	0.286	0.296	0.249	0.225
De-ethanizer	0.512	0.493	0.370	0.314
C2-splitter	0.612	0.640	0.488	0.487
Depropanizer	0.015	0.007	0.022	0.017
Total separation	1.526	1.618	1.355	1.233

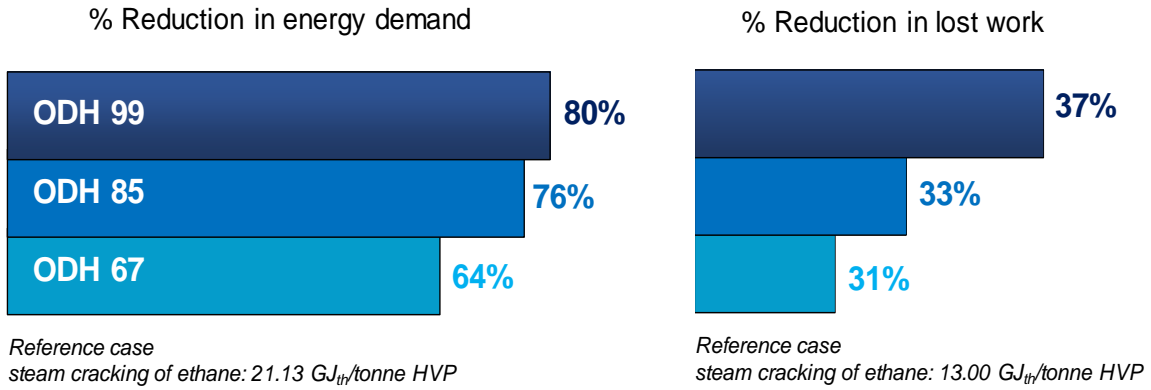


Figure C4: Comparison of ODH cases with ethane steam cracking; a) energy demand (left); and b) lost work (right).

Power Generation Block

The following approach, based on [6], was utilized while calculating the exergy losses in the power generation block as shown in Figure C5.

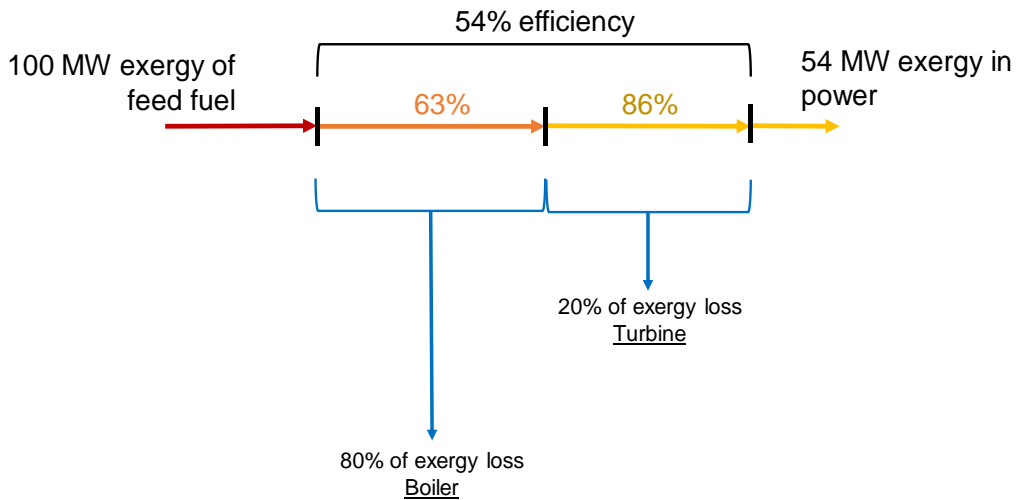


Figure C5: Approach for power generation exergy loss.

CO₂ emissions

Results obtained using the different assumptions, to compare the CO₂ emissions, are presented in Table C12 and Figure C6.

Table C12: CO₂ emissions using the various assumptions (as depicted in Figure C6).

	Steam Cracking	ODH 67	ODH 85	ODH 99
<i>No H₂ Credit</i>	1.256	0.475	0.355	0.306
<i>Mixed Fuel Gas</i>	0.689	0.332	0.265	0.238
<i>with H₂ Credit</i>	0.635	0.318	0.177	0.131
<i>CO₂ Capture Credit</i>	0.635	0.292	0.084	0.038

Available and imported fuel

In Figure C7, all the H₂ has been purified and separated via PSA. Available CO and CH₄ are assumed to be combusted first, with 100% efficiency. The remaining demand is met by importing CH₄.

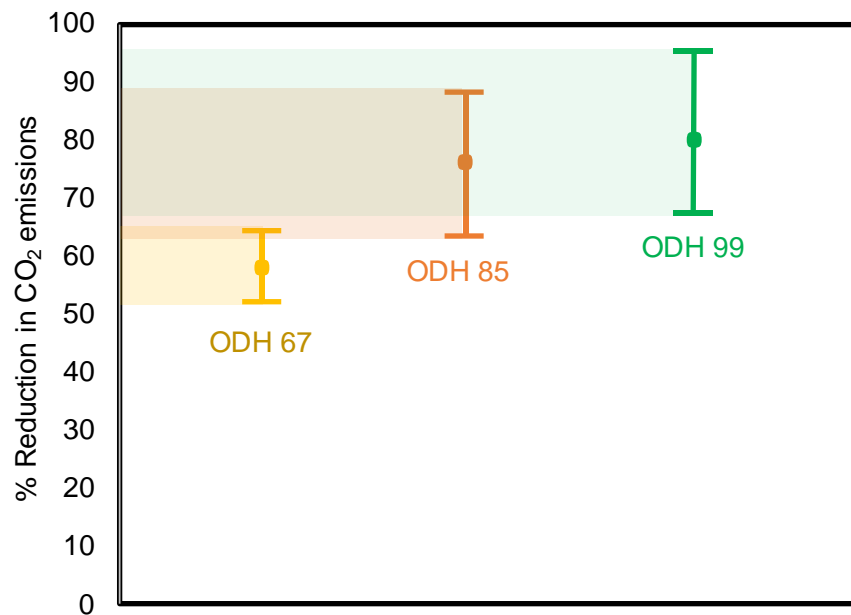


Figure C6: % Reduction in CO₂ emissions for the CL-ODH cases in comparison with steam cracking using different assumptions (range of reductions).

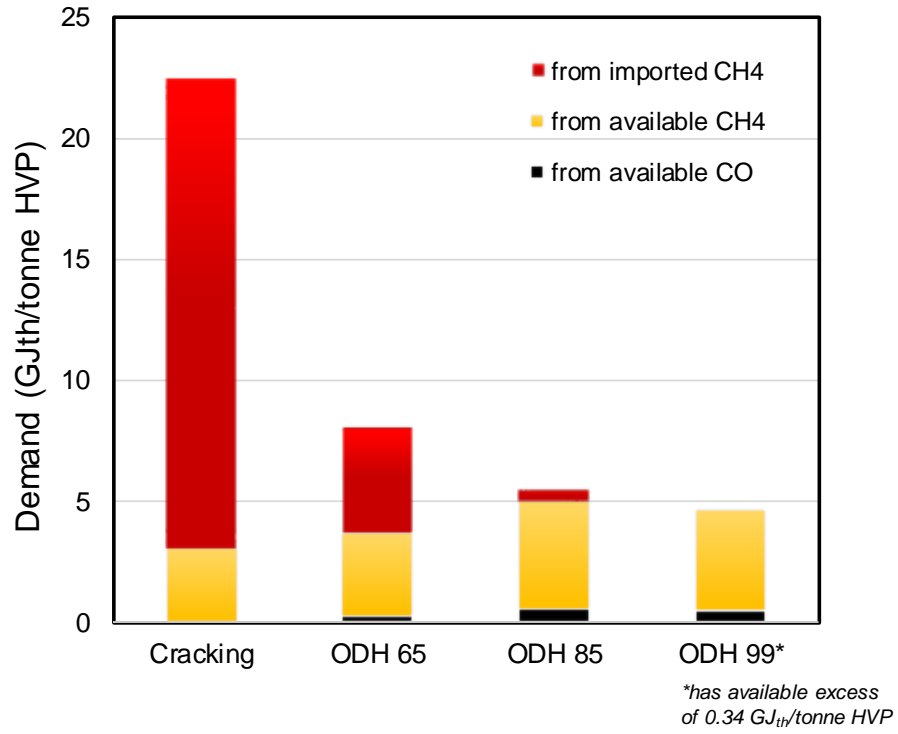


Figure C7: Comparison of the available and imported fuel among all the considered cases.

References

- [1] H. Zimmermann, R. Walzl, in *Ullmanns Encycl. Ind. Chem.*, Wiley & Sons, **2009**.
- [2] G. C. Battiston, L. Dalloro, G. R. Tauszik, *Appl. Catal.* **1982**, 2, 1.
- [3] E. Querol, B. Gonzalez-Regueral, J. L. Perez-Benedito, in *Pract. Approach Exergy Thermo-economic Anal. Ind. Process.*, Springer London, London, **2013**, pp. 9–28.
- [4] R. Rivero, M. Garfias, *Energy* **2006**, 31, 3310.
- [5] J. Szargut, *Appl. Energy* **1989**, 32, 269.
- [6] V. Siva Reddy, S. C. Kaushik, S. K. Tyagi, *Clean Technol. Environ. Policy* **2014**, 16, 489.

Appendix D: Supplementary Information for Chapter 5

Synthesis Procedures

In the solid-state synthesis method, metal oxide and/or metal carbonate precursors were ball milled, pressed into pellets, and then calcined to form the perovskite. In the modified Pechini method, nitrate precursors were dissolved in deionized water at room temperature. The solution was then heated to 50°C with a hot plate while stirring with a stir bar. Citric acid (Sigma-Aldrich, $\geq 99.5\%$) was added at a ratio of 1.75 mole citric acid per mole metal ions. After stirring for 30 minutes, ethylene glycol (Sigma-Aldrich, 99.8%) was added at a molar ratio of 1.5:1 mole ethylene glycol: mole citric acid. This solution was heated to 80°C for the citrate gel to form. Water was driven off until a sticky paste was achieved. The paste was dried and then calcined to form the perovskite. A or B site perovskite dopants were added during the initial synthesis steps and alkali dopants were added by wet impregnation followed by calcination at 900 °C.

Treatment of CL-ODH Product Impurities in the Oligomerizer

All non-ethylene components were treated before ethylene was converted. First, 50% of C4 was converted into C6 (with ethylene) and 50% to C8 through dimerization. The total conversion of 1,3-butadiene was held to 98%. C5 was converted into C7 and C9 (with C4) along the same distribution. Propylene was predicted to form C5, C7, C9, and C11 with C2, C4, C6, and C8 products in a 10%, 40%, 30%, 20% ratio respectively. Benzene was estimated to be inert. To account for complex hydrogenation chemistry over the nickel-based catalyst, all acetylene and methyl acetylene were estimated to be completely converted to ethylene and propylene. Additionally, it was estimated that 15% of the hydrogen recombined to form ethane and that 98%

of CO was methanized. As C6+ was estimated to be singly unsaturated, hydrogen was adjusted to achieve mass balance.

Table D1: Oligomerizer product distributions (wt. %).

Component	Base Case	High Case
Carbon Dioxide	6.24%	24.52%
Carbon Monoxide	0.00%	0.02%
methane	2.32%	2.87%
hydrogen	0.39%	0.01%
ethane	44.49%	23.99%
ethylene	0.88%	0.91%
acetylene	0.00%	0.00%
propane	0.13%	0.24%
propylene	0.00%	0.00%
methyl acetylene	0.00%	0.00%
n-butane	0.19%	0.01%
1-butene	1.16%	1.24%
trans-2-butene	2.59%	2.81%
c-2-butene	2.71%	2.92%
1,3-butadiene	0.01%	0.00%
C5	0.05%	0.06%
Benzene	0.17%	0.87%
C6	14.11%	12.90%
C7	0.48%	0.76%
C8	11.76%	12.32%
C9	0.34%	0.53%
C10	6.45%	7.01%
C11	0.14%	0.23%
C12	3.88%	4.17%
C14	1.51%	1.61%

Process Model Block Diagram and Assumptions

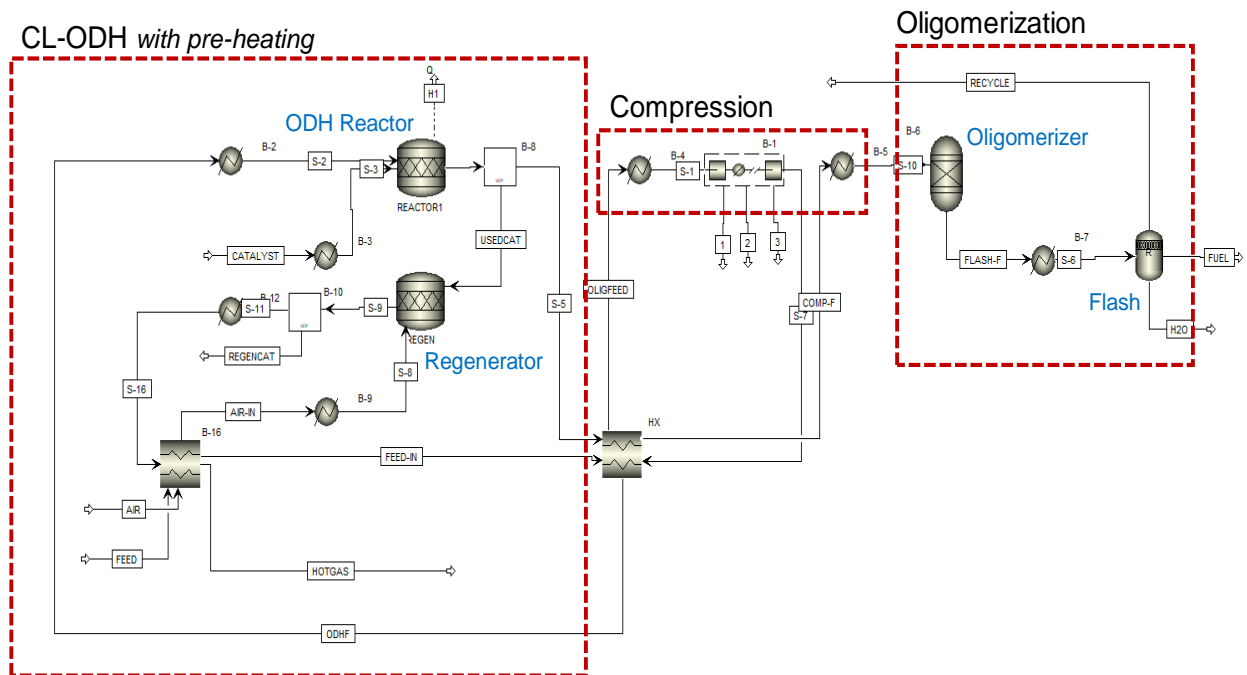


Figure D1: Process Model Flow Diagram.

Table D2: AspenPlus® Models Used.

Stream class	MIXCISLD
Databank	PURE, AQUEOUS, SOLIDS, INORGANIC
Solid components	Mn ₃ O ₄ , MnO, MgO
Property method	PR-BM and STEAM –TA for steam cycles
Unit operation models	
ODH Reactor and Regenerator	RStoic
Oligomerizer	RYield
Compressor	MCompr
Heat exchangers	Heater and MHeatX
Separation/Flash columns	Sep/Flash2

Table D3: AspenPlus® Model Assumptions.

Ambient condition	T = 25°C, P = 1 atm
Reaction assumptions	As per the carbon yield distribution in Table D1
Heat loss in chemical looping reactors	1% of the total thermal output
Chemical looping reactor operating pressure	1 atm
Compressor specifications	4 stage with intercooler at 40°C Isentropic efficiency of 0.72
Air feed (to the regenerator)	10% excess
Chemical to electric energy efficiency*	25% LHV (this system), 27.5% LHV (direct ethane to electric)

*Assumes the use of spark ignition engine to maintain low capital costs.

Table D4: Obtained liquid fuel using different parameters.

Stream	Parameter	Base	High
Ethane feed	kg/hr	162226	
	MW	2140	
Liquid fuel	MW	779.1	949.5
	bbbl/hr	597	731.6
	kg/hr	63596	78761
	kg/m ³	670	677
	gal/hr	25078	30729
	gal/g feed ethane	154.6	189.4
	bbbl/kJ feed ethane	3.25	3.99
	kJ liq fuel/kJ feed ethane	0.364	0.444
	kJ liq fuel/kJ input	0.364	0.468

Table D5: Composition of the liquid fuel obtained after one-stage flash.

Base	mol%	wt%	High	mol%	wt%
C8	25.26	29.80	C8	24.41	28.78
C6	31.31	27.70	C6	28.37	25.09
C10	11.30	16.67	C10	11.30	16.65
C12	5.67	10.03	C12	5.62	9.93
C14	1.89	3.90	C14	1.86	3.84
ethane	10.86	3.43	c-2-butene	4.35	2.56
c-2-butene	3.56	2.10	trans-2-butene	3.97	2.34
trans-2-butene	3.21	1.89	ethane	7.23	2.28
C7	1.11	1.15	Benzene	2.18	1.79
C9	0.65	0.86	CO2	3.74	1.73
1-butene	1.21	0.72	C7	1.65	1.71
C11	0.23	0.37	C9	0.95	1.26
Benzene	0.43	0.35	1-butene	1.50	0.88
CO2	0.76	0.35	C11	0.33	0.54
H2O	1.74	0.33	H2O	1.75	0.33
n-butane	0.22	0.13	C5	0.13	0.10
C5	0.09	0.07	propane	0.16	0.07
ethylene	0.16	0.05	ethylene	0.20	0.06
propane	0.07	0.03	methane	0.29	0.05
methane	0.19	0.03	n-butane	0.01	0.01
1,3-butadiene	0.02	0.01	1,3-butadiene	0.00	0.00
hydrogen	0.05	0.00	CO	0.00	0.00
acetylene	0.00	0.00	hydrogen	0.00	0.00

Table D6: Composition of the recycle gas obtained after one-stage flash.

Base			High		
LHV (MJ/kg)	42.9		LHV (MJ/kg)	27.85	
	mol%	wt%		mol%	wt%
Ethane	68.90	69.98	Ethane	46.41	39.49
H2	9.19	0.63	CO2	32.76	40.79
Methane	6.90	3.74	Methane	10.75	4.88
CO2	6.66	9.90	Cis-2-butene	1.99	3.16
C6	1.89	5.38	Trans-2-butene	1.97	3.13
Cis-2-butene	1.63	3.08	Ethylene	1.91	1.52
Trans-2-butene	1.59	3.01	C6	1.70	4.06
Ethylene	1.47	1.39	1-Butene	0.94	1.50
1-Butene	0.76	1.44	H2O	0.58	0.29
H2O	0.58	0.35	H2	0.37	0.02
C8	0.13	0.49	Propane	0.29	0.36
Propane	0.13	0.19	C8	0.13	0.40
N-butane	0.11	0.22	Benzene	0.10	0.21
Benzene	0.02	0.05	CO	0.04	0.03
C7	0.02	0.06	C7	0.03	0.07
N-pentane	0.01	0.04	N-pentane	0.02	0.04
Butadiene	0.01	0.02	C10	0.01	0.03
C10	0.01	0.03	N-butane	0.01	0.01
C9	0.00	0.00	Butadiene	0.00	0.00
C12	0.00	0.00	C9	0.00	0.01
C11	0.00	0.00	C12	0.00	0.00
C14	0.00	0.00	C11	0.00	0.00
Propylene	0.00	0.00	C14	0.00	0.00
Isobutane	0.00	0.00	Propylene	0.00	0.00
Propadiene	0.00	0.00	Isobutane	0.00	0.00
Acetylene	0.00	0.00	Propadiene	0.00	0.00
Iso-butylene	0.00	0.00	Acetylene	0.00	0.00
	0.00	0.00	Iso-butylene	0.00	0.00
Total	3424	101.4	Total	3095	109.4

Table D7: Results of the energy and power analyses of the two cases.

Base Case	Gcal/hr	MW	MW _{elec}	
Reactor	0		0	
Regenerator	-26		-9.1	Heat at 800. Assumed to be used for electricity generation with 35% efficiency
Pre-treatment	0		0	
Pre-compression cooling	-39		-13.65	Cooling from roughly 420 to 100. Used for electricity with 35% efficiency
Compression		23.56	23.56	
Oligomerizer	-49		0	Heat released at 150. Low quality heat. Is assumed to be negligible for electricity generation
Product flash (cooling)	-16		0	Cooling from 150 to 25. Low quality heat. Is assumed to be negligible for electricity generation
Total			0.81	
Total			23.56	Assuming power required only for compression

High Case	Gcal/hr	MW	MW _{elec}
Reactor	0		0
Regenerator	-134		-46.9
Pre-treatment	0		0
Pre-compression cooling	-57		-19.95
Compression		27.95	27.95
Oligomerizer	-57		0
Product flash (cooling)	-16		0
Total			-38.9
Total			27.95

High ROC case

The following Table E3 shows the product distribution used for the high ROC case:

Component	%C yield
Hydrogen	0.0
Methane	9.6
Acetylene	0.6
Ethylene	35.6
Ethane	2.8
Propadiene	0.7
Propylene	13.0
Propane	0.2
C4s	0.0
Butadiene	3.4
Butene	2.5
Butane	0.1
Benzene	14.2
Toluene	0.0
Xylene	0.0
Ethyl benzene	8.7
Styrene	0.0
Naphthalene	0.0
n-pentane	1.6
n-hexane	2.4
iso-heptane	0.0
iso-octane	0.0
cyclohexane	0.0
TMB	0.0
Dodecane	0.0
CO	1.3
CO ₂	3.4

Process material flow

Tables E4 and E5 show the molar flow rate of the components in various streams in the process, for the cracking the ROC case respectively. The results have been exported from the corresponding AspenPlus simulations.

Table E4: Material flow (kmol/hr) in the cracking process.

	Feed	Outlet	DM top	DE top	DP top	C2-split top	C3-split top	DB top
Hydrogen	0	327.6	16.9	0	0	1.4	0	0
Methane	0	287.5	218.3	0.2	0	0.2	0	0
Acetylene	0	8.3	0	7.9	0	1.2	0	0
Ethylene	0	409.1	2.0	391.4	0	397.7	0	0
Ethane	0	41.5	0	39.8	0.2	0	0.2	0
Propadiene	0	6.8	0	0	6.0	0	0	0
Propylene	0	102.9	0	0	93.9	0	93.5	0
Propane	0	2.5	0	0	2.3	0	0	0
Vinyl acetylene	0	1.2	0	0	0	0	0	0
Butadiene	0	25.7	0	0	0	0	0	0
Butene	0	17.6	0	0	0.2	0	0	1.5
Butane	0	0.9	0	0	0	0	0	0.7
Benzene	0	55.9	0	0	0	0	0	0
Toluene	0	9.2	0	0	0	0	0	0
Xylene	0	3.3	0	0	0	0	0	0
Ethyl benzene	0	1.3	0	0	0	0	0	0
Styrene	0	4.1	0	0	0	0	0	0
Dodecane	0	7.5	0	0	0	0	0	0
n-pentane	0	9.9	0	0	0	0	0	0
n-hexane	500	90.0	0	0	0	0	0	0
iso-heptane	0	7.1	0	0	0	0	0	0
iso-octane	0	3.1	0	0	0	0	0	0
cyclohexane	0	4.3	0	0	0	0	0	0
TMB	0	3.0	0	0	0	0	0	0
Dodecane	0	0.0	0	0	0	0	0	0

Table E5: Material flow (kmol/hr) in the ROC process

	Feed	Outlet	DM top	DE top	C2-split top	DP top	C3-split top	DB top
METHANE	0.0	229.8	211.9	0.2	0.2	0.0	0.0	0.0
ETHANE	0.0	30.9	0.0	29.6	0.0	0.1	0.1	0.0
ETHYLENE	0.0	479.3	2.2	464.9	467.2	0.0	0.0	0.0
PROPANE	0.0	5.7	0.0	0.0	0.0	5.1	0.0	0.0
PROPYLENE	0.0	162.4	0.0	0.0	0.0	146.7	146.1	0.0
ISOBUTANE	0.0	0.1	0.0	0.0	0.0	0.0	0.0	0.1
N-BUTANE	0.0	0.8	0.0	0.0	0.0	0.0	0.0	0.5
PROPADIENE	0.0	0.2	0.0	0.0	0.0	0.2	0.0	0.0
ACETYLENE	0.0	4.4	0.0	4.2	0.0	0.0	0.0	0.0
TRANS-2-BUTENE	0.0	2.3	0.0	0.0	0.0	0.0	0.0	1.5
1-BUTENE	0.0	51.8	0.0	0.0	0.0	0.0	0.0	37.8
ISOBUTYLENE	0.0	0.5	0.0	0.0	0.0	0.0	0.0	0.4
CARBON-DIOXIDE	0.0	39.9	0.0	0.0	0.0	0.0	0.0	0.0
CIS-2-BUTENE	0.0	1.9	0.0	0.0	0.0	0.0	0.0	1.2
2-METHYL-BUTANE	0.0	0.0	0.0	0.0	0.0	0.0	0.0	0.0
N-PENTANE	0.0	0.1	0.0	0.0	0.0	0.0	0.0	0.0
1,3-BUTADIENE	0.0	30.4	0.0	0.0	0.0	0.0	0.0	21.8
METHYL-ACETYLENE	0.0	0.7	0.0	0.0	0.0	0.6	0.0	0.0
TRANS-2-PENTENE	0.0	1.2	0.0	0.0	0.0	0.0	0.0	0.1
2-METHYL-2-BUTENE	0.0	5.6	0.0	0.0	0.0	0.0	0.0	0.2
1-PENTENE	0.0	0.5	0.0	0.0	0.0	0.0	0.0	0.1
CIS-2-PENTENE	0.0	0.8	0.0	0.0	0.0	0.0	0.0	0.0
CARBON-MONOXIDE	0.0	39.9	37.0	0.0	0.0	0.0	0.0	0.0
N-HEXANE	500.0	117.1	0.0	0.0	0.0	0.0	0.0	0.0
BENZENE	0.0	0.9	0.0	0.0	0.0	0.0	0.0	0.0
ETHYLBENZENE	0.0	6.9	0.0	0.0	0.0	0.0	0.0	0.0
HYDROGEN	0.0	40.3	37.4	0.0	0.0	0.0	0.0	0.0
WATER	0.0	214.1	0.0	0.0	0.0	0.0	0.0	0.0

References

- [1] H. Zimmermann and R. Walzl, "Ethylene," in *Ullmann's Encyclopedia of Industrial Chemistry*, Wiley & Sons, 2009.
- [2] G. C. Battiston, L. Dalloro, and G. R. Tauszik, "Performance and aging of catalysts for the selective hydrogenation of acetylene: a micropilot-plant study," *Appl. Catal.*, vol. 2, no. 1, pp. 1–17, Jan. 1982